12-12-2013

Influence of Morphology and Environment on the Electrochemical Reactivity of NiO

Neil Spinner
University of Connecticut, neil.spinner@gmail.com

Influence of Morphology and Environment on the Electrochemical Reactivity of NiO

Neil S. Spinner, Ph.D.

University of Connecticut, 2013

In this thesis, nickel oxide was investigated as an electrocatalyst and electrode material in both aqueous and non-aqueous media. The effects of morphology resulting from several different synthesis techniques were examined for the electrocatalytic oxidation of methanol in alkaline media and the Li^+ mass transport in lithium-ion batteries. Effects of environment changes, including electrocatalyst/electrode additives and choice of media, were also investigated to determine their influence on the reactivity and mechanism for the oxidation of organics such as methane and methanol. For the conversion of methane at room temperature, an array of oxygenate products were identified and theoretical reaction pathways and mechanisms were proposed. Using the current pulse relaxation technique, Li^+ diffusion coefficients were obtained, and a two-phase parallel resistance model was developed to deconvolute the diffusivity through multiple phases in nickel oxide anodes during lithium-ion battery charging. Identical-location transmission electron microscopy was also used to observe degradation of individual anode particles, and the importance of conductivity in addition to structure was examined.

Influence of Morphology and Environment on the Electrochemical Reactivity of NiO

Neil S. Spinner

B.S., University of New Hampshire, 2009

A Dissertation

Submitted in Partial Fulfillment of the

Requirements for the Degree of

Doctor of Philosophy

at the University of Connecticut

2013

APPROVAL PAGE

Doctor of Philosophy Dissertation

"Influence of Morphology and Environment on the Electrochemical Reactivity of NiO"

Presented by

Neil S. Spinner, B.S.

Major Advisor _____
William Mustain

Associate Advisor _____
Yu Lei

Associate Advisor _____
Radenka Maric

Associate Advisor _____
Steven Suib

Associate Advisor _____
Brian Willis

University of Connecticut

2013

ACKNOWLEDGMENTS

There are many people I need to thank who have all been positive influences in my life over the past four and a half years, and without whom I would undoubtedly not have completed this degree. First and foremost is my incredible wife, Kate. You are my best friend and I couldn't have dreamt of a more amazing partner to share my life with. I am also extremely grateful to my advisor, Dr. William Mustain, for guiding me through this whole process and showing me what it takes to be a Ph.D.-level engineer. I could not have handpicked a more perfect advisor or graduate school scenario, and I am immensely appreciative for everything you have done for me. I would also like to thank my family for being incredibly supportive during my Ph.D. studies.

Thank you to Pete Menard and Garry Barnes at the Center for Clean Energy Engineering for helping me with equipment setup and training, but especially for early morning chats and coffee/sandwich trips. I always looked forward to and really enjoyed those days, particularly when my research wasn't going as smoothly as anticipated. Appreciation is also due to Mark Drobney at Technical Services, who always patiently listened to my confusing explanations and skillfully crafted numerous custom designs. I am also indebted to my fellow labmates Jose Vega, Ying Liu, Sujan Shrestha, Greg Crettol, Travis Omasta,

Matteo Brambilla, and Alessandro Palmieri for their collaboration and especially their friendship.

Last but certainly not least, I must express my deepest gratitude to Aida Ghiaei, Kazem Kazerounian and Doug Cooper for affording me the opportunity to have the NSF GK-12 Fellowship for two years. Aida, you are a wonderful woman who made the lives of every GK-12 Fellow infinitely easier and more enjoyable, and I will never forget what a pleasure it was working and spending time with you, both inside and outside of GK-12 activities. Thank you also to John Hoyle at Howell Cheney Technical High School. Working with you and your CADD students during my two years as a GK-12 Fellow were some of the most enriching, educational, and wildly entertaining days during my time at UConn. Finally, to my friends Andrea, Juanpa, Justin and Andy: thank you for many fun conversations and social gatherings that helped me maintain my sanity.

TABLE OF CONTENTS

ACKNOWLEDGMENTS …… IV

LIST OF TABLES …… XIII

LIST OF FIGURES …… XIV

SECTION I: INTRODUCTION …… 1

CHAPTER 1: REVIEW OF VARIOUS NICKEL OXIDE MORPHOLOGIES AND ENVIRONMENTS …… 2

1.1 High Temperature Applications …… 2

1.2 NiO Morphologies for Aqueous Systems …… 3

1.3 NiO Electrocatalyst Additives and Alloys …… 6

1.4 Lithium-ion Battery Anodes …… 8

CHAPTER 2: REVIEW OF LOW TEMPERATURE CARBONATE AND CARBON DIOXIDE ELECTROCHEMICAL UTILIZATION SYSTEMS …… 14

2.1 Electrochemical Carbon Dioxide Utilization …… 14

2.1.1 Background 15

2.1.2 Syngas Production 17

2.1.3 Hydrocarbon Products 25

2.1.4 Summary of Electrochemical CO_2 Utilization 34

2.2 CO_2 in Low Temperature Fuel Cells 35

2.3 Room Temperature Carbonate Devices 37

SECTION II: CARBONATE AND HYDROXIDE ALKALINE ELECTROCHEMICAL SYSTEMS 39

CHAPTER 3: EFFECT OF NICKEL OXIDE SYNTHESIS CONDITIONS ON ITS PHYSICAL PROPERTIES AND ELECTROCATALYTIC OXIDATION OF METHANOL 40

3.1 Experimental 41

3.1.1 Materials Synthesis 41

3.1.2 Instrumentation and Techniques 42

3.1.3 Electrochemical Tests 43

3.2 Results and Discussion 44

3.2.1 SEM and BET Analysis 44

3.2.2 X-ray Diffraction 48

3.2.3 Simultaneous Thermal Analysis 53

3.2.4 X-ray Photoelectron Spectroscopy 56

3.2.5 Cyclic Voltammetry 61

3.2.6 Electrochemical Impedance Spectroscopy 75

3.3 Summary 82

CHAPTER 4: INFLUENCE OF NON-CONDUCTING ZIRCONIA ON THE ELECTROCHEMICAL PERFORMANCE OF NICKEL OXIDE IN ALKALINE MEDIA 84

4.1 Experimental 85

4.1.1 Materials Synthesis 85

4.1.2 Instrumentation and Techniques 86

4.1.3 Electrochemical Tests 87

4.2 Results and Discussion 88

4.2.1 Physical Characterization 88

4.2.2 Electrochemical Tests 99

4.3 Summary 107

CHAPTER 5: ELECTROCHEMICAL METHANE ACTIVATION AND CONVERSION TO OXYGENATES AT ROOM TEMPERATURE 109

5.1 Experimental 110

5.1.1 Electrocatalyst Synthesis Methods 110

5.1.2 Aqueous-Phase Electrochemical Tests 111

5.1.3 Flow Cells and MEA Preparation 113

5.1.4 Physical Characterization 117

5.2 Results and Discussion 118

5.2.1 NiO Performance 118

5.2.2 Activation of CH_4 with NiO-ZrO_2 122

5.3 Summary 138

SECTION III: LITHIUM-ION BATTERIES 140

CHAPTER 6: NANOSTRUCTURAL EFFECTS ON THE CYCLE LIFE AND Li^+ DIFFUSION COEFFICIENT OF NICKEL OXIDE ANODES 141

6.1 Experimental 142

6.1.1 Nickel Oxide Synthesis 142

6.1.2 Electrode Fabrication 143

6.1.3 Physical Characterization 143

6.1.4 Electrochemical Tests 144

6.2 Results and Discussion 145

6.2.1 Electrode Characterization and Battery Performance 145

6.2.2 Current Pulse Relaxation 163

6.2.3 Volume Expansion During Charging 173

6.2.4 Li^+ Mass Transport 177

6.3 Summary 185

6.4 Symbols and Nomenclature 185

CHAPTER 7: INVESTIGATION OF METAL OXIDE ANODE DEGRADATION IN LITHIUM-ION BATTERIES VIA IDENTICAL-LOCATION TEM 188

7.1 Experimental 189

7.1.1 OMNiO Synthesis 189

7.1.2 Anode Fabrication 191

7.1.3 Coin Cell Fabrication 191

7.1.4 Physical and Electrochemical Characterization 192

7.1.5 Identical-Location TEM Grid Experiments 193

7.2 Results and Discussion 193

7.2.1 Physical Characterization 193

7.2.2 Charge/Discharge Coin Cell Analysis 198

7.2.3 Identical-Location TEM 205

7.2.4 Electrochemical Impedance Spectroscopy 213

7.3 Summary …… 215

SECTION IV: OUTREACH ACTIVITIES …… 217

CHAPTER 8: UCONN NSF GK-12 PROGRAM …… 218

SECTION V: CONCLUSIONS …… 228

SECTION VI: RECOMMENDATIONS FOR FUTURE WORK ……. 233

REFERENCES …… 236

LIST OF TABLES

Table 3.1. XPS resolved peak positions and relative areas for Ni 2p and O 1s spectra, for reflux-NiO and RT NaOH-NiO. 60

Table 4.1. Binding energies for (80:20)NiO:t-ZrO_2 composite, (80:20)NiO:t-ZrO_2 physical mixture, single-phase NiO, and single-phase t-ZrO_2 particles for primary peak locations of elements O, Ni, and Zr. 94

Table 5.1. XPS binding energy values for NiO, ZrO_2, and NiO-ZrO_2 bifunctional electrocatalyst and physical mixtures for O 1s, Ni 2p, and Zr 3d spectra. 128

Table 6.1. Effective diffusion coefficients, D_{eff}, calculated from Current Pulse Relaxation (CPR) data as a function of state of charge (SOC). 172

LIST OF FIGURES

Figure 1.1. Candidate anode materials for lithium-ion batteries and their theoretical capacities. 10

Figure 2.1. Summary of electrochemical conversion pathways for CO_2; **EtOH**: ethanol; **PrOH**: propanol; **HAc**: acetic acid; **HCHO**: formaldehyde. 16

Figure 2.2. Polarization and power curves for a solid oxide fuel cell with a Ni-YSZ-CeO_2 catalyst operated at 800°C for (□,○): H_2 fuel and (■,●): CH_4/CO_2 fuels [66]. 19

Figure 2.3. Polarization curves for a solid oxide fuel cell with an LSCM-CZY-Pd in YSZ fuel side electrode operated at 800°C with various CO_2:CO fuel stream ratios. (♦): 100:0; (■): 90:10; (▲): 50:50; (●): 10:90 [68]. 20

Figure 2.4. Proposed molecular mechanisms for dry reforming over a Ni-YSZ-CeO_2 solid oxide fuel cell electrode [66]. 22

Figure 2.5. Reaction rates for (▲) CH_4 and (■) CO_2, and rates of formation of (●) CO and (○) coke as a function of temperature for a solid oxide fuel cell with a Ni-YSZ-CeO_2 electrode [66]. 23

Figure 2.6. Current efficiencies for (■) CO, (□) H_2, and (Δ) HCOOH, and (- - -) overall current density (plotted on secondary y-axis) as functions of (negative) electrode potential for aqueous phase CO_2 reductions over a cobalt-Pc gas-diffusion electrode [72]. 29

Figure 2.7. Current efficiencies as a function of (negative) electrode potential for (■) CO, (○) NH_3, (◊) urea, and (Δ) HCOOH products from aqueous phase CO_2 reductions with NO_2^- ions over (A) cobalt-Pc and (B) nickel-Pc gas-diffusion electrodes. Edited from [83]. 30

Figure 3.1. SEM micrographs of reflux-precipitated (A) $Ni(OH)_2$ and (B) NiO, and RT NaOH-precipitated (C) $Ni(OH)_2$ and (D) NiO. 45

Figure 3.2. SEM micrographs of (A) RT NaOH-NiO and (B) BT NaOH-NiO. All nanoparticles were calcined in air at 500°C for 6 hours. 47

Figure 3.3. XRD patterns for (A) reflux-$Ni(OH)_2$, (B) RT NaOH-$Ni(OH)_2$, and (C) BT NaOH-$Ni(OH)_2$ precursors. Inset shows the average grain boundary size calculated from the Scherrer Equation for all three precursors using data from peaks at 19.2°, 33.0°, 38.5°, 52.0°, 58.9°, and 62.6°. Error bars represent standard deviation. 49

Figure 3.4. XRD patterns for (A) reflux-NiO, (B) RT NaOH-NiO, and (C) BT NaOH-NiO. Inset shows average Scherrer Equation grain boundary sizes calculated from all five peak locations. Error bars represent standard deviation. 52

Figure 3.5. STA curves: (A) DSC and (B) TGA for reflux-$Ni(OH)_2$ and RT NaOH-$Ni(OH)_2$. Temperature range was 25-1100°C, and heating/cooling rate was 15°C/min. Negative DSC values corresponded to exothermic heat flow. 54

Figure 3.6. Deconvoluted XPS Ni 2p spectra for (A) reflux-NiO and (B) RT NaOH-NiO. 57

Figure 3.7. Deconvoluted XPS O 1s spectra for (A) reflux-NiO and (B) RT NaOH-NiO. 58

Figure 3.8. CVs from -0.1V to 1.05V vs. SCE in (A) 0.005M KOH and (B) 0.005M KOH/0.1M CH_3OH for reflux-NiO and RT NaOH-NiO. Scan number 20 is shown for each CV, and the scan rate was 20 mV/s. ... 62

Figure 3.9. CVs from -0.1V to 1.05V vs. SCE in (A) 0.005M KOH and (B) 0.005M KOH/0.1M CH_3OH for BT NaOH-NiO. Scan number 20 is shown for each CV, and the scan rate was 20 mV/s. 64

Figure 3.10. CVs from -0.1V to 1.05V vs. SCE in 0.1M Na_2CO_3/0.1M CH_3OH for reflux-NiO and RT NaOH-NiO. Scan number 20 is shown for each CV, and the scan rate was 20 mV/s. 65

Figure 3.11. CV from -0.1V to 1.05V vs. SCE in 0.1M Na_2CO_3/0.1M CH_3OH for BT NaOH-NiO. Scan number 20 is shown, and the scan rate was 20 mV/s. 66

Figure 3.12. Stability CVs for entire working range of -1.1V to 1.2V vs. SCE in 0.1M Na_2CO_3/0.1M CH_3OH: (A) reflux-NiO current build-up; (B) reflux-NiO current deterioration; (C) RT NaOH-NiO current build-up; (D) RT NaOH-NiO current deterioration. A total of 200 scans were run for each material at 20 mV/s. 69

Figure 3.13. Stability plot of percent of maximum methanol oxidation current over 200-scan range versus the number of the consecutive scan for (a) reflux-NiO and (b) RT NaOH-NiO. 73

Figure 3.14. IR-corrected Nyquist plots for reflux-NiO in (A),(B),(C) 0.005M KOH/0.1M CH_3OH and (D),(E),(F) 0.1M Na_2CO_3/0.1M CH_3OH. Data was taken every 50mV from 0.50 to 1.05V vs. SCE for KOH electrolyte and from 0.60 to 1.05V vs. SCE for carbonate electrolyte. Frequency was ranged from 100mHz to 1MHz. 76

Figure 3.15. IR-corrected Nyquist plots for RT NaOH-NiO in (A),(B),(C) 0.005M KOH/0.1M CH_3OH and (D),(E),(F) 0.1M Na_2CO_3/0.1M CH_3OH. Data was taken every 50mV from 0.50 to 1.05V vs. SCE for KOH electrolyte and from 0.60 to 1.05V vs. SCE for carbonate electrolyte. Frequency was ranged from 100mHz to 1MHz. 77

Figure 3.16. Equivalent electrical circuit for EIS data from NiO-catalyzed methanol oxidation in alkaline media. R_Ω was the ohmic resistance, $R_{ct,1}$, $R_{ct,2}$, and $R_{ct,3}$ were the charge transfer resistances and $C_{d,1}$, $C_{d,2}$, and $C_{d,3}$ were the double layer capacitances for the three reactions occurring in solution: Ni^{+2}/Ni^{+3} redox, methanol oxidation, and OER, respectively. 78

Figure 3.17. Comparison graphs for charge transfer resistances calculated from EIS data in 0.005M KOH/0.1M CH_3OH. Magnitude of resistance was shown as a function of potential for (A) the Ni^{+2}/Ni^{+3} redox reaction, $R_{ct,1}$, and (B) the methanol oxidation reaction, $R_{ct,2}$, over (a) reflux-NiO and (b) RT NaOH-NiO. 80

Figure 4.1. SEM micrographs of (A) single-phase NiO and (B) (80:20)NiO:t-ZrO_2 electrocatalysts. 89

Figure 4.2. Deconvoluted XPS spectra for Ni 2p, O 1s, and Zr 3d elemental regions for (80:20)NiO:t-ZrO_2. 93

Figure 4.3. XRD patterns for (A) precipitated precursors of (80:20)NiO:t-ZrO_2 composite, single-phase NiO ($Ni(OH)_2$), and single-phase t-ZrO_2 ($Zr(OH)_4$) materials; and (B) calcined (80:20)NiO:t-ZrO_2, NiO, and t-ZrO_2. Scans recorded at a rate of 1.3 °/min between 2θ values of 10-90°. 96

Figure 4.4. Electrochemical tests in N_2- and CH_4-saturated 0.1M Na_2CO_3: (A) CVs for single-phase NiO; (B) EIS for single-phase NiO at 0.7V vs. SCE; (C) CVs for (80:20)NiO:t-ZrO_2; and (D) EIS for (80:20)NiO:t-ZrO_2 at 0.7V vs. SCE. All scans performed at room temperature (25°C), CV scan rates were 20 mV/s, and EIS data collected between frequencies of 100mHz to 1MHz. 100

Figure 4.5. CVs in N_2- and CH_4- saturated 0.005M KOH for (80:20)NiO:t-ZrO_2. Scans performed at room temperature (25°C) and scan rates of 20 mV/s. 104

Figure 4.6. Physical characterization of partial oxidation products for CH_4 by CO_3^{2-}. (A) ATR-FTIR showing formaldehyde as the primary product; (B) and (C) air-free mass spectra for HCHO and CO dominated products. 106

Figure 5.1. Operational diagram of flow cell with anode effluent analyzed using Mass Spectrometry. 115

Figure 5.2. Polarization curves for flow cell with NiO-ZrO_2 bifunctional electrocatalyst as the anode and $Ca_2Ru_2O_7$ pyrochlore as the cathode electrocatalyst. **A:** and **C:** represent the gases flowed on the anode and cathode streams, respectively. Relative humidity was 90%, gas flow rates were 0.1L/min, scan rate was 50mV/s, and cell temperature was 40°C. 116

Figure 5.3. Physical characterization synthesized NiO electrocatalyst: a) SEM micrograph; b) XRD pattern; c) deconvoluted Ni 2p XPS spectrum; and d) deconvoluted O 1s XPS spectrum. 120

Figure 5.4. Electrochemical tests: a) CVs and b) EIS IR-corrected Nyquist plots for NiO electrocatalyst. All tests were conducted in N_2- and CH_4-saturated 0.1M Na_2CO_3 electrolyte at room temperature (25°C), CV scan rates were 20mV/s, and EIS data was obtained at 0.7V vs. SCE between 100mHz and 1MHz. 121

Figure 5.5. Physical characterization of synthesized $NiO\text{-}ZrO_2$ bifunctional electrocatalyst: a) SEM micrograph; and b) XRD pattern. 124

Figure 5.6. Deconvoluted Ni 2p XPS spectra for a) $NiO\text{-}ZrO_2$ bifunctional electrocatalyst; and b) physical mixture of NiO and ZrO_2. 125

Figure 5.7. Deconvoluted O 1s XPS spectra for a) tetragonal-phase ZrO_2; b) $NiO\text{-}ZrO_2$ bifunctional electrocatalyst; and c) physical mixture of NiO and ZrO_2, and deconvoluted Zr 3d XPS spectra for d) tetragonal-phase ZrO_2; e) $NiO\text{-}ZrO_2$ bifunctional electrocatalyst; and f) physical mixture of NiO and ZrO_2. 126

Figure 5.8. Electrochemical tests: a) CVs and b) EIS IR-corrected Nyquist plots for $NiO\text{-}ZrO_2$ bifunctional electrocatalyst. All tests were conducted in N_2- and CH_4-saturated 0.1M Na_2CO_3 electrolyte at room temperature (25°C), CV scan rates were 20mV/s, and EIS data was obtained at 0.7V vs. SCE between 100mHz and 1MHz. 129

Figure 5.9. Characteristic oxidation CVs in 0.1M Na_2CO_3 electrolyte using $NiO\text{-}ZrO_2$ bifunctional electrocatalyst for a) CH_3OH; b) CO; and c) HCHO. Scans were conducted at room temperature (25°C) and scan rates were 20mV/s. 131

Figure 5.10. Product characterization tests: a) ^{1}H-NMR spectrum collected at 1.8V electrode potential; and b) MS spectra for anode effluent collected at 2.0V device voltage for Case 1 (no ionomer) and Case 2 (with ionomer). 132

Figure 5.11. Reaction mechanisms for a) formation of CH_3OH from CH_4 and CO_3^{2-} with byproducts of CO_2 and $2e^-$; and b) formation of C-C bond in C_2H_5OH through C=O bond resonance in HCHO. 136

Figure 5.12. Proposed reaction pathways for activation of CH_4 with CO_3^{2-} anions. 137

Figure 6.1. SEM images for (A) R-NiO and (B) N-NiO anodes prior to testing. 146

Figure 6.2. Nitrogen adsorption isotherms at 77K for R-NiO and N-NiO. ... 148

Figure 6.3. First five CVs for (A) R-NiO and (B) N-NiO anodes between 0.001 – 3.0V vs. Li/Li^+ at a scan rate of 0.1 mV/s. 150

Figure 6.4. First 10 charge (C)/discharge (D) (lithiation/delithiation) cycles for (A) R-NiO and (B) N-NiO anodes between 0.001 – 3.0V vs. Li/Li^+ at C/5 rate. 152

Figure 6.5. Plot of capacities and energy losses for both R-NiO and N-NiO over the first 30 cycles at C/5 charge/discharge rate. Energy loss is defined as 100% • (1 – Faradaic efficiency), and it is the percent difference of charge and discharge capacities for each complete cycle. 153

Figure 6.6. First 10 charge (C)/discharge (D) (lithiation/delithiation) cycles for G5 graphite anode between 0.001 – 1.0V vs. Li/Li^+ at C/5 rate. 155

Figure 6.7. Plot of capacities and energy losses for G5 graphite anode over the first 30 cycles at C/5 charge/discharge rate. Energy loss is defined as 100% • (1 – Faradaic efficiency), and it is the percent difference of charge and discharge capacities for each complete cycle. 157

Figure 6.8. SEM images for (A) R-NiO and (B) N-NiO anodes after 100 charge/discharge cycles. 158

Figure 6.9. Reaction diagram illustrating volume expansion during NiO decomposition and reconstitution reactions for one complete charge/discharge cycle. 161

Figure 6.10. XRD for R-NiO and N-NiO anodes before and after 100 charge/discharge cycles. Spectra collected between 2θ values of 10° and 90° at a sweep rate of 1.3°/min. 162

Figure 6.11. Plot of open-circuit voltage (OCV) vs. x for R-NiO and N-NiO. 170

Figure 6.12. Plot of ΔE vs. $t^{-1/2}$ with linear fits used to calculate the Li^+ diffusion coefficients with the CPR method. Data shown for (A) R-NiO and (B) N-NiO anode for $0.5 \leq x \leq 1.0$ after a 1C rate current was pulsed for 5s. 171

Figure 6.13. Plot with linear fits using mass transport diffusion model for calculating NiO and Li_2O+Ni phase diffusion coefficients for both R-NiO and N-NiO. 180

Figure 7.1. Schematic for synthesis of ordered mesoporous nickel oxide (OMNiO). Adapted from [175]. 190

Figure 7.2. Pictures of (A) Teflon-shrouded copper rod electrode alone and (B) electrode with Teflon cap holding Cu TEM grid in place. 194

Figure 7.3. XRD spectrum for OMNiO. Acquisition rate was 1.3°/min. 195

Figure 7.4. (A) N_2 adsorption isotherm and (B) pore size distribution for OMNiO. 197

Figure 7.5. Charge/discharge curves for OMNiO anodes with (A) 0%, (B) 10%, and (C) 40% carbon black added. (D) shows C/5 capacity retention vs. cycle number. 199

Figure 7.6. Charge/discharge curves for plain carbon black anode with 10% binder at C/5 rate. 201

Figure 7.7. XRD spectra for NiO on Cu foil anode before and after 100 charge/discharge tests at C/5 rate. Acquisition rate was 1.3°/min. 203

Figure 7.8. Experimental setup for IL-TEM grid cycling is illustrated in (A) and (B). (C) through (F) show progression of TEM grid spots for identical-location images. 206

Figure 7.9. Progression of spots for IL-TEM images for OMNiO. 207

Figure 7.10. IL-TEM images for OMNiO on a Cu TEM grid before cycling, after two cycles, and after seven total cycles. Cyclic Voltammetry was performed at 0.1mV/s between 0.001-3V vs. Li/Li^+, in a 1M $LiPF_6$ in (1:1:1) EC:DMC:DEC electrolyte. 208

Figure 7.11. IL-TEM images for OMNiO on a Cu TEM grid. Images obtained before cycling, after two cycles, and after seven total cycles at 0.1mV/s between 0.001-3.0V. 209

Figure 7.12. Progression of spots for IL-TEM images for OMNiO with 40% carbon black. 211

Figure 7.13. IL-TEM images for OMNiO with 40% carbon black on a Cu TEM grid. Images obtained before cycling and after two cycles at 0.1mV/s between 0.001-3.0V. 212

Figure 7.14. EIS Nyquist plots for OMNiO anode coin cells with 0%, 10% and 40% carbon black. (B) shows green boxed section zoomed in. Batteries were cycled three times each at a 1C charge/discharge rate, and then allowed to rest several hours until a stable voltage was reached before conducting impedance tests. EIS was taken at the battery's open circuit voltage between frequencies of 100kHz – 50mHz with a 5mV voltage amplitude. 214

Figure 8.1. Photograph of UConn NSF GK-12 Fellows and Teachers. Notable people: 1st row, first person on the left – Aida Ghiaei, GK-12 Program Manager; 2nd row, first person on the left – Doug Cooper, GK-12 PI; 1st row, second person from the right – myself; 2nd row, fifth person from the right – Mr. John Hoyle, CADD Teacher at Howell Cheney Technical High School in Manchester, CT. 219

Figure 8.2. Photograph of freshmen in the CADD shop building an egg drop survival device. 221

Figure 8.3. Photograph of students with their bottle rocket modified from a 2L soda bottle and diagram of custom-designed and built platform for launching the bottle rockets with compressed air. 222

Figure 8.4. Photographs of senior CADD students working on their zipline bombers at a statewide competition held at Lake Compounce Amusement Park in Bristol, CT. 223

Figure 8.5. Photographs of students at Cheney Tech with their mousetrap cars. 225

Figure 8.6. Photographs of the VAWT, including alternator and various parts. 226

SECTION I:

INTRODUCTION

CHAPTER 1: REVIEW OF VARIOUS NICKEL OXIDE MORPHOLOGIES AND ENVIRONMENTS

1.1 High Temperature Applications

Nickel Oxide (NiO) is a versatile, inexpensive, p-type semiconductor and transition metal oxide that has received considerable attention for its use in a myriad of electrochemical applications. In high temperature systems, NiO and Ni-based materials have found widespread use as electrodes in solid oxide fuel cells, molten carbonate fuel cells, and Fischer-Tropsch reformers [1-4]. Elevated temperatures in these systems enable the use of NiO and other similar low-cost materials to replace more expensive noble metals (Pt, Pd, Au, Ag, Ru); however, high temperature systems suffer from major drawbacks such as high quality heat requirements, frequent catalyst poisoning, and stability concerns. As a result, many researchers have begun to shift their focus toward low temperature processes and reactors, and for many of these systems NiO functions as an attractive choice for the electrocatalyst or electrode material. This thesis will focus on several of these low temperature systems and investigate the effects of varying NiO morphologies and environments, including hydroxide and carbonate alkaline media for aqueous systems and organic electrolytes in lithium-ion batteries for non-aqueous systems.

1.2 NiO Morphologies for Aqueous Systems

The primary means through which researchers have tuned the morphology of NiO is through the synthesis procedure. Numerous methods have been demonstrated, including electrodeposition to produce thin films [5-12], direct calcination of nickel salts [13-15], spray pyrolysis [16-21], and aqueous-phase precipitation techniques [13,22-27]. For these different morphologies, the most common usage for NiO and Ni-based materials is as an electrocatalyst for the oxidation of organics in aqueous media [5-7,9,11,28-30].

Electrodeposition is either carried out galvanostatically (modulating current) or potentiostatically (modulating voltage), and can be performed on a variety of substrates, including glassy carbon/graphite [5,6,8,9], electronically-conductive polymers [7], indium tin oxide-coated glass [10], or stainless steel/nickel/gold metal disc electrodes [8,10-12]. Most electrodeposited materials exhibit similar physical characteristics of smooth, homogeneous films, though the morphology can vary depending on the type of electrochemical treatment. For instance, increased uniformity has been observed for films deposited either using cyclic voltammetry or chronopotentiometry under relatively high current densities.

The synthesis of NiO prepared through direct calcination of nickel salts typically results in a heterogeneous morphology consisting of agglomerates of

octahedral particles. Different nickel salts, such as nickel nitrate [13], nickel acetate [13,15], nickel oxalate [14,15], and nickel lactate [15] have been used, and when calcined at similar temperatures and durations, comparable morphologies are observed. Relatively low surface areas are typical (around 10-40 m^2/g) , although Yu et al. reported high specific surface area (179 m^2/g) and a well-defined mesoporous structure despite ubiquitous clusters of varying sizes of NiO polyhedrons [14]. Tunability of the physical properties can be achieved through varying the calcination temperature and time [13,14]. Additionally, changing the nickel salt used results in both physical and crystallographic changes. Estellé et al. showed that calcination of nickel acetate resulted in formation of metallic nickel in addition to NiO, and pyrolysis under inert gas flow produced an even greater ratio of Ni:NiO [13]. Similarly, Marciuš et al. reported the formation of metallic Ni in addition to NiO from calcination of nickel lactate, and elevated temperatures were necessary to synthesize pure NiO, though sintering and growth of large micron-sized agglomerates resulted from the higher calcination temperatures [15].

Spray pyrolysis is used to fabricate NiO by feeding a precursor solution through a nozzle where it is atomized and combined with oxygen gas. This mixture is combusted while being directed at a cool substrate for deposition. Macroscopically, spray pyrolysis results in apparently homogeneous films;

however, SEM analysis typically reveals agglomerates of nanosized spherical particles of uniform size [16,18,19,21]. One of the great benefits of spray pyrolysis is the high level of control which is possible through the tuning of numerous parameters, such as flame temperature, flow rate, precursor concentration, and deposition time. Yu and Kim demonstrated this kind of control by synthesizing NiO of varying particle sizes and specific surface areas through the tuning of procedure parameters [18]. Another benefit of spray pyrolysis is the ease with which additional components can be alloyed together, and this technique is a very popular choice for production of NiO-composite materials [16,17,19,21].

Aqueous-phase precipitation techniques for NiO are conducted in two stages. First, an aqueous solution containing a dissolved nickel salt precursor is combined with a second solution (typically a strong base), causing precipitation of hydrated nickel hydroxide. Second, the nickel hydroxide is dried, rinsed, and calcined to form NiO. Similar to spray pyrolysis, aqueous-phase precipitation frequently results in agglomeration of nanosized particles, though some differences can be achieved through use of additional components during synthesis. For example, Song et al. showed that agglomeration of nickel hydroxide via NaOH-induced precipitation can be somewhat mitigated by adding a surfactant and using high-intensity ultrasound radiation during the reaction [26].

Ramesh and Kamath also demonstrated that various degrees of structural disorder can be achieved by adjusting the solution temperature during addition of NH_4OH and by varying the aging time in the mother liquor [27]. Formation of NiO via aqueous-phase precipitation is often preferred since it does not usually require complex systems or equipment, uses ambient conditions, and can generate large quantities of product in a single batch.

NiO synthesized using these different techniques have been used for a myriad of aqueous electrochemical applications, such as electrocatalytic oxidation of organics [5-7,9,11,12], oxygen evolution [8], capacitors [14,22], and sensors [17,24]. Other studies demonstrate solely structural and mechanical properties of NiO synthesized using one or more of these methods [10,13,15,16,18,19,21,25,26]. However, what is often lacking is a fundamental connection between the catalyst morphology and its electrochemical reactivity; hence, in this thesis some of those connections will be highlighted. In particular, the effects of NiO synthesis procedure on electrocatalytic performance for methanol oxidation in alkaline aqueous media will be discussed in Chapter 3.

1.3 NiO Electrocatalyst Additives and Alloys

One way researchers have attempted to improve the electrocatalytic

performance of NiO and Ni-based catalysts is through additives and alloying with secondary materials, such as Co, Mn, Cu (and their respective oxides), Li, Pt, Si, carbon, and mixed-metal complexes [8,9,12,16,17,24,30]. The incorporation of additional materials frequently results in enhanced activity for the electrocatalyst. Hattori and coworkers showed an increase in the adsorptivity of methane over a NiO-activated carbon fiber catalyst [24], and Danaee et al. demonstrated improved electrocatalytic activity for methanol oxidation over a nickel-copper electrode compared to the pure nickel species [9]. Alloying of multiple species enabled high levels of reactivity that were otherwise unattainable with the pure electrocatalyst material.

Other means by which catalyst additives are useful are by lowering activation barriers and improving stability. Garduño-Wilches and Alonso showed that the addition of Li and Pt to NiO thin films for hydrogen sensors not only improved the response time, but also changed the working temperature range, enabling sensing at temperatures that were not possible with the individual species [17]. Casella and Gatta also studied electrocatalytic glucose oxidation over a nickel-copper alloy film and found that the copper stabilized the β/β crystallographic phases of the nickel oxyhydroxide/nickel hydroxide, creating a more stable electrode and allowing longer cycle life and improved reactivity [12]. In Chapters 4 and 5 of this thesis, the role of zirconia as an electrocatalyst additive

to nickel oxide will be investigated for its activity toward room temperature methane activation and conversion to oxygenates.

1.4 Lithium-ion Battery Anodes

Beginning with their commercialization by Sony in the early 1990s, lithium-ion batteries have become the leading power source for portable electronics in the 21st century [31,32]. Lithium is the most electropositive metal on earth with a standard reduction potential of -3.04V vs. NHE for the reaction $Li^+ + e^- \rightarrow Li$, making lithium-ion batteries extremely useful as a versatile, high power energy source. The lithium-ion battery industry has been fueled by research efforts over the past few decades focusing primarily on new electrode materials, beginning most notably with pioneering work from Goodenough [33,34] and Yazami [35]. Their discoveries resulted in widespread commercialization and a lucrative industry that grosses around $12 billion annually [36]. As a result, there is an increasing demand for improvements in safety, capacity, and cost for potential future applications like electric vehicles and grid-scale energy storage [37].

The most promising opportunity for improving the capacity of lithium-ion batteries is the anode, where relatively low capacity graphite (372 mAh/g) is used in nearly all commercial batteries. Instead of graphite, an ideal anode

replacement material should have a relatively small molecular weight (compared to 72 g/mol for C_6), low density, favorable stoichiometric ratios for accepting Li (to enable more than 1 electron transfer), and be able to demonstrate excellent capacity retention during repeated charge-discharge cycles [36]. Several different classes of materials have been investigated as potential replacements for graphite, such as pure elemental species/metals (Si, Ge, Sn, Sb), metal hydrides, and metal oxides [36,38-42]; Figure 1.1 compares anode materials based on their theoretical capacities. Among anode types, metal oxides are the most diverse and have been well-studied over the past several years. As shown in the right half of Fig. 1.1, many metal oxides offer superior capacity to graphite, along with low cost and facile synthesis.

Lithium-ion battery anodes function via three possible reaction mechanisms: Li intercalation, alloying, or decomposition. For the metal oxides shown in Fig. 1.1, the most common of these reaction mechanisms is decomposition (though some materials can also form alloys with Li [36] – i.e. Sb_2O_3, Sn-oxides and GeO_2). NiO has become one of the most popular choices of metal oxide due to its low cost, ease of synthesis, and high theoretical capacity of 718 mAh/g. The decomposition/reconstitution reaction for NiO during charge/discharge is:

$$NiO + 2Li^+ + 2e^- \leftrightarrow Ni + Li_2O \qquad (1.1)$$

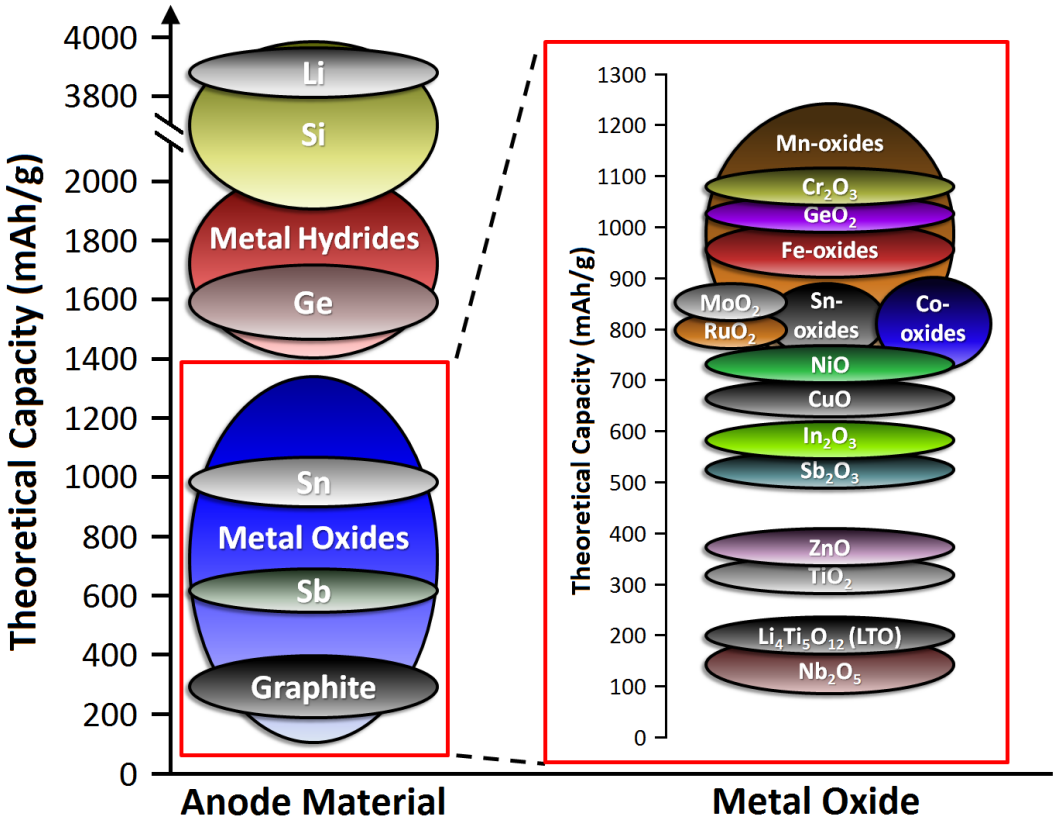

Figure 1.1. Candidate anode materials for lithium-ion batteries and their theoretical capacities.

A consequence of the NiO charge/discharge reaction shown in Eq. 1.1 is the formation of a secondary Li_2O+Ni phase, and this introduces potential concerns for the anode capacity retention. This secondary phase brings about volumetric expansion and phase separation, and large pockets of Li_2O are undesirable since they become electronically-inactive once they grow too large in size [38,43-46]. Therefore, one of the biggest goals of researchers studying NiO anodes for lithium-ion batteries has been to improve cyclability by mitigating the electrode degradation as much as possible. To do this, it is also crucial to improve understanding of the charge/discharge process, and in Chapter 6 the diffusion coefficient of Li^+ was determined for NiO anodes during charge/discharge to connect morphology with electrode performance and better understand Li^+ diffusivity through multiple phases.

Traditional graphite anodes for lithium-ion batteries are designed to have low specific surface areas and large features to avoid excessive electrolyte decomposition and heat generation [31,32,47]. However, this conventional wisdom likely will not apply for next generation metal oxide anodes since large particles will encourage phase separation, particle pulverization, and a rapid loss in capacity. Many different morphologies and composites of NiO have been synthesized for use in lithium-ion batteries with varying results, including porous films [43,44,46,48,49], nanowalls [50,51], nanotubes [45], mixed-metal oxide

composites [48,52,53], and NiO/graphene mixtures [54,55]. Chen et al. demonstrated capacity of around 300 mAh/g at 2C charge-discharge rate, and Wu et al. showed similarly high capacity using NiO porous films [43,46]. Nanosized NiO anodes also showed good cyclability in the works by Varghese et al. [50], Yan et al. [51], however Needham, Wang and Liu reported poor capacity retention after just 20 cycles using NiO nanotubes [45]. In many cases, reduced capacity in NiO anodes still exceeded the theoretical capacity of graphite (372 mAh/g), making NiO a viable and attractive alternative to graphite.

Similarly to the previously-described electrocatalysts for aqueous systems, NiO morphology is primarily controlled through the synthesis procedure, and two of the most popular techniques are aqueous-phase precipitations [45,48,51-53,55,56] and template-based syntheses [43,45,46,49,57]. The number of different morphologies and various synthesis techniques available for producing NiO make it one of the most promising materials for lithium-ion battery anodes, and for this reason it is one of the most-studied alternative anodes in the literature. The approach for most of these NiO anodes has been to produce nanosized features to enable sustained capacity over repeated charge/discharge cycles.

Of these two types of synthesis procedures, template-based methods are particularly interesting since they can be used to produce specific structures in a controlled and repeatable way. Interestingly though, not all reports of template-

synthesized NiO show desirable performance, but either show rapid capacity loss or very limited results [45,46]. Others, however, do in fact show impressive rate capacity and cyclability over a greater number of charge/discharge cycles [43,49,57]. In some of these cases, the electrode either contained a low loading of active material or a high content of conductive carbon additive, which leads to a question whether structure is indeed the determining factor for NiO anode performance, or another factor, such as electronic conductivity, plays a more crucial role in preventing degradation and capacity loss. In Chapter 7, this question will be investigated through the use of template-synthesized ordered mesoporous NiO anodes and identical-location transmission electron microscopy experiments.

CHAPTER 2: REVIEW OF LOW TEMPERATURE CARBONATE AND CARBON DIOXIDE ELECTROCHEMICAL UTILIZATION SYSTEMS

2.1 Electrochemical Carbon Dioxide Utilization

Carbon dioxide (CO_2) utilization is a topic that has become increasingly relevant as concerns over global climate change have grown in recent years [58-62]. Compared to heterogeneous chemical reactors, electrochemical utilization systems offer three distinct advantages: i) electrochemical devices are not limited by traditional thermochemical cycles, meaning that their achievable efficiency is most often significantly higher than their chemical/combustion counterpart; ii) direct control of the surface free energy of the catalyst through the electrode potential, allowing the reaction rate and pathway selectivity to be dialed in precisely; and iii) non-direct reaction between precursors through complementary redox processes on two separate catalysts, which permits researchers to tailor the properties needed for each redox process independently. This can facilitate different reaction pathways depending on catalyst selection with identical precursors at the same temperature, etc. while minimizing competition between alternate pathways. This enables unique chemistries to occur that would not be possible in conventional systems [63]. The following subchapters detail some of these unique chemistries for electrochemical CO_2 conversion, and this work was

published in the journal *Catalysis Science & Technology* [63].

2.1.1 Background

Multiple pathways have been investigated for the electrochemical conversion of CO_2, including gaseous, aqueous, and non-aqueous phase techniques at both high and low temperatures. Figure 2.1 shows a summary of these pathways, including a variety of possible products formed. High temperature CO_2 conversions are typically carried out using variations of the solid oxide fuel cell (SOFC), whereas low temperature systems largely utilize transition metal electrodes in both aqueous and non-aqueous electrolytes, such as methanol, acetonitrile, propylene carbonate, or dimethyl sulfoxide. The scope of products formed at low temperatures is broader than at high temperatures, but the selectivity and performance of SOFC devices often exceed those observed in low temperature systems. Applied potentials of several volts are also necessary in low temperature aqueous and non-aqueous phase electroreductions, resulting in large power requirements. In this section, these systems and pathways for electrochemical CO_2 reduction will be analyzed in terms of the products formed and the electrochemical performance and stability.

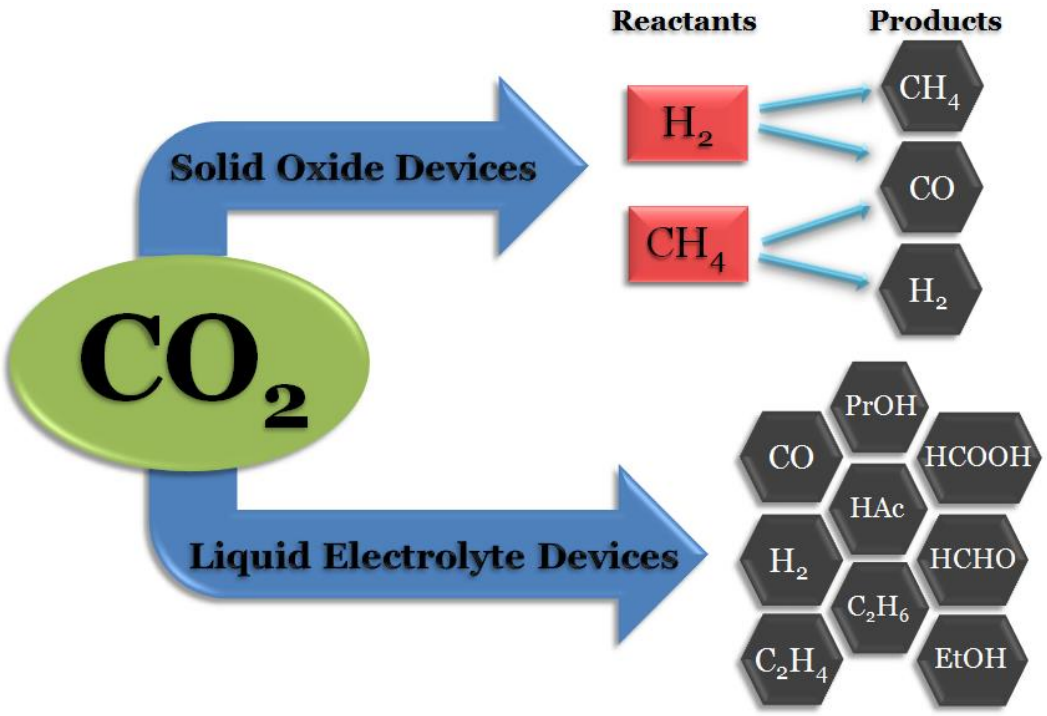

Figure 2.1. Summary of electrochemical conversion pathways for CO_2; **EtOH**: ethanol; **PrOH**: propanol; **HAc**: acetic acid; **HCHO**: formaldehyde.

2.1.2 Syngas Production

Conversion of CO_2 electrochemically to syngas (CO and H_2) is a highly promising pathway for CO_2 utilization and mitigation. Syngas is an industrially-important precursor used in the synthesis of methanol and other hydrocarbons [64]. Among the methods reported for syngas production, SOFCs are a popular choice due to high current densities and the potential for power-generating, rather than power-intensive, devices. Heat produced electrochemically through anodic oxidation is sufficient to sustain the SOFC operating temperature, and, as a result, heat required to dissociate gaseous CO_2 to CO and surface oxygen species is readily available. This heat utilization enables SOFCs to generate power, compared to low temperature, aqueous systems which require an applied current to electrochemically reduce CO_2 [65].

As an alternative to traditional steam reforming of methane (CH_4), which is a highly endothermic and energy-intensive process, dry reforming, or CO_2 reforming of CH_4, has been reported to produce syngas with more favorable H_2/CO ratios (Eq. 2.1) [64,66]:

$$CH_4 + CO_2 \rightarrow 2CO + 2H_2 \qquad (2.1)$$

Dry reforming is a particularly attractive method in addition since it not only addresses improved syngas formation, but also elimination of greenhouse

gases and utilization of cheap, abundant, industrially-relevant, carbon-containing materials [66]. As illustrated in Figure 2.2, Kim et al. showed that performance in an SOFC setup using CH_4 and CO_2 as reactants is also comparable to using H_2 as fuel. These high temperature cells typically utilize an yttria-stabilized zirconia (YSZ) electrolyte or tube with various metal and/or mixed-metal catalysts at the anode and cathode. Belyaev, Galvita, and Sobyanin varied inlet CO_2/CH_4 fuel ratios over porous platinum electrodes and obtained syngas with a favorable composition for Fischer-Tropsch processes, which is reported to contain an H_2/CO ratio between 1 and 2 [64,67]. Other researchers have produced syngas in SOFCs using nickel-based catalysts, such as ceria-doped nickel-YSZ or nickel oxide-calcium oxide mixed metal electrodes, through CH_4 reforming with CO_2 and/or O_2 [66,67]. When CO_2 is used as the fuel without CH_4, CO alone can be synthesized at the cathode (Eq. 2.2) for use in syngas or for different processes, along with oxygen ions, which are transformed to pure oxygen gas at the anode (Eq. 2.3) [65,68]:

$$CO_2 + 2e^- \rightarrow O^{2-} + CO \tag{2.2}$$

$$O^{2-} \rightarrow 2e^- + {}^1\!/_2\, O_2 \tag{2.3}$$

Bidrawn et al. demonstrated this CO_2 electrolysis with current densities over 1 A/cm^2 (Fig. 2.3), and suggested this technology could rival efficiencies for

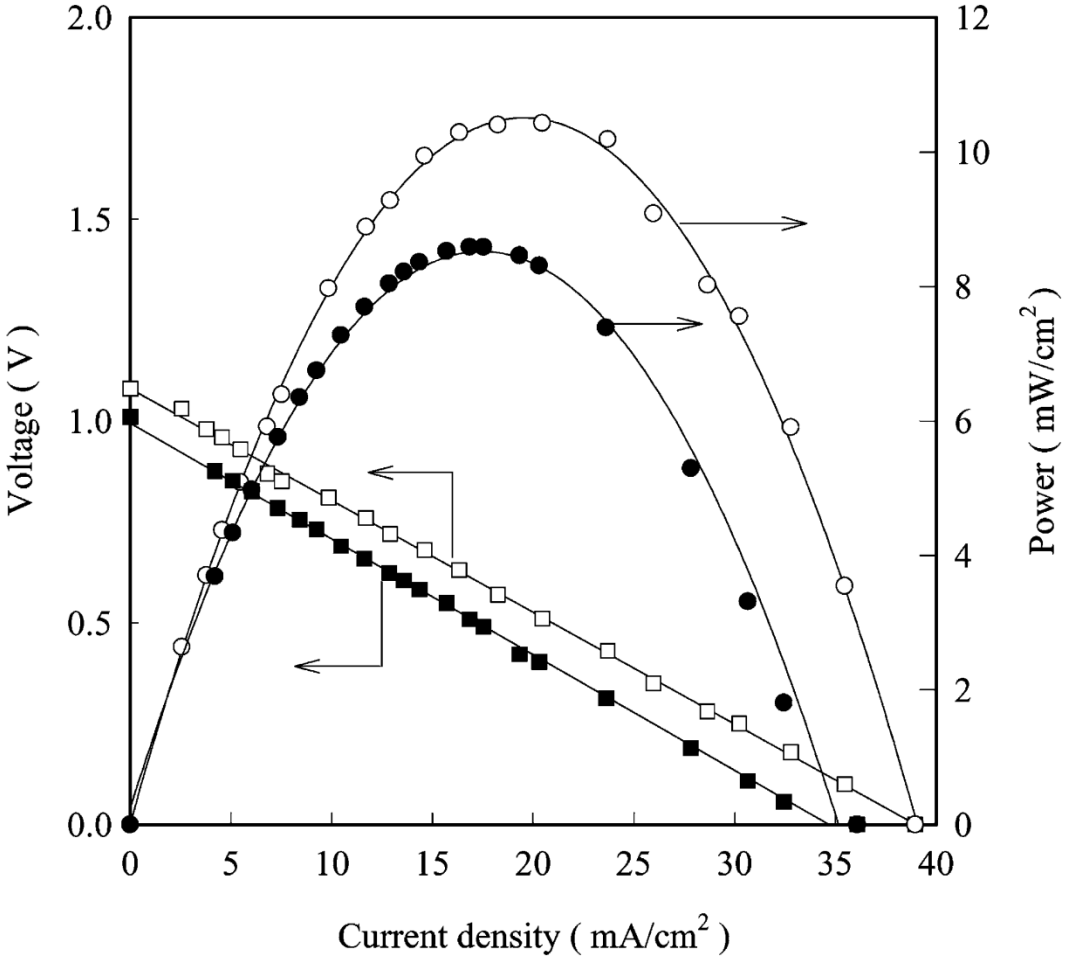

Figure 2.2. Polarization and power curves for a solid oxide fuel cell with a Ni-YSZ-CeO_2 catalyst operated at 800°C for (□,○): H_2 fuel and (■,●): CH_4/CO_2 fuels [66].

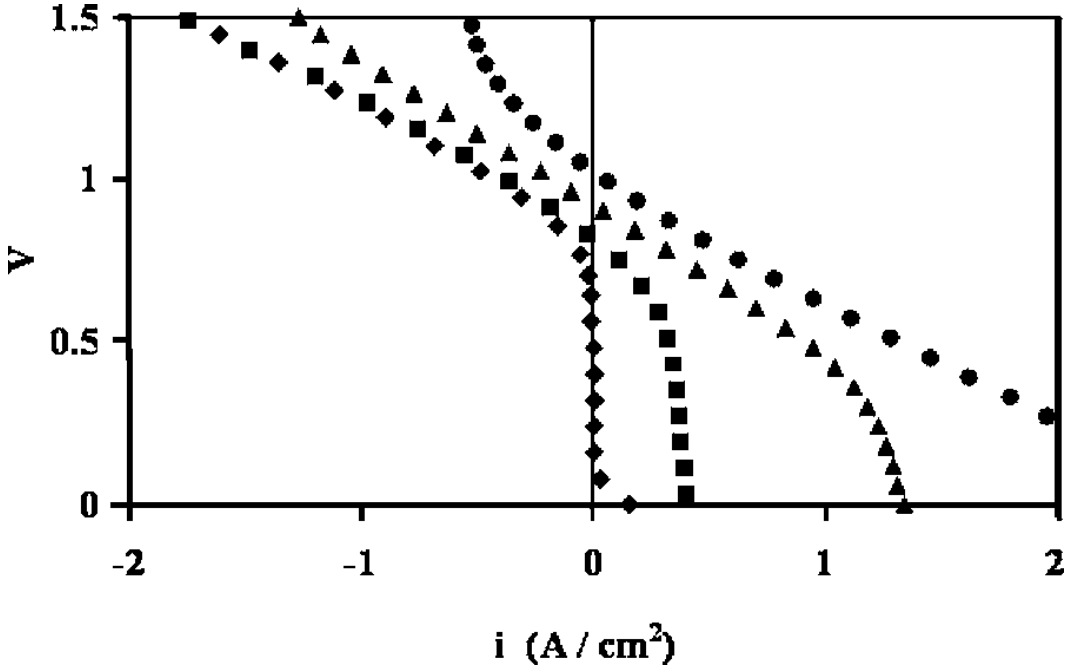

Figure 2.3. Polarization curves for a solid oxide fuel cell with an LSCM-CZY-Pd in YSZ fuel side electrode operated at 800°C with various CO_2:CO fuel stream ratios. (♦): 100:0; (■): 90:10; (▲): 50:50; (●): 10:90 [68].

similar H_2O electrolysis systems and make a significant impact on greenhouse gas mitigation [68]. H_2 fuel was applied by Furukawa and coworkers using a lower temperature (500°C) SOFC cell with nickel/zeolite and silver electrodes to convert CO_2 into CH_4 and H_2O (Eq. 2.4) with yields up to 80% [69]:

$$CO_2 + 4H_2 \rightarrow CH_4 + 2H_2O \quad (2.4)$$

In all SOFC cases, gaseous CO_2 is readily reduced to usable products as a result of the heat available at temperatures as high as 800-900°C [65].

One of the biggest challenges facing prolonged SOFC usage is finding solutions to the electrode deactivation that occurs from coke, or pure carbon, formation and other mechanisms. Coke formation and deposition can occur through several different reactions, including CH_4 decomposition (Eq. 2.5) and CO disproportion (Eq. 2.6) [65,66,68]:

$$CH_4 \rightarrow 2H_2 + C \quad (2.5)$$

$$2CO \rightarrow CO_2 + C \quad (2.6)$$

In Figure 2.4, Kim et al. proposed molecular mechanisms for dry reforming over a Ni-YSZ-CeO_2 SOFC electrode, presenting potential pathways for Eqs. 2.1, 2.5, and 2.6 [66]. They also illustrate in Figure 2.5 that, fortunately, the rate of coke formation is lower than both the rates of reaction for CH_4 and CO_2 and the rate of

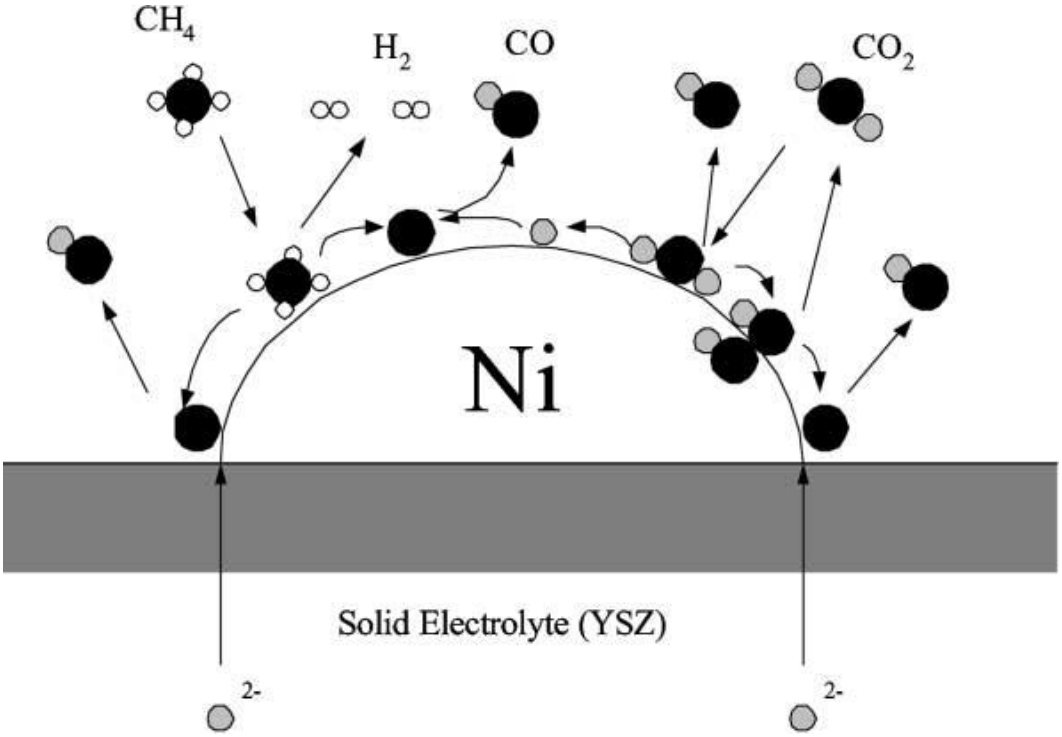

Figure 2.4. Proposed molecular mechanisms for dry reforming over a Ni-YSZ-CeO_2 solid oxide fuel cell electrode [66].

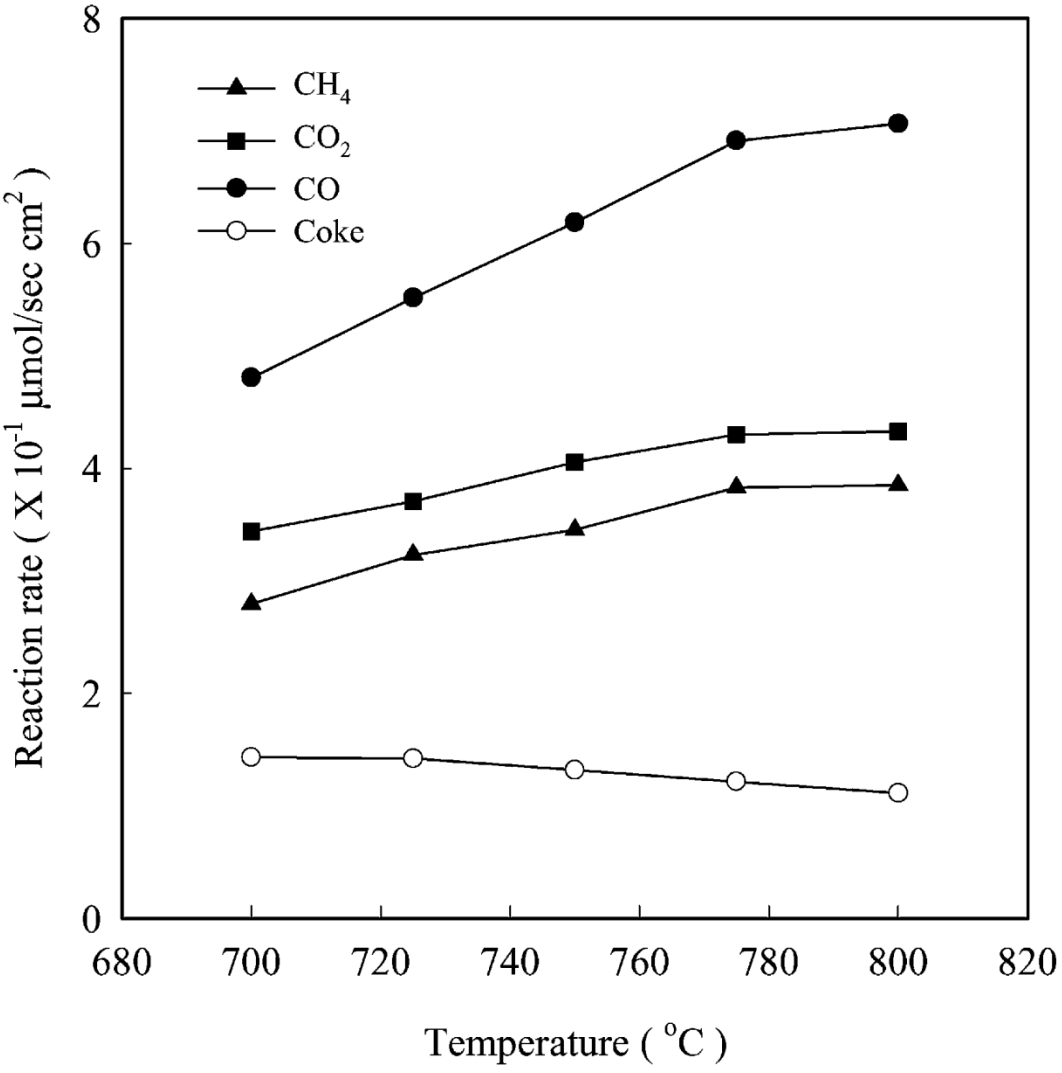

Figure 2.5. Reaction rates for (▲) CH_4 and (■) CO_2, and rates of formation of (●) CO and (○) coke as a function of temperature for a solid oxide fuel cell with a Ni-YSZ-CeO_2 electrode [66].

formation of CO [66]. Over long periods of operation, however, coking is still a significant problem, and efforts have been made in attempts to minimize its impact. Choudhary et al. reformed CH_4 with both CO_2 and O_2 to partially mitigate coking that stems from the use of CO_2 as a reforming fuel [67]. Electrode modification via alloying small fractions of additional metal or metal oxide phases has also been shown to be highly beneficial to SOFC operation, such as the inclusion of 4% CeO_2 to a Ni-YSZ electrode which improved the cell performance and stability, and resulted in less coking [66]. Others have alloyed numerous materials including gadolinia-doped ceria (GDC), copper, palladium, and $Ce_{0.48}Zr_{0.48}Y_{0.04}$ (CZY) into various SOFC electrodes in attempts to improve SOFC performance and stability [65,68]. However, high temperature operation still poses other problems for electrode degradation, particularly for nickel-based electrodes. Formation of volatile nickel-carbonyls deactivates the electrode over time and imposes significant limitations on continuous, long-term operation of SOFC reactors [68]. Hence, to fully realize the potential for nonstop CO_2 utilization with SOFCs, permanent solutions to the problems of coking and electrode degradation must be found.

A few reports exist concerning syngas production under ambient conditions in aqueous solutions. Due to the lack of accessible heat at atmospheric temperatures and pressures, gaseous CO_2 cannot be as easily electroreduced as

with SOFCs. Dissociation of CO_2 in aqueous solutions requires applied current, and therefore generally large applied (negative) potentials [65]. Yano et al. converted CO_2 to CO and H_2 at applied potentials as high as -2.4V over a silver mesh electrode, but conversions were much lower than those reported for SOFCs [70]. Delacourt and coworkers achieved current densities up to 100 mA/cm^2 over Ag and Pt-Ir gas-diffusion electrodes in fuel cell and modified aqueous-fuel cell experimental setups; however, they primarily reported H_2 evolution with low CO formation, and insertion of an aqueous buffer layer increased cell resistance and lacks commercial feasibility [71]. Low CO_2 solubility in aqueous solutions under ambient conditions severely limits the output for these devices, and imposes the need for extremely large applied potentials in order to obtain a reasonable amount of product. Promising current densities as high as 50 mA/cm^2 have been reported, however, for applied potentials up to -2.5V over various metal-phthalocyanine (M-Pc) gas-diffusion electrodes [72]. The primary product from these electrocatalysts was CO, though H_2 formation occurred in nearly all cases as well.

2.1.3 Hydrocarbon Products

The most commonly-used materials for electrochemical CO_2 conversion under ambient temperatures and pressures are transition metals and metal oxides, specifically copper-based electrodes. Gattrell, Gupta and Co summarized

aqueous electrochemical CO_2 reduction methods using different copper electrodes, and found a variety of products formed depending on the electrode structure and reaction conditions [73]. Disadvantages of CO_2 reduction under ambient conditions are applied potentials as high as -4V, however a wide range of hydrocarbon products can be synthesized in various aqueous electrolytes [74-80]. While many low temperature systems also produce byproducts of CO and/or H_2, compositions and purities are not ideal for syngas-related operations. In most cases, H_2 forms at the cathode not directly from the CO_2 reduction reaction, but rather from the concurrent hydrogen evolution reaction, in either acidic (Eq. 2.7) or alkaline (Eq. 2.8) media, due to extremely large overpotentials [81]:

$$2H^+ + 2e^- \rightarrow H_2; \qquad E^0 = 0.000\text{V vs. NHE} \qquad (2.7)$$

$$2H_2O + 2e^- \rightarrow H_2 + 2OH^-; \quad E^0 = -0.828\text{V vs. NHE} \qquad (2.8)$$

With the high applied potentials necessary for aqueous-phase CO_2 electroreduction, in virtually all cases hydrogen evolution is an unavoidable side-reaction and occurs spontaneously. As a result, in nearly all reports of hydrocarbon production, H_2 current efficiencies are minimized as much as possible without compromising product selectivity.

High surface area and surface-modified copper electrodes have a high selectivity at low temperatures towards simple hydrocarbons like ethylene (C_2H_4)

and CH_4, but numerous other products have also been reported, such as CO, H_2, formic acid (HCOOH), ethane, ethanol, propanol, acetic acid, and lactic acid [75-78]. Others report larger current efficiencies for different species, such as CO or HCOOH, than for C_2H_4 or CH_4, along with acetone, methanol, and aldehydes as additional minor species [79,80]. Poisoning of these copper electrodes is a common issue that plagues long-term operation and limits their viability for commercialization. Use of acidic solutions can result in activity losses due to copper dissolution, evidenced by increased blue coloring of the solution from aqueous copper species over time [77,78]. On the other hand, highly alkaline solutions cause copper oxides to form on the electrode surface, which are generally considered undesirable, though Yano et al. noted favorable C_2H_4 synthesis using copper oxide electrodes compared to pure a copper electrode [78]. Other harmful species reported to form on copper electrodes are graphitic carbon and organic intermediates, such as formate ions, that can react either chemically (Eq. 2.9) or electrochemically (Eq. 2.10) to form unwanted surface species [77,80]:

$$Cu + HCOO^- \rightarrow CuO + C + OH^- \quad (2.9)$$

$$HCOO^- + H_2O + 2e^- \rightarrow C + 3OH^- \quad (2.10)$$

Among these mechanisms of electrode poisoning, however, Smith and coworkers disputed coke deposition by closely examining repeated CO_2 reduction over a

copper electrode and finding only copper oxides, copper hydroxides, and surface tarnishing patina with no evidence of carbon deposition [82]. Irrespective of the cause and identity, however, efforts have been made to mitigate surface poisons, including copper halide-modification and use of a three-phase reaction cell [76,77,80].

Researchers have also investigated the use of various other transition metals, alloys, and complexes as electrocatalysts for CO_2 reduction in aqueous-phase cells. Shibata and Furuya studied a bevy of transition metals in M-Pc complexes as gas-diffusion electrodes and produced mostly CO and/or H_2 products for the majority of metals [72]. Figure 2.6 shows current efficiencies and densities for product formations from the reduction of aqueous phase CO_2 as functions of potential gathered by Shibata and Furuya over cobalt-Pc catalysts [72]. The main product was CO, with H_2 formation suppressed as low as possible for potentials up to -2.5V, and no HCOOH formation was observed for overall current densities up to around 50 mA/cm^2. Some of these electrocatalysts also produced different products outside the scope of those seen with copper-based electrodes. Cobalt-, nickel-, and palladium-Pc electrodes showed the highest activity among all M-Pc electrodes, particularly for ammonia (NH_3) formation from nitrite ions (NO_2^-) and urea synthesis from CO_2 and NO_2^- [72,83]. Figure 2.7 shows product current efficiencies over cobalt- and nickel-Pc electrodes for

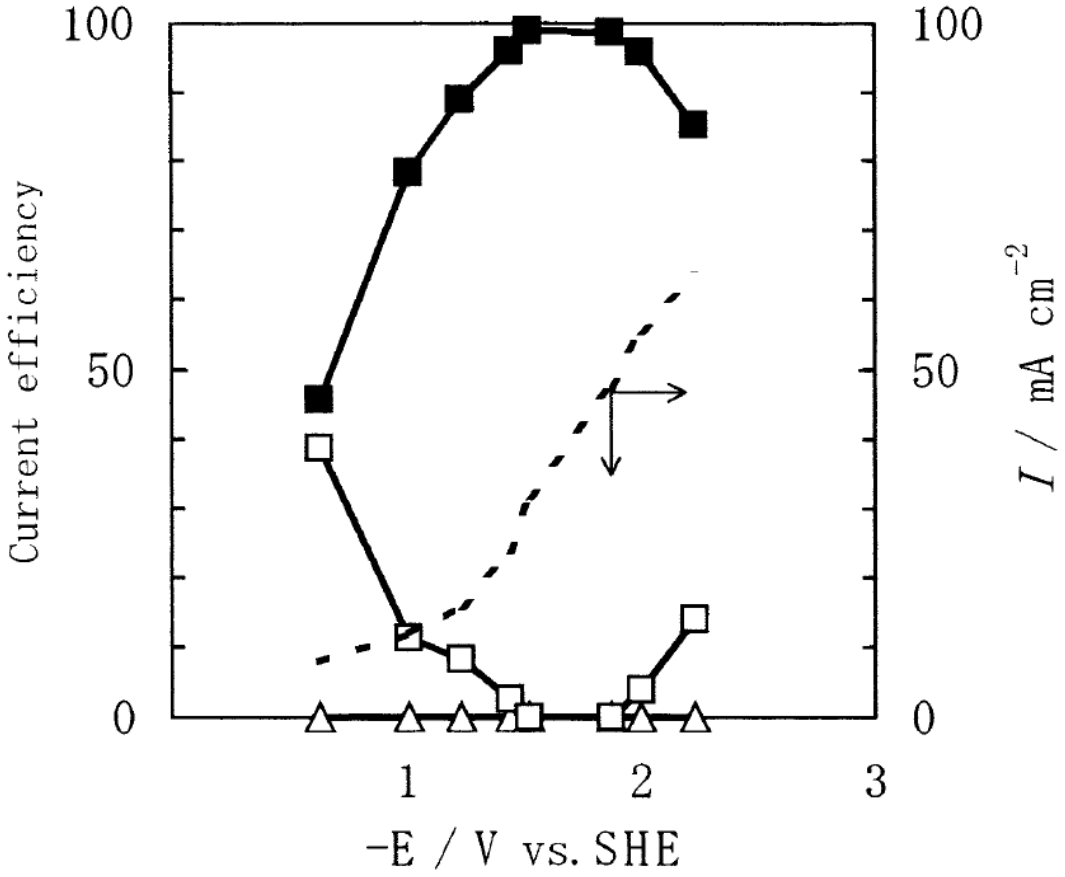

Figure 2.6. Current efficiencies for (■) CO, (□) H_2, and (Δ) HCOOH, and (- - -) overall current density (plotted on secondary y-axis) as functions of (negative) electrode potential for aqueous phase CO_2 reductions over a cobalt-Pc gas-diffusion electrode [72].

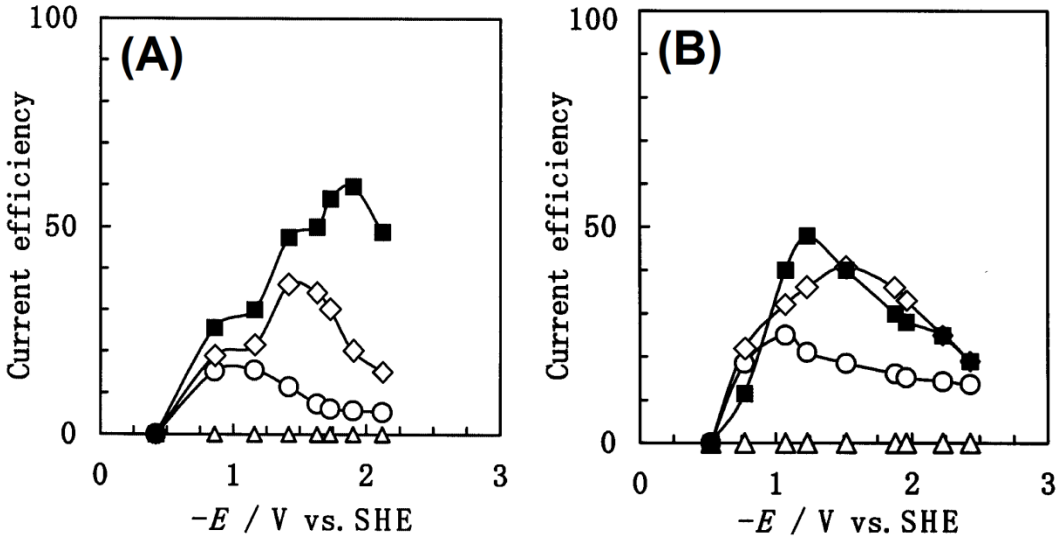

Figure 2.7. Current efficiencies as a function of (negative) electrode potential for (■) CO, (○) NH_3, (◊) urea, and (Δ) HCOOH products from aqueous phase CO_2 reductions with NO_2^- ions over (A) cobalt-Pc and (B) nickel-Pc gas-diffusion electrodes. Edited from [83].

CO_2 reduction with the addition of NO_2^-, and once again no HCOOH formation was detected for potentials up to -2.5V [83]. Formation of H_2 likely occurred in all experiments as well similar to those performed without NO_2^- (Fig. 2.6), however that data was omitted in this case. Other electrode materials researchers have used include Monel metal (an alloy of nickel, cobalt, copper, and iron), stainless steel (chromium, nickel, and iron), numerous pure transition metals and powders, and boron-doped diamond (BDD) [76,79,84,85]. Various products were formed, including sodium formate and HCOOH reported by Narayanan and coworkers over indium and lead powders at the cathodes of Na^+ and OH^- exchange cells, and peroxycarbonate examined by Saha et al. using a BDD electrode in a CO_2-saturated sodium hydroxide electrolyte at low temperature [84,85].

In addition to varying the electrode material, some researchers have tried different reaction media to either improve the CO_2 reduction reaction or tailor specific product selectivity. Ikeda et al. reduced CO_2 to oxalic acid with faradaic efficiencies around 70-85% over lead and indium electrodes in propylene carbonate, acetonitrile, and dimethyl sulfoxide electrolytes at ambient conditions [79]. Trifluoroacetic acid and trifluoromethane have also been produced from simultaneous bubbling of CO_2 and $CClF_3$ gases in a 0.1M tetra(n-butyl ammonium) bromide in acetonitrile electrolyte over a silver wire electrode in a

stainless steel autoclave [86]. A review by Sanchez-Sanchez et al. of electrochemical CO_2 conversions in various aqueous and non-aqueous media, as well as gas-diffusion electrodes, detailed the potential for electrocarboxylation of CO_2 to useful pharmaceutical products, in addition to other low temperature methods, over transition metal catalysts [87]. In general, higher current densities were observed in non-aqueous media and at higher pressures, but in all cases high overpotentials were required, there was significant competition with the H_2 evolution reaction, and experiments showed poor product selectivity [87]. Aside from liquid electrolytes, Yoshida, Yosue, and Nogami demonstrated a direct-current discharge plasma gas chamber with CO_2 and H_2 as fuels to synthesize CH_4 and other hydrocarbon gases over copper and iron electrodes [88]. However, due to the extreme applied potentials needed to create the excited plasma state, conventional efficiencies for this cell are very low, and these electrodes also suffer from poisoning caused by graphitic carbon deposition over prolonged usage [88].

An especially popular choice of medium among non-aqueous electrolytes for use in electrochemical CO_2 conversion devices is methanol. At temperatures at or below 15°C, methanol is a much more effective solvent for CO_2 dissolution than water. Kaneco and coworkers have studied CO_2 reduction in methanol with various alkali metal salts over copper, lead, zinc and indium foil electrodes at

temperatures ranging from -30 to 15°C, and numerous hydrocarbon products were formed, such as CH_4, HCOOH, C_2H_4, CO, and H_2 (Eq. 2.11-2.14) [89-92].

$$CO_2 + 8H^+ + 8e^- \rightarrow CH_4 + 2H_2O \quad (2.11)$$

$$CO_2 + H^+ + 2e^- \rightarrow HCOO^- \quad (2.12)$$

$$2CO_2 + 12H^+ + 12e^- \rightarrow C_2H_4 + 4H_2O \quad (2.13)$$

$$CO_2 + 2H^+ + 2e^- \rightarrow CO + H_2O \quad (2.14)$$

Similar applied potentials to aqueous-phase systems are still necessary (around -2 to -3V), but the higher CO_2 solubility in methanol compared to water increases reactant availability at the electrode surface which may improve overall products yields. It is unclear, however, how much of this product formation can be attributed directly to CO_2 electroreduction versus the activity of the methanol solvent itself, which could hypothetically act as an independent carbon source regardless of CO_2 present in solution. H_2 formation is also generally unwanted in these hydrocarbon synthesis systems, and current efficiencies were suppressed down to around 10% [89-92]. As an alternative to metal foil electrodes, Aydin and Köleli performed electrocatalytic reductions of CO_2 in methanol at a pressure of 20 bar over polypyrrole and polyaniline film electrodes [93,94]. Acetic acid was the main product formed, with formaldehyde and HCOOH produced as minor products as well, but current densities were much lower when compared to similar

systems using metal electrodes. However, the scope of minor byproducts detected was much smaller using these polymer film electrodes compared to metal electrodes, which could potentially lead to better product selectivity and purity.

2.1.4 Summary of Electrochemical CO_2 Utilization

Conversion of CO_2 into industrially-relevant products is an area of research that has attracted global attention due to the potential threat of disaster as a result of climbing atmospheric CO_2 concentrations. Electrochemical techniques are particularly attractive when compared to heterogeneous chemical methods in part due to greater potential efficiencies and more tailorable reaction pathways. Pure electrochemical conversions have been performed through a myriad of routes, including high temperature solid oxide fuel cell devices and low temperature aqueous and non-aqueous reactors. Among these methods, solid oxide fuel cell devices have exhibited the highest current densities and efficiencies, whereas many low temperature CO_2 conversions resulted in comparatively diminished performance, low product selectivity, and in some cases high power requirements. Despite the added strain and electrode/electrolyte degradation that accompanies solid oxide devices due to operation at temperatures upwards of 500°C, they show promise as a viable CO_2 conversion technique. On

the other hand, aqueous and non-aqueous methods, while appealing as a result of their facile operating conditions, will likely need drastic performance improvements and/or reductions in required power loads before they could become practical solutions to this problem. However, the diversity of products formed and relative ease of operation of low temperature electrochemical systems still make them attractive topics for further research.

2.2 CO_2 in Low Temperature Fuel Cells

While CO_2 can be utilized in high temperature fuel cells for conversion to syngas and power generation, in low temperature devices it has been traditionally viewed as a poison, particularly in the case of alkaline fuel cells (AFCs) which operate with a liquid KOH electrolyte. High-purity oxygen is typically used at the cathode to carry out the alkaline media oxygen reduction reaction, Equation 2.15 [95]:

$$O_2 + 2H_2O + 4e^- \rightarrow 4OH^- \quad (2.15)$$

The presence of ambient CO_2 can result in the formation of bicarbonate (HCO_3^-) (Eq. 2.16) and carbonate anions (Eq. 2.17) through thermodynamic equilibrium with hydroxide, which then combines with K^+ cations and precipitates out as solid K_2CO_3 (Eq. 2.18).

$$OH^- + CO_2 \rightarrow HCO_3^- \quad (2.16)$$

$$OH^- + HCO_3^- \leftrightarrow H_2O + CO_3^{2-} \quad (2.17)$$

$$2K^+ + CO_3^{2-} \rightarrow K_2CO_{3(s)} \quad (2.18)$$

Precipitated K_2CO_3 lowers AFC performance by blocking pores which reduce the electrochemically active surface area, "using up" available OH^- anions and decreasing the ionic conductivity [96,97].

The anion exchange membrane fuel cell (AEMFC) offers a potential solution to the CO_2 poisoning issue that plagues conventional AFCs. Rather than a liquid electrolyte, a polymer membrane electrolyte is used that facilitates anion transport from the cathode to the anode, making AEMFCs not susceptible to carbonate salt precipitation due to the absence of K^+ or other free cations. In fact, a few studies have shown either no adverse effects or even improved current density in the presence of CO_2 flow [98,99]. These results suggest that the formation of carbonate anions from CO_2 exposure may not be detrimental to cell performance, and introduce the possibility of operating a low temperature AEMFC using CO_3^{2-} as opposed to OH^- as the primary charge-carrying anion.

2.3 Room Temperature Carbonate Devices

The feasibility of operating an AEMFC at room temperature using carbonate instead of hydroxide has been investigated in several key areas [100]. First, greatly improved anion exchange membrane stability has been demonstrated in CO_3^{2-} compared to OH^- electrolytes [101,102]. This is primarily due to the less caustic nature of aqueous CO_3^{2-} stemming from its lower pH than that of concentrated OH^- solutions. CO_3^{2-} is also a weaker nucleophile than OH^-, which causes severe membrane degradation through direct nucleophilic displacement and Hofmann elimination [103]. Second, hydrogen oxidation in CO_3^{2-} electrolyte was shown to have a higher exchange current density than in OH^-, owing in part to favorable bond dissociation thermodynamics and smaller intermediate activation energies [104].

Finally, a CO_3^{2-}-selective cathode material was developed to catalyze the direct production of carbonate from the oxygen reduction reaction with CO_2 (Eq. 2.19) in addition to the indirect pathway (Eqs. 2.16-2.17) [105,106].

$$O_2 + 2CO_2 + 4e^- \rightarrow 2CO_3^{2-} \tag{2.19}$$

This preferential synthesis of CO_3^{2-} opens new areas of research for devices operating on the carbonate cycle, and introduces the potential for new and interesting chemistries to be explored that utilize the oxidation of CO_3^{2-} for either

energy generation (room temperature carbonate fuel cells) or the synthesis of useful product(s). In Chapters 4 and 5 of this section, the latter was performed using a NiO-ZrO_2 electrocatalyst to carry out room temperature activation of CH_4, and several hydrocarbon and low molecular weight oxygenate products were identified.

SECTION II:

CARBONATE AND HYDROXIDE ALKALINE ELECTROCHEMICAL SYSTEMS

CHAPTER 3: EFFECT OF NICKEL OXIDE SYNTHESIS CONDITIONS ON ITS PHYSICAL PROPERTIES AND ELECTROCATALYTIC OXIDATION OF METHANOL

The purpose of this work was to correlate the physical characteristics of several different synthesis methods for NiO to its electrocatalytic activity in alkaline media. Physical characterization was performed using Scanning Electron Microscopy, Brunauer-Emmett-Teller analysis, X-ray Diffraction, X-ray Photoelectron Spectroscopy, and Simultaneous Thermal Analysis to investigate differences in NiO morphology and structure. Cyclic Voltammetry and Electrochemical Impedance Spectroscopy were used to study the Ni^{2+}/Ni^{3+} redox, methanol oxidation, and oxygen evolution reactions. The electrocatalytic behavior was compared in both hydroxide and carbonate aqueous media of comparable alkalinity. The work presented in this chapter won first place in the Electrochemical Science and Technology General Poster Session at the 219th Meeting of the Electrochemical Society (Montreal, QC, Canada, May 2011), and was also published in the journals *Electrochimica Acta* [107] and *ECS Transactions* [108].

3.1 Experimental

3.1.1 Materials Synthesis

All reagents were used as received, and all water used was ultra-pure 18.2 MΩ deionized water from a Millipore Direct-Q 3UV purification system. Reflux-precipitated nickel oxide (reflux-NiO) was synthesized by preparing 50 mL of 0.5M $Ni(NO_3)_2 \cdot 6H_2O$ (Acros, 99%) in 10M NH_4OH (Fisher, certified ACS Plus) and boiling the solution under reflux for 24 hours, then allowing it to rest at room temperature for 24 hours. The resulting green, precipitated precursor (reflux-$Ni(OH)_2$) was rinsed several times with deionized water, then dried on a hot plate at 90°C overnight. The resulting powder was calcined in air at 500°C for 2 hours yielding NiO.

Sodium hydroxide-precipitated nickel oxide (NaOH-NiO) was synthesized by preparing 50 mL of aqueous 0.5M $Ni(NO_3)_2 \cdot 6H_2O$ under constant stirring. Two $Ni(OH)_2$ precipitation temperatures were investigated, room temperature (~20°C) and the solution boiling point (~102°C). Solution temperature was measured using a Hannah instruments HI9063 K-Type Thermocouple. NaOH pellets (Fisher, NF/EP/BP/FCC) were ground into a fine powder and then gradually added until the pH rose to between 8-10 to ensure complete precipitation of $Ni(OH)_2$. Solution pH was actively measured using an Accumet Excel XL60 Dual Channel pH/Ion/Conductivity/DO Meter. The solution was

then capped and set aside for 24 hours. The resulting green, precipitated precursors from each solution were rinsed several times with deionized water, dried overnight on a hot plate at 90°C and then calcined in air at 500°C for 6 hours. Nickel hydroxide precursors and nickel oxide powders prepared by this method at room temperature are denoted RT NaOH-$Ni(OH)_2$ and RT NaOH-NiO, respectively, and those synthesized at the boiling temperature are denoted BT NaOH-$Ni(OH)_2$ and BT NaOH-NiO, respectively.

3.1.2 Instrumentation and Techniques

Catalyst microstructure was determined using an FEI Quanta FEG250 Scanning Electron Microscope (SEM). Specific surface areas were obtained through Brunauer-Emmett-Teller analysis (BET) using a Micromeritics ASAP 2020 system. A Bruker D8 Advance X-ray Diffractometer (XRD) with a Cu $K\alpha_1$ ceramic x-ray tube (λ = 0.1540562 nm) was used to evaluate crystal structure and average grain boundary size. X-ray photoelectron spectroscopy (XPS) was performed using a Physical Electronics Multiprobe with a Perkin-Elmer Dual Anode X-ray Source. Thermogravimetric analysis (TGA) was performed concurrently with differential scanning calorimetry (DSC) using a Netzsch STA 449 F3 Jupiter Simultaneous TG-DTA/DSC Apparatus. For each of these

simultaneous thermal analysis (STA) tests, approximately 20 mg of catalyst precursor was placed into a sample alumina crucible with a punctured lid to allow vapors that formed during calcination to escape. An empty alumina crucible with a punctured lid was used as a reference.

3.1.3 Electrochemical Tests

Electrochemical tests were performed in a custom three electrode cell (Adams & Chittenden) using an Autolab PGSTAT302N Potentiostat (Eco Chemie) with a platinum flag as the counter electrode and a saturated calomel electrode (SCE) as the reference electrode. All working electrodes were fabricated by preparing between 10-20 mL of a 0.3 mg/mL dispersion of the selected catalyst in deionized water and placing it in an ultrasonic bath until the catalyst particles were uniformly distributed throughout. Next, 20 μL of the dispersion was deposited onto a glassy carbon (GC) disk electrode (Pine Instrument Company, A = 0.196 cm^2) and spin dried at 450 rpm for 1 hour using a Pine AFMSRCE Modulated Speed Rotator. Once dry, 20 μL of a 0.05 wt.% Nafion solution (DuPont) was deposited on the GC electrode and spin dried. Nitrogen gas (Airgas) was bubbled in each solution for 1 hour prior to each electrochemical test to remove any dissolved gases. Anhydrous sodium carbonate

(Fisher, certified ACS grade, 99.9%), potassium hydroxide (Acros, ca. 85%), and methanol (Fisher, Optima ACS grade, 99.9%) were used to create the aqueous electrolytes used in all electrochemical tests. The GC electrode was polished prior to each test using Buehler alpha 5.0 μm and gamma 0.05 μm alumina micropolish suspensions, with an ultrasonication step in between for 10 minutes to remove any loose particles.

3.2 Results and Discussion

3.2.1 SEM and BET Analysis

Figure 3.1 shows SEM micrographs for precursor $Ni(OH)_2$ and calcined NiO nanoparticles, prepared through both reflux- and NaOH-precipitation methods. The reflux-$Ni(OH)_2$ and reflux-NiO nanoparticles (Fig. 3.1A and 3.1B) exhibited similar thin, bladelike structures. A comparable structure was seen for RT NaOH-$Ni(OH)_2$ nanoparticles (Fig. 3.1C), however the average size appeared much smaller than that of the reflux-$Ni(OH)_2$, and they displayed somewhat spherical agglomerations that were not present in reflux-precipitated nanoparticles [22]. Specific surface areas from BET analysis of precursors showed an order of magnitude larger value for both RT NaOH-$Ni(OH)_2$ (140 m^2/g) and BT NaOH-$Ni(OH)_2$ (212 m^2/g) than for reflux-$Ni(OH)_2$ (17 m^2/g), which supported the size

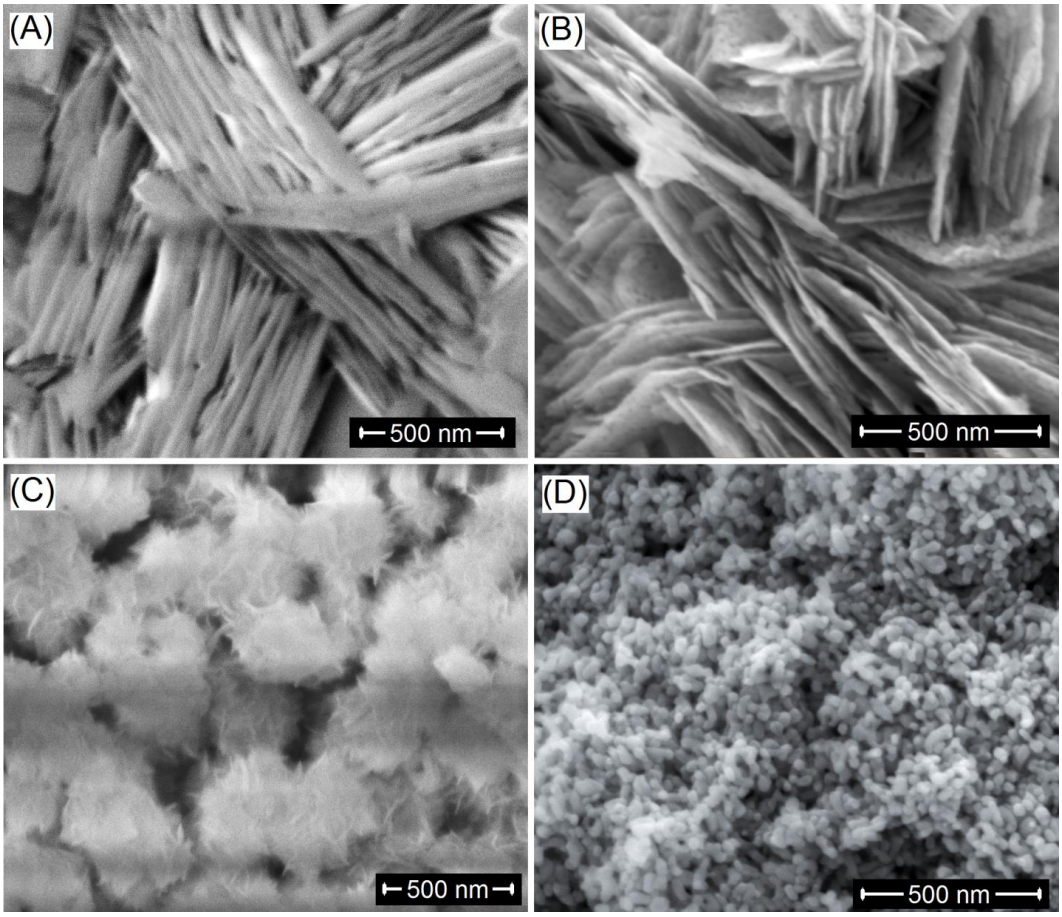

Figure 3.1. SEM micrographs of reflux-precipitated (A) $Ni(OH)_2$ and (B) NiO, and RT NaOH-precipitated (C) $Ni(OH)_2$ and (D) NiO.

distributions seen in SEM images in Fig. 3.1. RT NaOH-NiO (Fig. 3.1D) displayed clusters of spherical nanoparticles which were in stark contrast to the bladelike reflux-NiO nanoparticles [13,22]. It was observed during the electrode preparation for electrochemical tests that reflux-NiO nanoparticles were much more easily-dispersed in water than RT NaOH-NiO nanoparticles, which tended to flocculate at the bottom of the beaker. The bladelike nanostructure of the reflux-NiO likely contributed to its enhanced wetting ability over RT NaOH-NiO, where spherical nanostructure and agglomerated clusters may have led to flocculation and non-uniform dispersion. The observed sizes of RT NaOH-NiO nanoparticles were also much smaller than that of reflux-NiO nanoparticles which suggests RT NaOH-NiO had a larger specific surface area than reflux-NiO. BET results revealed an opposite trend; however, as the area for reflux-NiO (42 m^2/g) was actually greater than both RT NaOH-NiO (22 m^2/g) and BT NaOH-NiO (31 m^2/g). This was likely the result of excessive crystallite agglomeration that occurred during calcination of RT NaOH-NiO and BT NaOH-NiO nanoparticles due to longer calcination times (6 hours) compared to reflux-NiO (2 hours), essentially raising the average particle sizes and lowering the specific surface areas.

Figure 3.2 shows the calcined NiO nanoparticles prepared from both temperature synthesis methods of NaOH-induced precipitation. Zhu et al.

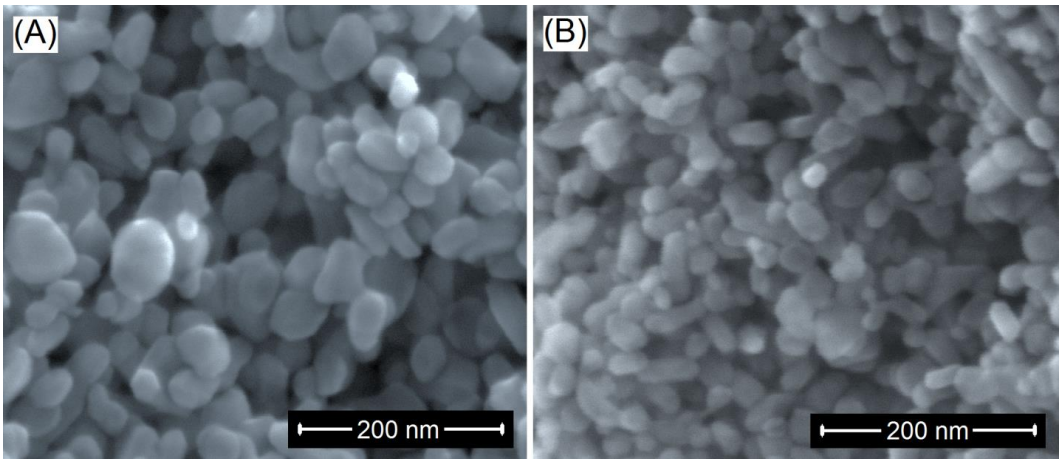

Figure 3.2. SEM micrographs of (A) RT NaOH-NiO and (B) BT NaOH-NiO. All nanoparticles were calcined in air at 500°C for 6 hours.

reported that NaOH-induced precipitation of CuO nanoparticles under boiling conditions caused a more rapid crystallization than at room temperature, resulting in smaller crystals and less aggregation [109]. They reported that the elevated temperature caused an increased rate for the precipitation reaction, forming nuclei much more quickly and preventing cluster agglomeration. Both methods produced similarly-shaped nanoparticles of comparable size, though BT NaOH-NiO appeared slightly smaller in average particle size than RT NaOH-NiO. The specific surface areas from BET analysis confirmed this observation; however, there was not a significant difference in electrochemical response of the materials prepared at BT and RT. Consequently, in this study, primarily RT NaOH-NiO was compared to reflux-NiO due to its ease of synthesis over BT NaOH-NiO.

3.2.2 X-ray Diffraction

Peak positions observed in Figure 3.3 for as-prepared $Ni(OH)_2$ precursor nanoparticles (with crystal faces) were as follows: 19.2° (001), 33.0° (100), 38.5° (101), 52.0° (102), 58.9° (110), 62.6° (111), 69.2° and 70.3° (103), and 72.7° (201) [25-27,110,111]. The intensities and narrow widths of the peaks for reflux-$Ni(OH)_2$ (Fig. 3.3A) identified it as pure, hexagonal β-$Ni(OH)_2$ [25,110]. The strong alkalinity of the concentrated NH_4OH solution likely caused a majority of b-$Ni(OH)_2$ to form over a-$Ni(OH)_2$, and prolonged aging in NH_4OH may have

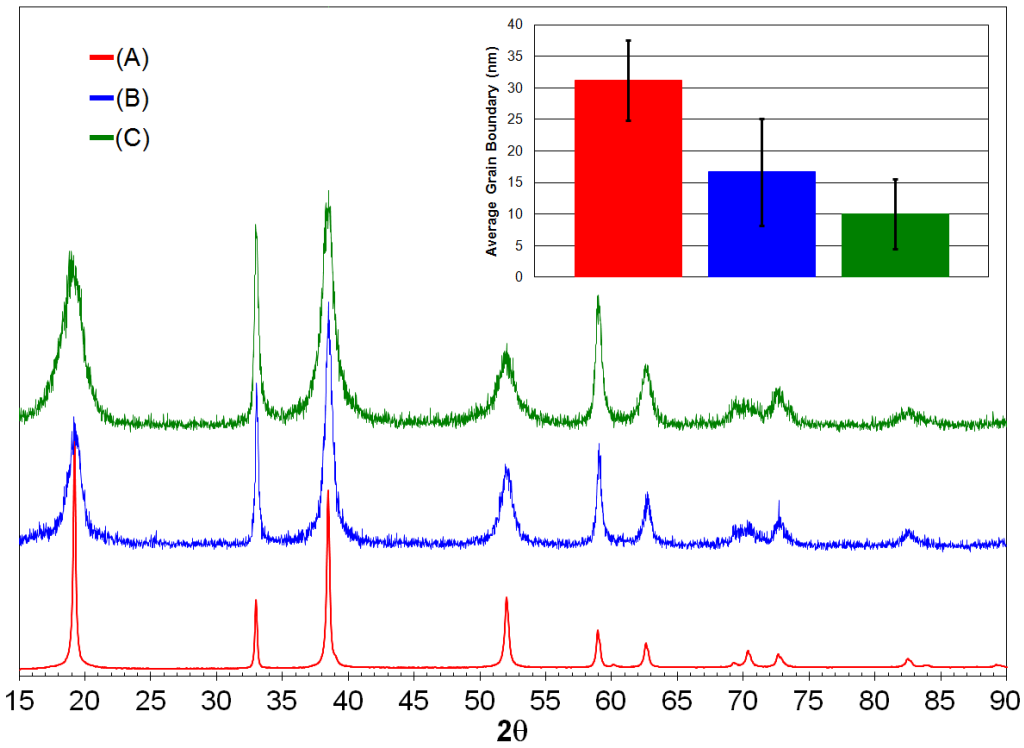

Figure 3.3. XRD patterns for (A) reflux-$Ni(OH)_2$, (B) RT NaOH-$Ni(OH)_2$, and (C) BT NaOH-$Ni(OH)_2$ precursors. Inset shows the average grain boundary size calculated from the Scherrer Equation for all three precursors using data from peaks at 19.2°, 33.0°, 38.5°, 52.0°, 58.9°, and 62.6°. Error bars represent standard deviation.

further transformed any remaining α-$Ni(OH)_2$ into β-$Ni(OH)_2$ [27]. The narrow peak widths for reflux-$Ni(OH)_2$ nanoparticles indicated they had a larger average grain size than RT and BT NaOH-$Ni(OH)_2$ (Fig. 3.3B-C) [22,27,110]. The inset of Fig. 3.3 confirms this conclusion, showing the average grain boundary sizes for each synthesis method calculated from the Scherrer Equation, Equation 3.1:

$$D = k\lambda/Bcos\theta \tag{3.1}$$

where D is the grain boundary size (in nm), k is the shape factor (taken as 0.9), λ is the x-ray wavelength (0.1540562 nm), B is the width (in radians) at half the maximum peak intensity, and θ is the Bragg angle. The calculated size for reflux-$Ni(OH)_2$ (31.2 nm) was about double the size of RT NaOH-$Ni(OH)_2$ (16.7 nm), and more than three times the size of BT NaOH-$Ni(OH)_2$ (10.0 nm). BET analysis reinforced these results as well, with the smaller RT NaOH-$Ni(OH)_2$ and BT NaOH-$Ni(OH)_2$ particles possessing larger specific surface areas than reflux-$Ni(OH)_2$. On the other hand, the broadening of the 19.2°, 38.5°, and 52.0° peaks for both RT NaOH-$Ni(OH)_2$ and BT NaOH-$Ni(OH)_2$ compared with reflux-$Ni(OH)_2$, along with variations in peak intensity, suggests: i) the average crystal/grain boundary size was smaller than that of reflux-$Ni(OH)_2$ and led to higher specific surface area; ii) the presence of disordered stacking/growth faults and/or proton vacancies in the β-$Ni(OH)_2$ structure; and iii) an additional and less stable amorphous, or at least poorly crystalline, α-phase existed along with the β-

phase [23,26,27,110-112].

A discrepancy is evident between the magnitudes of grain boundary sizes obtained through XRD patterns and particle sizes observed in SEM images. However, these two magnitudes are not necessarily interchangeable since $Ni(OH)_2$ and NiO particles viewed via SEM may consist of numerous smaller, agglomerated crystallites. The Scherrer Equation calculates the size of these individual crystallites rather than the particle as a whole, and consequently the data obtained through SEM and XRD are fundamentally different and should not be considered interchangeable [113]. The trends stemming from SEM and XRD data concerning crystallite/particle sizes, however, do correlate well, and reinforce conclusions drawn from other characterization and electrochemical data.

Figure 3.4 shows the XRD patterns for as-prepared NiO nanoparticles from all three synthesis methods calcined in air at 500°C. Peak positions (with crystal faces) were 37.2° (111), 43.3° (200), 62.8° (220), 75.4° (311), and 79.3° (222) [13,16,22,25]. While it is well-documented that NiO forms at temperatures just below 300°C [13,22,25,26,114], a calcination temperature of 500°C was chosen based on literature results to ensure complete dehydration of $Ni(OH)_2$ into NiO, leaving no precursor materials remaining [25,114]. It was observed that for reflux-$Ni(OH)_2$, 2 hours of calcination time was sufficient to achieve this goal, while NaOH-$Ni(OH)_2$ precursors required 6 hours at 500°C to complete the

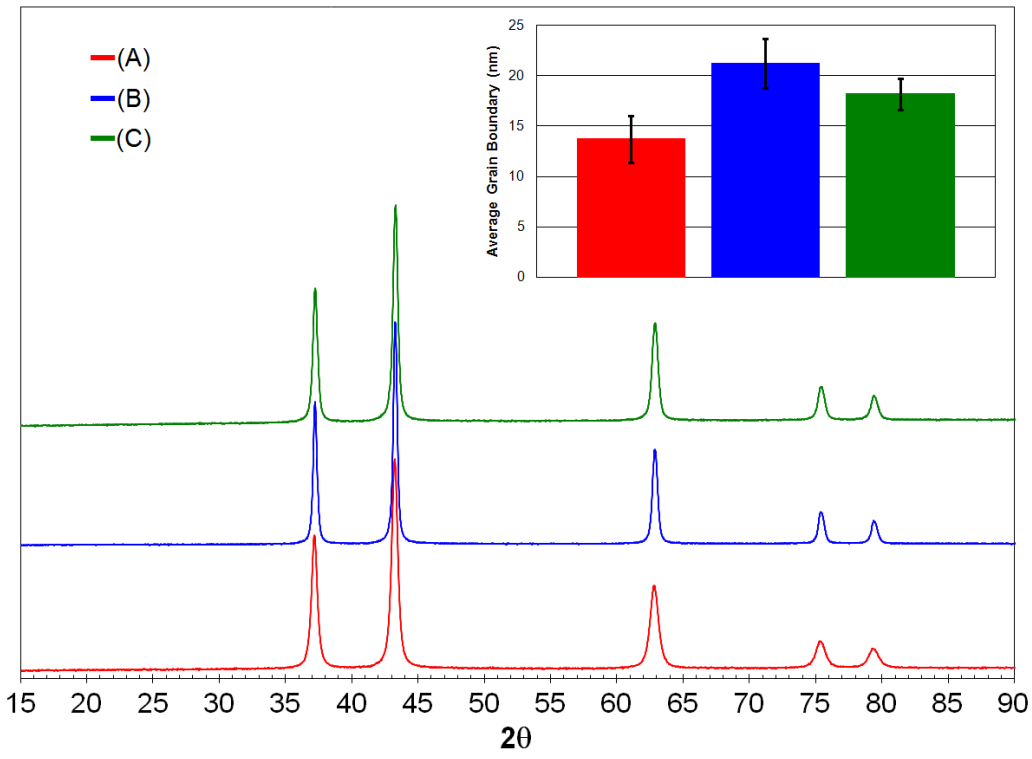

Figure 3.4. XRD patterns for (A) reflux-NiO, (B) RT NaOH-NiO, and (C) BT NaOH-NiO. Inset shows average Scherrer Equation grain boundary sizes calculated from all five peak locations. Error bars represent standard deviation.

reaction. Increased time at this elevated temperature likely caused increased particle agglomeration for RT NaOH-NiO and BT NaOH-NiO, leading to larger average grain boundaries than reflux-NiO (Fig. 3.4 inset), which is opposite to the trend observed with their respective precursors (Fig. 3.3 inset). In this case, this trend was confirmed through BET results, which showed the largest specific surface area for reflux-NiO and smaller values for RT NaOH-NiO and BT NaOH-NiO. However, despite minor grain boundary size differences, there were no dramatic differences in any NiO peak widths or positions as with the $Ni(OH)_2$ precursors. Based on these results, the question arises whether distinguishing characteristics seen in Fig. 3.3 with the pre-calcined nanoparticles still played a role in their electrochemical performance post-calcination, considering the increased uniformity among XRD patterns shown in Fig. 3.4.

3.2.3 Simultaneous Thermal Analysis

Figure 3.5 shows the DSC and TGA curves for reflux-$Ni(OH)_2$ and RT NaOH-$Ni(OH)_2$ up to 1100°C from room temperature, followed by cooling back to room temperature, at a rate of 15°C/min. The STA curves for BT NaOH-$Ni(OH)_2$ were identical to those for RT NaOH-$Ni(OH)_2$, therefore that data was omitted. The calcination of $Ni(OH)_2$ to NiO involved two processes, shown in Equations 3.2 and 3.3 [13,22,25,26,114]:

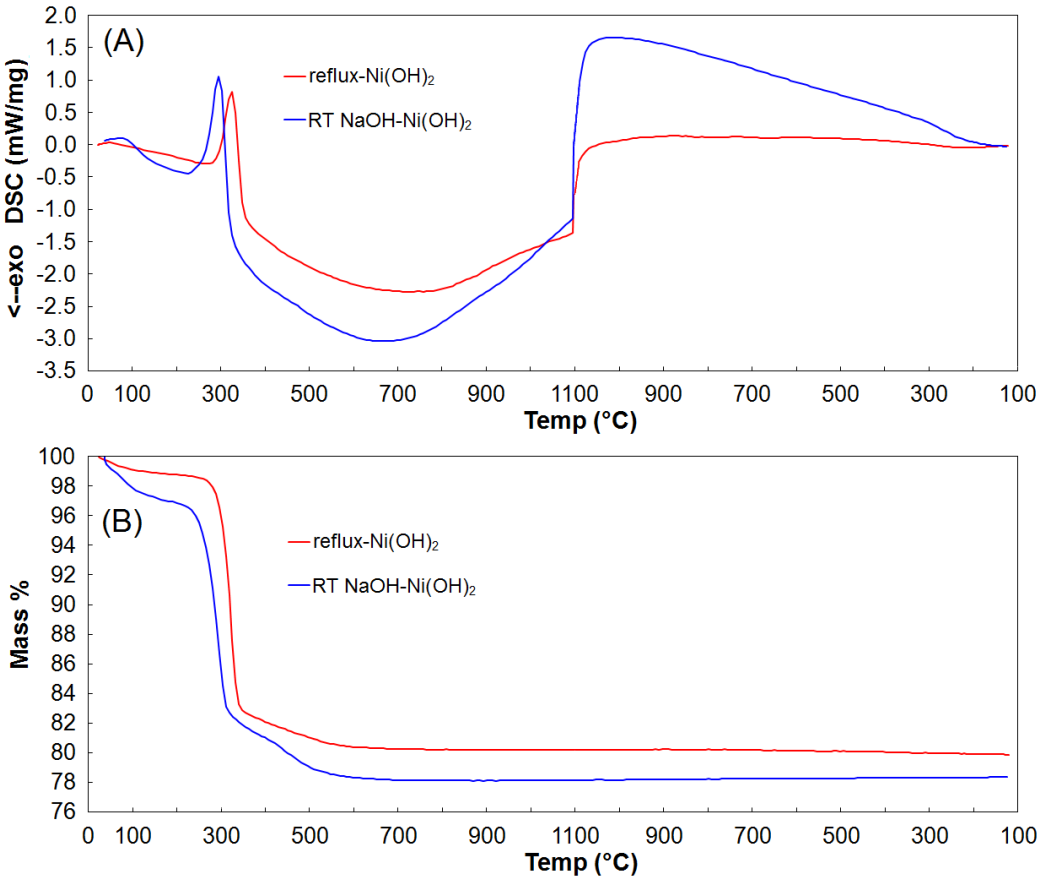

Figure 3.5. STA curves: (A) DSC and (B) TGA for reflux-$Ni(OH)_2$ and RT NaOH-$Ni(OH)_2$. Temperature range was 25-1100°C, and heating/cooling rate was 15°C/min. Negative DSC values corresponded to exothermic heat flow.

$$Ni(OH)_2 \bullet x_w H_2O \rightarrow Ni(OH)_2 + x_w H_2O \quad (3.2)$$

$$Ni(OH)_2 \rightarrow NiO + H_2O \quad (3.3)$$

Eq. 3.2, which accounted for a weight loss of around 1-4%, is the removal of chemically adsorbed and/or structurally bonded water molecules. Eq. 3.3 is the decomposition of $Ni(OH)_2$ to NiO and was responsible for the majority of the overall weight loss (~20-22%) and the sharp, endothermic peak around 300°C seen in the DSC curves (Fig. 3.5A). Both reactions were irreversible as evidenced by the constant mass observed throughout the entire cooling cycle back down from 1100°C to room temperature (Fig. 3.5B). While Eq. 3.2 occurred continuously up to around 200°C for both reflux-$Ni(OH)_2$ and RT NaOH-$Ni(OH)_2$, the onset temperatures for the endothermic peaks in Figure 3.5A differed significantly. The DSC decomposition reaction peak (Eq. 3.3) for reflux-$Ni(OH)_2$ was at 325°C and the peak for RT NaOH-$Ni(OH)_2$ was at 295°C. This 30°C difference in DSC and TGA responses was consistent throughout the entire temperature range, and was likely a result of the smaller crystal size of RT NaOH-$Ni(OH)_2$ over reflux-$Ni(OH)_2$ [26].

A possible third section was visible directly after the decomposition reaction, marked by a sharp decrease in the slope of the TGA curves, before the slope approached zero at around 600°C. This may have corresponded to the $Ni(OH)_2$ decomposition reaction approaching 100% completion, or it may have

represented the decomposition of a small fraction of various unstable, unstoichiometric nickel oxides (NiO_x) formed during the first decomposition step to NiO [25]. This potential third decomposition reaction of unstoichiometric nickel oxides could account for a discrepancy in the atomic ratios of O to Ni for reflux-NiO and RT NaOH-NiO. Since the larger crystal size of reflux-$Ni(OH)_2$ caused a 30°C delay in this decomposition reaction, the result of calcining in air at 500°C may only have been a partially completed decomposition, leaving more unstoichiometric NiO_x present, increasing the overall O:Ni ratio. On the other hand, the smaller crystal size and lower decomposition reaction temperature for RT NaOH-$Ni(OH)_2$ caused the 500°C calcination temperature to be much closer to the completion of this decomposition, which led to almost purely stoichiometric NiO. A higher calcination temperature for reflux-$Ni(OH)_2$ would likely lower the O:Ni ratio, but would also cause more particle agglomeration and reduce the specific surface area. Therefore, the NaOH-precipitation method should be preferred over the reflux-method since purely stoichiometric NiO is obtainable at a lower calcination temperature and greater surface area.

3.2.4 X-ray Photoelectron Spectroscopy

Deconvoluted XPS spectra for reflux-NiO and RT NaOH-NiO are shown in Figures 3.6 and 3.7. The Ni 2p and O 1s resolved peak locations and relative

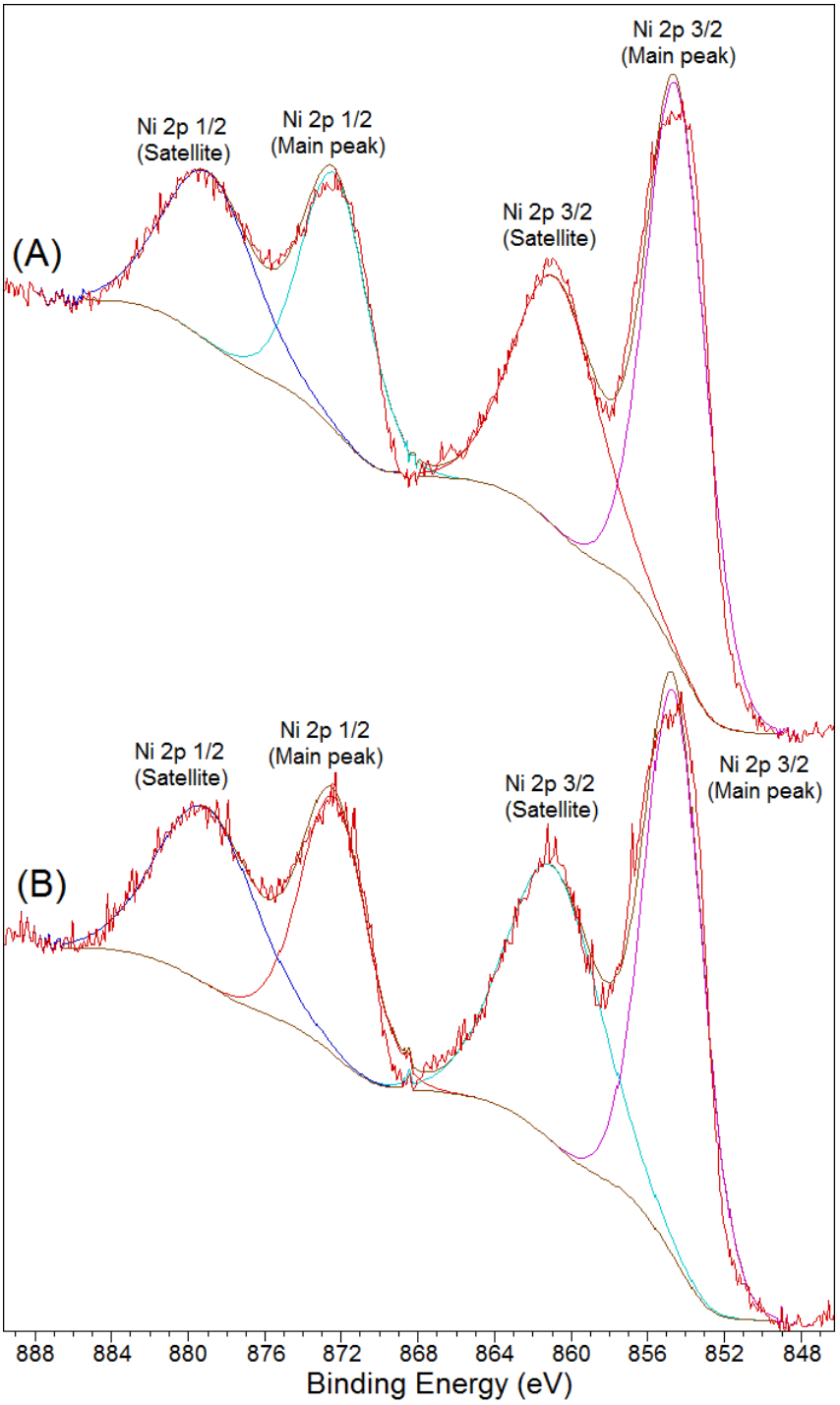

Figure 3.6. Deconvoluted XPS Ni 2p spectra for (A) reflux-NiO and (B) RT NaOH-NiO.

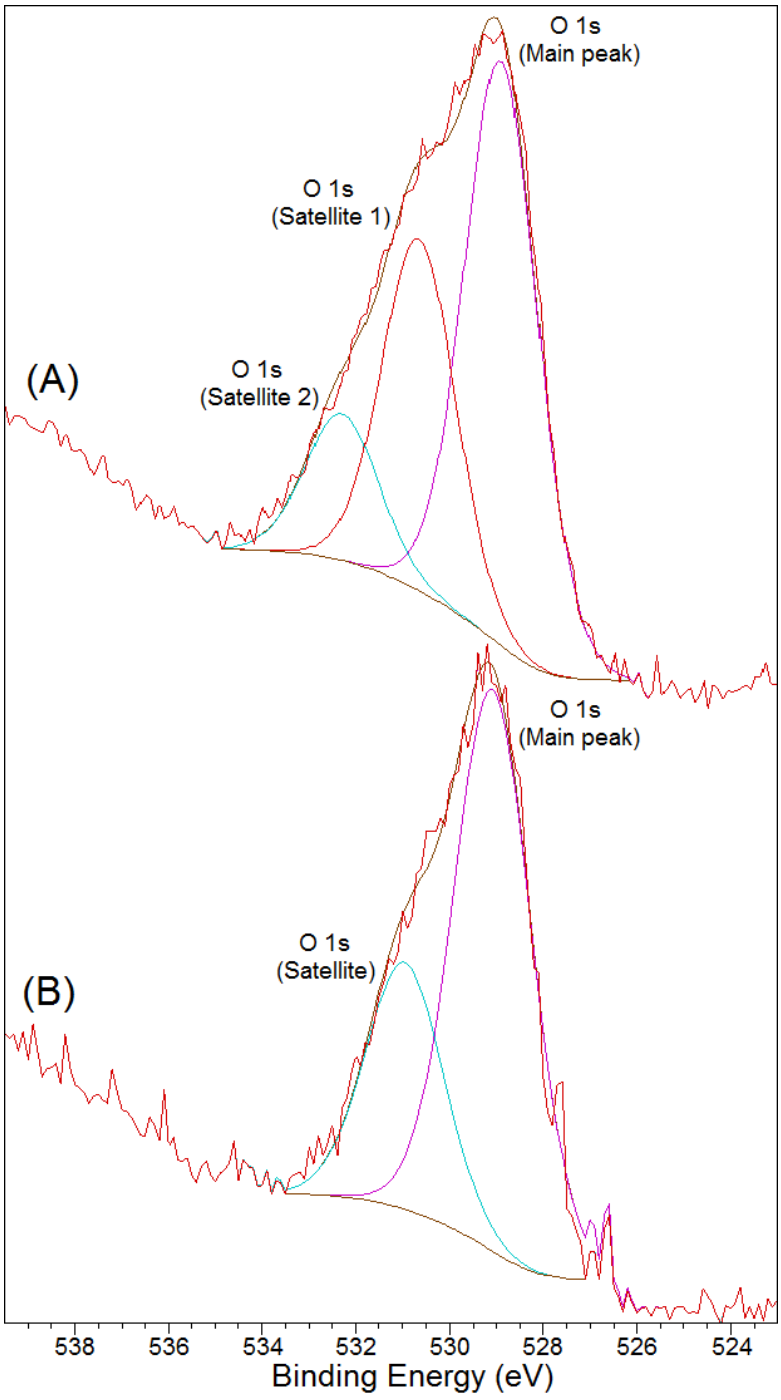

Figure 3.7. Deconvoluted XPS O 1s spectra for (A) reflux-NiO and (B) RT NaOH-NiO.

areas are listed in Table 3.1, with the area percents summed to 100% separately for each individual element line designation. The prominent features visible in all spectra, particularly the Ni 2p spectra, were satellite peaks in addition to the main peaks for each line designation. All main and satellite peak binding energies listed in Table 3.1 matched well with those reported in the literature for NiO [24,115-119]. There are several possible explanations for these satellite peaks. Multiplet splitting may have existed within the Ni valence sub-shell where unpaired electrons produced two final states with different binding energies separated by around 3-15 eV [116,119]. Another possibility was the creation of plasmons from positive core hole coupling, which is also a trait indicative of conducting materials [116]. It could also be explained by a ligand-to-metal charge transfer whereby the core hole pulled down the nickel metal d-band to below the top of the ligand 2p band, causing a transfer of charge [24,115]. The magnitude of satellite peaks for the Ni 2p 1/2 and Ni 2p 3/2 spectra could therefore be equated to the relative amount of charge transfer occurring within that NiO compound. The area percents for the Ni 2p satellite peaks for RT NaOH-NiO (Table 3.1) showed a greater amount of compound charge transfer from oxygen to nickel compared to reflux-NiO. Conversely, the O 1s spectra (Fig. 3.7) displayed an opposite trend. It follows that if the nickel satellite peaks increased due to higher charge transfer, then the oxygen satellite peaks would decrease accordingly. This was evident in the O 1s spectrum for reflux-NaOH-

Table 3.1. XPS resolved peak positions and relative areas for Ni 2p and O 1s spectra, for reflux-NiO and RT NaOH-NiO.

Configuration	Peak Type	Reflux-NiO			RT NaOH-NiO		
		Binding Energy (eV)	Area %	Total %	Binding Energy (eV)	Area %	Total %
Ni 2p 3/2	Main	854.5	61.5	100	854.7	56.0	100
Ni 2p 3/2	Satellite	860.8	38.5		861.0	44.0	
Ni 2p 1/2	Main	872.3	52.6	100	872.5	49.2	100
Ni 2p 1/2	Satellite	878.9	47.4		879.1	50.8	
O 1s	Main	528.9	54.0	100	529.1	69.5	100
O 1s	Satellite 1	530.7	32.5		531.0	30.5	
O 1s	Satellite 2	532.3	13.5				

NiO (Fig. 3.7A) which had two satellite peaks and a broader range of binding energies than the corresponding spectrum for RT NaOH-NiO (Fig. 3.7B), which showed only one satellite peak.

Finally, the O:Ni ratios obtained from the XPS spectra confirmed that RT NaOH-NiO was closer to purely stoichiometric NiO than reflux-NiO. A 14% increase in the O:Ni ratio was observed for reflux-NiO (1.21) over RT NaOH-NiO (1.06), which likely stemmed from the differences in decomposition reaction temperatures of the two precursors. The larger fraction of O atoms in reflux-NiO may also partially explain the appearance of multiple satellite peaks in its O 1s spectrum. Thus, the corresponding spectrum for RT NaOH-NiO displayed fewer satellite peaks and a narrower range due to its more stoichiometric composition.

3.2.5 Cyclic Voltammetry

The electrocatalytic activity of NiO was examined in both hydroxide and carbonate alkaline media. Concentrations of KOH (0.005M) and Na_2CO_3 (0.1M) electrolytes were selected to normalize the pH at around 11.5 for all tests due to the fact that peak potentials shift at a rate of roughly 60 mV per pH unit [7,28,120]. Figure 3.8 shows the CVs for both reflux-NiO and RT NaOH-NiO in 0.005M KOH (Fig. 3.8A) and 0.005M KOH/0.1M CH_3OH (Fig. 3.8B) solutions.

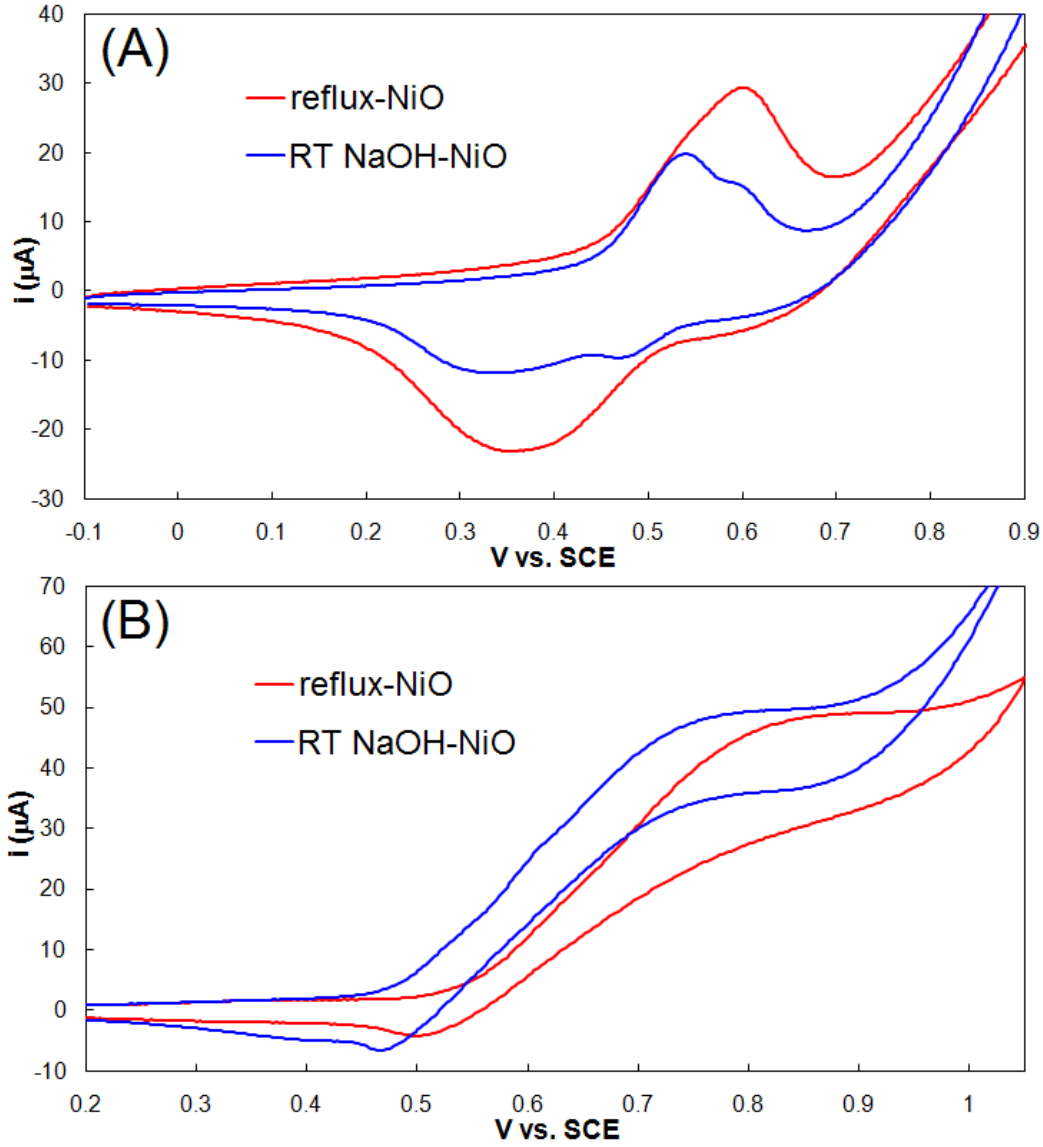

Figure 3.8. CVs from -0.1V to 1.05V vs. SCE in (A) 0.005M KOH and (B) 0.005M KOH/0.1M CH_3OH for reflux-NiO and RT NaOH-NiO. Scan number 20 is shown for each CV, and the scan rate was 20 mV/s.

The CVs for BT NaOH-NiO in the same two electrolytes are shown in Figure 3.9, and no significant differences were observed between BT NaOH-NiO and RT NaOH-NiO data. Differences in peak current ranges between voltammograms from the same electrolyte were attributed to minor differences in NiO catalyst loading on the GC electrode surface.

A distinct difference in current ranges was apparent between the hydroxide and carbonate electrolytes. Figure 3.10 shows the cyclic voltammograms for reflux-NiO and RT NaOH-NiO in 0.1M Na_2CO_3/0.1M CH_3OH, which were comparable to the CVs in Fig. 3.8B. BT NaOH-NiO CVs in the same electrolyte are shown in Figure 3.11, and once again no significant differences between BT NaOH-NiO and RT NaOH-NiO were seen. Measured currents were 3-4 times larger on average in carbonate media than in hydroxide media. This equates to a major advantage of using a carbonate electrolyte over a hydroxide electrolyte since it exhibited the potential for improved activity in solutions of more moderate alkalinity. Considering the pH for all solutions was kept at a uniform value of 11.5, this current increase in carbonate solution could not be attributed to a larger OH^- concentration which would have raised the peak current due to an increased rate of OH^- incorporation into the $Ni(OH)_2$ film [6,29]. It was also contrary to the expectation that carbonate current ranges should have been smaller than hydroxide current ranges due to larger anions competing for

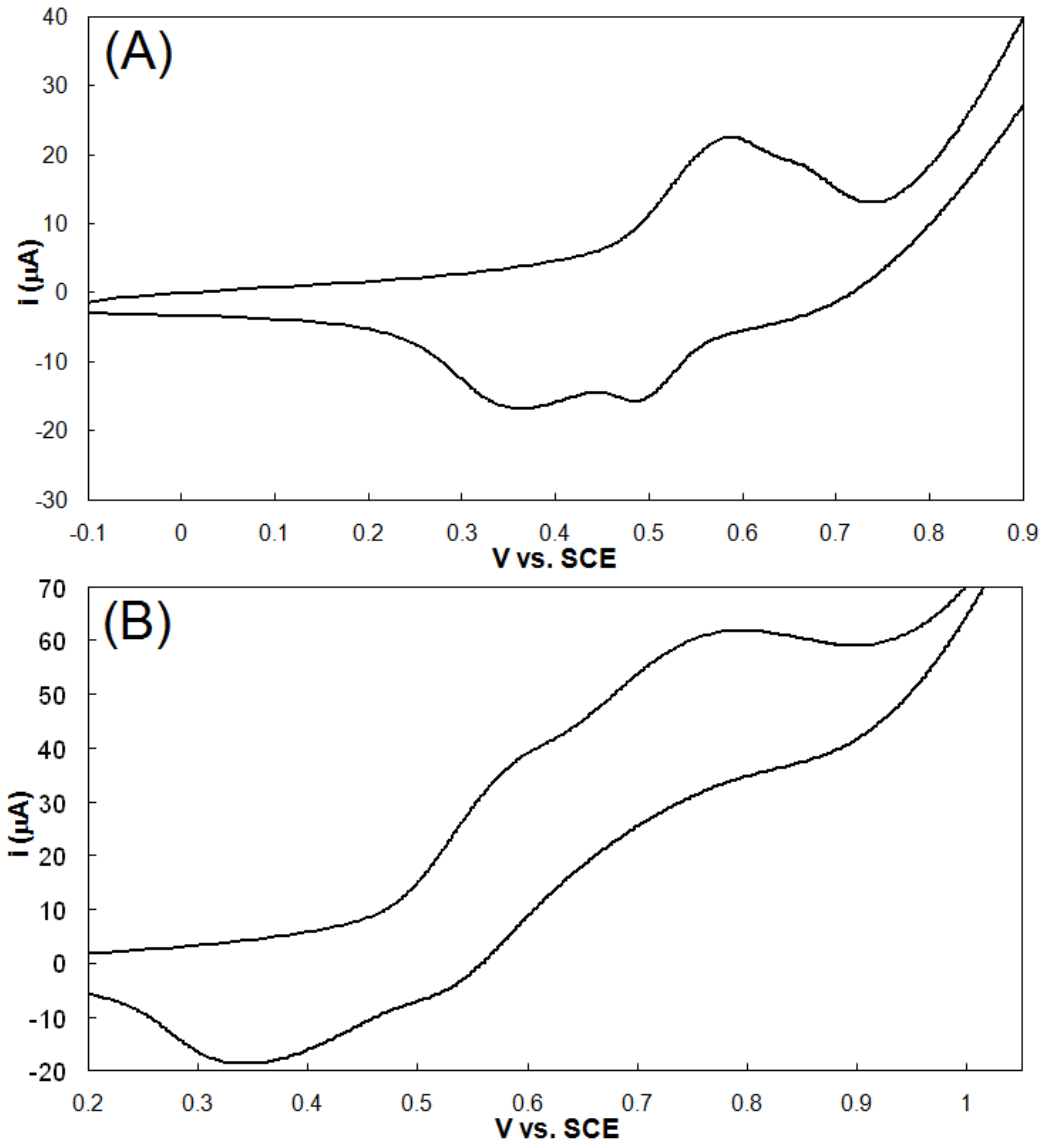

Figure 3.9. CVs from -0.1V to 1.05V vs. SCE in (A) 0.005M KOH and (B) 0.005M KOH/0.1M CH_3OH for BT NaOH-NiO. Scan number 20 is shown for each CV, and the scan rate was 20 mV/s.

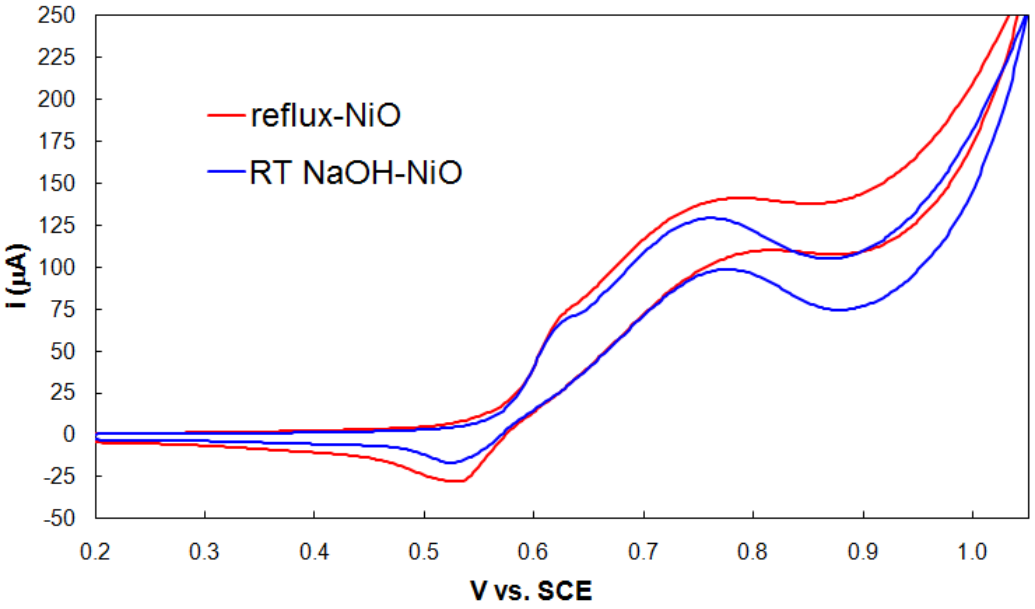

Figure 3.10. CVs from -0.1V to 1.05V vs. SCE in 0.1M Na_2CO_3/0.1M CH_3OH for reflux-NiO and RT NaOH-NiO. Scan number 20 is shown for each CV, and the scan rate was 20 mV/s.

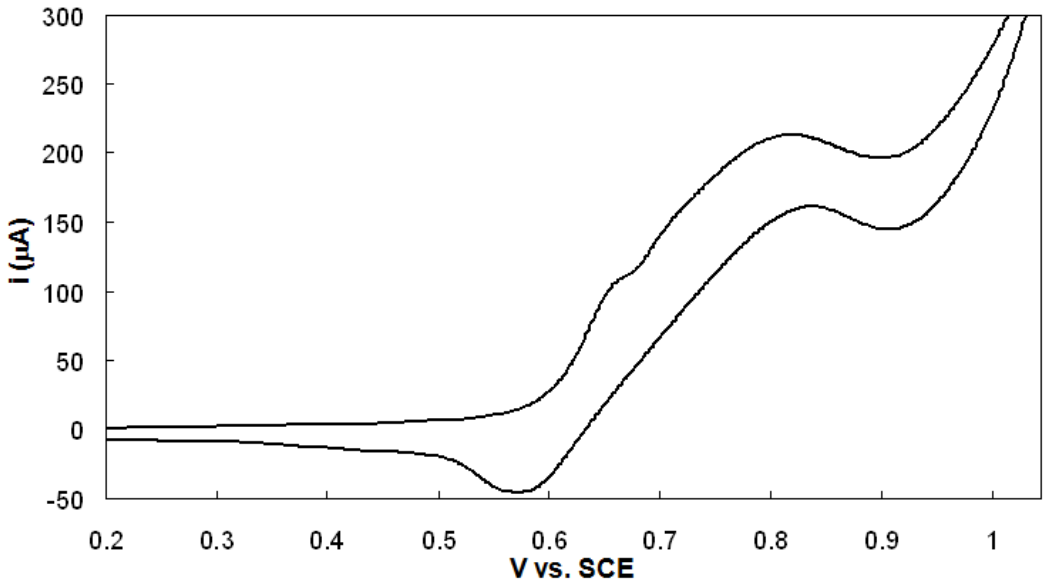

Figure 3.11. CV from -0.1V to 1.05V vs. SCE in 0.1M Na_2CO_3/0.1M CH_3OH for BT NaOH-NiO. Scan number 20 is shown, and the scan rate was 20 mV/s.

surface adsorption, as has been reported for Pt-based electrocatalysts [120,121]. However, this trend has been recently observed for the hydrogen oxidation reaction over a Pt electrocatalyst where the exchange current density was significantly higher in a carbonate electrolyte than a hydroxide electrolyte, owing in part to more favorable bond dissociation thermodynamics and low intermediate activation energies [104]. In addition, the smaller ratio of hydration radii of solvated CO_3^{-2} to OH^- anions (1.31) compared to the simple anion radius ratio (1.59), in addition to carbonate's higher valence (-2 vs. -1) partially compensating for its larger size and lower mobility, likely explains the differences seen between current ranges [102].

Upon immersion in alkaline media, a layer of $Ni(OH)_2$ immediately forms on the NiO electrode surface [9,28,122]. This $Ni(OH)_2$ layer is electrochemically active and undergoes a well-documented Ni^{+2}/Ni^{+3} redox process, Equation 3.4 [5-7,9-12,22,28-30,110,112,122,123]:

$$Ni(OH)_2 + OH^- \leftrightarrow NiOOH + H_2O + e^- \quad (3.4)$$

Two clear oxidation peaks for RT NaOH-NiO in 0.005M KOH (Fig. 3.8A) were visible at 0.52V and 0.58V vs. SCE, along with two corresponding reduction peaks at 0.35V and 0.48V vs. SCE, respectively. This phenomenon, originally reported by Bode, Dehmelt, and Witte [124], was caused by the phase transformation of β-NiOOH to γ-NiOOH due to slow, irreversible overcharging

during cycling, and the corresponding reduction to α-$Ni(OH)_2$, creating two distinct, simultaneously-occurring redox processes on the electrode surface [9,12,23,110,112,123]. The redox peaks at 0.52V and 0.35V vs. SCE correspond to the β-$Ni(OH)_2$/β-NiOOH redox couple, while those at 0.58V and 0.48V vs. SCE correspond to the α-$Ni(OH)_2$/γ-NiOOH redox couple. The γ-phase is associated with volume expansion and swelling, which leads to the formation of microcracks and disintegration of the NiO film [9,12,23,110,112,123]. In addition, γ-NiOOH was reported to be the passivating species while β-NiOOH was the electrochemically active phase for organic compound oxidation [9,12]. This phase transformation partially explains the stability results seen in Figure 3.12. The potential for the methanol oxidation peak shifted roughly 130mV over the course of 100+ scans for reflux-NiO (Fig. 3.12A-B), compared to only about 70mV for RT NaOH-NiO (Fig. 3.12C-D), which suggests reflux-NiO was more readily overcharged from β- to γ-NiOOH resulting in lower electrochemical activity and poorer cyclability than RT NaOH-NiO.

The cathodic Ni^{+3}/Ni^{+2} reduction peak currents at around 0.4-0.5V vs. SCE for both reflux-NiO and RT NaOH-NiO were diminished in the presence of methanol compared to purely alkaline solutions [11,28,29]. This was a result of the irreversible, rate-determining methanol oxidation step which took place only over electrocatalytically active NiOOH [5]. The reaction resulted in the reduction

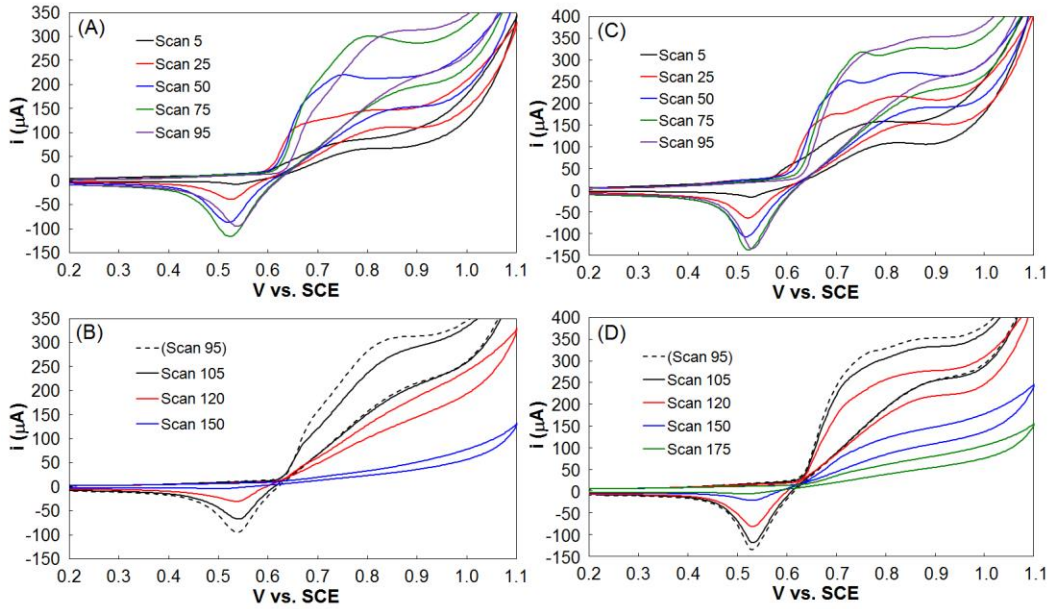

Figure 3.12. Stability CVs for entire working range of -1.1V to 1.2V vs. SCE in 0.1M Na_2CO_3/0.1M CH_3OH: (A) reflux-NiO current build-up; (B) reflux-NiO current deterioration; (C) RT NaOH-NiO current build-up; (D) RT NaOH-NiO current deterioration. A total of 200 scans were run for each material at 20 mV/s.

from NiOOH back to $Ni(OH)_2$, as originally reported by Fleischmann [28]:

$$NiOOH + organic\ compound \rightarrow Ni(OH)_2 + product \quad (3.5)$$

Since NiOOH was constantly being reduced back to $Ni(OH)_2$ once methanol oxidation started, some anodic current could always be attributed to the continuous re-oxidation of $Ni(OH)_2$ back to NiOOH (Eq. 3.4). Furthermore, during the cathodic scans, lingering methanol oxidation caused some portion of the electrode surface to be prematurely reduced to the Ni^{+2} oxidation state before the Ni^{+3}/Ni^{+2} reduction occurred, thus decreasing the amount of NiOOH on the surface and the magnitude of the corresponding peak.

The identity of products formed from the methanol oxidation (Eq. 3.5) is typically unspecified, though Singh et al. reported the detection of CO_3^{-2} anions from the evolution of CO_2 in a hydroxide solution after methanol oxidation over a Ni electrocatalyst, and also noted the lack of CO gas, though they expressed the possibility of the formation of other gaseous products [30]. Others mentioned formate anions ($HCOO^-$) or formic acid (HCOOH) as possible theoretical products following a 4-electron pathway [11,28]. The production of formic acid could hypothetically provide additional reasoning for the positive shift in redox potentials and catalyst degradation observed over time. Small amounts of formic acid formed continuously could cause a decrease in the local pH of the solution over time, and this negative change in pH would result in a positive shift for redox

peak potentials. Also, as the electrolyte alkalinity diminished, less β-$Ni(OH)_2$ would be transformed back from α-$Ni(OH)_2$, which is unstable in strongly alkaline environments and would therefore become increasingly stable over time. This would cause more of the α/γ redox couple to remain on the electrode surface and expedite the associated microcracking/electrode disintegration leading to electrocatalyst degradation.

Another cause of electrode degradation, in addition to microcracking and disintegration of the unstable γ-NiOOH phase, is the oxygen evolution reaction (OER). Ni-based electrodes are well-known catalysts for the OER. The alkaline OER is shown in Equation 3.6 [8,10,123]:

$$4OH^- \rightleftharpoons O_2 + 2H_2O + 4e^- \quad (3.6)$$

The OER was responsible for the sharp anodic current spike at high potentials immediately following methanol oxidation (Fig. 3.8-3.12), but its onset potential was convoluted and difficult to pinpoint exactly, consistent with the literature [123]. It was generally considered to begin when the background current increased by an arbitrary amount, but could have been affected by the Ni^{+2}/Ni^{+3} redox process and $Ni(OH)_2$ film resistance [123]. It is probable that the Ni^{+2}/Ni^{+3} redox and methanol oxidation reactions were mixed with the OER, causing some level of electrode degradation in all tests independent of the NiO sample.

However, with methanol in solution, the current spike occurred at a potential 200mV or greater than without methanol, which may have been the result of the primary OER being delayed significantly by adsorbed methanol and/or intermediates on the electrode surface.

Figure 3.13 shows the rates at which the methanol oxidation currents for reflux-NiO and RT NaOH-NiO grew and decayed as a function of the number of scans. The root cause for the current decay is tied to the electrode degradation and disintegration associated with γ-NiOOH and the OER. Methanol oxidation currents for both reflux-NiO and RT NaOH-NiO increased at roughly the same rate as a result of the continuous addition of OH^- ions into the $Ni(OH)_2$ film on the electrode surface [6,10,29]. They also both reached a maximum current after around 95-100 scans, though reflux-NiO decayed at a much more rapid rate than RT NaOH-NiO. The oxidation current for reflux-NiO was severely diminished or almost entirely indistinguishable about 50 fewer scans than for RT NaOH-NiO. This rapid loss in electrocatalytic activity agrees with the previous conclusion that reflux-NiO overcharged from β- to γ-NiOOH faster than RT NaOH-NiO, and is consistent with earlier observations made from XRD, STA, and XPS. The stacking/growth faults and/or proton vacancies seen in the RT NaOH-$Ni(OH)_2$ precursor, along with its lower decomposition temperature which led to a nearly stoichiometric O:Ni ratio, and the improved O-to-Ni electron transferability of RT

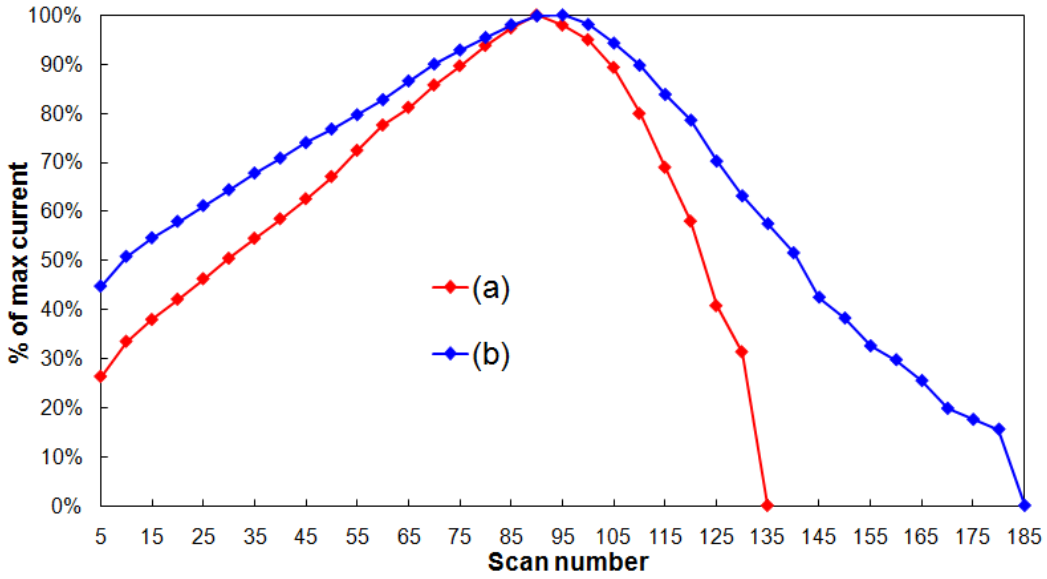

Figure 3.13. Stability plot of percent of maximum methanol oxidation current over 200-scan range versus the number of the consecutive scan for (a) reflux-NiO and (b) RT NaOH-NiO.

NaOH-NiO, all likely contributed to this difference in electrocatalytic performance even after calcination to NiO [26,110,111].

Another quality indicative of RT NaOH-NiO's electrocatalytic advantage over reflux-NiO was the appearance of a second anodic methanol oxidation peak on the reverse cathodic scan. This trend was more visible in the carbonate electrolyte (Fig. 3.10) than the hydroxide electrolyte (Fig. 3.8B), and was similar to the behavior of Pt-based electrodes towards methanol oxidation. The surface became cleaned and reactivated as the passive film that formed on the anodic scan was divested, and methanol oxidation occurred again until all NiOOH was completely reduced back to the electrocatalytically-inactive $Ni(OH)_2$ (Eq. 3.4) [120,125,126]. The current for reflux-NiO in carbonate medium flattened out at around 0.9V vs. SCE on the cathodic scan, but did not crest to a clear, definitive peak like RT NaOH-NiO did at a similar potential. Also, while neither displayed a complete anodic peak on their reverse scans in hydroxide medium, the current flattened out much more dramatically for RT NaOH-NiO than reflux-NiO, which had only a slight decrease in slope from the OER before reaching the Ni^{+3}/Ni^{+2} reduction at around 0.5V vs. SCE. This passive film that became divested for surface reactivation on the cathodic scan was likely γ-NiOOH, which was described as the passivating species, while β-NiOOH was reported to be the active species [9,12]. In agreement with the stability data, this suggests that

reflux-NiO was more readily and irreversibly transformed into the undesirable and unstable α-$Ni(OH)_2$/γ-NiOOH species redox couple than RT NaOH-NiO, and as a result not only deactivated more rapidly, but was also less electrochemically active throughout its lifetime.

3.2.6 Electrochemical Impedance Spectroscopy

IR-corrected Nyquist plots for reflux-NiO and RT NaOH-NiO in both hydroxide and carbonate media are shown in Figures 3.14 and 3.15. As expected, the Ohmic resistance (R_Ω) for all Nyquist plots was negligible. Two semicircles were visible in all plots, and at higher potentials a third semicircle was also observed. These three semicircles resulted from the three different reactions occurring: the Ni^{+2}/Ni^{+3} redox (Eq. 3.4), the methanol oxidation reaction (Eq. 3.5), and at larger potentials, the OER (Eq. 3.6), respectively. Figure 3.16 shows the equivalent electrical circuit for the electrochemical reactions that occurred in solution, with subscripts 1, 2, and 3 for each resistor-capacitor-in-parallel sub-circuit representing the three aforementioned reactions in parallel, and is similar to those reported in the literature [30,81,127].

A major observation consistent throughout all impedance data was the smaller resistance for NiO in carbonate electrolyte compared to hydroxide

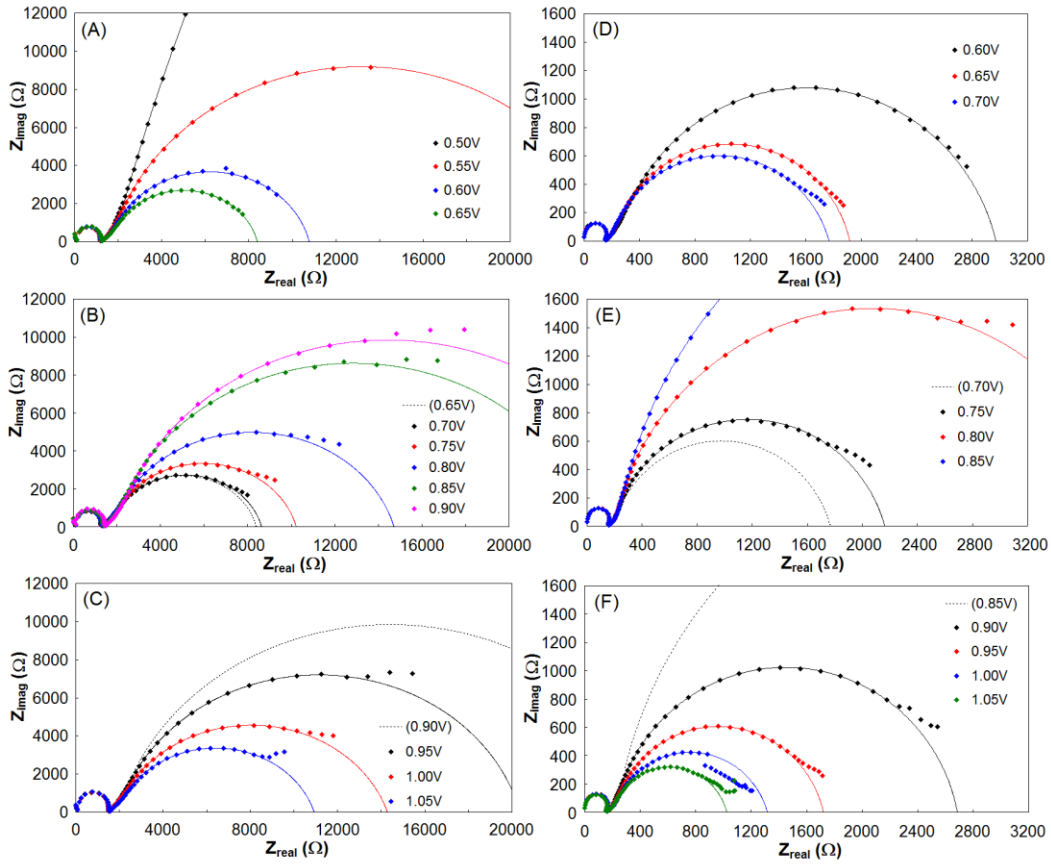

Figure 3.14. IR-corrected Nyquist plots for reflux-NiO in (A),(B),(C) 0.005M KOH/0.1M CH_3OH and (D),(E),(F) 0.1M Na_2CO_3/0.1M CH_3OH. Data was taken every 50mV from 0.50 to 1.05V vs. SCE for KOH electrolyte and from 0.60 to 1.05V vs. SCE for carbonate electrolyte. Frequency was ranged from 100mHz to 1MHz.

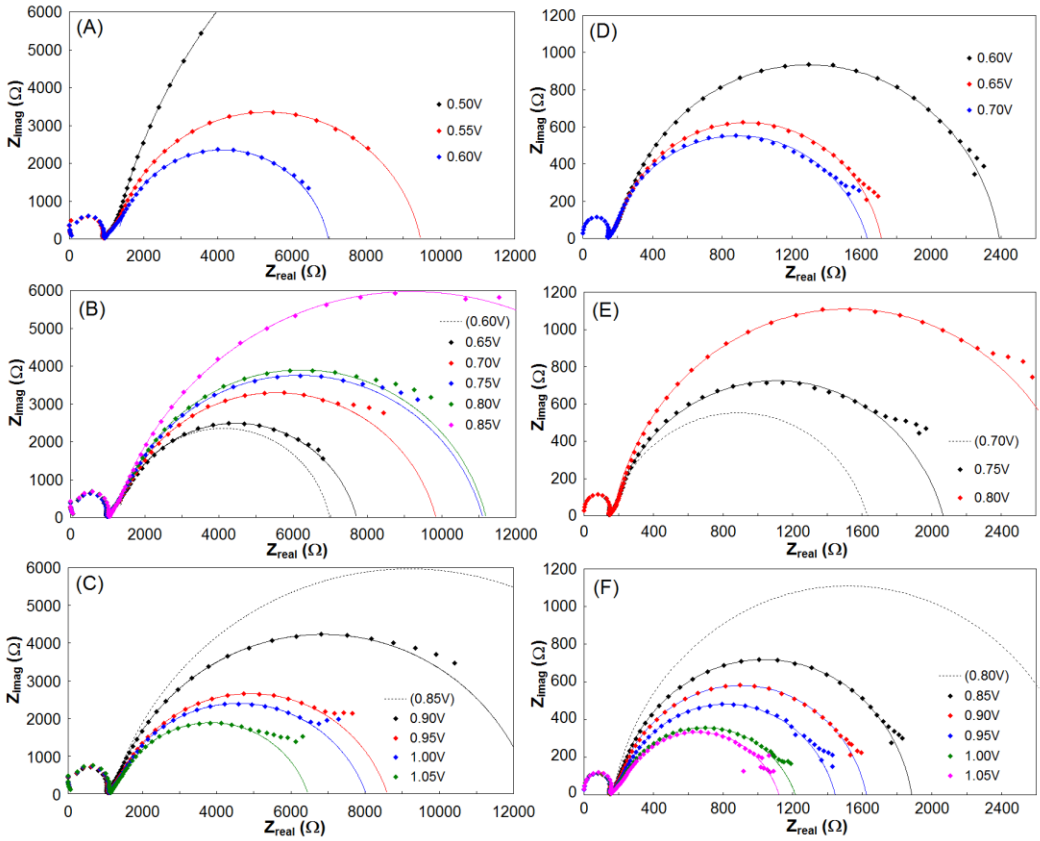

Figure 3.15. IR-corrected Nyquist plots for RT NaOH-NiO in (A),(B),(C) 0.005M KOH/0.1M CH_3OH and (D),(E),(F) 0.1M Na_2CO_3/0.1M CH_3OH. Data was taken every 50mV from 0.50 to 1.05V vs. SCE for KOH electrolyte and from 0.60 to 1.05V vs. SCE for carbonate electrolyte. Frequency was ranged from 100mHz to 1MHz.

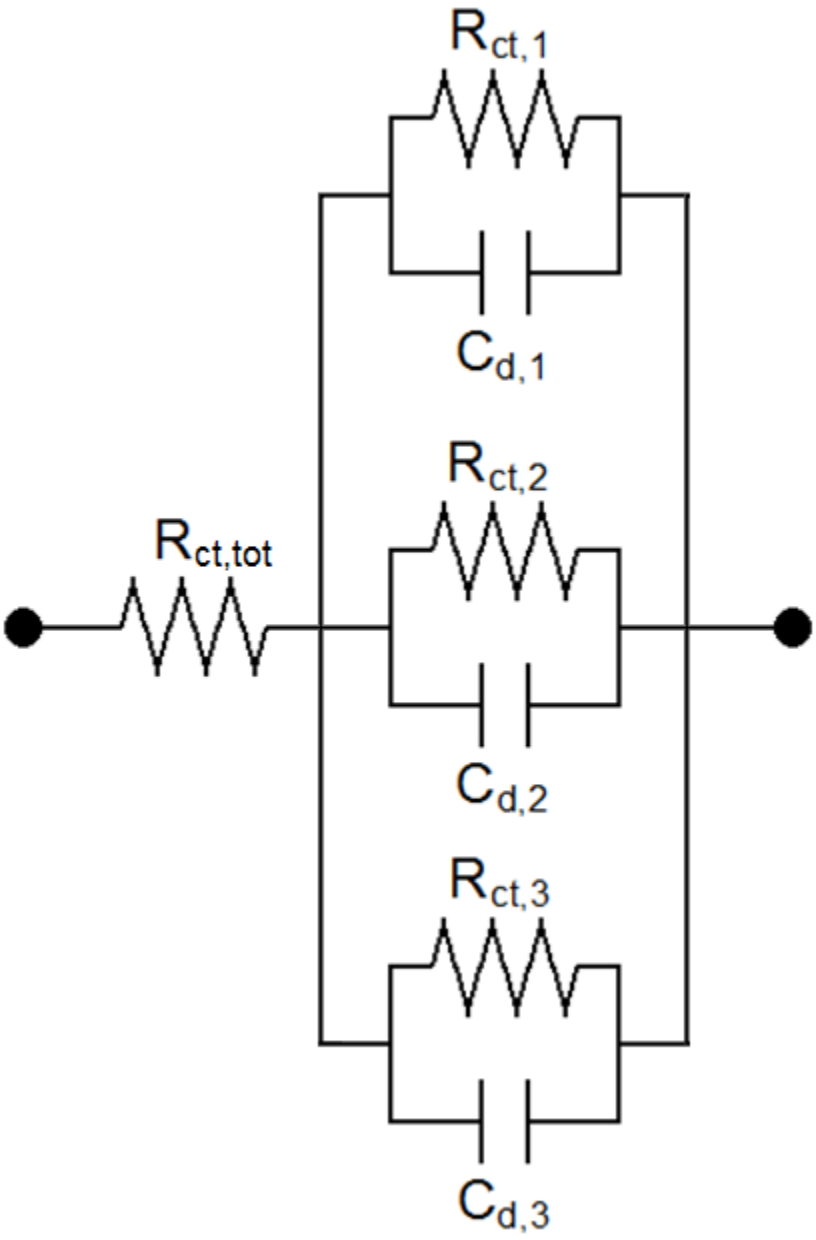

Figure 3.16. Equivalent electrical circuit for EIS data from NiO-catalyzed methanol oxidation in alkaline media. R_{Ω} was the ohmic resistance, $R_{ct,1}$, $R_{ct,2}$, and $R_{ct,3}$ were the charge transfer resistances and $C_{d,1}$, $C_{d,2}$, and $C_{d,3}$ were the double layer capacitances for the three reactions occurring in solution: Ni^{+2}/Ni^{+3} redox, methanol oxidation, and OER, respectively.

electrolyte. The Nyquist plots in Figures 3.14 and 3.15 showed approximately an 85% average decrease in resistance for all reactions in 0.1M Na_2CO_3 compared to 0.005M KOH, which was also consistent with the previous observation of currentdifferences observed in CVs for both electrolytes (Fig. 3.8-3.11) where measured currents were 3-4 times larger in carbonate media than in hydroxide media. The reduced charge transfer resistances for electrochemical reactions in carbonate medium reinforce its advantage over using hydroxide medium of similar alkalinity.

Despite the significant difference in the magnitude of the charge transfer resistances, impedance data for both hydroxide and carbonate media independently followed similar trends. Figure 3.17 shows the trends in charge transfer resistances as a function of potential for reflux-NiO and RT NaOH-NiO. The first conclusion from this data was that the charge transfer resistances for the Ni^{+2}/Ni^{+3} redox ($R_{ct,1}$) and methanol oxidation ($R_{ct,2}$) for RT NaOH-NiO were about 30% lower on average than for reflux-NiO. This suggests that these reactions proceeded more easily over RT NaOH-NiO than reflux-NiO, and is consistent with the previous evidence that RT NaOH-NiO was a better electrocatalyst than reflux-NiO. Another trend with this data was the slight increase in the magnitude of $R_{ct,1}$ with increasing potential. This could be attributed to minor interference caused by surface-adsorbed species and/or

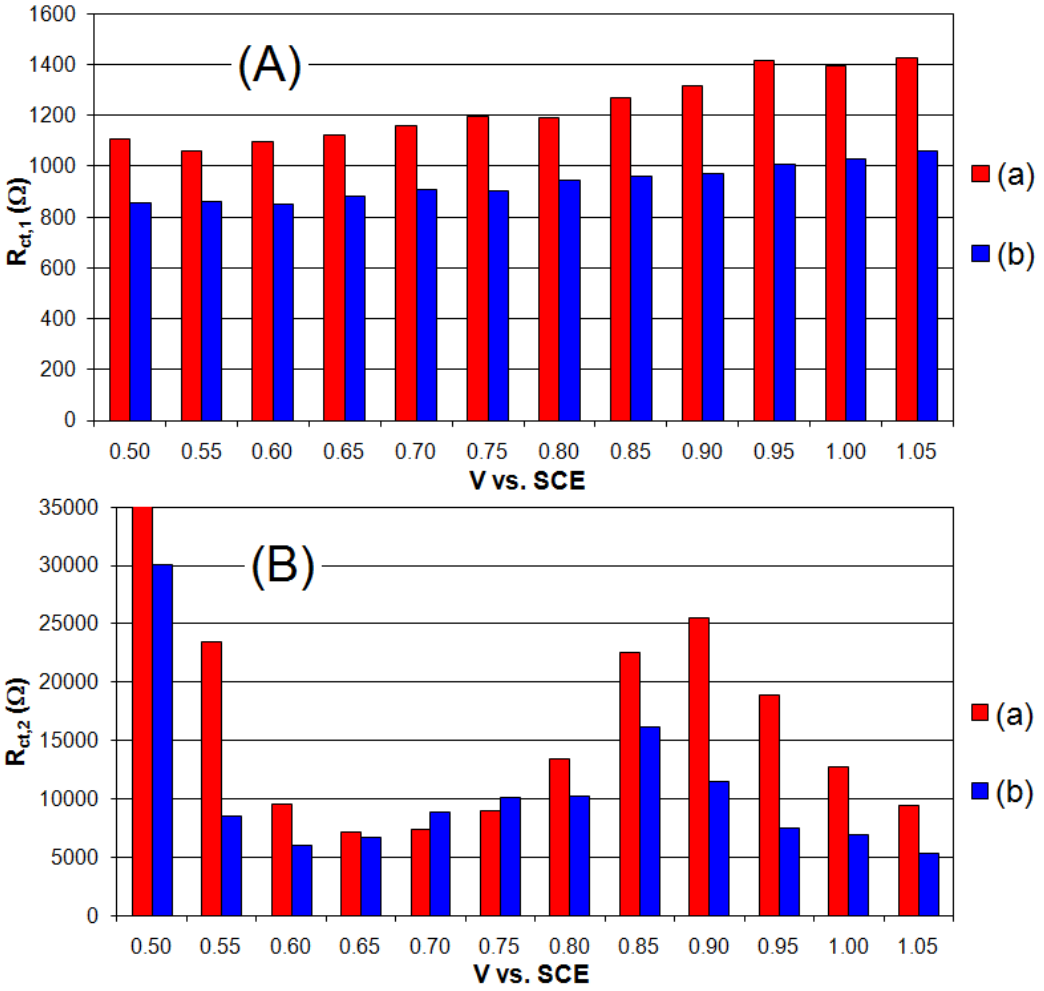

Figure 3.17. Comparison graphs for charge transfer resistances calculated from EIS data in 0.005M KOH/0.1M CH_3OH. Magnitude of resistance was shown as a function of potential for (A) the Ni^{+2}/Ni^{+3} redox reaction, $R_{ct,1}$, and (B) the methanol oxidation reaction, $R_{ct,2}$, over (a) reflux-NiO and (b) RT NaOH-NiO.

intermediates from the methanol oxidation reaction [5,28].

On the other hand, $R_{ct,2}$ experienced three sections of changing magnitudes. Over the first 100-150mV it decreased sharply (Fig. 3.14-3.15, (A) and (D)), then increased moderately for 100-200mV (Fig. 3.14-3.15, (B) and (E)) before dropping steadily over the final 100-200mV (Fig. 3.14-3.15, (C) and (F)). Conversely to the Ni^{+2}/Ni^{+3} redox, the slower methanol oxidation reaction was likely more affected by overpotential and surface-adsorbed species and/or intermediates. The changing magnitudes of $R_{ct,2}$ could also be correlated well to the current patterns from CV data. Immediately following the oxidation to NiOOH, the current increased rapidly (Fig. 3.8-3.11) and $R_{ct,2}$ decreased accordingly likely due to the growing overpotential and surface coverage of electrocatalytically active NiOOH facilitating methanol oxidation. The current then reached a peak and either decreased or remained relatively constant while $R_{ct,2}$ increased steadily as active sites became saturated with adsorbed species/intermediates. It is also possible that constant reduction of NiOOH back to $Ni(OH)_2$ through the methanol oxidation (Eq. 3.5) was partially responsible for this increase in resistance. Finally, the current spiked up and $R_{ct,2}$ diminished as the overpotential grew even more for both reactions, saturating the electrode with virtually all NiOOH and quickening the turnover of adsorbed intermediates.

A third semicircle developed around 0.65V vs. SCE and became more

visible in the low frequency range as the potential was increased up to 1.05V vs. SCE. This was likely the response from the OER, though its charge transfer resistance ($R_{ct,3}$) was difficult to ascertain due to O_2 gas formation and evolution at the electrode/electrolyte interface. However, the appearance of this third semicircle serves as a validation that the OER was mixed with the other two reactions occurring simultaneously on the electrode surface.

3.3 Summary

Nickel oxide functions as an electrocatalyst for the oxidation of methanol in alkaline media and is a potential candidate for organic sensor applications. Several synthesis techniques were carried out, and their effects on physical attributes and electrochemical performance were investigated. Greater variation in physical traits was observed through SEM, BET, and XRD analyses for $Ni(OH)_2$ precursors than for calcined NiO nanoparticles; however, significant differences between NiO synthesis methods in CV and EIS data were evident. Though small disparities in physical characteristics were seen between NaOH-precipitated $Ni(OH)_2$ and NiO at room temperature and boiling temperature, electrochemical data yielded no measurable advantages. Additionally, physical deficiencies in reflux-precipitated $Ni(OH)_2$ and NiO compared to RT NaOH-$Ni(OH)_2$ and NiO translated to weaker electrocatalytic activity and decreased

stability. As a result, RT NaOH-NiO was the best studied catalyst due to its ease of synthesis, improved electrochemical performance and stability characteristics.

Aqueous carbonate electrolytes presented average current ranges about 3-4 times higher than hydroxide solutions of similar alkalinity. Charge transfer resistances from EIS data were also around 85% lower for carbonate than for hydroxide. This suggests that carbonate may be a more favorable medium for electrochemical reactions than hydroxide, and its more moderate alkalinity could prevent degradation that occurs in hydroxide media at elevated pH.

CHAPTER 4: INFLUENCE OF NON-CONDUCTING ZIRCONIA ON THE ELECTROCHEMICAL PERFORMANCE OF NICKEL OXIDE IN ALKALINE MEDIA

The purpose of this work was to introduce zirconia as a non-conducting additive to nickel oxide and examine its electrocatalytic activity in alkaline media. A NiO-ZrO_2 bifunctional electrocatalyst was synthesized using a novel co-precipitation technique and it was physically characterized using Scanning Electron Microscopy, Brunauer-Emmett-Teller analysis, X-ray Diffraction, and X-ray Photoelectron Spectroscopy. Electrocatalytic activity in the presence of methane was investigated in both hydroxide and carbonate media using Cyclic Voltammetry and Electrochemical Impedance Spectroscopy. The role of zirconia in the bifunctional electrocatalyst was examined through low temperature methane activation. The work presented in this chapter was published in the *Journal of the Electrochemical Society* [128].

4.1 Experimental

4.1.1 Materials Synthesis

All reagents were used as received and all water used was ultra-pure 18.2 MΩ deionized water from a Millipore Direct-Q 3UV purification system. A nickel oxide-zirconia composite electrocatalyst with a Ni:Zr molar ratio of 80:20 (denoted (80:20)NiO:t-ZrO_2) was synthesized using a co-precipitation method slightly modified from our previously-published procedure [107]. In a large beaker under constant stirring, 100 mL of aqueous solution was prepared containing 0.4M $Ni(NO_3)_2$ (Acros, 99%) and 0.1M $ZrOCl_2$ (Acros, 98+%) and heated to its boiling point (~102°C). The solution temperature was measured using a Hannah Instruments HI9063 K-Type Thermocouple. In a separate beaker, an aqueous solution of 10M NaOH (Fisher, NF/EP/BP/FCC) was prepared, and then added rapidly to the boiling, stirring solution until the pH rose to between 8-10 to ensure complete precipitation. The solution pH was actively measured using an Accumet Excel XL60 Dual Channel pH/Ion/Conductivity/DO Meter. The solution was then capped and set aside for 24 hours. The resulting precipitated precursor (Ni species: $Ni(OH)_2$; Zr species: $Zr(OH)_4$) was rinsed repeatedly with deionized water to remove all trace of Cl^- ions. This was tested by adding a drop of aqueous $AgNO_3$ solution to a small volume of each filtrate until no white AgCl precipitation was visible. The chloride-free precipitated

precursor was then dried overnight at 90°C, followed by calcination in air at 500°C for 3 hours.

Single-phase nickel oxide (NiO) and tetragonal-phase zirconia (t-ZrO_2) were synthesized using similar NaOH-induced precipitation procedures. Two aqueous solutions were prepared, each containing 0.5M total concentration – $Ni(NO_3)_2$ for NiO synthesis and $ZrOCl_2$ for t-ZrO_2 synthesis – and under constant stirring were brought to a boil. Aqueous 10M NaOH solution was then quickly added to each until the pH rose to between 8-10, and the solutions were capped and set aside for 24 hours. The resulting precipitated precursors – green $Ni(OH)_2$ or white $Zr(OH)_4$ – were rinsed with copious deionized water, and with $Zr(OH)_4$ the filtrate was tested for the presence of Cl^- ions using the previously-described $AgNO_3$ test. Rinsed precipitated precursors were then dried overnight at 90°C, followed by calcination – NiO was prepared at 500°C in air for 3 hours, while t-ZrO_2 was prepared at 305°C in air for 32 hours.

4.1.2 Instrumentation and Techniques

The catalyst microstructure was investigated using an FEI Quanta FEG250 Scanning Electron Microscope (SEM). Specific surface areas were obtained through Brunauer-Emmett-Teller (BET) analysis using a Micromeritics ASAP

2020 system. A Bruker D8 Advance X-ray Diffractometer (XRD) with Cu $K\alpha_1$ radiation (λ = 0.1540562 nm) was used to evaluate crystal structure and average grain boundary size. X-ray photoelectron spectroscopy (XPS) was performed using a Physical Electronics Multiprobe with a Perkin-Elmer Dual Anode X-ray Source to investigate catalyst surface properties and elemental composition.

4.1.3 Electrochemical Tests

Thin-film disk electrodes were fabricated, and Cyclic Voltammetry (CV) and Electrochemical Impedance Spectroscopy (EIS) tests were performed. A custom three electrode cell (Adams & Chittenden) was used with an Autolab PGSTAT302N Potentiostat (Eco Chemie). For all tests, a platinum flag was used as the counter electrode and a saturated calomel electrode (SCE) was used as the reference electrode. All working electrodes were fabricated by preparing 15 mL of a 0.3 mg/mL dispersion of the selected catalyst in deionized water and placing it in an ultrasonic bath until the catalyst particles were uniformly distributed. Next, 20 μL of the dispersion was deposited onto a glassy carbon (GC) disk electrode (Pine Instrument Company, A = 0.196 cm^2) and it was spin dried in air at 200 rpm for 1 hour using a Pine AFMSRCE Modulated Speed Rotator. Once dry, 20 μL of a 0.05 wt.% Nafion solution (DuPont) was deposited on the GC

electrode and it was again spin dried in air at 200 rpm for 1 hour. Ultra high purity nitrogen (N_2, $\geq$ 99.999%) and chemical grade methane (CH_4, $\geq$ 99.0%) gases were used (Airgas). Prior to each electrochemical test, the electrolyte was bubbled with N_2 for 1 hour to remove any dissolved gases. Anhydrous sodium carbonate (Fisher, certified ACS grade, 99.9%) and potassium hydroxide (Acros, ca. 85%) were solvated in Millipore water to prepare the aqueous electrolytes used in all electrochemical tests. After each experiment, the catalyst particles were removed from the GC electrode surface by polishing with Buehler alpha 5.0 μm and gamma 0.05 μm alumina micropolish suspensions, with an ultrasonication step in between for 10 minutes to remove any loose particles.

4.2 Results and Discussion

4.2.1 Physical Characterization

Figure 4.1 shows SEM micrographs of (A) single-phase NiO and (B) (80:20)NiO:t-ZrO_2 electrocatalysts. Single-phase NiO formed spherical agglomerates with an average particle diameter of 20-30 nm, and a similar structure was visible in the co-precipitated materials. With the composite electrocatalyst, long, thin, blade-like t-ZrO_2 particles averaging around 100 nm in length were uniformly distributed throughout, suggesting close contact between

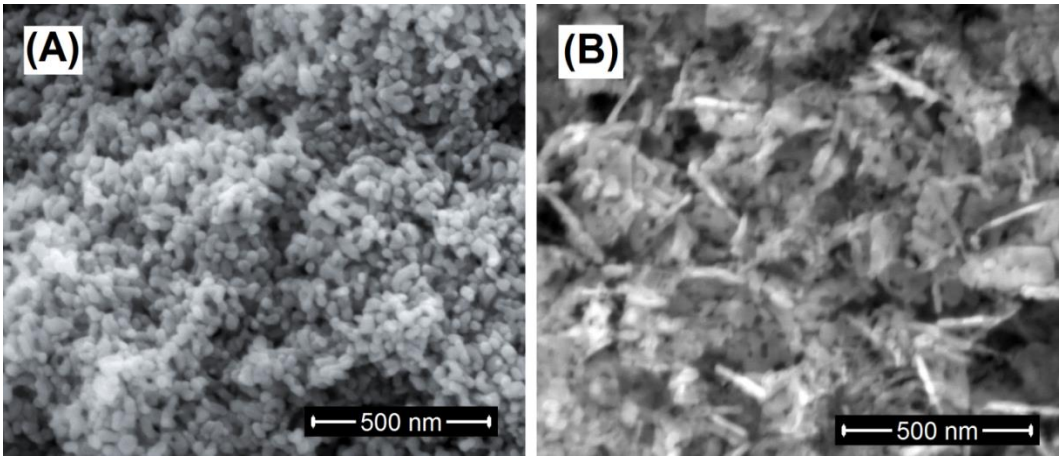

Figure 4.1. SEM micrographs of (A) single-phase NiO and (B) (80:20)NiO:t-ZrO_2 electrocatalysts.

NiO and t-ZrO_2. Several factors may have contributed to the observed intimate contact and homogeneous distribution. Constant stirring of the solution during synthesis prevented settling and ensured that the synthesis bath was well-mixed. Also, carrying out the procedure under boiling conditions may have facilitated more rapid precipitation kinetics. Improved kinetics, along with the quick addition of NaOH, likely resulted in a more rapid co-precipitation that may have prevented nucleation site agglomeration and led to uniform distribution, smaller average particle sizes, and a greater surface area [107,109]. Additionally, the prolonged aging in alkaline pH immediately after the rapid co-precipitation likely caused poor crystallinity and stacking/growth faults, which could lead to favorable electrocatalytic activity and electron transferability [129,130].

The BET specific surface area of single-phase NiO was found to be 23.4 m^2/g, which was similar to the value determined in our previous study using a slightly different synthesis procedure [107]. The specific surface area of (80:20)NiO:t-ZrO_2 was found to be 97.6 m^2/g, which was a dramatic increase compared to single-phase NiO. This increase could not be attributed to decreased agglomeration during calcination, however, since both were calcined at the same temperature for the same duration (500°C for 3 hours). The larger t-ZrO_2 particles may have sterically hindered crystallization and/or agglomeration of NiO spheres to some degree during precipitation and calcination, resulting in smaller

particles and greater surface area. Another factor that may have contributed to the high specific surface area of (80:20)NiO:t-ZrO_2 was the high intrinsic specific surface area of t-ZrO_2, which was found to be 146.0 m^2/g for single-phase t-ZrO_2. While the lower calcination temperature for t-ZrO_2 (305°C) compared to (80:20)NiO:t-ZrO_2 (500°C) likely played a role in this high surface area, it is possible that the addition of t-ZrO_2 to the composite material simply raised the value by virtue of its own improved surface area compared to single-phase NiO.

The small average particle size and spherical shape of agglomerated NiO leads to a large percentage of the Ni atoms contributing to the exposed surface area, whereas the larger, blade-like t-ZrO_2 particles have a much lower ratio of surface:bulk Zr. Since XPS is a surface sensitive technique with limited penetration depth, these differences in particle size and shape are expected to show significant deviation in the surface composition compared to the bulk ratio of 4-to-1. This is exactly what was observed; elemental analysis of the (80:20)NiO:t-ZrO_2 electrocatalyst surface using XPS revealed 52.12% O, 44.84% Ni, and 3.04% Zr. Additionally, the stoichiometric amount of oxygen (52.12%) closely matched what was predicted from the aggregate contributions of NiO (44.84%) and ZrO_2 (6.08%), meaning there likely was no appreciable amount of unexpected oxidation states or unstoichiometric oxides for either Ni or Zr other than the expected 2+ and 4+ states, respectively.

To understand the potential interaction between NiO and t-ZrO_2, individual elemental spectra were further analyzed. Deconvoluted XPS spectra for Ni 2p, O 1s, and Zr 3d regions are shown in Figure 4.2, and resolved primary binding energy peak locations for all elements are displayed in Table 4.1 along with corresponding peak locations for single-phase NiO and single-phase t-ZrO_2 [131-133]. Some key differences in binding energy values were observed between column 1 ((80:20)NiO:t-ZrO_2) and column 3 (NiO) and column 1 and column 4 (t-ZrO_2) in Table 4.1. The O 1s binding energy peak for (80:20)NiO:t-ZrO_2 (530.0 eV) was 0.8 eV lower than the value for single-phase t-ZrO_2 (530.8 eV), but 1.6 eV higher than the value for single-phase NiO (528.4 eV). This trend was also consistent with the Zr 3d and Ni 2p primary peak locations. For (80:20)NiO:t-ZrO_2, both Zr 3d 5/2 and Zr 3d 3/2 binding energies were each 1.6 eV lower than for single-phase t-ZrO_2, and the Ni 2p 3/2 and Ni 2p 1/2 values were each ca. 2.5 eV higher than for single-phase NiO. These shifts in binding energies suggest substantial electronic interaction between t-ZrO_2 and NiO. This electronic interaction can arise from intimate contact between the two species, which is supported by SEM, and/or the presence of a minority mixed oxide species, which is supported by the stacking faults observed by XRD. From an electrochemical perspective, intimate contact is preferred to a simple physical mixture since it would likely yield the highest interfacial area between NiO and t-ZrO_2, enhancing activity.

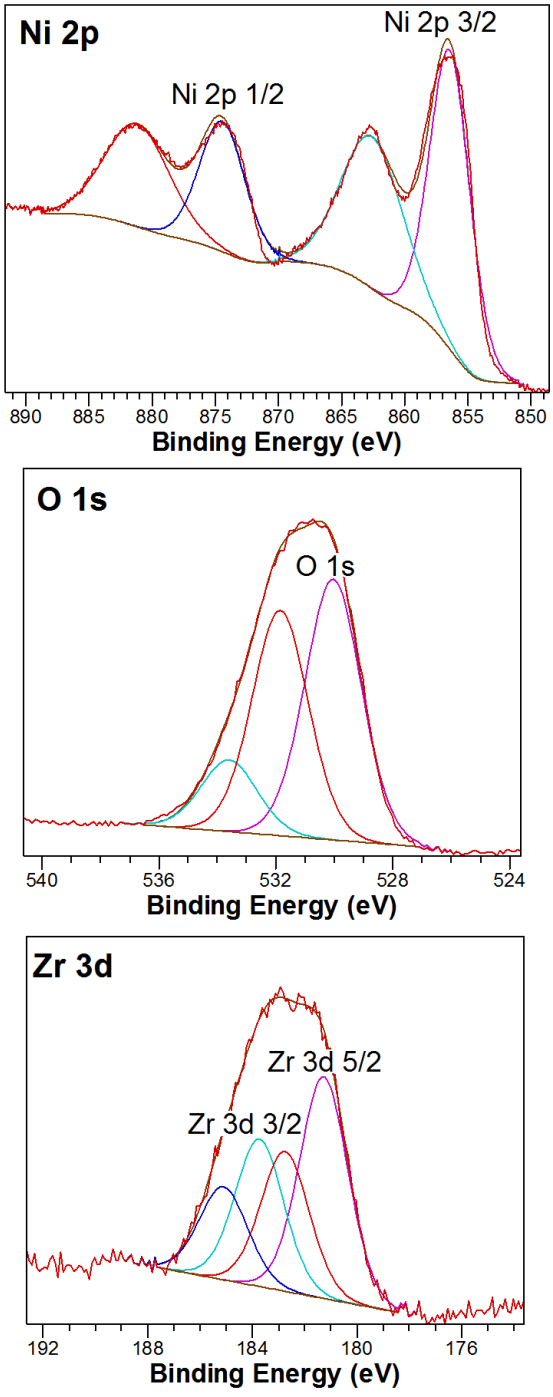

Figure 4.2. Deconvoluted XPS spectra for Ni 2p, O 1s, and Zr 3d elemental regions for (80:20)NiO:t-ZrO_2.

Table 4.1. Binding energies for (80:20)NiO:t-ZrO_2 composite, (80:20)NiO:t-ZrO_2 physical mixture, single-phase NiO, and single-phase t-ZrO_2 particles for primary peak locations of elements O, Ni, and Zr.

Configuration	(80:20)NiO:t-ZrO_2 composite	(80:20)NiO:t-ZrO_2 physical mixture	NiO	t-ZrO_2
	Binding Energy (eV)	Binding Energy (eV)	Binding Energy (eV)	Binding Energy (eV)
O 1s	530.0	528.9 and 531.3	528.4	530.8
Ni 2p 3/2	856.4	854.1	853.9	----------
Ni 2p 1/2	874.4	872.2	871.8	----------
Zr 3d 5/2	181.3	182.9	----------	182.9
Zr 3d 3/2	183.7	185.3	----------	185.3

To further illustrate the importance of the interface between t-ZrO_2 and NiO, XPS was performed on a physical mixture of single-phase NiO and single-phase t-ZrO_2 with the same (80:20) molar ratio, and the resolved primary binding energy peaks locations are shown in column 2 of Table 4.1. Unlike the co-precipitated catalyst, the primary binding energy peak positions for the physical mixture very closely correlated with the values for the respective single-phase species. For instance, the Zr 3d values for the physical mixture were identical to those for the composite. Additionally, two resolved peak locations were observed for the O 1s region which correlated to the two primary locations for single-phase NiO and single-phase t-ZrO_2, respectively. The lack of substantial binding energy shifts observed in the physical mixture of single-phase NiO and single-phase t-ZrO_2 corroborates the suggestion that those shifts seen in the (80:20)NiO:t-ZrO_2 composite may be indicative of electronic interaction and/or the formation of a minority mixed oxide species.

Figure 4.3A shows XRD patterns of the precipitated precursors for the Ni-Zr composite and both single-phase metal oxide species. No peaks were observed in the sloping XRD pattern for the t-ZrO_2 precipitated precursor, which was previously identified as amorphous zirconium hydroxide ($Zr(OH)_4$) [134,135]. Peak positions (with corresponding crystal faces) for the NiO precipitated precursor confirmed that the species present was $Ni(OH)_2$: 19.18° (001), 33.04°

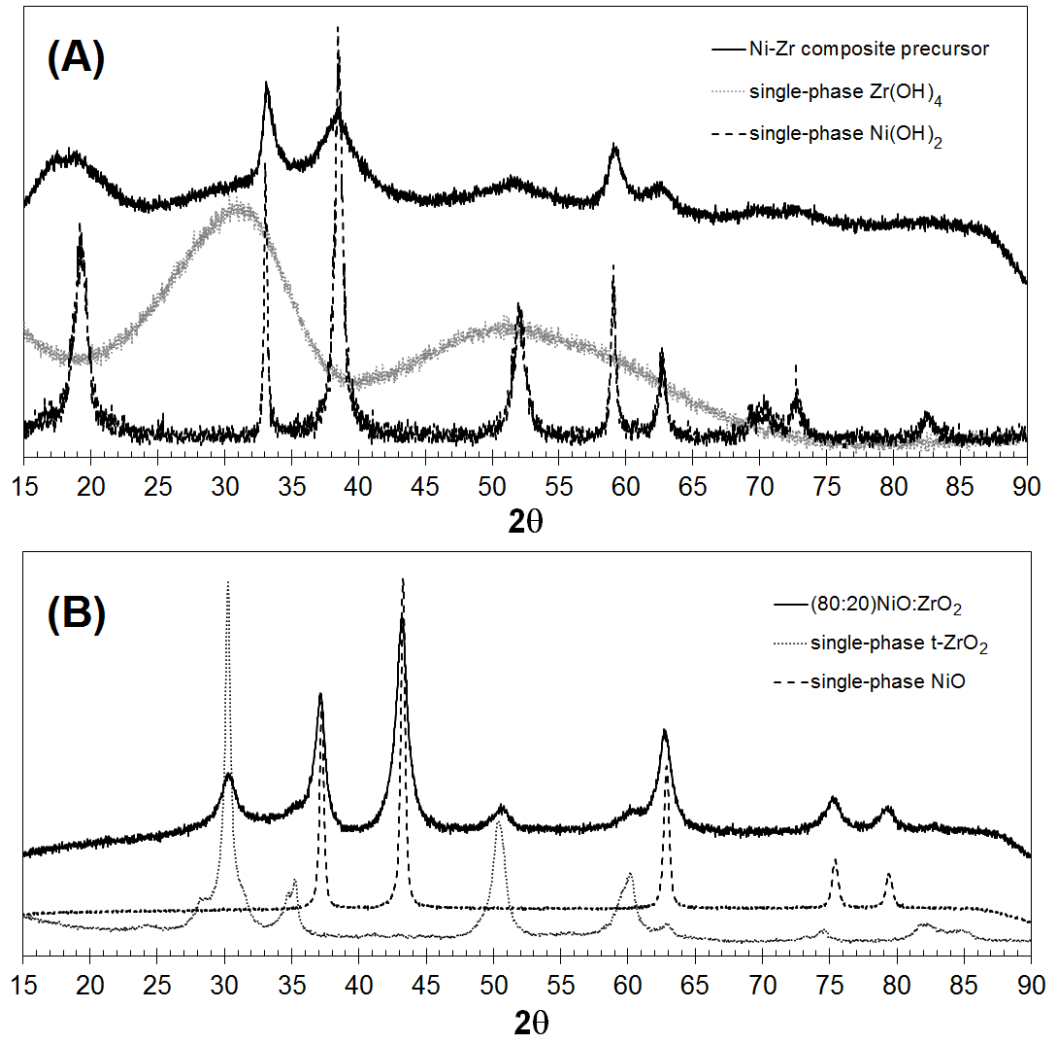

Figure 4.3. XRD patterns for (A) precipitated precursors of (80:20)NiO:t-ZrO_2 composite, single-phase NiO ($Ni(OH)_2$), and single-phase t-ZrO_2 ($Zr(OH)_4$) materials; and (B) calcined (80:20)NiO:t-ZrO_2, NiO, and t-ZrO_2. Scans recorded at a rate of 1.3 °/min between 2θ values of 10-90°.

(100), 38.48° (101), 51.92° (102), 59.06° (110), 62.70° (111), 69.28° and 70.32° (103), and 72.70° (201) [25,110]. For the Ni-Zr co-precipitated precipitated precursor, only three clearly distinguishable peaks were observed at 33.12°, 38.41°, and 59.08°. At all other peak locations corresponding to those seen in the $Ni(OH)_2$ pattern, broad peaks were visible but exact Bragg angles were difficult to pinpoint. These broad peaks suggest the Ni-Zr composite precipitated precursor had a smaller grain boundary size and potential stacking faults and/or poor crystallinity compared to the single-phase $Ni(OH)_2$ precipitated precursor.

Following calcination, XRD was performed on the composite and single-phase materials, and the patterns are shown in Figure 4.3B. Peak positions were observed as follows: for single-phase t-ZrO_2: 30.24° (101), 50.39° (200), and 60.12° (211); for single-phase NiO: 37.22° (111), 43.26° (200), 62.87° (220), 75.43° (311), and 79.40° (222); and for (80:20)NiO:t-ZrO_2: 30.27°, 37.15°, 43.20°, 50.54°, 62.70°, 75.23°, and 79.33° [13,25,136]. In addition, a third peak corresponding to t-ZrO_2 ca. 60° was visible in the (80:20)NiO:t-ZrO_2 pattern; however, it was broad and its precise location was difficult to identify. An average negative 2θ peak shift of about 0.11° was observed for (80:20)NiO:t-ZrO_2 compared to single-phase NiO for the five peaks corresponding to NiO, and an average positive 2θ peak shift of about 0.09° was observed for (80:20)NiO:t-ZrO_2 compared to single-phase t-ZrO_2 for the two identifiable peaks

corresponding to t-ZrO_2. This peak-shifting phenomenon suggests the presence of stacking faults in the (80:20)NiO:t-ZrO_2 lattice, and indicates that these stacking faults were maintained throughout calcination [137].

For the preparation of single-phase NiO, 500°C was chosen as the calcination temperature to completely ensure no $Ni(OH)_2$ precipitated precursor remained. It was important to convert $Ni(OH)_2$ to NiO because bulk $Ni(OH)_2$ has a much lower electronic conductivity than NiO [138]. For single-phase ZrO_2 preparation, it would typically be expected that calcinations of $Zr(OH)_4$ at temperatures in excess of 305°C would result in almost entirely monoclinic-phase ZrO_2 [25,107]. However, the three major XRD peaks observed for ZrO_2 in both the composite and single-phase metal oxide species (Fig. 4.3B) indicate that the ZrO_2 present was almost exclusively in the tetragonal phase. For single-phase t-ZrO_2, a low calcination temperature was applied (305°C) for a longer duration of time (32 hours) to preferentially stabilize the tetragonal phase. In the composite, however, t-ZrO_2 was likely stabilized by the presence of NiO which prevented it from crystallizing into the monoclinic phase even at a calcination temperature of 500°C [135,139]. This stabilization phenomenon of t-ZrO_2 by NiO, which is smaller in size and valence than t-ZrO_2, may also have resulted in the formation of oxygen vacancies and/or lattice defects resulting from a decreased unit cell volume, further enhancing electrocatalytic activity [135].

4.2.2 Electrochemical Tests

The electrocatalytic activities of (80:20)NiO:t-ZrO_2 and single-phase NiO were examined in both hydroxide and carbonate electrolytes by CV and EIS. Concentrations of KOH (0.005M) and Na_2CO_3 (0.1M) electrolytes were selected to normalize the pH at around 11.5 for all tests due to the fact that peak potentials shift at a rate of roughly -60 mV per pH unit [7,28]. Differences in peak current ranges between CVs from the same electrolyte are consistent with previously-published results, and were attributed to minor differences in catalyst loading on the GC electrode surface [107].

For the partial oxidation of methane with carbonate anions, single-phase NiO was first considered as the material of choice since it is a well-known electrocatalyst for the oxidation of organic compounds in alkaline media [9,28,29,107]. Figure 4.4A shows the typical behavior of NiO electrodes in alkaline media. In all CVs shown in this work, there were several phenomena that occurred that will be systematically discussed to provide a fundamental understanding of the behavior of nickel-based electrodes in alkaline media. First, it is well known that a thin layer of $Ni(OH)_2$ forms spontaneously on the surface of NiO as soon as the electrode is introduced to an aqueous alkaline solution [9,28,107,122]. Second, upon subsequent potential cycling, the electrochemically

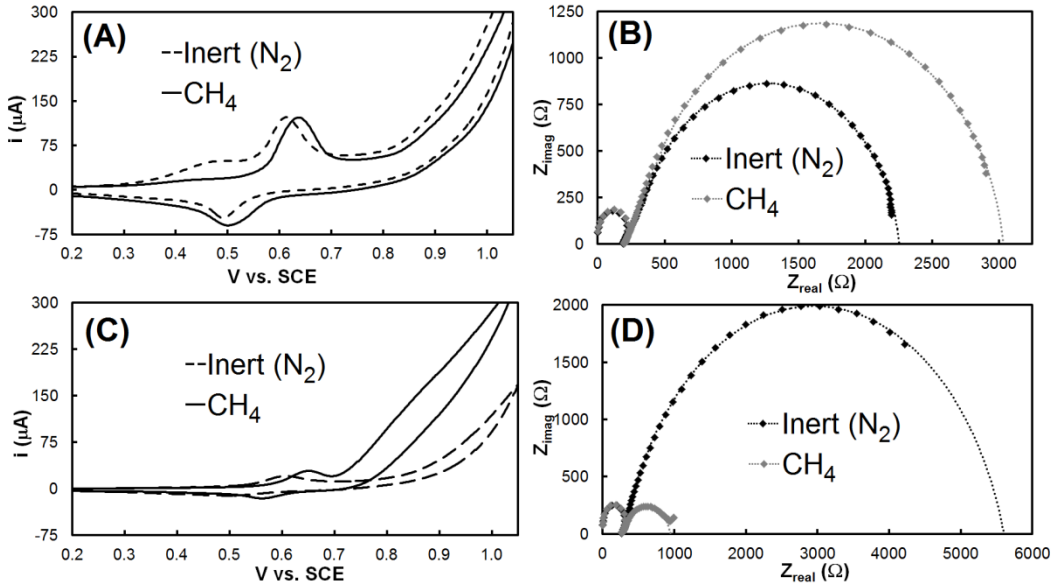

Figure 4.4. Electrochemical tests in N_2- and CH_4-saturated 0.1M Na_2CO_3: (A) CVs for single-phase NiO; (B) EIS for single-phase NiO at 0.7V vs. SCE; (C) CVs for (80:20)NiO:t-ZrO_2; and (D) EIS for (80:20)NiO:t-ZrO_2 at 0.7V vs. SCE. All scans performed at room temperature (25°C), CV scan rates were 20 mV/s, and EIS data collected between frequencies of 100mHz to 1MHz.

active $Ni(OH)_2$ undergoes a reversible Ni^{2+}/Ni^{3+} redox process [7,9,28,29,107,110,122] shown in Equation 4.1:

$$Ni(OH)_2 + OH^- \leftrightarrow NiOOH + H_2O + e^- \quad (4.1)$$

The Ni^{2+}/Ni^{3+} redox couple was clearly visible on both the anodic and cathodic scans between ca. 0.5-0.6V vs. SCE. Finally, a second reaction was observed in all CVs, the oxygen evolution reaction (OER), which occurred at potentials greater than the Ni^{2+}/Ni^{3+} redox reaction and was catalyzed by NiOOH [8,123]:

$$4OH^- \rightarrow O_2 + 2H_2O + 4e^- \quad (4.2)$$

The onset potential for the OER appeared to be around 0.85V vs. SCE; however, its exact onset potential was difficult to pinpoint and the OER was seen primarily in the sharp anodic current spikes after the Ni^{2+}/Ni^{3+} redox [123]. Also, since the OER was catalyzed by NiOOH, it can be assumed that at potentials greater than ca. 0.6V vs. SCE when NiOOH was being formed via Eq. 4.1 the OER may have been constantly contributing to the anodic current.

Fig. 4.4A shows that in both N_2- and CH_4-saturated 0.1M Na_2CO_3 only the Ni^{2+}/Ni^{3+} redox (Eq. 4.1) and OER (Eq. 4.2) were observed. The absence of additional anodic activity under methane saturation indicated that single-phase NiO did not catalyze CH_4 oxidation. Additionally, a small, positive shift of ca. 20 mV was observed in Fig. 4.4A for the CH_4-saturated electrolyte compared to the

N_2-saturated electrolyte. EIS was also performed at 0.7V vs. SCE on the same system, and Figure 4.4B shows the resulting IR-corrected Nyquist plots. A 37% increase was observed between CH_4- and N_2-saturation in the projected x-axis intercept for the low frequency semicircle, which suggested an increase in the resistance of the OER over the NiO catalyst in the presence of methane versus an inert gas. This increase in the resistance likely resulted from the reduced OER overpotential at the selected EIS potential due to the positive shift in potential observed in Fig. 4.4A, thereby lowering the OER driving force. The most likely cause for this positive potential shift and increase in resistance was the adsorption of activity-blocking methane on the NiO surface, thereby blocking active OER sites. This adsorption without oxidation of methane is in contrast to the authors' previous publication where adsorption and oxidation of methanol was observed in aqueous carbonate media [107]. However, since methanol oxidation proceeds though proton donation whereas methane requires an oxygen atom and charge to be donated for its oxidation to proceed, it is clear that single-phase NiO was unable to adsorb the necessary oxygen donor, namely CO_3^{2-}, in order to fully catalyze the partial oxidation of methane [140].

As a result, (80:20)NiO:t-ZrO_2 was used as the electrocatalyst with the hypothesis that tetragonal-phase zirconia's surface acidity would adsorb carbonate and facilitate oxygen abstraction and donation. Fig. 4.4C shows that in CH_4-

saturated 0.1M Na_2CO_3 a new oxidation response was observed after ca. 0.7V vs. SCE. The IR-corrected Nyquist plots in Fig. 4.4D also show an 87% decrease in the projected x-axis intercept of the low frequency semicircle for CH_4-saturated electrolyte compared to N_2-saturated electrolyte. This is in stark contrast to Fig. 4.4B where the resistance increased, rather than decreased, over single-phase NiO upon saturation with CH_4. These results indicate that methane was adsorbed and oxidized by (80:20)NiO:t-ZrO_2 using CO_3^{2-} as the oxygen donating species.

Additional CVs were performed in hydroxide alkaline media to further illustrate the necessity of CO_3^{2-} for the oxidation of methane. Figure 4.5 shows CVs over (80:20)NiO:t-ZrO_2 in N_2- and CH_4-saturated 0.005M KOH. Similarly to Fig. 4.4A, only the Ni^{2+}/Ni^{3+} redox (Eq. 4.1) and OER (Eq. 4.2) were observed. In addition, compared to the N_2-saturated electrolyte, the current density actually decreased under CH_4-saturation, further illustrating that CH_4 was not oxidized. This makes sense since OH^- anions tend to oxidize species by accepting protons rather than donating oxygen, giving OH^- a limited ability to attack methane, and virtually no activity has been previously reported for methane oxidation in hydroxide alkaline media [141]. This further supports the observation that the oxidation of methane takes place through the donation of oxygen from adsorbed carbonate anions in solution.

Preliminary characterization tests have been conducted to identify the

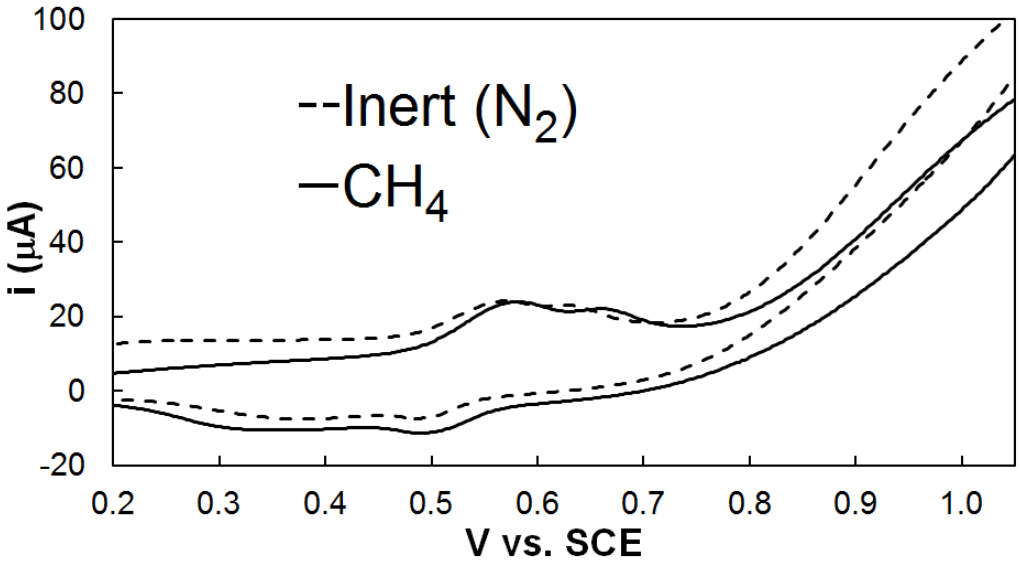

Figure 4.5. CVs in N_2- and CH_4- saturated 0.005M KOH for (80:20)NiO:t-ZrO_2. Scans performed at room temperature (25°C) and scan rates of 20 mV/s.

product or products formed from this new oxidation reaction combining CH_4 with CO_3^{2-} over (80:20)NiO:t-ZrO_2. Initial results using Mass Spectrometry (MS), Gas Chromatography (GC), and Attenuated Total Reflectance Fourier Transform Infrared Spectroscopy (ATR-FTIR) are shown in Figure 4.6 and have shown the formation of oxygenate products carbon monoxide (CO) and formaldehyde (HCHO), perhaps through the following two-electron pathways:

$$CH_4 + CO_3^{2-} \rightarrow CO + 2H_2 + CO_2 + 2e^- \quad (4.3)$$

$$CH_4 + CO_3^{2-} \rightarrow HCHO + H_2 + CO_2 + 2e^- \quad (4.4)$$

Experimental results from ATR-FTIR (Fig. 4.6A) and air-free MS (Figs. 4.6B and 4.6C) indicate the potential of HCHO-dominated and CO-dominated product pathways. At the time this article was written, however, we have not quantified the product profile and preferred reaction pathways and future work will focus in this area to allow for dynamic control of the product.

Another important property to consider is that nickel-based materials also function as alkaline media electrocatalysts for the oxidation of organic compounds [9,28,29,107]. This phenomenon, which was originally reported by Fleischmann, Korinek and Pletcher, takes place over NiOOH and results in the concurrent reduction of NiOOH (3+ oxidation state) back to $Ni(OH)_2$ (2+ oxidation state), Equation 4.5 [28]:

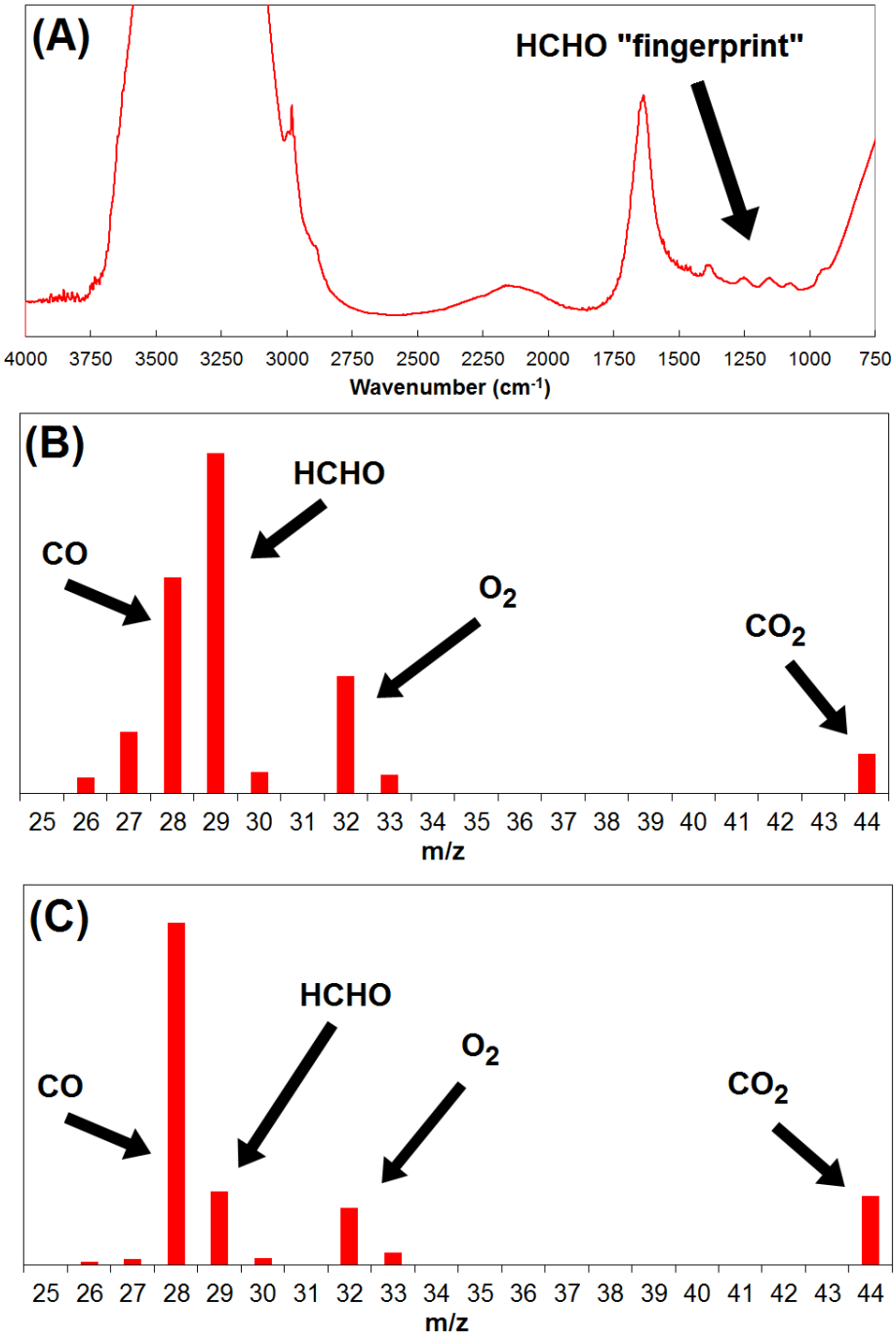

Figure 4.6. Physical characterization of partial oxidation products for CH_4 by CO_3^{2-}. (A) ATR-FTIR showing formaldehyde as the primary product; (B) and (C) air-free mass spectra for HCHO and CO dominated products.

$$NiOOH + organic\ compound \rightarrow Ni(OH)_2 + product \quad (4.5)$$

Therefore, the new oxidation peak seen in Fig. 4.4C may have arisen from one (or both) of the proposed oxidation reactions shown in Eqs. 4.3 and 4.4, as an indicator peak from the subsequent oxidation of oxygenate products via Eq. 4.5, or from both phenomena. In this way, the (80:20)NiO:t-ZrO_2 composite may act as both an electrocatalyst for the reaction of CH_4 and CO_3^{2-} at room temperature and as a pseudo-sensor for any oxygenate products formed from that reaction.

4.3 Summary

A composite (80:20)NiO:t-ZrO_2 electrocatalyst was synthesized using an aqueous-phase co-precipitation synthesis method and characterized using physical and electrochemical techniques. Nickel oxide formed agglomerated spheres around 20-30 nm in diameter, and zirconia was found to have been stabilized in the desired tetragonal phase while exhibiting uniform distribution of blade-like particles around 100 nm in length. High specific surface area (97.6 m^2/g), in addition to results from XPS and XRD, may have indicated the presence of intimate contact between NiO and t-ZrO_2 along with poor crystallinity and stacking and/or growth faults that may have resulted in favorable electrocatalytic activity.

Electrochemical testing using thin film disk-type electrodes revealed a new oxidation reaction combining carbonate anions with CH_4 at room temperature over the (80:20)NiO:t-ZrO_2 electrocatalyst. Further tests showed CO_3^{2-} actively participated as a reactant and that t-ZrO_2 was a necessary, non-conducting additive which enabled CO_3^{2-} adsorption for the oxidation of methane at room temperature. This could potentially open up new avenues for research of carbonate-based electrochemical cells operating at room temperature for electrochemical synthesis reactors and broaden the horizons of alternative technologies utilizing novel, low-cost catalysts.

CHAPTER 5: ELECTROCHEMICAL METHANE ACTIVATION AND CONVERSION TO OXYGENATES AT ROOM TEMPERATURE

The purpose of this work was to expand upon results shown in the previous chapter concerning the room temperature activation of methane with carbonate anions over a novel $NiO\text{-}ZrO_2$ bifunctional electrocatalyst. Electrochemical activity was studied using Cyclic Voltammetry, Electrochemical Impedance Spectroscopy, and Linear Sweep Voltammetry in both aqueous-phase three electrode cells and flow cell configuration. Products formed were identified using Mass Spectrometry and ^{1}H-Nuclear Magnetic Resonance Spectroscopy, and new theoretical pathways for low temperature methane activation were proposed. The work presented in this chapter was published in the *Journal of the Electrochemical Society* [142] and in *ECS Transactions* [143].

5.1 Experimental

5.1.1 Electrocatalyst Synthesis Methods

All reagents were used as received and all water used was ultra-pure 18.2 MΩ deionized water from a Millipore Direct-Q 3UV purification system. Nickel oxide (NiO) was synthesized using an aqueous-phase precipitation technique similar to the authors' previously-published procedure [107]. A 0.5M $Ni(NO_3)_2$ (Acros, 99%) solution in water was prepared and heated under constant stirring to its boiling point (~102°C). The solution temperature was measured using a Hannah Instruments HI9063 K-Type Thermocouple. Aqueous 10M NaOH (Fisher, NF/EP/BP/FCC) was then quickly added until the pH rose to between 8-10 to induce precipitation, and the beaker was capped and set aside for 24 hours. The solution pH was determined using an Accumet Excel XL60 Dual Channel pH/Ion/Conductivity/DO Meter. The resulting green precipitated precursor, nickel hydroxide ($Ni(OH)_2$), was then copiously rinsed with deionized water and dried overnight at 90°C. It was then calcined at 500°C in air for 3 hours to obtain NiO.

Zirconia (ZrO_2) was prepared via a similar precipitation method. A 0.5M $ZrOCl_2$ (Acros, 98+%) solution was heated under constant stirring to its boiling point, and 10M NaOH was quickly added until the pH reached 8-10. The solution was then capped and set aside for 24 hours, followed by rigorous rinsing with

deionized water. During rinsing, each filtrate was tested for the presence of chloride ions by adding a drop of $AgNO_3$ solution and looking for AgCl precipitation. This test was performed until a negative result was obtained, indicating that the precursor was chloride-free. The rinsed precursor was then dried overnight at 90°C followed by calcination at 305°C in air for 32 hours.

The NiO-ZrO_2 bifunctional electrocatalyst was synthesized by preparing an aqueous solution with 0.4M $Ni(NO_3)_2$ and 0.1M $ZrOCl_2$, giving a total concentration of 0.5M and an overall Ni-to-Zr ratio of 4-to-1. The solution was heated to its boiling point under constant stirring, 10M NaOH was added to induce precipitation, and it was capped and set aside for 24 hours. The precipitated precursor was then rinsed repeatedly with deionized water, including the aforementioned $AgNO_3$ test for chloride ions. The chloride-free precipitated precursor was then dried overnight at 90°C, followed by calcination in air at 500°C for 3 hours.

5.1.2 Aqueous-Phase Electrochemical Tests

Cyclic Voltammetry (CV) and Electrochemical Impedance Spectroscopy (EIS) tests were conducted on thin film disk-type electrodes. A custom three-electrode cell (Adams & Chittenden) was used with an Autolab PGSTAT302N

Potentiostat (Eco Chemie). In all tests, a platinum flag was used as the counter electrode and a saturated calomel electrode (SCE) was used as the reference electrode. All working electrodes were created by preparing 15 mL of a 0.3 mg/mL dispersion of electrocatalyst particles in deionized water and ultrasonicating until the particles were uniformly distributed. Next, 20 μL of the dispersion was dropped onto a glassy carbon (GC) disk electrode (Pine Instrument Company, A = 0.196 cm^2) and it was spin dried in air at 200 rpm for 1 hour using a Pine AFMSRCE Modulated Speed Rotator. Once dry, 20 μL of a 0.05 wt.% Nafion DE 520 solution (DuPont) was deposited on the GC electrode and it was again spin dried in air at 200 rpm for 1 hour. Ultra high purity nitrogen (N_2, $\geq$ 99.999%) and chemical grade methane (CH_4, $\geq$ 99.0%) gases were used (Airgas). Prior to each electrochemical test, the electrolyte was bubbled with N_2 for 1 hour to remove any dissolved gases. Anhydrous sodium carbonate (Fisher, certified ACS grade, 99.9%) and potassium hydroxide (Acros, ca. 85%) were solvated in Millipore water to prepare the aqueous electrolytes used in all electrochemical tests. After each experiment, the catalyst particles were removed from the GC electrode surface by polishing with Buehler alpha 5.0 μm and gamma 0.05 μm alumina micropolish suspensions, with an ultrasonication step in between for 10 minutes to remove any loose particles.

Proton Nuclear Magnetic Resonance (^{1}H-NMR) samples were obtained in

an aqueous batch cell with an applied electrode potential of 1.8V. ^{1}H-NMR was performed using a Varian 700MHz NMR Spectrometer at 25°C with a 30 degree pulse angle, water suppression, a 5s relaxation time, and no spinning. Each ^{1}H-NMR trial consisted of 700μL sample solution, 65μL of D_2O, and 35 μL of 10mM DMSO used as a reference peak.

5.1.3 Flow Cells and MEA Preparation

Linear Sweep Voltammetry (LSV) at a 50mV/s scan rate and Chronoamperometry (CA) experiments were performed with an Autolab PGSTAT302N Potentiostat to obtain polarization curves and to collect anode effluent at a set potential, respectively. Ultra high purity oxygen (O_2, $\geq$ 99.994%), carbon dioxide (CO_2, $\geq$ 99.9%), N_2 and CH_4 were used as gases for the cathode and anode streams, and cell temperature was maintained at 40°C with both streams at 90% relative humidity. Prior to each experiment, flow cells were humidified overnight under inert N_2 gas flow.

To fabricate membrane-electrode assemblies (MEAs), a ca. 500μm-thick Ralex AM-PAD anion exchange membrane (Mega a.s.) was exchanged from the chloride form to carbonate by soaking in 1M Na_2CO_3 for 24 hours, followed by a 4 hour soak in dimethylformamide (DMF) (Acros, extra dry). Catalyst inks were

fabricated by sonicating 300 μL of DMF and 50mg of catalyst particles until well-mixed, then adding a fumion FAA two-component anion-exchange ionomer (FuMA-Tech GmbH) to a total weight fraction of 30% and mixing for 5 minutes. The use of DMF with the membrane and in catalyst inks ensured chemical compatibility with the ionomer. The cathode and anode inks were then painted onto separate 5 cm^2 pieces of carbon paper (BASF Fuel Cell Inc.) and these gas-diffusion layers were pressed onto either side of the membrane at 1500 lbs under vacuum for 45 minutes.

Figure 5.1 shows an operational diagram for the flow cells constructed in this work, which were conducted at room temperature utilizing CO_3^{2-} as the transport ion. Carbonate anions were produced through the reaction of CO_2 and O_2 at the cathode on either the calcium-ruthenium oxide from our previous work [105,106] or Pt/C. In this context, any traditional ORR-active catalyst (i.e.Pt) is usable; it simply forms carbonate through an indirect route where OH^- reacts with CO_2 as opposed to direct electrochemical reduction, which has no impact on the anode reaction. CO_3^{2-} then traveled from the cathode, across the anion-exchange membrane, to the anode, where the NiO-ZrO_2 bifunctional electrocatalyst was applied. CH_4 was used on the anode stream, and the effluent from this stream was collected and analyzed under an applied voltage of 2.0V. Polarization curves at 50mV/s scan rate for the electrochemical cell shown in Figure 5.2 show that a

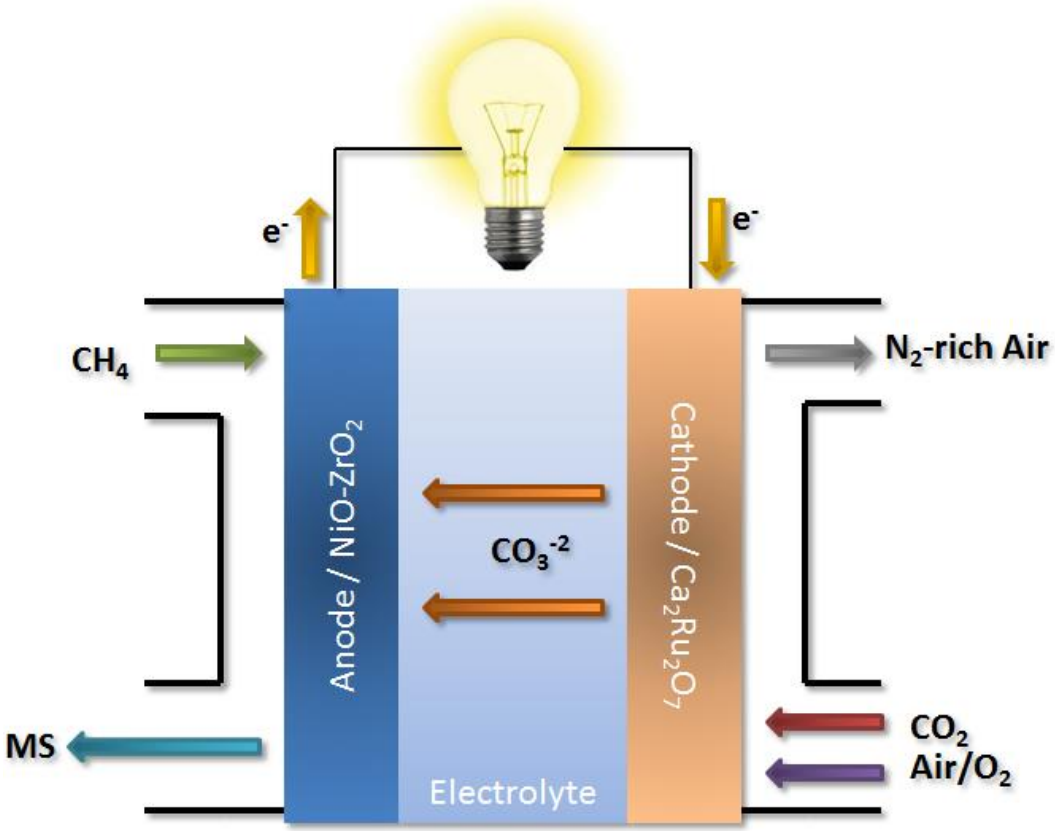

Figure 5.1. Operational diagram of flow cell with anode effluent analyzed using Mass Spectrometry.

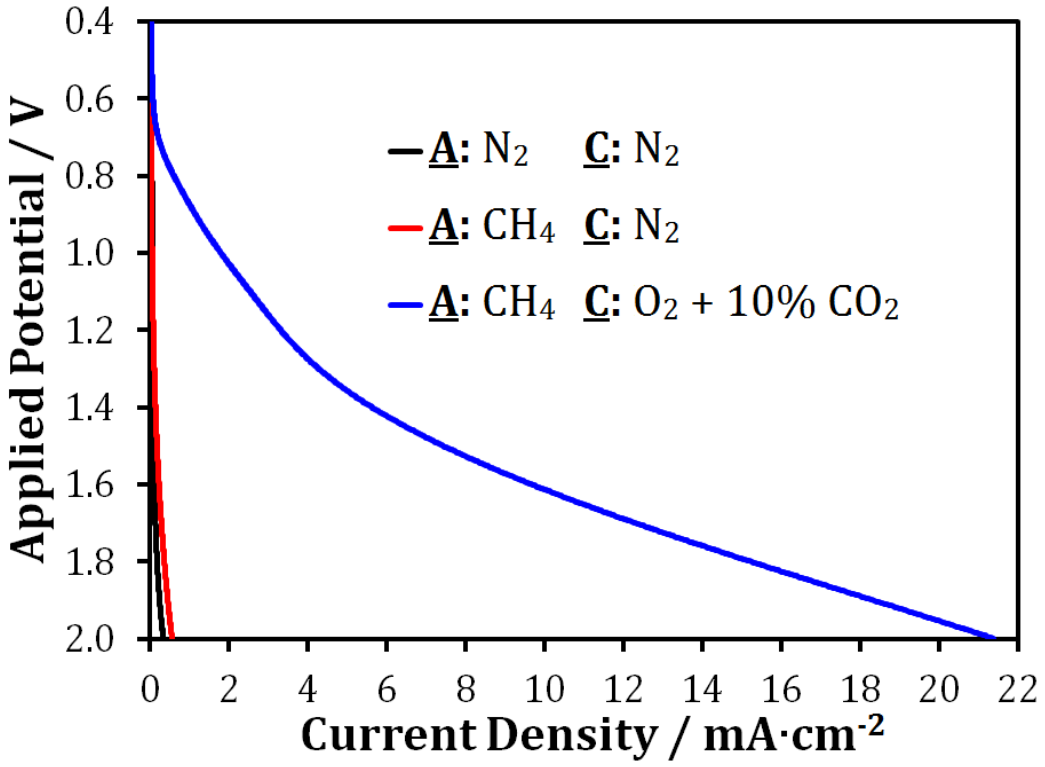

Figure 5.2. Polarization curves for flow cell with NiO-ZrO_2 bifunctional electrocatalyst as the anode and $Ca_2Ru_2O_7$ pyrochlore as the cathode electrocatalyst. **A:** and **C:** represent the gases flowed on the anode and cathode streams, respectively. Relative humidity was 90%, gas flow rates were 0.1L/min, scan rate was 50mV/s, and cell temperature was 40°C.

current density of 21 mA/cm^2 was obtained at 2.0V device voltage. Mass Spectrometry (MS) was used to analyze the collected anode effluent. For MS, the stream was directly analyzed without further modification using a Stanford Research Systems QMS 100 Series Gas Analyzer.

5.1.4 Physical Characterization

The catalyst microstructure was investigated using an FEI Quanta FEG250 Scanning Electron Microscope (SEM). Specific surface area was determined using N_2 adsorption isotherms at 77K via Brunauer-Emmett-Teller analysis (BET) using a Micromeritics ASAP 2020 Surface Area and Porosity Analyzer. Samples were first degased at 150°C for 16 hours prior to N_2 adsorption analysis. A Bruker D8 Advance X-ray Diffractometer (XRD) with Cu $K\alpha_1$ radiation (λ = 0.1540562 nm) was used to evaluate crystal structure. X-ray photoelectron spectroscopy (XPS) was performed using a Physical Electronics Multiprobe with a Perkin-Elmer Dual Anode X-ray Source to investigate catalyst surface properties and elemental composition.

5.2 Results and Discussion

In conventional alkaline electrochemical systems, hydroxide (OH^-) functions as an oxidizing agent by accepting protons from a fuel source (i.e. H_2 or CH_4 gas) to become water, which is desorbed. Because of its C-H bond strength, CH_4 could not be expected to have a proton readily abstracted by OH^- at low temperature, and consequently, negligible activity has been previously reported for CH_4 oxidation in OH^- solution [141]. Carbonate (CO_3^{2-}), on the other hand, oxidizes species by donating a charged oxygen atom to become CO_2. Due to this oxidation mechanism, large enthalpy of reaction for CO_2, and favorable oxidation kinetics, CO_3^{2-} is an attractive alternative to OH^- for alkaline electrochemical systems [63,107,128]. Hence, low temperature electrochemical CH_4 activation with CO_3^{2-} anions would require an electrocatalyst capable of adsorbing and activating CH_4 while abstracting oxygen from adsorbed CO_3^{2-}.

5.2.1 NiO Performance

Ni-based materials are well-known, active catalysts for CH_4 activation and reforming [3,141], and NiO is also a semiconductor at room temperature that is electrocatalytically active for the alkaline media oxidation of organics [28]. This makes NiO one of the most promising initial materials for the electrochemical

partial oxidation of methane to oxygenates with CO_3^{2-} anions.

As-synthesized NiO was examined using SEM, XRD, and XPS, and those results are shown in Figure 5.3. SEM images, shown in Figure 5.3a, revealed agglomerations of spherical NiO particles around $\leq$ 50nm in diameter. Additionally, the XRD pattern in Figure 5.3b showed peaks consistent with NiO (with corresponding crystal faces) at 37.2° (111), 43.3° (200), 62.8° (220), 75.4° (311), and 79.3° (222) [107,128]. Deconvoluted Ni 2p and O 1s XPS spectra are shown in Figures 5.3c and 5.3d, respectively. Binding energies shown in Figs. 5.3c-d were consistent with those found in literature [24,107]

Figure 5.4a shows CVs for NiO in inert N_2- and CH_4-saturated 0.1M Na_2CO_3 electrolyte. In both environments, two processes were observed. First, the Ni^{2+}/Ni^{3+} redox couple was observed between 0.5-0.6V vs. SCE, Equation 5.1:

$$Ni(OH)_2 + OH^- \leftrightarrow NiOOH + H_2O + e^- \quad (5.1)$$

Second, the oxygen evolution reaction (OER), which is catalyzed by NiOOH [144], was observed after 0.85V vs. SCE, Equation 5.2:

$$4OH^- \rightarrow O_2 + 2H_2O + 4e^- \quad (5.2)$$

The lack of additional anodic activity under CH_4-saturation indicated that there

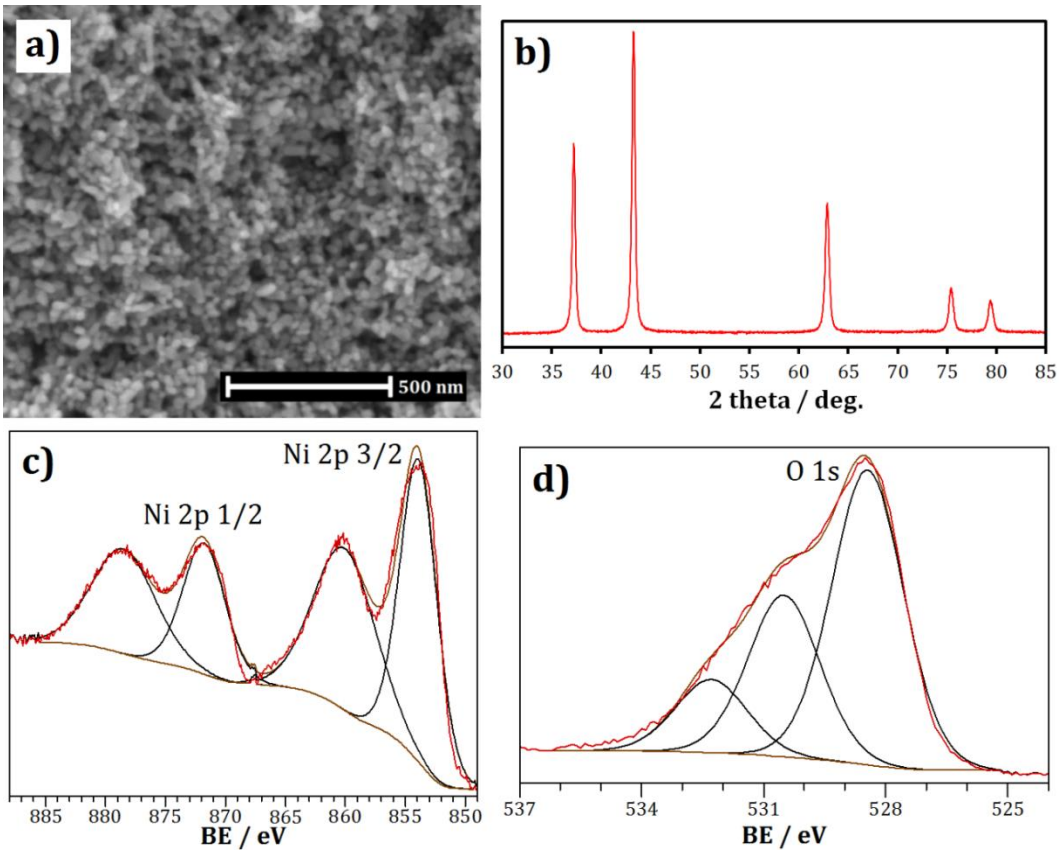

Figure 5.3. Physical characterization synthesized NiO electrocatalyst: a) SEM micrograph; b) XRD pattern; c) deconvoluted Ni 2p XPS spectrum; and d) deconvoluted O 1s XPS spectrum.

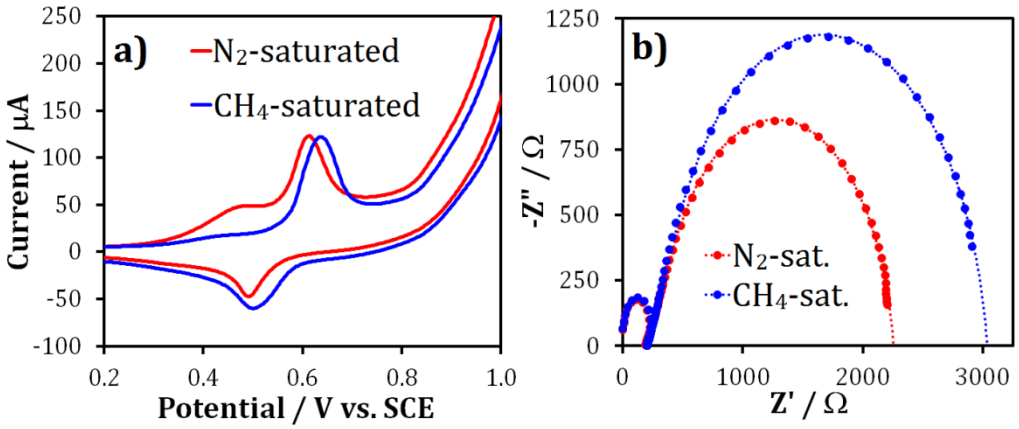

Figure 5.4. Electrochemical tests: a) CVs and b) EIS IR-corrected Nyquist plots for NiO electrocatalyst. All tests were conducted in N_2- and CH_4-saturated 0.1M Na_2CO_3 electrolyte at room temperature (25°C), CV scan rates were 20mV/s, and EIS data was obtained at 0.7V vs. SCE between 100mHz and 1MHz.

was no activation of CH_4 taking place on the NiO surface. However, a slight positive shift in potential of about 20mV was observed between N_2- and CH_4-saturation. This potential shift was accompanied by a 37% increase in the resistance for the OER, measured by EIS at 0.7V vs. SCE, and IR-corrected Nyquist plots for NiO are shown in Figure 5.4b. Combined, the CV and EIS data suggest adsorption, without subsequent activation, of CH_4 onto the NiO surface. Overall, Figure 5.4 shows that despite the ability of NiO to adsorb CH_4, NiO was incapable of adsorbing the necessary oxygen donor present, CO_3^{2-}, to activate CH_4 at room temperature.

5.2.2 Activation of CH_4 with NiO-ZrO_2

ZrO_2 was selected as a catalyst additive to facilitate CO_3^{2-} adsorption [128]. As an inexpensive transition metal oxide used as a catalyst and catalyst support for various heterogeneous systems, ZrO_2 possesses surface Lewis acid sites with electron-accepting capabilities that are expected to enable CO_3^{2-} adsorption [145-147]. However, the band gap for ZrO_2 is above 5 eV [148], making it unsuitable for use as a room temperature electrocatalyst by itself. To take advantage of the surface acidity of ZrO_2 and the proven ability of NiO to adsorb and oxidize organic species, a bifunctional electrocatalyst with a 4-to-1 molar ratio of NiO-to-ZrO_2 was synthesized using a co-precipitation technique

similar to that used to prepare NiO. The majority of NiO compared to ZrO_2 retained high overall electronic conductivity, and possessed a large interfacial area to maximize bifunctional activity from NiO and ZrO_2.

Physical characterization of the NiO-ZrO_2 bifunctional electrocatalyst was conducted using SEM, BET, XRD, and XPS. The SEM micrograph shown in Figure 5.5a revealed agglomerations of spherical NiO particles similar to Fig. 5.3a, along with thin, blade-like ZrO_2 particles around 100nm in length homogeneously mixed throughout. BET analysis also showed a high specific surface area of 97.6 m^2/g, along with single-phase values of 146.0 m^2/g for t-ZrO_2 and 23.4 m^2/g for NiO. The XRD pattern for NiO-ZrO_2 is shown in Figure 5.5b. The observed peaks corresponding to NiO were 37.2° (111), 43.2° (200), 62.7° (220), 75.2° (311), and 79.3° (222), and those corresponding to ZrO_2 were 30.3° (101), 50.5° (200), and 60.2° (211) [107,128]. These peak positions confirmed that ZrO_2 crystallized primarily in the tetragonal phase, which was stabilized by the presence of NiO [147]. This stabilization phenomenon also explains why a lower calcination temperature (305°C) for a longer duration (32 hours) was needed to synthesize single-phase t-ZrO_2. It was observed that calcination temperatures in excess of 305°C resulted in monoclinic-phase ZrO_2 without the presence of a secondary material.

Figures 5.6-5.7 show deconvoluted Ni 2p, O 1s, and Zr 3d XPS spectra for

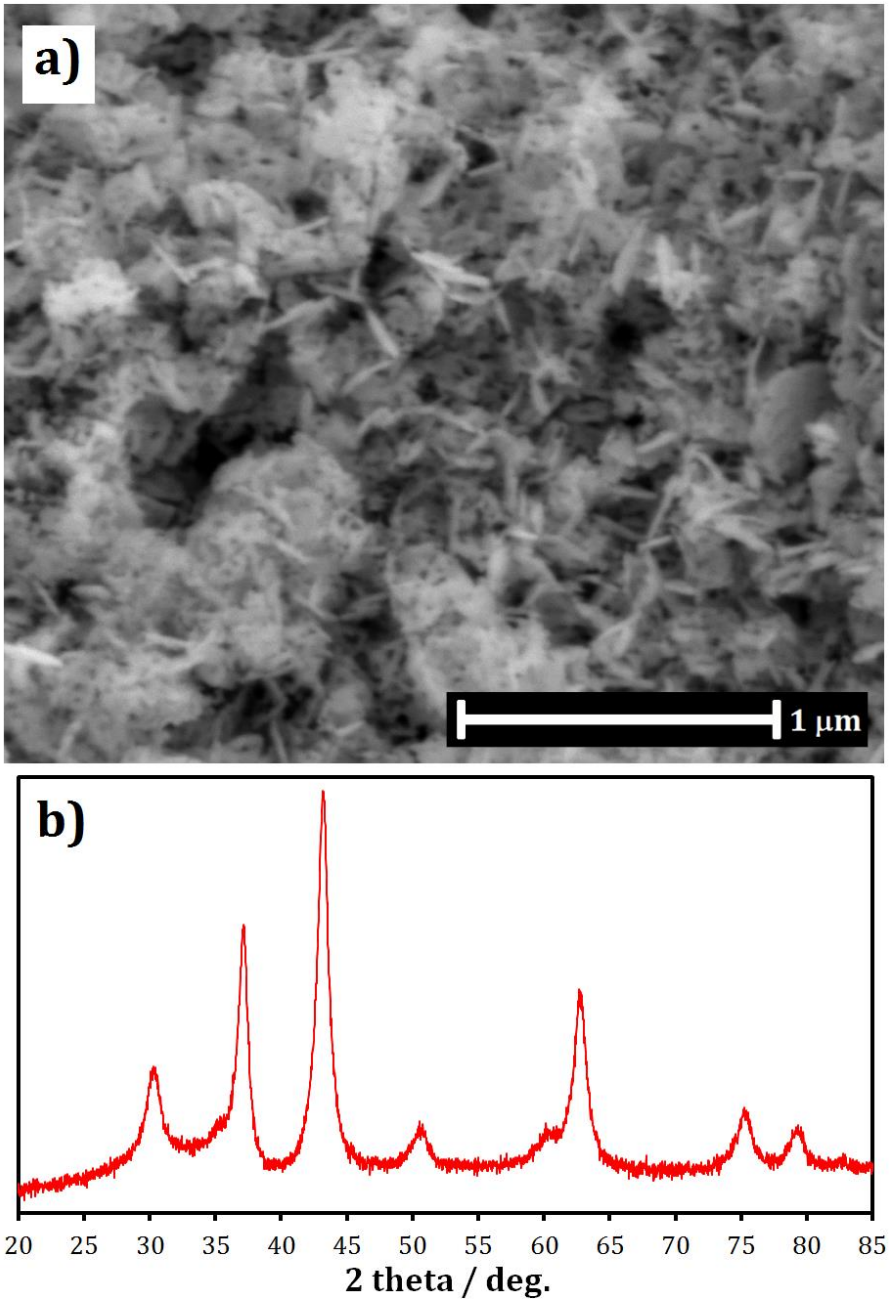

Figure 5.5. Physical characterization of synthesized NiO-ZrO_2 bifunctional electrocatalyst: a) SEM micrograph; and b) XRD pattern.

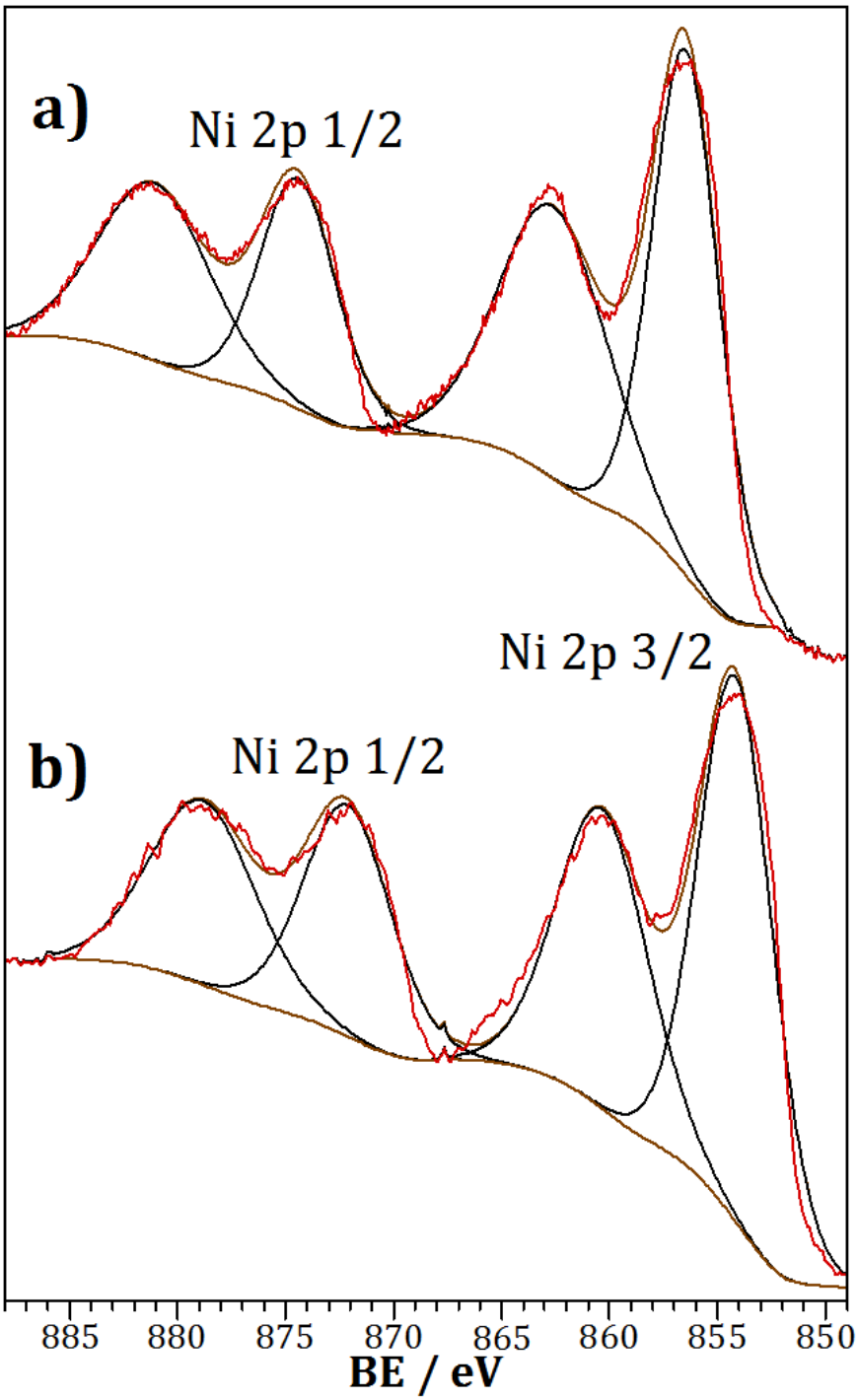

Figure 5.6. Deconvoluted Ni 2p XPS spectra for a) NiO-ZrO_2 bifunctional electrocatalyst; and b) physical mixture of NiO and ZrO_2.

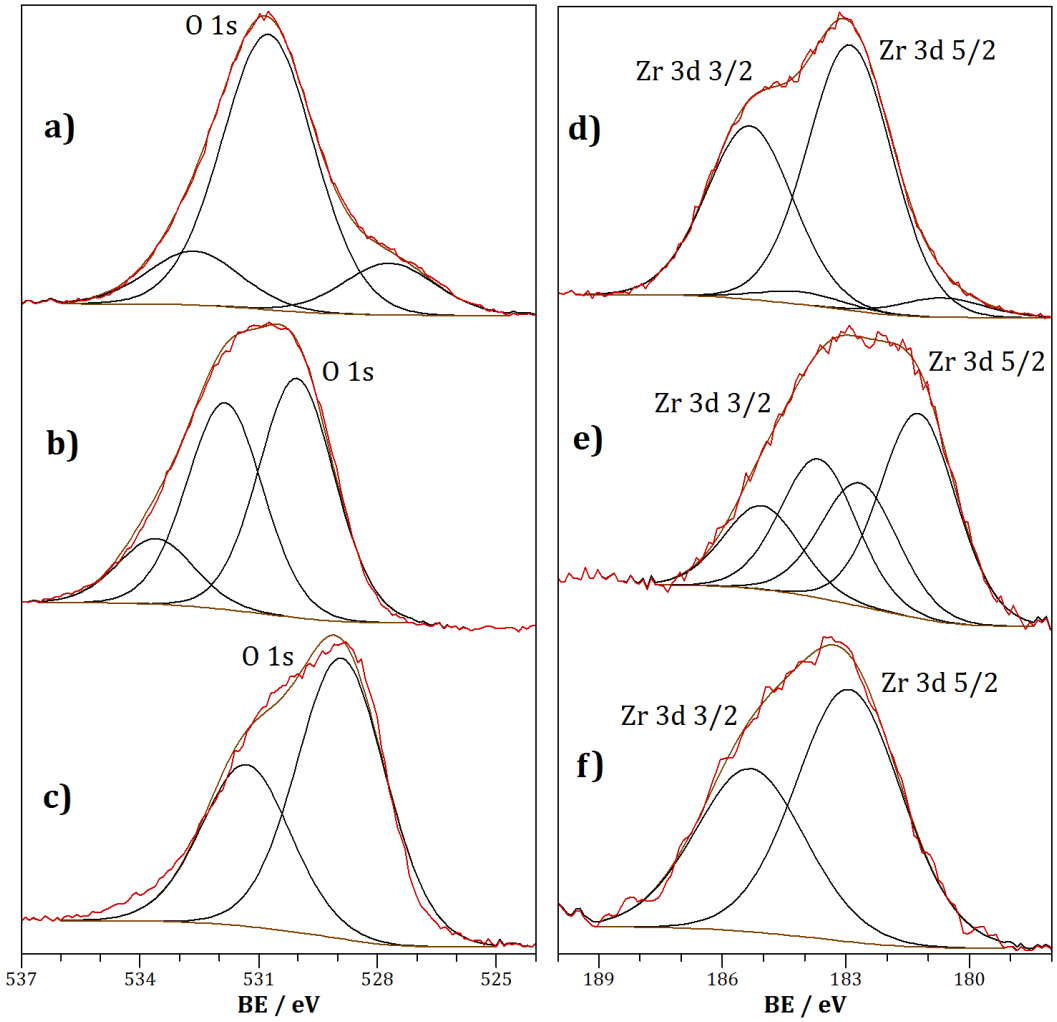

Figure 5.7. Deconvoluted O 1s XPS spectra for a) tetragonal-phase ZrO_2; b) NiO-ZrO_2 bifunctional electrocatalyst; and c) physical mixture of NiO and ZrO_2, and deconvoluted Zr 3d XPS spectra for d) tetragonal-phase ZrO_2; e) NiO-ZrO_2 bifunctional electrocatalyst; and f) physical mixture of NiO and ZrO_2.

the NiO-ZrO_2 bifunctional catalyst, tetragonal-phase ZrO_2, and a physical mixture with equal proportions of NiO and ZrO_2. Peak positions for all deconvoluted XPS spectra are also summarized in Table 5.1. Ni 2p binding energy peaks for the bifunctional electrocatalyst showed an average shift of 2.5 eV compared to NiO, whereas the physical mixture showed shifts of only 0.2-0.4 eV. The O 1s binding energy peak for the bifunctional electrocatalyst was also between the values for NiO and ZrO_2. Zr 3d binding energy peaks were identical for ZrO_2 and the physical mixture, and the shapes of the XPS spectra for the two materials (Fig. 5.7d and 5.7f) looked very similar. On the other hand, the Zr 3d spectrum shape for the bifunctional electrocatalyst was distinctly different, coupled with a shift in binding energy peaks of 1.6 eV. These binding energy shifts and XPS spectra shapes for the NiO-ZrO_2 bifunctional electrocatalyst suggest substantial electronic interaction rather than merely a simple physical mixture of NiO and ZrO_2.

Figure 5.8 shows CVs and IR-corrected Nyquist plots for the bifunctional electrocatalyst in N_2- and CH_4-saturated electrolytes. The NiO-ZrO_2 catalyst showed electrocatalytic activity not observed on raw NiO around 0.7V vs. SCE (Fig. 5.4). In addition, the EIS data in Figure 5.8b revealed an 87% decrease in resistance with CH_4 compared to N_2 over the NiO-ZrO_2 bifunctional electrocatalyst, which is in contrast to the 37% increase observed in Figure 5.4b with NiO as the electrocatalyst. This new anodic activity suggests CH_4 was

Table 5.1. XPS binding energy values for NiO, ZrO_2, and NiO-ZrO_2 bifunctional electrocatalyst and physical mixtures for O 1s, Ni 2p, and Zr 3d spectra.

Configuration	(80:20)NiO:ZrO_2 bifunctional	(80:20)NiO:t-ZrO_2 physical mixture	NiO	ZrO_2
	BE (eV)	BE (eV)	BE (eV)	BE (eV)
O 1s	530.0	528.9 and 531.3	528.4	530.8
Ni 2p 3/2	856.4	854.1	853.9	----------
Ni 2p 1/2	874.4	872.2	871.8	----------
Zr 3d 5/2	181.3	182.9	----------	182.9
Zr 3d 3/2	183.7	185.3	----------	185.3

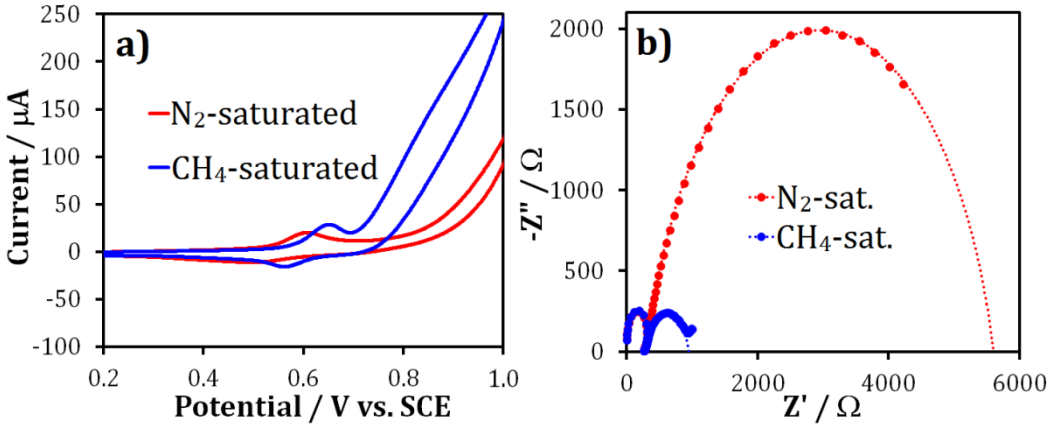

Figure 5.8. Electrochemical tests: a) CVs and b) EIS IR-corrected Nyquist plots for NiO-ZrO_2 bifunctional electrocatalyst. All tests were conducted in N_2- and CH_4-saturated 0.1M Na_2CO_3 electrolyte at room temperature (25°C), CV scan rates were 20mV/s, and EIS data was obtained at 0.7V vs. SCE between 100mHz and 1MHz.

activated using CO_3^{2-} as an oxygen donor, which was adsorbed on the electrocatalyst surface by non-conducting ZrO_2.

NiO (specifically, the Ni^{3+} species NiOOH) is electrocatalytically active towards the oxidation of many organics [28,107,128,144], so the anodic activity seen in Figure 5.8a likely indicates the oxidation of several intermediate oxygenates. This point is illustrated in Figure 5.9, which shows that oxidation CVs over the NiO-ZrO_2 composite for methanol (CH_3OH), formaldehyde (HCHO), and carbon monoxide (CO) all look similar. Therefore, to determine the identity of product(s) formed, Proton Nuclear Magnetic Resonance Spectroscopy (^{1}H-NMR) was performed using an aqueous batch cell, and flow cells were also constructed with the NiO-ZrO_2 composite at the anode. The anode effluent was collected from these flow cells under electrolytic cell conditions and analyzed using Mass Spectrometry (MS). The flow cells showed an initially positive open-circuit voltage between ca. 0.1-0.2V, suggesting the possibility of running galvanically. However, for this study, cells were operated electrolytically so that sufficient product could be collected for adequate characterization.

In the batch cell, samples were collected after applying an electrode potential of 1.8V, and ^{1}H-NMR results are shown in Figure 5.10a. A strong peak for CH_3OH was observed, along with peaks indicating other products including isopropanol (C_3H_6O), acetate/acetic acid (H_3CCOO^-/H_3CCOOH), acetone

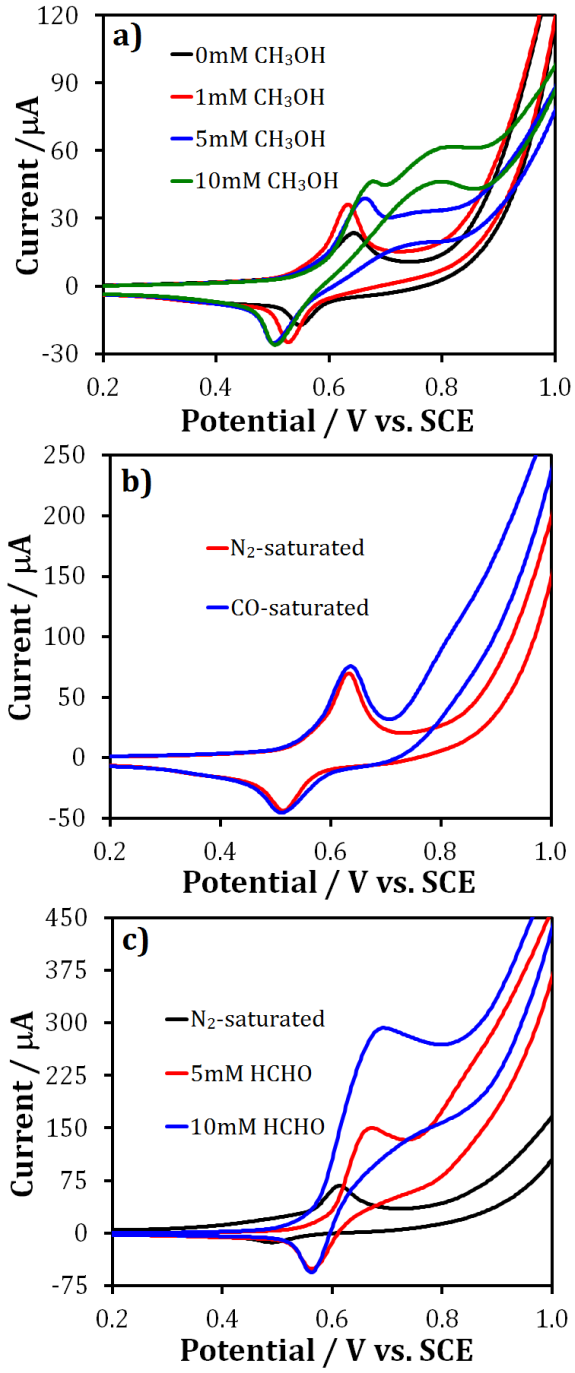

Figure 5.9. Characteristic oxidation CVs in 0.1M Na_2CO_3 electrolyte using NiO-ZrO_2 bifunctional electrocatalyst for a) CH_3OH; b) CO; and c) HCHO. Scans were conducted at room temperature (25°C) and scan rates were 20mV/s.

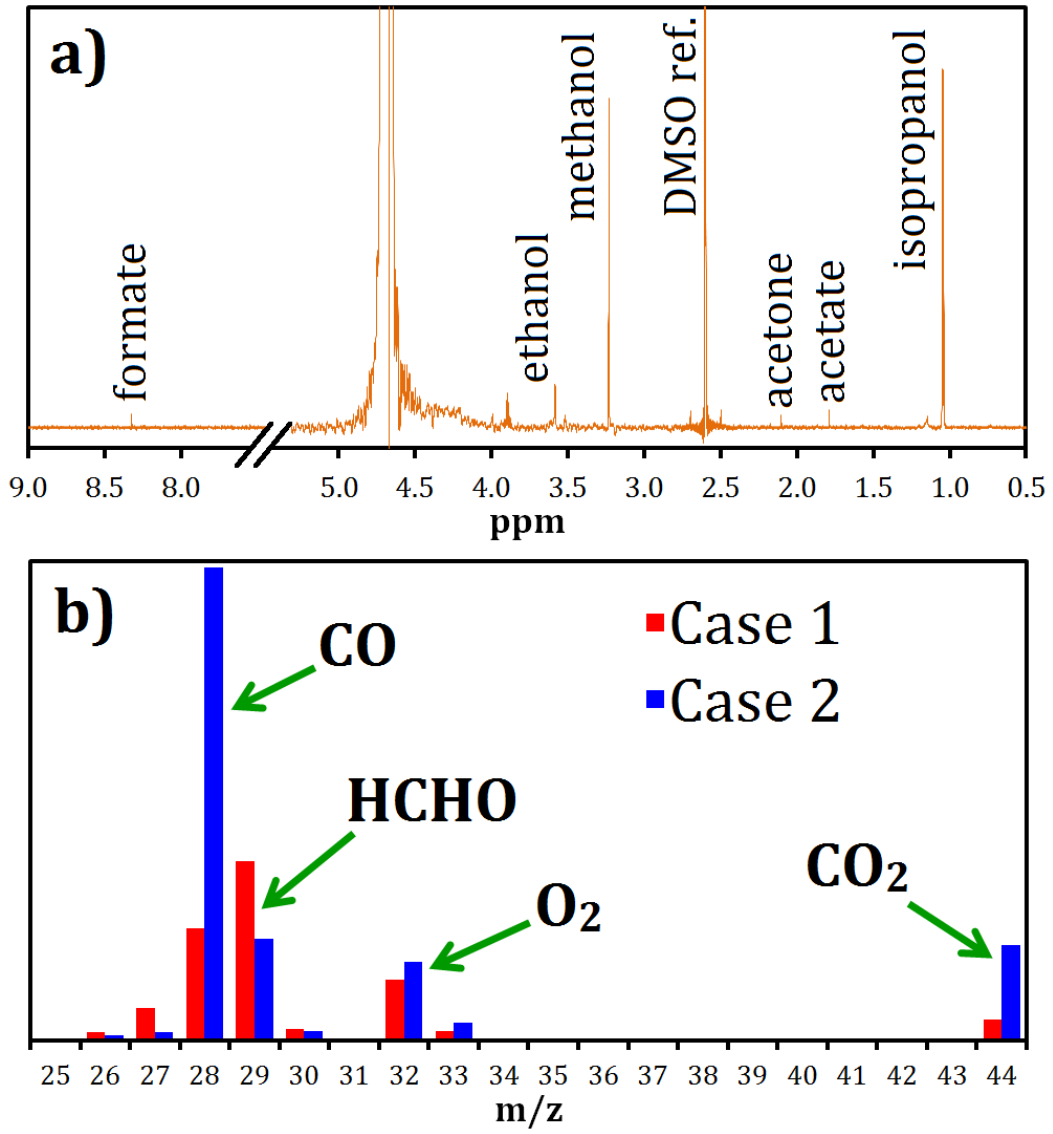

Figure 5.10. Product characterization tests: a) ^{1}H-NMR spectrum collected at 1.8V electrode potential; and b) MS spectra for anode effluent collected at 2.0V device voltage for Case 1 (no ionomer) and Case 2 (with ionomer).

(C_3H_8O), ethanol (C_2H_5OH), and formate/formic acid ($HCOO^-$/HCOOH) [149-151]. Formation of CH_3OH was expected and suggests a series pathway in the order of $CH_4 \rightarrow CH_3OH \rightarrow HCHO \rightarrow CO$, which is in agreement with theoretical observations by Nørskov concerning reduction of CO_2 on transition metal surfaces [152]. The presence of the two- and three-carbon oxygenates was surprising; however, these results are preliminary and more work will be forthcoming to study their formation in greater detail. Additionally, ^{1}H-NMR peak magnitudes were relatively small compared to the background H_2O/D_2O peak at 4.80ppm which suggests low product selectivity, and more research is needed to improve this. HCHO was likely not seen in Fig. 5.10a due to self-catalytic decomposition in alkaline media [149,153], and CO cannot be detected with ^{1}H-NMR because it contains no protons.

To detect the lower molecular weight products, electrochemical flow cells were constructed. The anode effluent of the flow cells operating at 2.0V applied was analyzed using MS, and results are shown in Figure 5.10b. Two cases were examined; Case 1 (with no ionomer in the catalyst layer) revealed the strongest peak at an m/z of 29 and was consistent with the NIST mass spectra for formaldehyde [154], suggesting the main product formed was HCHO, while Case 2 (with ionomer in the catalyst layer) showed the strongest peak at an m/z of 28, suggesting CO was the primary product. It is possible that for Case 1 and 2

secondary species may have contributed to the primary peaks at 29 and 28, respectively. However, based on the ratio of peak magnitudes, HCHO and CO can still be identified as the majority products formed. Without ionomer, the catalyst layer was nearly two-dimensional and residence times for adsorbed species and intermediates were short, limiting access to reactants. With ionomer, on the other hand, the three-dimensional catalyst layer facilitated further oxidation of the intermediate HCHO to CO. The impact of increased residence time is supported by the fact that CH_3OH was not observed in the MS spectra in Figure 5.10b for either cell configuration. This could also be due to the intrinsic electrocatalytic activity of NiO for the electrochemical oxidation of methanol [107].

Though it is clear from Figure 5.10 that a majority of the oxidation products were constrained to low molecular weight intermediates, CH_3OH, HCHO and CO, we have not yet optimized the reaction conditions to obtain a high selectivity of a targeted product. This is not unexpected as this study represents novel technology with the electrochemical partial oxidation of methane to oxygenate products at room temperature, and much work still remains. However, this initial study has identified the electrode potential and surface residence time as key factors in the product profile.

To control the product selectivity, it will be critical for researchers to fully

uncover the reaction mechanism. This includes the identification of elementary reaction steps and key intermediates. In addition, it is currently unclear whether carbonate anions are required for each oxidation step or only for methane activation. The most likely first step in the electrochemical oxidation of CH_4 by CO_3^{2-} is illustrated in Figure 5.11a. A charged oxygen atom is donated from CO_3^{2-} to CH_4 and inserted between a destabilized C and H, forming a new C-O bond as well as byproducts CO_2 and two electrons. The adsorbed methoxy (CH_3O^-) can then become protonated to CH_3OH and desorb from the electrocatalyst surface as a product, or it can be further oxidized to HCHO or CO by either further attack from CO_3^{2-} or decomposition via proton donation.

One of the most interesting findings in this work was the formation of two and three carbon products that were observed by NMR. Figure 5.11b proposes the mechanism of C-C bond formation to two- and three-carbon products. Using HCHO as an example intermediate with a C=O bond, a resonance structure can be written where the O atom is electron withdrawing and will possess a negative charge, while the C atom becomes an electropositive center. This creates a point of attack for a second adsorbed CH_4 molecule, creating C_2H_5OH. The approach detailed in Figure 5.11b can also be applied to other intermediates with a C=O bond to facilitate additional C-C bonds for various oxygenate products.

Figure 5.12 shows a map of reaction pathways for the products formed

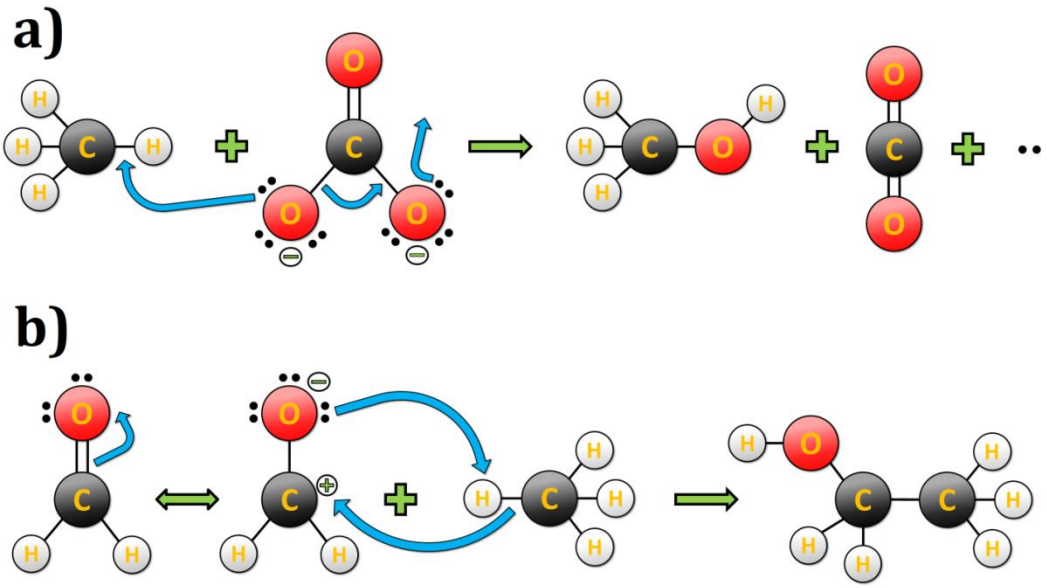

Figure 5.11. Reaction mechanisms for a) formation of CH_3OH from CH_4 and CO_3^{2-} with byproducts of CO_2 and $2e^-$; and b) formation of C-C bond in C_2H_5OH through C=O bond resonance in HCHO.

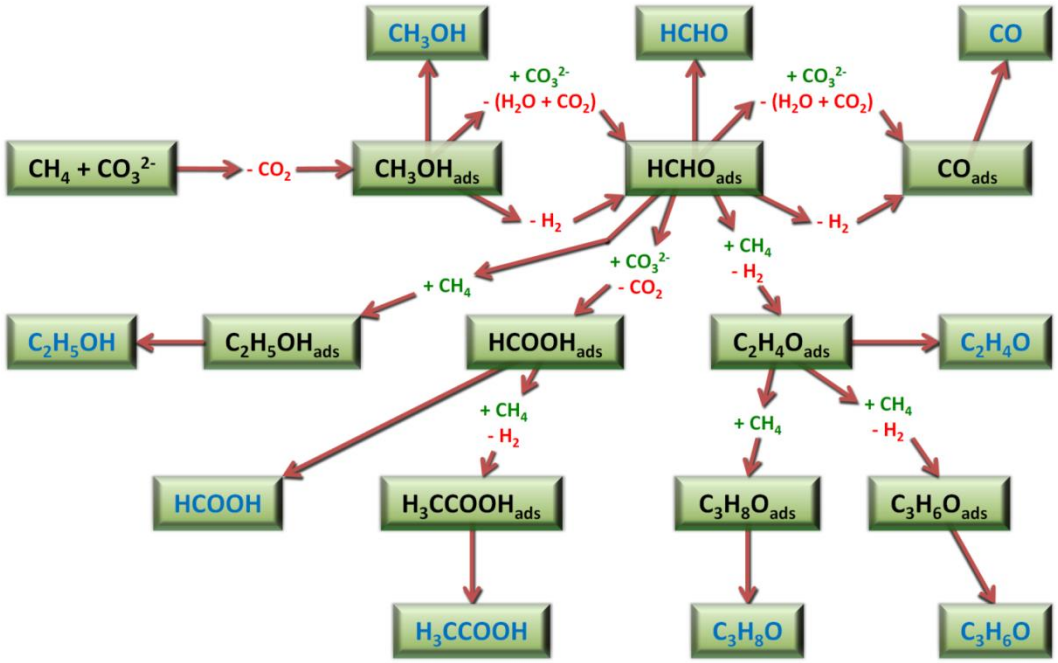

Figure 5.12. Proposed reaction pathways for activation of CH_4 with CO_3^{2-} anions.

from the activation of CH_4 with CO_3^{2-} anions in this study. After the CH_3OH formation step, HCHO can be formed either from two hydrogen atoms escaping as H_2 gas, or from a second CO_3^{2-} anion donating another oxygen atom to form H_2O and CO_2. This step can then occur once more to produce CO, or the donated oxygen can form a second C-O bond to make $HCOO^-$, or HCOOH through subsequent protonation. The presence of $HCOO^-$ can also be partially attributed to the separate electrooxidation of CH_3OH by NiO, from which $HCOO^-$ is a well-known product.

5.3 Summary

Methane was activated electrochemically at room temperature over a NiO-ZrO_2 bifunctional electrocatalyst to produce various oxygenates. Carbonate anions were used as an oxygen donator to facilitate methane activation. ZrO_2, a non-conducting, low temperature electrocatalyst promoter, adsorbed and donated carbonate anions to active sites on NiO where methane was adsorbed and activated. Products formed include methanol, formaldehyde, carbon monoxide, formate, ethanol, acetate, acetone, and isopropanol, in addition to oxygen and carbon dioxide from carbonate electrolysis and the oxygen evolution reaction. The electrode potential and surface residence time were identified as key factors that will be studied in the future, along with temperature and pH, to improve the

product selectivity for specific oxygenates. Based on this initial work, the possibility for directed oxygenate synthesis at room temperature is promising.

SECTION III:

LITHIUM-ION BATTERIES

CHAPTER 6: NANOSTRUCTURAL EFFECTS ON THE CYCLE LIFE AND Li^+ DIFFUSION COEFFICIENT OF NICKEL OXIDE ANODES

The purpose of this work was to examine the charge/discharge cyclability and Li^+ diffusivity of two different morphologies of NiO as lithium-ion battery anodes. Coin cells were fabricated and anode performance was analyzed using Cyclic Voltammetry and charge/discharge tests. The current pulse relaxation technique was derived mathematically and then applied to the different NiO anodes, from which values for the Li^+ diffusion coefficients were obtained. A multiphase parallel resistance model was also derived and applied to deconvolute Li^+ diffusion through two distinct phases in the anode structure during charge/discharge. The work presented in this chapter was published in the *Journal of Electroanalytical Chemistry* [155].

6.1 Experimental

6.1.1 Nickel Oxide Synthesis

The water used in this study was ultra-pure 18.2 MΩ deionized water from a Millipore Direct-Q 3UV purification system, and all reagents were used as received without further modification. Nickel oxide was prepared two ways, similarly to the authors' previous publication [107]. Reflux-precipitated nickel oxide (R-NiO) was synthesized by preparing 0.5M $Ni(NO_3)_2$ (Acros, 99%) in 10M NH_4OH (Fisher, certified ACS Plus) and boiling the solution under reflux for 24 hours, then allowing it to rest at room temperature for another 24 hours. The precipitate was filtered, rinsed thoroughly with deionized water, dried overnight at 90°C, and calcined in air at 500°C for 15 hours.

Sodium hydroxide-precipitated nickel oxide (N-NiO) was synthesized by preparing aqueous 0.5M $Ni(NO_3)_2$, and quickly adding 10M NaOH (Fisher, NF/EP/BP/FCC) under constant stirring until the pH rose to around 10. Measurement of the pH was performed using an Accumet Excel XL60 Dual Channel pH/Ion/Conductivity/DO Meter. The solution was then capped and allowed to rest for 24 hours. The precipitate was filtered, rinsed thoroughly with deionized water, dried at 90°C overnight, and calcined in air at 500°C for 15 hours.

6.1.2 Electrode Fabrication

Inks were prepared with 90% active material and 10% polyvinylidene fluoride (PVDF) binder (Kynar blend) using N-methylpyrrolidone (NMP) as a solvent (Acros, 99.5% Extra Dry). Copper foil (Alfa Aesar, 99.999%) was used as the current collector, and prior to anode deposition, the Cu surface was mechanically roughened and rinsed with isopropanol (Fisher, Optima) and hydrochloric acid (Acros, 37%). After sonication, the well-mixed ink was spread thinly over the pre-treated Cu foil, and the electrode was heated at 100°C under vacuum for 24 hours. The electrode was then pressed at 1500 lbs and massed. For all electrodes in this study, active material loadings were 1-2 mg/cm^2.

6.1.3 Physical Characterization

The electrode microstructure was investigated using an FEI Quanta FEG250 Scanning Electron Microscope (SEM). Specific surface areas were obtained from N_2 adsorption isotherms at 77K through Brunauer-Emmett-Teller analysis (BET) using a Micromeritics ASAP 2020 system. Samples were degased under vacuum at 150°C for 16 hours prior to N_2 adsorption analysis. Crystallinity before and after cycling was examined with X-ray Diffraction (XRD) using a Bruker D8 Advance X-ray Diffractometer with Cu Kα_1 radiation (λ = 0.1540562

nm). Batteries were assembled in 20 mm diameter coin cells (Hohsen Corp.) using lithium metal (Aldrich, 99.9%) as the cathode and Celgard 2320 Trilayer PP/PE/PP as the separator. As a control material, graphite (CPreme G5 Graphite Anode) was also tested. Lithium hexafluorophosphate ($LiPF_6$) (Acros, 98%), dimethyl carbonate (DMC) (Acros, 98+%), diethyl carbonate (DEC) (Acros, 99%), and ethylene carbonate (EC) (Acros, 99+%) were used for the electrolyte, which consisted of 1M $LiPF_6$ in (1:1:1)EC:DEC:DMC. For each material and test, at least 10 duplicate coin cells were fabricated and results shown in this work are representative data from all tests.

6.1.4 Electrochemical Tests

Charge/discharge cycles were obtained between 0.001 – 1.0V vs. Li/Li^+ for graphite and between 0.001 – 3.0V vs. Li/Li^+ for NiO. Cyclic voltammograms (CVs) were collected at a scan rate of 0.1 mV/s over the same voltage windows as the charge/discharge cycles for graphite and NiO. All electrochemical data was collected using an Arbin MSTAT battery test system. For all materials, the theoretical capacity was used to determine the charge/discharge rate.

Prior to CPR tests, cells were cycled once to avoid any effects from

irreversible behavior associated with the first charge/discharge. *dOCV*/*dx* was then obtained by slow charging at C/20 rate to a desired state of charge in the range $0.5 \leq x \leq 1.0$ for NiO, and allowing the battery to rest for 24 hours to reach an equilibrium voltage. This procedure was repeated for multiple values of *x*, and the slope of *OCV* vs. *x* was calculated to obtain *dOCV*/*dx*. CPR tests were performed at each equilibrium voltage by applying a short (5s) pulse of current at 1C rate, causing excess Li^+ ions to be drawn into the electrode. The subsequent voltage relaxation was then monitored as a function of time.

6.2 Results and Discussion

6.2.1 Electrode Characterization and Battery Performance

Figure 6.1 shows SEM images of both R-NiO and N-NiO electrodes prior to any testing. R-NiO (Fig. 6.1A) exhibited a blade-like nanostructure with sharp, irregular shapes and features of varying size from ca. 500nm to 2μm, whereas N-NiO (Fig. 6.1B) formed small, spherical particles around 20-30nm in diameter which agglomerated into micrometer-sized clusters. These results are consistent with the authors' previously published observations concerning NiO nanoparticles prepared using similar synthesis procedures [107,128]. The large agglomerations can be attributed to the temperature and time of calcination (500°C for 15 hours);

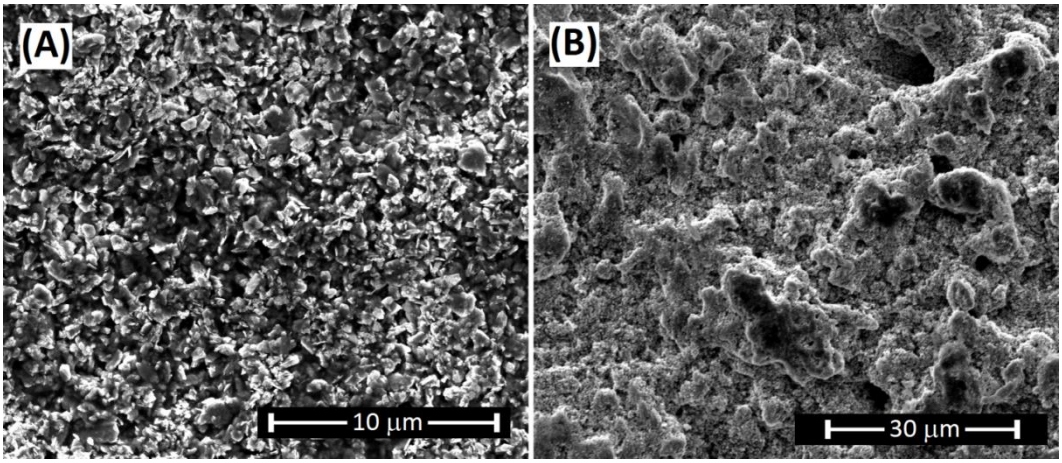

Figure 6.1. SEM images for (A) R-NiO and (B) N-NiO anodes prior to testing.

the former of which was selected to ensure complete dehydration of NiO to avoid adverse effects from the reaction of Li and H_2O [25,107]. The long calcination time was chosen to reduce the specific surface area in an attempt to avoid excessive electrolyte decomposition and subsequent heat generation, which can cause thermal runaway, self-discharge, and potential battery destruction [31,32,47].

N_2 adsorption isotherms shown in Figure 6.2 exhibited type IV behavior with only a small hysteresis at relative pressures around 0.9 and above, indicating dense particles lacking appreciable internal porosity or external mesoporosity [156]. Furthermore, the shapes of the high relative pressure hystereses for R-NiO and N-NiO were indicative of slit- or blade-like shapes and clusters of spherical agglomerates, respectively [156], which is in agreement with observations seen in SEM images. BET analysis evaluated in the monolayer adsorption region between values of P/P_o of 0.05 to 0.2 revealed low specific surface areas for both R-NiO (27.2 m^2/g) and N-NiO (7.8 m^2/g). The reduction in specific surface area for N-NiO was likely caused by the ubiquitous micrometer-sized agglomerations of N-NiO, while such clustering was not observed with R-NiO. However, despite agglomerations that caused a desired lower specific surface area, the average diameter of individual N-NiO nanoparticles remained similar to those calcined for a shorter period of time. This facilitated more rapid diffusion of Li^+ to active sites

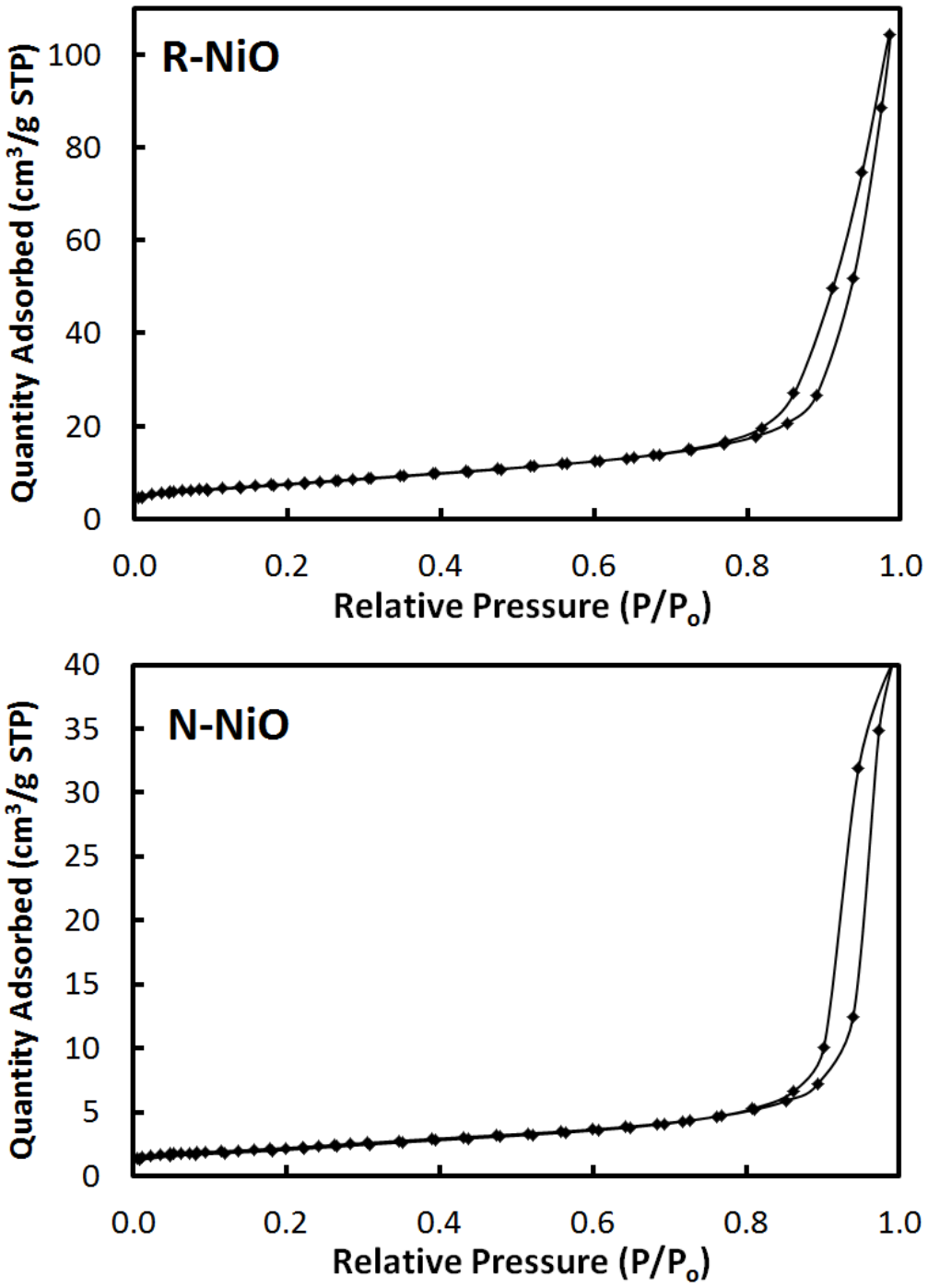

Figure 6.2. Nitrogen adsorption isotherms at 77K for R-NiO and N-NiO.

and helped maintain electronic conductivity throughout charge/discharge [38,45,46].

The first five CVs for R-NiO and N-NiO anodes at a scan rate of 0.1 mV/s are shown in Figure 6.3. A large, irreversible cathodic peak was observed during the first cycle around 0.3-0.4V vs. Li/Li^+ corresponding to a combination of solid-electrolyte interphase (SEI) formation and the primary charge/discharge decomposition reaction, Equation 6.1 [45,46,49,53-55]:

$$NiO + 2Li^+ + 2e^- \leftrightarrow Ni + Li_2O \quad (6.1)$$

The SEI is an insulating barrier consisting of various organic and inorganic compounds (i.e. LiF, Li_2O, Li_2CO_3, ethylene oxide-based oligomers, lithium alkyl carbonate) [32,53]. The SEI formation plays a beneficial role in battery performance by insulating the electrode, preventing further reaction/decomposition of the electrolyte, and acting as a passivating layer to prevent lithium corrosion [31,32,157]. However, the SEI also has detrimental effects including the large irreversible capacity loss associated with its formation during the first charge/discharge cycle, and the promotion of both reversible and irreversible self-discharge mechanisms [43,47,54,158]. The main cathodic and anodic peaks in subsequent cycles at ca. 1.1 and 2.2V vs. Li/Li^+, respectively, corresponded to Equation 6.1, and the positions of these peaks illustrate the essential nature of the SEI since the complete redox couple did not appear until

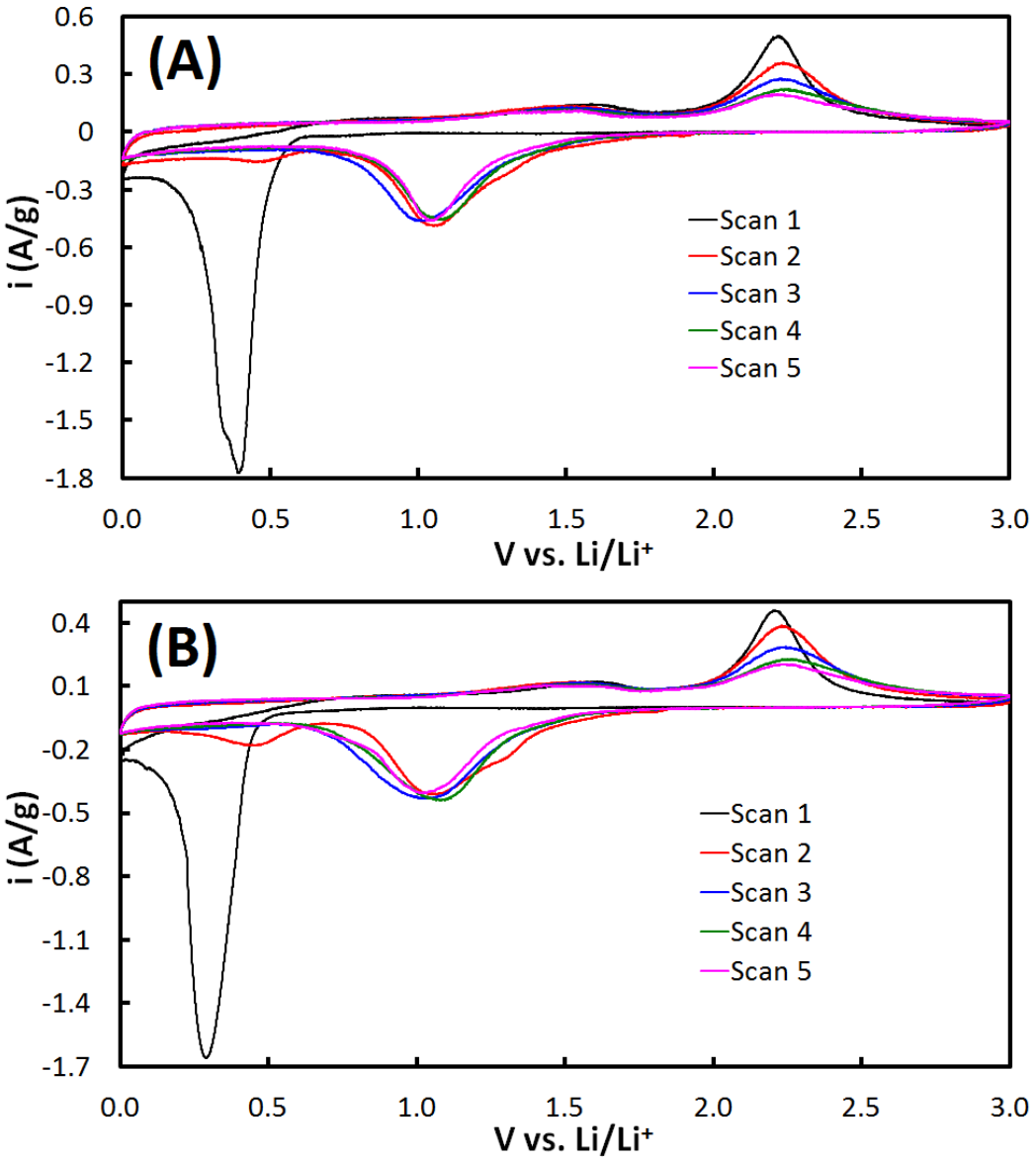

Figure 6.3. First five CVs for (A) R-NiO and (B) N-NiO anodes between 0.001 – 3.0V vs. Li/Li^+ at a scan rate of 0.1 mV/s.

after the SEI had been formed during the initial charge. The presence of the anodic discharge peak at 2.2V vs. Li/Li^+ during the first cycle is also validation that the large cathodic peak around 0.3-0.4V vs. Li/Li^+ resulted from both the SEI formation and the charge decomposition reaction (Eq. 6.1). Additionally, a small anodic peak was observed near 1.55V vs. Li/Li^+ that was indicative of partial SEI decomposition [44], which may explain why the main decomposition reduction peaks were smaller in magnitude than their corresponding oxidation peaks. During each cathodic scan, the SEI was partially regenerated as a result of the previous decomposition, contributing to a larger observed current. Constant volume expansion and contraction of the NiO electrode may also have caused partial collapse of the SEI, requiring regeneration during each charge and leading to capacity loss [49,55]. In addition to SEI decomposition/regeneration, the second factor that led to a discrepancy in sizes of the oxidation and reduction peaks was partial irreversible growth of the Li_2O+Ni phase during charging. This phenomenon will be discussed in detail later.

Figure 6.4 shows the first 10 charge/discharge cycles for cells with R-NiO and N-NiO anodes, and the capacities of each electrode for the first 30 cycles, along with energy losses from charge to discharge, are shown in Figure 6.5. Energy loss is defined as 100% • (1 – Faradaic efficiency), and it represents the percent difference of the charge and discharge capacities for a given cycle. For

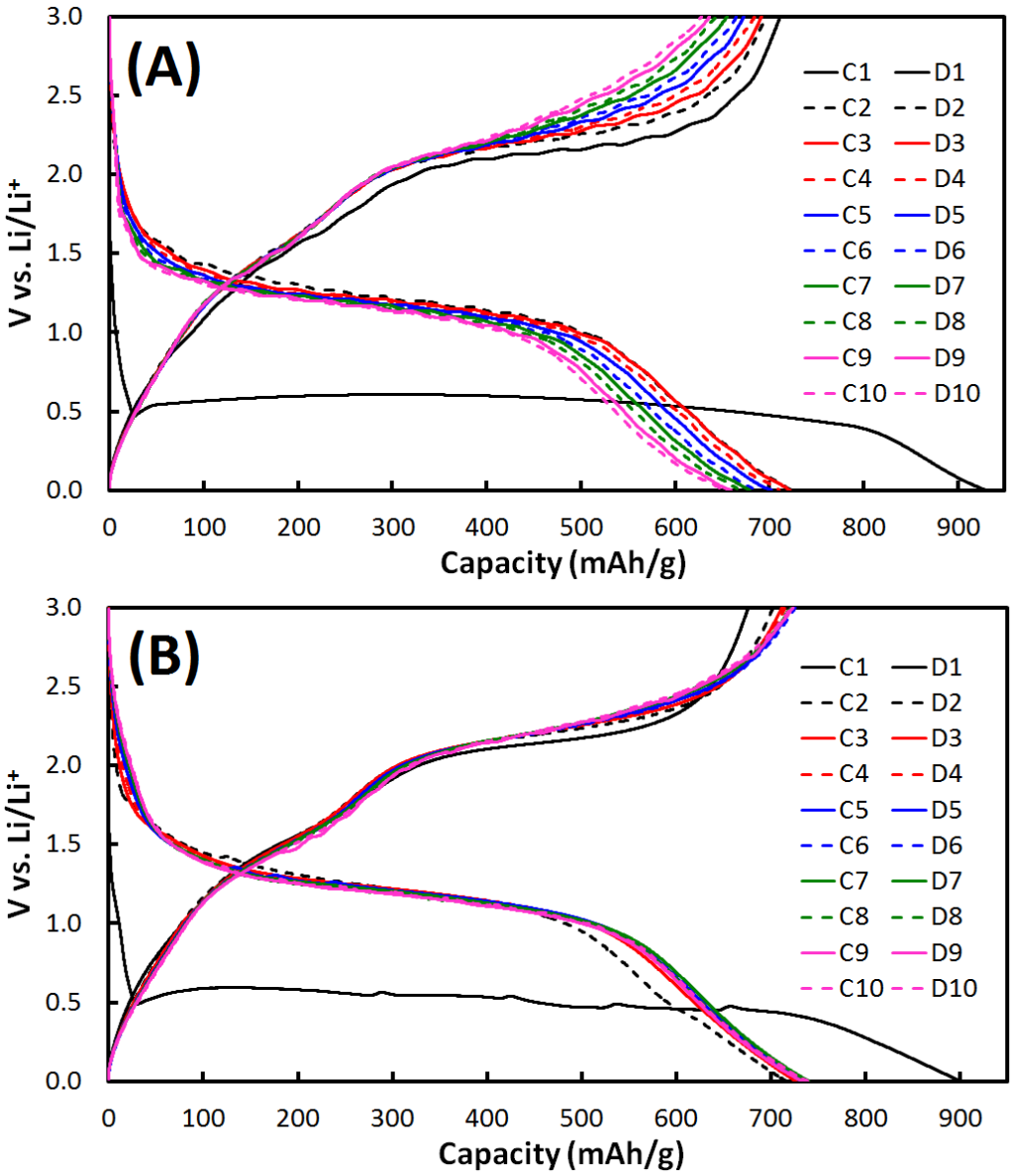

Figure 6.4. First 10 charge (C)/discharge (D) (lithiation/delithiation) cycles for (A) R-NiO and (B) N-NiO anodes between 0.001 – 3.0V vs. Li/Li^+ at C/5 rate.

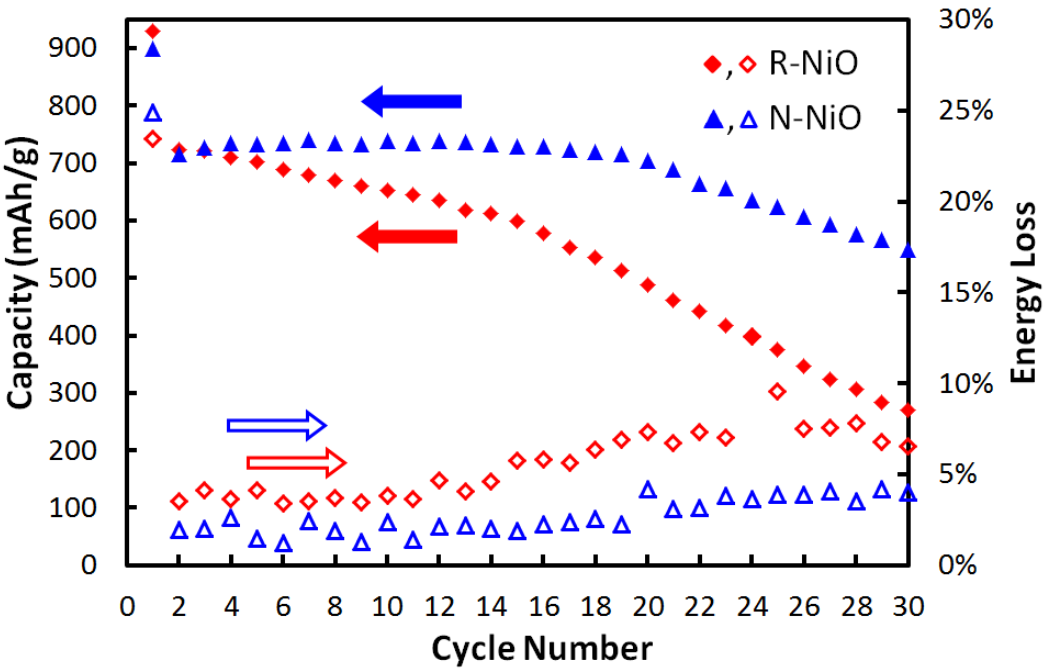

Figure 6.5. Plot of capacities and energy losses for both R-NiO and N-NiO over the first 30 cycles at C/5 charge/discharge rate. Energy loss is defined as 100% • (1 – Faradaic efficiency), and it is the percent difference of charge and discharge capacities for each complete cycle.

both electrodes, the effect of SEI formation was seen clearly in the prolonged voltage lag in Fig. 6.4 during the first charge around 0.5V vs. Li/Li^+, leading to apparent capacities around 900 mAh/g that were not recovered in subsequent cycles. Following the first charge/discharge cycle, N-NiO demonstrated greater capacity retention than R-NiO. Over the course of cycles 2 through 10, the capacity decreased noticeably and regularly for R-NiO (Fig. 6.4A) whereas for N-NiO the charge/discharge curves were almost entirely consistent and repeatable (Fig. 6.4B). By the end of the 30^{th} cycle, the capacity for R-NiO dropped from 722.9 to 269.8 mAh/g (Fig. 6.5, neglecting the first charge), retaining only 37.3% of the initial (2^{nd} charge cycle) capacity. N-NiO, on the other hand, showed much better capacity retention, 76.7%, only dropping from 716.3 to 549.3 mAh/g. The energy losses for each individual cycle shown in Fig. 6.5 also indicate R-NiO suffered more dramatic capacity losses between charge and discharge tests for the same cycle than N-NiO. Again neglecting the first cycle, the energy loss for N-NiO never rose above 5% and showed an average energy loss of only 2.7%. R-NiO consistently had higher energy losses and showed an average value of 5.8%, over double that of N-NiO.

Figure 6.6 shows the first 10 charge/discharge cycles for a G5 graphitic carbon anode. During the first scan, similarly to results observed with NiO anodes, a long potential lag was observed stemming from the SEI formation that

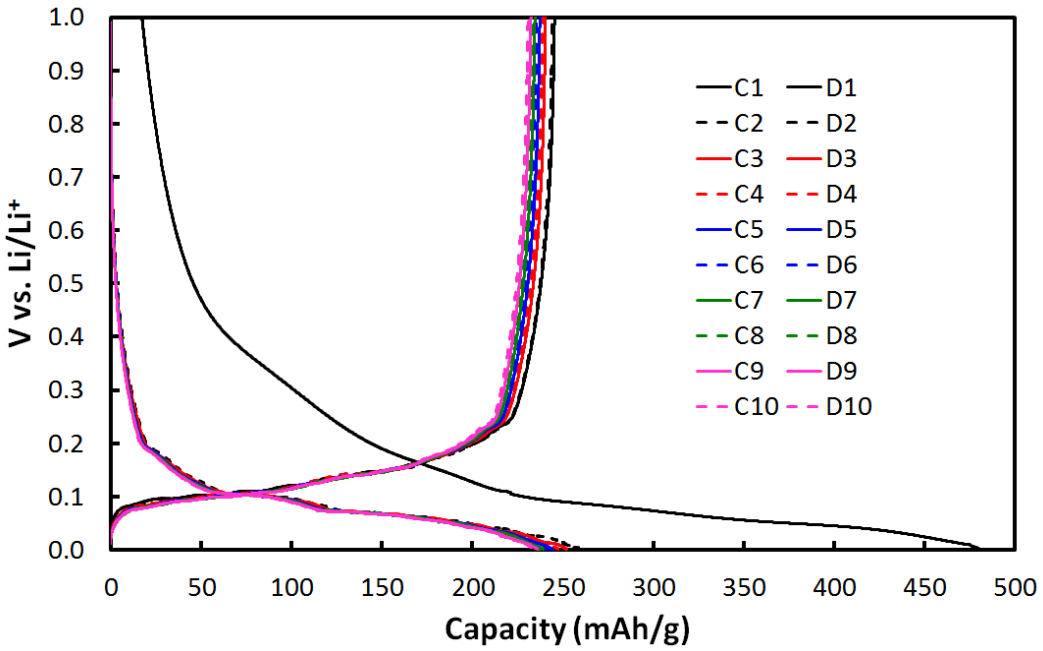

Figure 6.6. First 10 charge (C)/discharge (D) (lithiation/delithiation) cycles for G5 graphite anode between 0.001 – 1.0V vs. Li/Li^+ at C/5 rate.

led to a non-recoverable charge capacity of ca. 480 mAh/g. In subsequent cycles, the capacity remained relatively steady and repeatable as Li^+ was intercalated and deintercalated into the graphite structure according to Equation 6.2 [159,160]:

$$6C + xLi^+ + xe^- \leftrightarrow Li_xC_6 \quad (6.2)$$

One of the reasons for this consistent cyclability in graphite anodes is the low hysteresis in potentials between charge and discharge, which occurred between ca. 0.0 – 0.25V vs. Li/Li+ [54]. Figure 6.7 shows the charge capacities as a function of cycle number for the first 30 cycles, along with the energy losses for each individual cycle. Excluding the first cycle due to the large capacity from SEI formation, the capacity only dropped from 263.9 mAh/g to 210.6 mAh/g between cycles 2 – 30, retaining 79.8% of the original capacity. The energy losses between individual charge and discharge cycles were also much lower, averaging just 1.5% loss for cycles 2 – 30 and consistently showing less than 1% energy loss after cycle 13. These results illustrate the benefits of using graphite as anodes in Li-ion batteries for maintaining capacity over numerous cycles. However, the low observed capacities highlight the need for greater-capacity anode materials such as NiO.

The physical effects of extensive charge/discharge cycling are shown in the SEM images in Figure 6.8. After 100 cycles, it is clear that R-NiO (Fig. 6.8A) underwent dramatic structural changes. Some of the original blade-like

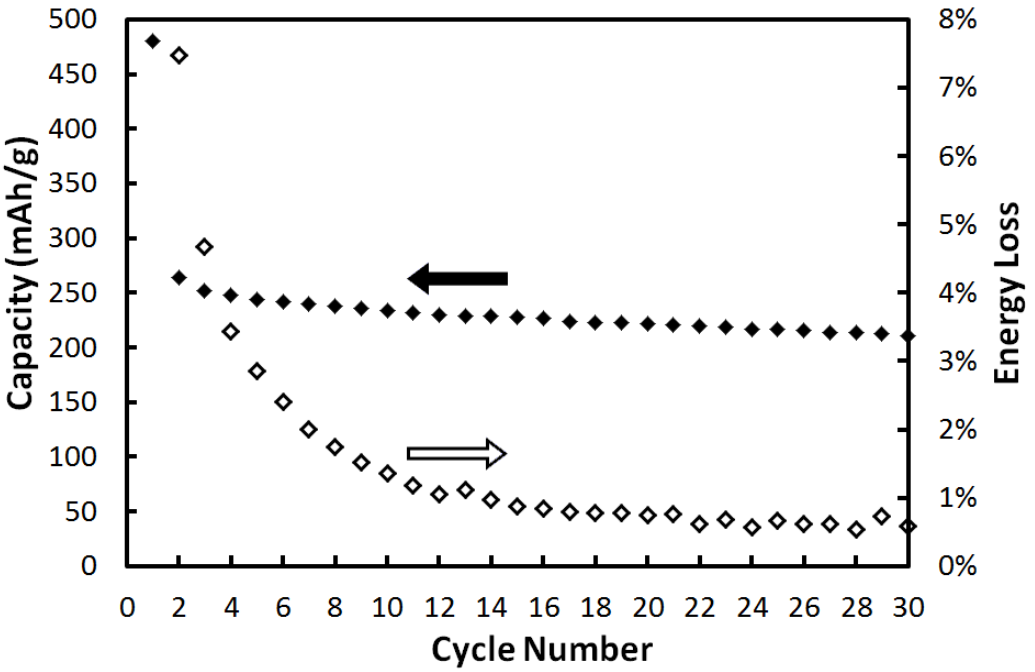

Figure 6.7. Plot of capacities and energy losses for G5 graphite anode over the first 30 cycles at C/5 charge/discharge rate. Energy loss is defined as 100% • (1 – Faradaic efficiency), and it is the percent difference of charge and discharge capacities for each complete cycle.

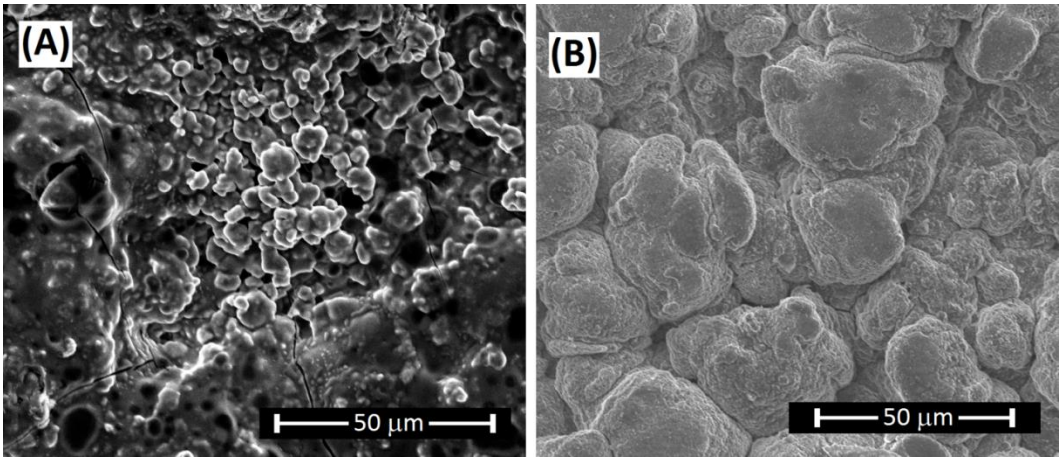

Figure 6.8. SEM images for (A) R-NiO and (B) N-NiO anodes after 100 charge/discharge cycles.

nanostructure seen in Fig. 6.1A was still observed; however, the particles were roughly an order of magnitude larger in size (from ca. 500nm to around 5-10μm) and not nearly as homogeneous. Other sections of the R-NiO electrode surface appeared to have smoothed out and completely lost all semblance of the initial nanostructure, and the entire electrode surface was wrought with cracks and fissures. The most likely cause of these cracks and fissures was excessive volume expansion, and the capacity suffered as a result of the pulverization of the electrode and possible delamination from the copper current collector [49,55]. N-NiO (Fig. 6.8B), on the other hand, did not exhibit as striking a transformation compared to its original nanostructure (Fig. 6.1B). Larger agglomerated particles were visible after cycling than before cycling, but an increased level of texture and nanostructure was observed compared to R-NiO, along with an absence of cracks and fissures. These physical observations make sense in light of the previously-discussed performance and stability advantages of N-NiO over R-NiO.

For both R-NiO and N-NiO, the primary causes of irreversibility and capacity loss were large pockets of electrochemically-inactive Li_2O [38,43-46]. On the nanoscale, Li_2O can be reversibly transformed with Ni back to Li^+ ions and NiO during discharge (Eq. 6.1); however, if excessive agglomeration of individual Li_2O and Ni particles occurs, sections of the Li_2O+Ni phase will become irreversibly transformed and will no longer participate in the

charge/discharge reaction. This phenomenon is illustrated in Figure 6.9, which shows that after a certain number of cycles there will be inactive sections of the Li_2O+Ni phase dispersed within the NiO phase, increasing the overall particle volume. Because the rate at which this takes place will determine the speed of electrode deactivation and degradation, it can be concluded that the R-NiO electrode produced large Li_2O agglomerates more rapidly than N-NiO.

Figure 6.10 shows XRD spectra for R-NiO and N-NiO electrodes before and after 100 charge/discharge cycles. In both before and after spectra, dominant peaks were observed at 43.3°, 50.4° and 74.1°, which corresponded to the (111), (200) and (220) facets, respectively, of the Cu current collector [161]. Smaller peaks corresponding to NiO were visible in the non-tested spectra at 37.2° (111) and 62.8° (220), and the primary peak at 43.3° (200) overlapped with the peak for Cu [107]. In the cycled electrodes, no peaks for NiO could be identified; however, a broad peak around 44.5° was identified and is consistent with the (111) reflection for metallic Ni [162]. This illustrates how the final state of NiO anodes, once drained almost completely of usable capacity, consisted of large pockets of inactive Li_2O and Ni particles; or, that the charge/discharge reaction (Eq. 6.1) was irreversibly stuck in the charged state. To determine the domain size for Ni in the spent electrodes, the Scherrer Equation was used to calculate average grain boundary sizes, Equation 6.3:

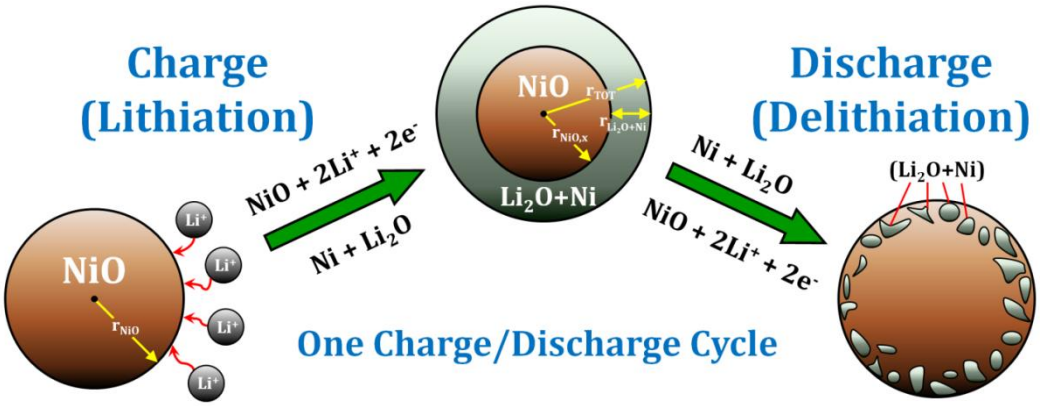

Figure 6.9. Reaction diagram illustrating volume expansion during NiO decomposition and reconstitution reactions for one complete charge/discharge cycle.

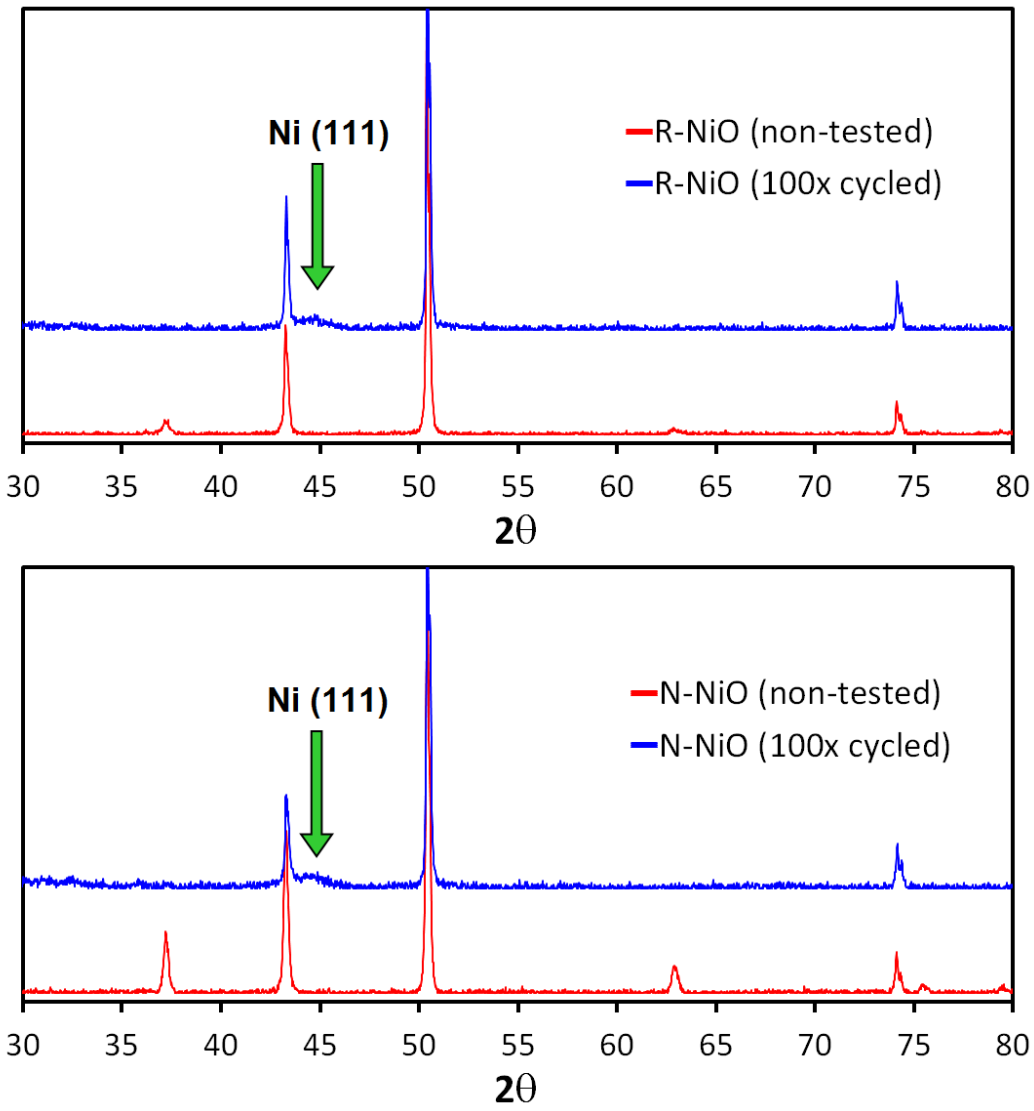

Figure 6.10. XRD for R-NiO and N-NiO anodes before and after 100 charge/discharge cycles. Spectra collected between 2θ values of 10° and 90° at a sweep rate of 1.3°/min.

$$d = \frac{k\lambda}{B\cos\theta} \tag{6.3}$$

where d is the average grain boundary size, k is the shape factor (taken as 0.9), λ is the X-ray wavelength (0.1540562 nm), B is the full width of the XRD peak (in radians) at half the maximum intensity, and θ is the Bragg angle. Values for the Ni particle d were calculated as 3.50 nm for R-NiO and 3.16 nm for N-NiO. While the Ni (111) peaks in Fig. 6.10 were broad and showed relatively poor resolution, the Scherrer Equation at least provides a qualitative comparison of the average grain boundary sizes between R-NiO and N-NiO. This size discrepancy follows logically from the previous discussion of large particles leading to capacity loss and the differences between R-NiO and N-NiO. If the average size of Ni (and, by extension, Li_2O) particles was larger for R-NiO than for N-NiO, a faster rate of capacity loss would be expected, and this is precisely the result that was observed. The difference in the Li_2O+Ni domain in R-NiO vs. N-NiO is also expected to impact the diffusion of Li^+ during charge/discharge.

6.2.2 Current Pulse Relaxation

Li^+ diffusion coefficients were calculated for both R-NiO and N-NiO using the CPR method. Before discussing the results, since no location exists in the literature where the entire derivation of the CPR equation can be found, we

have provided the derivation in full for the first time here.

The concentration of Li^+ ions, *C*, at any time, *t*, and position, *z*, can be described using Fick's 2nd Law of Linear Diffusion in differential form, Equation 6.4:

$$\frac{\partial C(z,t)}{\partial t} = D_{eff}\frac{\partial^2 C(z,t)}{\partial z^2} \tag{6.4}$$

where D_{eff} is the effective Li^+ diffusion coefficient. A common solution to Eq. 6.4 is:

$$C - C_i = \frac{\eta}{t^{1/2}} e^{-z^2/4D_{eff}t} \tag{6.5}$$

where C_i is the initial Li^+ concentration and η is the integration constant. Mathematical proof for Eq. 6.5 as a solution to Eq. 6.4 is as follows. The partial derivative of *C* with respect to *t* is

$$\frac{\partial C}{\partial t} = \frac{\eta}{t^{1/2}} \cdot \frac{\partial}{\partial t}\left(e^{-z^2/4D_{eff}t}\right) + e^{-z^2/4D_{eff}t} \cdot \frac{\partial}{\partial t}\left(\frac{\eta}{t^{1/2}}\right) + \frac{\partial C_i}{\partial t} \tag{6.6}$$

$$= \frac{\eta}{t^{1/2}} \cdot \left(e^{-z^2/4D_{eff}t}\right) \cdot \left(\frac{z^2}{4D_{eff}t^2}\right) + e^{-z^2/4D_{eff}t} \cdot \left(\frac{-\eta}{2t^{3/2}}\right) \tag{6.7}$$

Factoring out the common term $\eta\left(e^{-z^2/4D_{eff}t}\right)$ yields

$$= \eta\left(e^{-z^2/4D_{eff}t}\right)\left[\left(\frac{z^2}{4D_{eff}t^{5/2}}\right) - \left(\frac{1}{2t^{3/2}}\right)\right] \tag{6.8}$$

The first partial derivative of C with respect to z is

$$\frac{\partial C}{\partial z} = \frac{\eta}{t^{1/2}} \cdot \left(\frac{-z}{2D_{eff}t}\right) e^{-z^2/4D_{eff}t} = \frac{-\eta}{2D_{eff}t^{3/2}} \cdot ze^{-z^2/4D_{eff}t} + \frac{\partial C_i}{\partial z} \qquad (6.9)$$

and the second partial derivative with respect to z is

$$\frac{\partial^2 C}{\partial z^2} = \frac{-\eta}{2D_{eff}t^{3/2}}\left[z\frac{\partial}{\partial z}\left(e^{-z^2/4D_{eff}t}\right) + \left(e^{-z^2/4D_{eff}t}\right)\frac{\partial z}{\partial z}\right] \qquad (6.10)$$

$$= \frac{-\eta}{2D_{eff}t^{3/2}}\left[z\left(\frac{-z}{2D_{eff}t}\right)\left(e^{-z^2/4D_{eff}t}\right) + \left(e^{-z^2/4D_{eff}t}\right)\right] \qquad (6.11)$$

Factoring out the similar term $\eta\left(e^{-z^2/4D_{eff}t}\right)$ as in Eq. 6.8 yields

$$= \eta\left(e^{-z^2/4D_{eff}t}\right)\left[\left(\frac{z^2}{2D_{eff}t}\right)\left(\frac{1}{2D_{eff}t^{3/2}}\right) - \left(\frac{1}{2D_{eff}t^{3/2}}\right)\right] \qquad (6.12)$$

$$= \eta\left(e^{-z^2/4D_{eff}t}\right)\left[\left(\frac{z^2}{4{D_{eff}}^2t^{5/2}}\right) - \left(\frac{1}{2D_{eff}t^{3/2}}\right)\right] \qquad (6.13)$$

Comparing Eq. 6.8 with Eq. 6.13 shows they differ only by a factor of D_{eff}, confirming that Eq. 6.5 is a valid solution to Eq. 6.4, Fick's 2nd Law of Diffusion.

If a short pulse of current is applied to the anode, a small amount of excess Li^+ is drawn into the electrode, resulting in a transient condition where the open-circuit voltage (OCV) is elevated relative to its equilibrium value. As the excess Li^+ diffuses from the electrode, the voltage relaxes to the equilibrium value [163]. During the early part of this relaxation, the Li^+ diffusion layer near the surface can

be assumed to be a flat plane independent of the electrode geometry [160]. The total amount of a substance per unit area, *M*, diffusing through a geometry of semi-infinite length and unit cross section can be determined by Equation 6.14 [164]:

$$M = \int_0^\infty (C - C_i) dz \tag{6.14}$$

Substituting the expression for C - C_i in Eq. 6.5 into Eq. 6.14 yields

$$M = \int_0^\infty \frac{\eta}{t^{1/2}} e^{-z^2/4D_{eff}t} dz \tag{6.15}$$

$$M = \frac{\eta}{t^{1/2}} \cdot \left(\sqrt{4D_{eff}t}\right) \int_0^\infty e^{-z^2/4D_{eff}t} d\left(z/\sqrt{4D_{eff}t}\right) \tag{6.16}$$

Using the definition of the error function, Equation 6.17,

$$\text{erf}(\alpha) = \frac{2}{\sqrt{\pi}} \int_0^\alpha e^{-\beta^2} d\beta \tag{6.17}$$

Eq. 6.16 is transformed to

$$M = 2\eta\sqrt{D_{eff}} \cdot \frac{\sqrt{\pi}}{2} [\text{erf}(\infty) - \text{erf}(0)] \tag{6.18}$$

$$M = \eta\sqrt{\pi D_{eff}} \tag{6.19}$$

Solving Eq. 6.19 for the constant η in terms of D_{eff} and M and plugging it into Eq. 6.5 yields

$$C - C_i = \frac{M}{\sqrt{\pi D_{eff} t}} e^{-z^2/4D_{eff}t} \tag{6.20}$$

For a short current pulse of i amps pulsed for τ seconds, the total of moles of electrons transferred will equal the moles of Li^+ ions introduced into the electrode. Thus,

$$\frac{i\tau}{nF} = MA \tag{6.21}$$

where n is the equivalence (stoichiometric ratio of moles of electrons to moles of Li^+), F is Faraday's constant and A is the electrode surface area. Inserting Eq. 6.21 into Eq. 6.20, realizing n=1, and considering diffusion only at the electrode surface ($z = 0$):

$$C - C_i = \frac{i\tau}{AF\sqrt{\pi D_{eff} t}} \tag{6.22}$$

Basu and Worrell reported that the voltage of a Li-ion battery, E, is a linear function of x, the molar fraction of Li intercalated, over a limited compositional range [163]. For graphite, x is simply the state of charge (SOC) ($0 \leq x \leq 1$); however, due to its reaction stoichiometry, the SOC is equivalent to $0.5x$ ($0 \leq x \leq 2$) for NiO. Following the example set by Basu and Worrell, for any particular system an equation can be written in the form

$$E = \left(dOCV/_{dx}\right)x + b \tag{6.23}$$

where *dOCV*/*dx* is the linear slope, or the change in OCV with respect to *x*, and *b* is the y-intercept. *x* can be related to *C* through V_m, the electrode molar volume:

$$C = \frac{x}{V_m} \tag{6.24}$$

Eq. 6.22 can now be rewritten by substituting for *C*, C_i, and *x* via Eqs. 6.23-6.24:

$$\left(\frac{E-b}{(dOCV/dx)V_m}\right) - \left(\frac{E_i-b}{(dOCV/dx)V_m}\right) = \frac{i\tau}{AF\sqrt{\pi D_{eff}t}} \tag{6.25}$$

Further simplification yields

$$E - E_i = \Delta E = \frac{(dOCV/dx)V_m i\tau}{AF\sqrt{\pi D_{eff}t}} \tag{6.26}$$

Equation 6.26 is the CPR equation typically used to calculate experimental values for D_{eff}. Considering *dOCV*/*dx*, V_m, *i*, τ, *A*, *F*, and π are all experimentally-determined values or universal constants, a plot of ΔE vs. $1/t^{1/2}$ will have a linear slope from which D_{eff} can be extracted [159,160,163,165,166]. Since the Li^+ diffusion coefficient in the electrolyte is on the order of 10^{-5} cm^2/s, several orders of magnitude greater than D_{eff}, the rate of Li^+ diffusion through the electrolyte is significantly faster than the solid-state diffusion of Li^+ ions within the electrode, allowing the effects of electrolyte diffusion to be neglected [159,165].

Equilibrium voltages for R-NiO and N-NiO anodes were limited to the

compositional range $0.5 \leq x \leq 1.0$ since the CPR method is typically restricted to where the behavior is most linear [160,163,167]. The resulting plots of OCV vs. x are shown in Figure 6.11. The slopes of the linear regressions were -0.485V and -0.429V for R-NiO and N-NiO, respectively, and these values were taken as $dOCV/dx$. The lower magnitude of $dOCV/dx$ for N-NiO compared to R-NiO showed that the voltage did not drop as quickly across the same range of x, leading to increased time during discharge and therefore higher capacity. At each x, CPR tests were conducted and the linear plots of ΔE vs. $1/t^{1/2}$ are shown in Figure 6.12. Using Eq. 6.26, values for D_{eff} were obtained, and these are listed as a function of x (and the SOC, equivalent to $0.5x$) in Table 6.1. The order of magnitude of Li^+ diffusion coefficients shown in Table 6.1 is comparable to those found in the literature for graphite anodes [160,163]. For all SOC, D_{eff} was a factor of 2-3 times larger for N-NiO than for R-NiO, which was likely due to contributions to D_{eff} from the individual diffusion coefficients in both the NiO and Li_2O+Ni phases during charge/discharge. To date, researchers have not proposed a methodology to deconvolute the diffusion coefficient of Li^+ through a multiphase electrode. Therefore, the next section outlines a novel model for deconvoluting D_{eff} as a function of the SOC to gain insight into the mass transport of Li^+ in each phase.

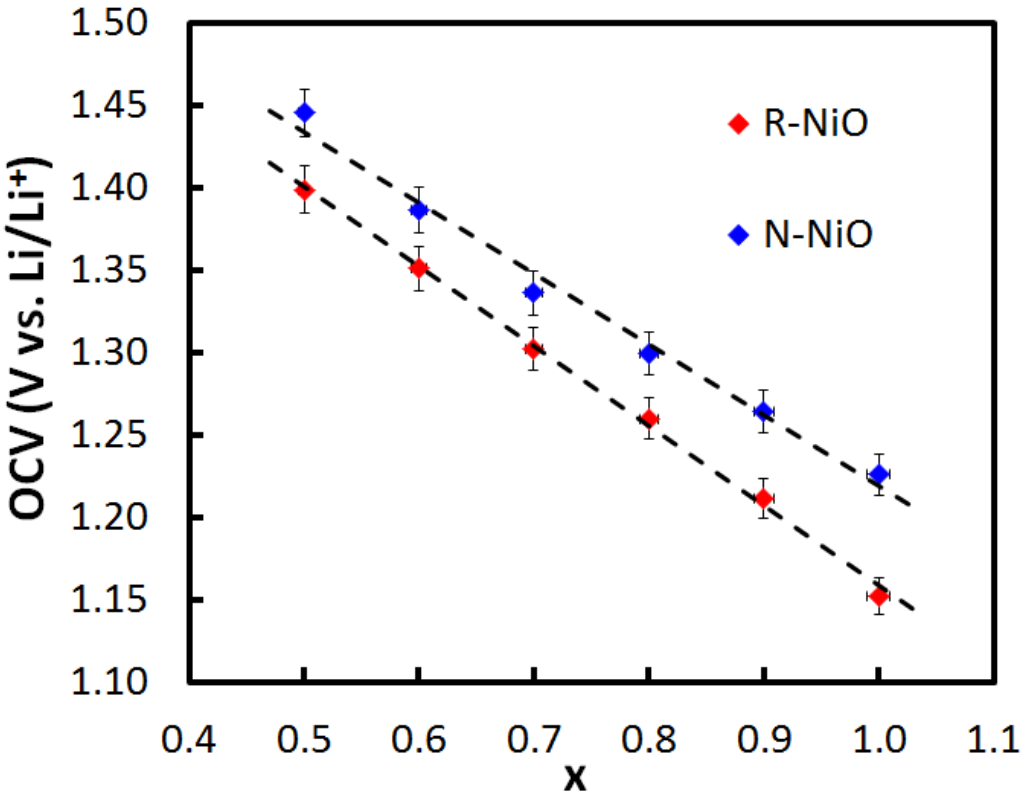

Figure 6.11. Plot of open-circuit voltage (OCV) vs. x for R-NiO and N-NiO.

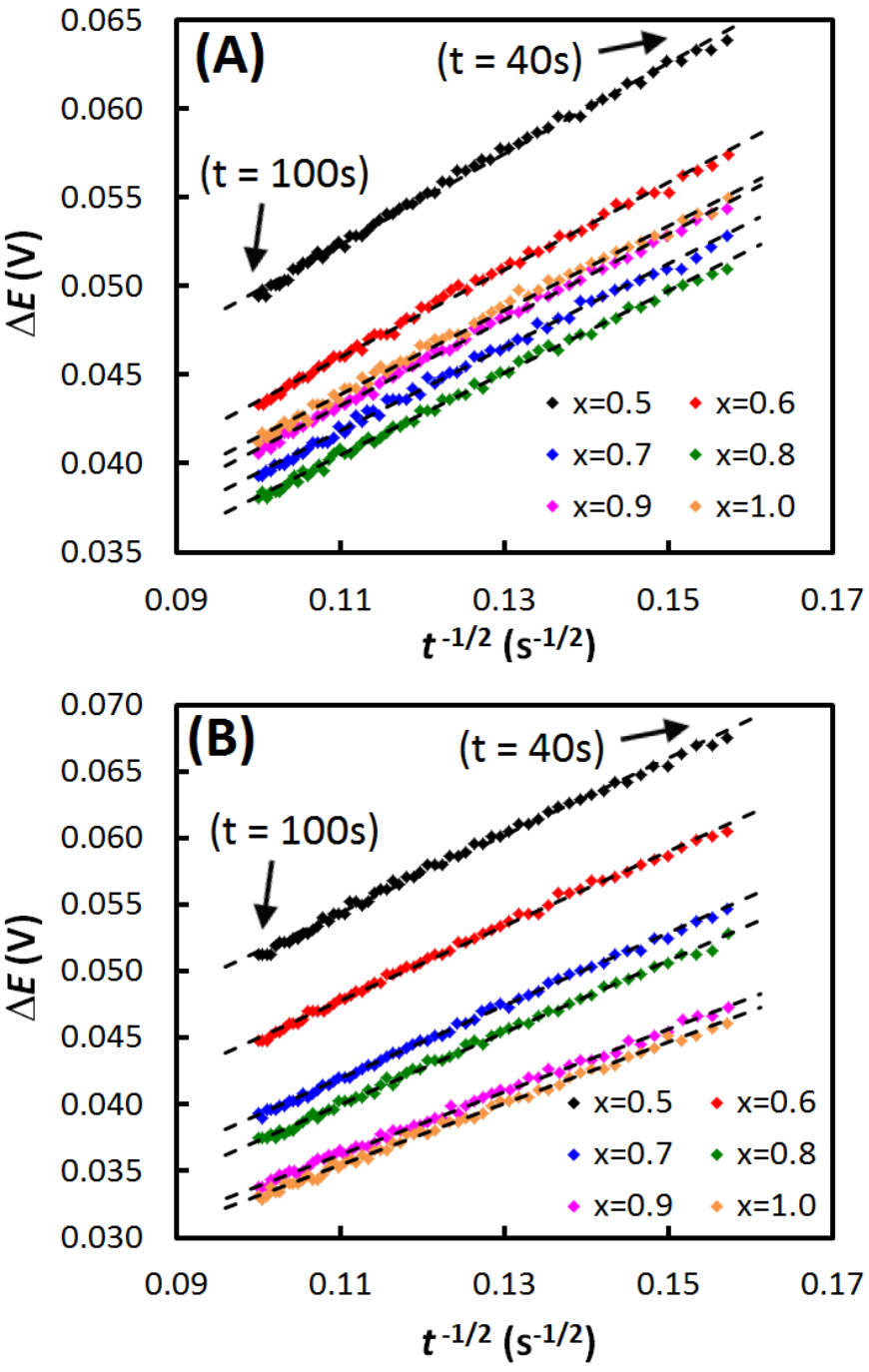

Figure 6.12. Plot of ΔE vs. $t^{-1/2}$ with linear fits used to calculate the Li^+ diffusion coefficients with the CPR method. Data shown for (A) R-NiO and (B) N-NiO anode for $0.5 \leq x \leq 1.0$ after a 1C rate current was pulsed for 5s.

Table 6.1. Effective diffusion coefficients, D_{eff}, calculated from Current Pulse Relaxation (CPR) data as a function of state of charge (SOC).

x	SOC	D_{eff} ($cm^2/s \times 10^{11}$)	
		R-NiO	N-NiO
0.5	0.25	3.580	7.522
0.6	0.30	3.859	8.048
0.7	0.35	4.242	8.502
0.8	0.40	4.356	8.737
0.9	0.45	3.985	11.515
1.0	0.50	4.135	11.957

6.2.3 Volume Expansion During Charging

The formation of Ni and Li_2O during battery charging results in volume expansion, and repeated charge/discharge cycles can cause particle pulverization that limits capacity retention [43,49,55]. Figure 6.9 illustrates this process using a spherical geometry for NiO particles. Assuming Eq. 6.1 takes place primarily at the electrode surface, the Li_2O+Ni layer will grow radially outward as NiO is consumed, progressively reducing the initial NiO particle radius (r_{NiO}). At any particular SOC, the expansion in length of the Li_2O+Ni phase ($r_{Li2O+Ni}$) can be expressed as a function of the portion of NiO that has reacted, Equation 6.27:

$$r_{Li2O+Ni} = K(r_{NiO} - r_{NiO,SOC}) \tag{6.27}$$

where $r_{NiO,SOC}$ is the NiO particle radius at any SOC and K is an expansion constant. At 100% SOC, all NiO will have reacted, meaning $r_{NiO,SOC}$ goes to zero and the equation can be simplified into an expression for K:

$$K = \frac{r_{Li2O+Ni}}{r_{NiO}} \tag{6.28}$$

Following the proposed spherical model, the volume of a NiO particle, V_{NiO}, can be calculated using Equation 6.29:

$$V_{NiO} = \frac{4}{3}\pi(r_{NiO})^3 \tag{6.29}$$

The number of atoms present in a NiO particle can be estimated by first approximating a characteristic cubic length, ℓ_{NiO}, with an equivalent volume to the value calculated in Eq. 6.29, shown in Equation 6.30:

$$\ell_{NiO} = r_{NiO}\left(\frac{4\pi}{3}\right)^{1/3} \tag{6.30}$$

Next, the number of atoms per length can be calculated by dividing ℓ_{NiO} by the NiO lattice parameter (LP_{NiO} = 4.181Å) [168]. Finally, cubing the number of atoms per length yields the total number of atoms in a NiO particle, N_{NiO}:

$$N_{NiO} = \left(\frac{\ell_{NiO}}{LP_{NiO}}\right)^3 \tag{6.31}$$

Combining Eqs. 6.30-6.31 in more general terms, the total number of atoms in any particle, N, can therefore be calculated more directly using Equation 6.32:

$$N = \frac{4}{3}\pi\left(\frac{r}{LP}\right)^3 \tag{6.32}$$

And rearranging Eq. 6.32 to obtain an expression for r_{NiO} yields

$$r_{NiO} = \left(\frac{3}{4\pi}N_{NiO}\right)^{1/3} LP_{NiO} \tag{6.33}$$

At 100% SOC, half of the original NiO atoms (which are Ni) will become metallic Ni, while the other half (O atoms) will form Li_2O. However, due to Li_2O's antifluorite structure and 2:1 ratio of Li:O, the number of O atoms must be

doubled when using the lattice parameter to calculate particle volume. Incorporating the lattice parameters for Ni (LP_{Ni} = 3.524Å) [169] and Li_2O (LP_{Li2O} = 4.620Å) [170], Equations 6.34-6.35 can be written to solve for the volumes of Ni, V_{Ni}, and Li_2O, V_{Li2O}, respectively:

$$V_{Ni} = 0.5N_{NiO}(LP_{Ni})^3 \tag{6.34}$$

$$V_{Li2O} = N_{NiO}(LP_{Li2O})^3 \tag{6.35}$$

Adding V_{Ni} and V_{Li2O} together gives the total volume of transformed particles, and following with the spherical geometry assumption, $r_{Li2O+Ni}$ can be determined via Equation 6.36:

$$r_{Li2O+Ni} = \left[\frac{3}{4\pi}(V_{Ni} + V_{Li2O})\right]^{1/3} \tag{6.36}$$

Substituting for V_{Ni} and V_{Li2O} with Eqs. 6.34-6.35, respectively, and factoring yields

$$r_{Li2O+Ni} = \left(\frac{3}{4\pi}N_{NiO}\right)^{1/3}[0.5(LP_{Ni})^3 + (LP_{Li2O})^3]^{1/3} \tag{6.37}$$

The expressions for r_{NiO} and $r_{Li2O+Ni}$ in Eqs. 6.33 and 6.37, respectively, are substituted into Eq. 6.28 to give the equation for calculating *K*, Equation 6.38:

$$K = \frac{[0.5(LP_{Ni})^3 + (LP_{Li2O})^3]^{1/3}}{LP_{NiO}} \tag{6.38}$$

Using the values for the lattice parameters gives a value for *K* of 1.18. This result suggests that the NiO particle radius expands by ca. 18% during complete charge to Li_2O and Ni, which is ca. a 65% increase in the volume.

Since the volume of NiO is linearly proportional to the SOC, the ratio of the NiO particle volume at any SOC, $V_{NiO,SOC}$, to its initial value, V_{NiO}, can be expressed with Equation 6.39:

$$\frac{V_{NiO,SOC}}{V_{NiO}} = 1 - \mathrm{SOC} = \left(\frac{r_{NiO,SOC}}{r_{NiO}}\right)^3 \tag{6.39}$$

Rearranging Eq. 6.39 into an expression for $r_{NiO,SOC}$ yields

$$r_{NiO,SOC} = r_{NiO}(1 - \mathrm{SOC})^{1/3} \tag{6.40}$$

The total particle radius at any time, r_{tot}, can be expressed as a sum of the lengths from both NiO and Li_2O+Ni phases, Equation 6.41:

$$r_{tot} = r_{NiO,SOC} + r_{Li2O+Ni} \tag{6.41}$$

Substituting Eq. 6.37 for $r_{Li2O+Ni}$ into Eq. 6.41 gives

$$r_{tot} = r_{NiO,SOC} + K\left(r_{NiO} - r_{NiO,SOC}\right) \tag{6.42}$$

Finally, replacing $r_{NiO,SOC}$ with Eq. 6.40 and factoring gives Equation 6.43:

$$r_{tot} = r_{NiO}\left[K + (1-K)(1-\mathrm{SOC})^{1/3}\right] \quad (6.43)$$

We have now obtained expressions for lengths of the NiO phase (Eq. 6.40), Li_2O+Ni phase (Eq. 6.37) and the total length (Eq. 6.43) as a function of the state of charge.

6.2.4 Li^+ Mass Transport

The nature of the CPR tests causes excess Li^+ to be drawn into the entire electrode structure during the current pulse. Therefore, after the current pulse, as the system relaxes back to OCV, the diffusion of Li^+ occurs throughout the entire particle simultaneously. In the system studied in this work, this means that the effective diffusion coefficient includes information from both the Li_2O+Ni and NiO phases, where diffusion of Li^+ occurs in both phases in parallel. Therefore, the total Li^+ mass transport resistance, ϕ_{tot}, at any SOC can be expressed as a parallel function of the mass transport resistances from the NiO ($\phi_{NiO,SOC}$) and Li_2O+Ni ($\phi_{Li2O+Ni}$) phases, Equation 6.44:

$$\frac{1}{\phi_{tot}} = \frac{1}{\phi_{NiO,SoC}} + \frac{1}{\phi_{Li2O+Ni}} \quad (6.44)$$

Generally, the mass transport resistance, ϕ_i, can be expressed using Equation 6.45 [81]:

$$\phi_i = \frac{RT}{n^2F^2Am_{Li}C} \tag{6.45}$$

where R is the ideal gas constant, T is the temperature, and m_{Li} is the mass-transfer coefficient, which is defined as:

$$m_{Li} = \frac{D_{Li}}{\ell} \tag{6.46}$$

where ℓ is the characteristic length. Combining Eqs. 6.44-6.46 and taking the individual radii as the characteristic lengths gives:

$$\frac{n^2F^2A_{tot}CD_{tot}}{RTr_{tot}} = \frac{n^2F^2A_{NiO,SOC}CD_{NiO}}{RTr_{NiO,SOC}} + \frac{n^2F^2A_{Li2O+Ni}CD_{Li2O+Ni}}{RTr_{Li2O+Ni}} \tag{6.47}$$

where D_{NiO} and $D_{Li2O+Ni}$ are the diffusion coefficients in each phase and D_{tot} is the effective diffusion coefficient measured by CPR (D_{eff}). Considering the surface area of a sphere is equal to $4\pi r^2$, simplification of Eq. 6.47 leads to the following expression:

$$r_{tot}D_{eff} = r_{NiO,SOC}D_{NiO} + r_{Li2O+Ni}D_{Li2O+Ni} \tag{6.48}$$

And dividing Eq. 6.48 by $r_{NiO,SOC}$ gives

$$\left(\frac{r_{tot}}{r_{NiO,SOC}}\right)D_{eff} = D_{NiO} + \left(\frac{r_{Li2O+Ni}}{r_{NiO,SOC}}\right)D_{Li2O+Ni} \tag{6.49}$$

Substituting the expressions for $r_{Li2O+Ni}$, $r_{NiO,SOC}$ and r_{tot} from Eqs. 6.37, 6.40 and

6.43, respectively, into Eq. 6.49 and simplifying yields

$$\left[K(1-\mathrm{SOC})^{-1/3}+1-K\right]D_{eff}=D_{NiO}+K\left[(1-\mathrm{SOC})^{-1/3}-1\right]D_{Li2O+Ni} \tag{6.50}$$

Eq. 6.50 shows that the effective Li^+ diffusion coefficient can be decoupled into individual diffusion coefficients for both the NiO and Li_2O+Ni phases. By determining values for D_{eff} at different SOCs via the CPR technique and plotting $\left[K(1-\mathrm{SOC})^{-1/3}+1-K\right]D_{eff}$ vs. $K\left[(1-\mathrm{SOC})^{-1/3}-1\right]$, we can determine $D_{Li2O+Ni}$ and D_{NiO} by linear regression. $D_{Li2O+Ni}$ will be equal to the slope and D_{NiO} to the y- intercept.

Plots of $\left[K(1-\mathrm{SOC})^{-1/3}+1-K\right]D_{eff}$ vs. $K\left[(1-\mathrm{SOC})^{-1/3}-1\right]$ were prepared for both R-NiO and N-NiO, Figure 6.13. In both cases, the plots were linear, as expected. Using the results of the parallel resistance model, D_{NiO} and $D_{Li2O+Ni}$ were obtained from the y-intercepts and slopes of the linear plots. For R-NiO, these values were found to be D_{NiO} = 3.49 ± 0.41 x 10^{-11} cm^2/s and $D_{Li2O+Ni}$ = 6.67 ± 1.92 x 10^{-11} cm^2/s; for N-NiO they were found to be D_{NiO} = 3.07 ± 1.18 x 10^{-11} cm^2/s and $D_{Li2O+Ni}$ = 40.47 ± 5.47 x 10^{-11} cm^2/s.

Uncertainties in calculated values were obtained using the NIST method for propagation of uncertainty [171]. For any value, *Y*, that is a function of any

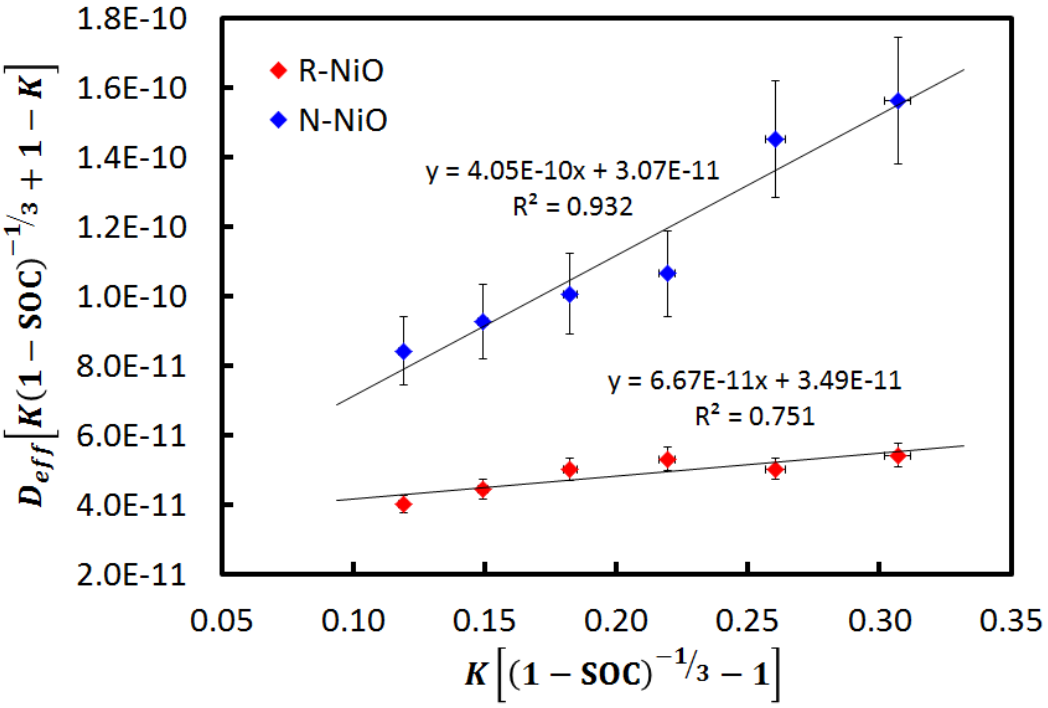

Figure 6.13. Plot with linear fits using mass transport diffusion model for calculating NiO and Li_2O+Ni phase diffusion coefficients for both R-NiO and N-NiO.

number of variables,

$$Y = f(X_1, X_2, X_3 \ldots) \tag{6.51}$$

the uncertainty in Y, ΔY, can be determined using the partial derivative technique, Equation 6.52:

$$\Delta Y = \sqrt{\left(\frac{\partial Y}{\partial X_1}\right)^2 (\Delta X_1)^2 + \left(\frac{\partial Y}{\partial X_2}\right)^2 (\Delta X_2)^2 + \left(\frac{\partial Y}{\partial X_3}\right)^2 (\Delta X_3)^2 + \cdots} \tag{6.52}$$

where ΔX_i are the relative uncertainties of each variable X_i. To calculate the uncertainties in diffusion coefficients calculated from CPR data, the terms in Eq. 6.26 present in the slope of ΔE vs. $1/t^{1/2}$ plots, m, can be rearranged into an expression for D_{eff}, Equation 6.53:

$$D_{eff} = \frac{1}{\pi}\left(\frac{(dOCV/dx)V_m i\tau}{AFm}\right)^2 \tag{6.53}$$

Applying Eq. 6.52 to Eq. 6.53 and factoring gives an expression for ΔD_{eff}, Equation 6.54:

$$\Delta D_{eff} = 2D_{eff}\sqrt{\left(\frac{\Delta(dOCV/dx)}{(dOCV/dx)}\right)^2 + \left(\frac{\Delta V_m}{V_m}\right)^2 + \left(\frac{\Delta i}{i}\right)^2 + \left(\frac{\Delta \tau}{\tau}\right)^2 + \left(\frac{\Delta A}{A}\right)^2 + \left(\frac{\Delta m}{m}\right)^2} \tag{6.54}$$

Error bars visible in Fig. 6.13 were calculated by applying Eq. 6.52 to the expressions for the *x*- and *y*-axes shown in Eq. 6.50:

$$\Delta x = \frac{K}{3}(1 - \mathrm{SOC})^{-4/3} \cdot \Delta\mathrm{SOC} \tag{6.55}$$

$$y = \sqrt{\left[K(1 - \mathrm{SOC})^{-1/3} + 1 - K\right]^2 \left(\Delta D_{eff}\right)^2 + \left[\frac{KD_{eff}}{3}(1 - \mathrm{SOC})^{-4/3}\right]^2 (\Delta\mathrm{SOC})^2} \tag{6.56}$$

Finally, the errors reported in the values for $D_{Li2O+Ni}$ and D_{NiO} were the standard errors of regression from the slopes and y-axis intercepts of the linear fits shown in Fig. 6.13.

Statistical analysis was performed using the F-observed values from the linear fits shown in Fig. 6.13. For R-NiO the F-observed value was 12.1 and for N-NiO it was 54.6. Using an assumed confidence level of 95% (or a 5% probability of incorrectly concluding that there is a correlation within the data), for the given degrees of freedom (four) the F critical value was 7.71. Since both F-observed values were greater than the F critical value, it can be concluded that there was a correlation within the data sets. Furthermore, using the F probability distributions for each F-observed value, the probability of correlation within the data sets for R-NiO and N-NiO were 97.5% and 99.8%, respectively; in other words, there was only a 2.5% chance for R-NiO and a 0.2% chance for N-NiO that the observed correlations occurred simply by chance

Extracting the diffusion coefficients for both the NiO and Li_2O+Ni phases

from D_{eff} revealed unique insight into the influence of the beginning NiO nanostructure on the diffusivity of the NiO and Li_2O+Ni phases that results from charging the cell. Firstly, the values for D_{NiO} for the R-NiO and N-NiO anodes were statistically equivalent. This shows that while structural differences were observed between R-NiO and N-NiO, they both consisted of dense, non-porous crystallites that were elementally identical (which was confirmed by N_2 isotherms shown in Fig. 6.2). On the other hand, $D_{Li2O+Ni}$ was strongly dependent on the initial NiO nanostructure: in fact, $D_{Li2O+Ni}$ for N-NiO was approximately 6 times greater than that of R-NiO, indicating more facile diffusion through the Li_2O+Ni phase for N-NiO than for R-NiO.

Fundamentally, the Li^+ diffusion coefficient can be correlated to the diffusional path length, δ, the charge transfer time per Li^+ ion, t, and the fraction of vacant sites in the active material lattice, α, via Equation 6.57:

$$t = \frac{\delta^2}{\alpha^2 D} \tag{6.57}$$

Considering the charge transfer time is inversely proportional to the diffusion coefficient, this partially explains the improved performance of N-NiO compared to R-NiO. Greater effective diffusion coefficients led to decreased charge transfer times, which facilitated the charge-discharge process and led to improved rate capability. The increased diffusion coefficients in the Li_2O+Ni phase for N-NiO

compared to R-NiO was also likely responsible for the better capacity retention by enabling quicker Li^+ ion access to active sites during discharge.

The difference in the diffusivity of the Li_2O+Ni phase between R-NiO and N-NiO electrodes was likely the result of two phenomena related to the Li_2O and Ni crystallites that formed during charging. First, XRD showed that for R-NiO, the average size of the Li_2O and Ni crystallites were larger, which led to longer path lengths for Li^+ ion transport and greater tortuosity, therefore decreasing the overall diffusivity compared to N-NiO. The smaller Ni and Li_2O particles that were present in N-NiO likely also helped maintain electronic conductivity throughout the anode during cycling, which led to improved electrode cyclability. Second, smaller grain boundary sizes observed for Li_2O and Ni in the N-NiO anode means there were more uncoordinated surface sites available for in-plane Li^+ transport. Since ionic transport along the grain boundary is more facile than the bulk crystal [172,173], N-NiO benefitted from having more exposed grain boundary area than R-NiO. These observations illustrate the distinct advantages of the spherical nanoparticle geometry of N-NiO compared to the blade-like, irregular geometries found with R-NiO, and also suggest that controlled, nanosized structures that maximize electronic connectivity are essential in metal oxide-based Li-ion anodes compared to bulk materials for improved capacity and cyclability [50,54,57].

6.3 Summary

A parallel resistance model was derived and applied to nickel oxide anodes during charge/discharge to deconvolute the contribution of two phases, NiO and Li_2O+Ni, in the multiphase electrode to the observed diffusivity. D_{NiO} was found to be independent of the initial geometry. However, the initial structure of the NiO played a significant role in $D_{Li2O+Ni}$. It was found that smaller, spherical NiO articles are advantageous over larger, blade-like NiO particles because they provide a less tortuous ionic pathway, larger grain boundary area that facilitates in-plane Li^+ ion transport, and improved interparticle electronic contact. The advantages of the smaller, more spherical nanostructure also manifested itself through less structural degradation during cycling, greater capacity retention and higher Faradaic efficiency.

6.4 Symbols and Nomenclature

A	Geometric area
B	Full width at half maximum intensity
BET	Brunauer-Emmett-Teller Analysis
C	Li^+ ion concentration
CPR	Current Pulse Relaxation

CV	Cyclic Voltammetry
D	Diffusion coefficient
DEC	Diethyl carbonate
DMC	Dimethyl carbonate
E	Voltage
EC	Ethylene carbonate
F	Faraday's constant
K	Expansion constant
LP	Lattice parameter
M	Total amount of substance per unit area
N	Total number of atoms
N-NiO	NaOH-precipitated nickel oxide
OCV	Open-circuit voltage
R	Universal gas constant
R-NiO	Reflux-precipitated nickel oxide
SEM	Scanning Electron Microscopy
SOC	State of charge
T	Temperature
V	Volume
V_m	Molar volume
XRD	X-ray Diffraction

b	y-intercept
d	Grain boundary size
i	Current
k	Scherrer Equation shape factor
ℓ	Characteristic length
m	Mass-transfer coefficient
n	Moles of electrons transferred
r	Radius
t	Time
x	Molar fraction of Li intercalated in anode
z	Position
α	Fraction of vacant sites in the active material lattice
δ	Diffusional path length
η	Integration constant
θ	Bragg angle
λ	X-ray wavelength
τ	Time (pulse duration)
ϕ	Mass transport resistance

CHAPTER 7: INVESTIGATION OF METAL OXIDE ANODE DEGRADATION IN LITHIUM-ION BATTERIES VIA IDENTICAL-LOCATION TEM

The purpose of this work was to connect the capacity retention and overall performance of NiO anodes in lithium-ion batteries to nanoscale structural degradation and electronic conductivity. Ordered mesoporous NiO was synthesized and used as an anode material with easily distinguishable nanosized features, and structural changes were observed for specific NiO particles before and after charge/discharge tests using identical-location transmission electron microscopy. These observations were analyzed in concert with coin cell test results using anodes of varying carbon black additive, and effects of electronic conductivity were discussed in addition to the NiO structure. The work presented in this chapter was accepted for publication in the *Journal of Materials Chemistry A* [174].

7.1 Experimental

7.1.1 OMNiO Synthesis

Ordered mesoporous nickel oxide (OMNiO) was fabricated using a template-based synthesis technique which is illustrated in Figure 7.1. First, a mesoporous silica template (SBA-15) was synthesized using a previously-published technique [175,176]. Briefly, Pluronic P123 (BASF) triblock copolymer was dissolved in a solution of HCl and deionized water (Millipore Direct-Q 3UV, 18.2 MΩ). After addition of tetraethyl orthosilicate and two separate heating stages (20h at 45°C and 24h at 100°C), the template was washed and filtered with ethanol and deionized water, followed by drying under vacuum and calcination in air at 500°C for 3h.

OMNiO was prepared using a wet impregnation method with the SBA-15 template. Aqueous 0.5M $Ni(NO_3)_2$ (Acros, 99%) was added dropwise to dry SBA-15 until a ratio of approximately 6.3 mL of 0.5M $Ni(NO_3)_2$ per g SBA-15 was achieved. The resulting gel was stirred manually until homogeneous, followed by calcination in air at 400°C for 3.5h. Template was then removed using two identical etching steps in hot (100°C) 5M KOH for 24h each, along with a thorough deionized water rinse in between. The OMNiO was then rinsed once more with copious deionized water and dried.

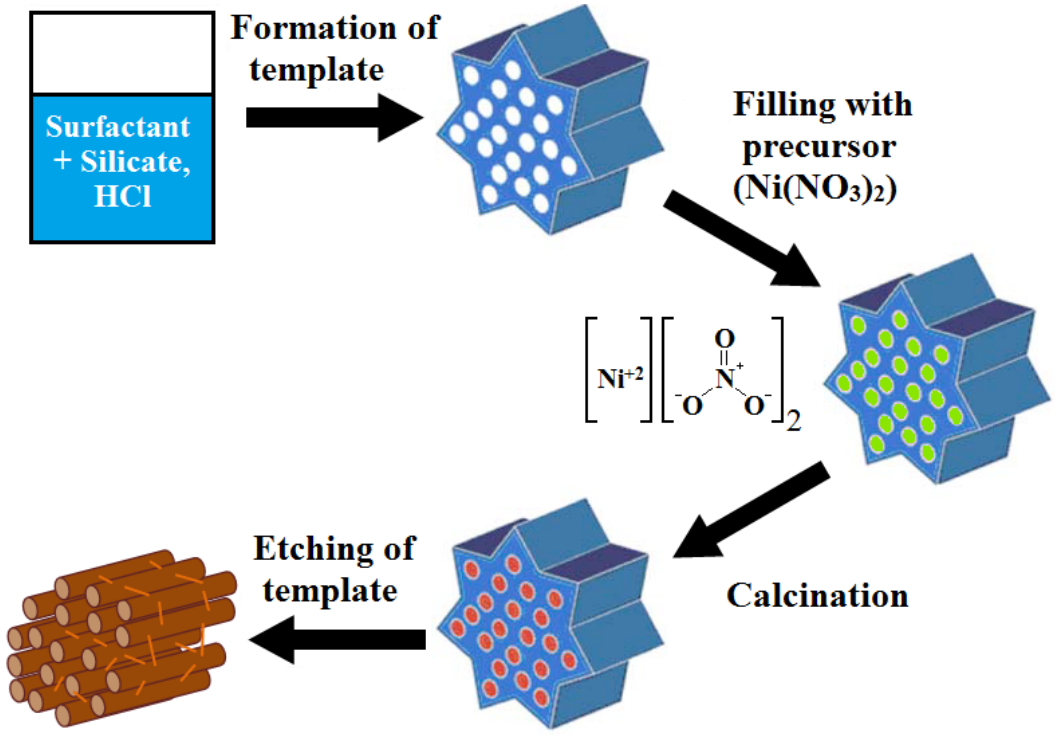

Figure 7.1. Schematic for synthesis of ordered mesoporous nickel oxide (OMNiO). Adapted from [175].

7.1.2 Anode Fabrication

Anodes were fabricated by preparing inks with varying amounts of OMNiO, carbon black (Vulcan XC-72R, Cabot), and polyvinylidene fluoride (PVDF) binder (Kynar blend) dispersed in N-methylpyrrolidone (NMP) solvent (Acros, 99.5% Extra Dry) through successive sonication and stirring steps until homogeneous. A copper foil (Alfa Aesar, 99.999%) was used as the current collector, and prior to ink deposition it was mechanically roughened and rinsed with isopropanol (Fisher, Optima). The ink was then sprayed onto the Cu foil to a uniform thickness, followed by heating under vacuum at 100°C for 24h. The electrode was then pressed at 1500 lbs and massed. Active loadings of anodes were around 0.5-2.0 mg/cm^2.

7.1.3 Coin Cell Fabrication

Batteries were tested using 2.0 cm diameter coin cells (Hohsen Corp.) with lithium metal (Alfa Aesar, 99.9%) as the cathode and Celgard 2320 trilayer PP/PE/PP as the separator. The electrolyte used for all tests was 1M lithium hexafluorophosphate ($LiPF_6$, Acros 98%) in a solution of (1:1:1) volume ratio ethylene carbonate (EC, Acros 99+%):dimethyl carbonate (DMC, Acros 98+%):diethyl carbonate (DEC, Acros 99%). 15 μL of electrolyte was applied to

each side of the separator, which was punched to a 1.9 cm diameter circle, while the anode and cathode were punched to 1.5 cm diameter coins. All coin cells were constructed inside an argon-purged glove box (Labconco).

7.1.4 Physical and Electrochemical Characterization

Coin cells were cycled using charge/discharge tests at a rate of C/5 (based on theoretical capacity of 718 mAh/g for NiO) between 0.001 – 3.0V vs. Li/Li^+ using an Arbin MSTAT battery test system. All other electrochemical tests were performed using an Autolab PGSTAT302N Potentiostat (Eco Chemie). Electrochemical Impedance Spectroscopy (EIS) was conducted between 100kHz – 50mHz with a 5mV amplitude at the coin cell open circuit voltage. Cyclic Voltammetry (CV) was performed between 0.001 – 3.0V at a scan rate of 0.1mV/s. Transmission Electron Microscopy (TEM) was conducted using a JEOL 2010 FasTEM. X-ray Diffraction (XRD) was performed using a Bruker D8 Advance X-ray Diffractometer with Cu $K\alpha_1$ radiation (λ = 0.154 nm). Brunauer-Emmett-Teller (BET) specific surface area analysis and N_2 adsorption isotherms were obtained using a Micromeritics ASAP 2020 system. Samples were degased under vacuum at 150°C for 16h prior to N_2 adsorption.

7.1.5 Identical-Location TEM Grid Experiments

For identical-location TEM (IL-TEM) experiments, a 3mm diameter copper TEM finder grid (Ted Pella, Inc., 100 mesh) was lightly sprayed with an OMNiO ink containing 10% PVDF binder and dried on a hot plate at 100°C. After initial TEM imaging, the Cu grid was cycled using a custom-built Teflon-shrouded copper electrode with a Teflon cap, which is pictured in Figure 7.2. The cap applied pressure to the grid to ensure contact with the Cu electrode and overall electronic conductivity, and also facilitated electrolyte access to the TEM grid via the tapered opening in the center. Inside the argon-purged glove box, the electrode/TEM grid setup was pressed into a strip of Celgard and lithium metal and dipped into a beaker containing (1:1:1)EC:DMC:DEC electrolyte. Two CVs were then performed between 0.001 – 3.0V at 0.1mV/s to cycle the OMNiO particles, and then the electrode/TEM grid setup was gently dried without rinsing to prevent excessive particle detachment. After a second stage of TEM imaging, five more CVs were performed followed by a final set of TEM images.

7.2 Results and Discussion

7.2.1 Physical Characterization

Figure 7.3 shows the XRD spectrum for OMNiO. Peak positions for NiO,

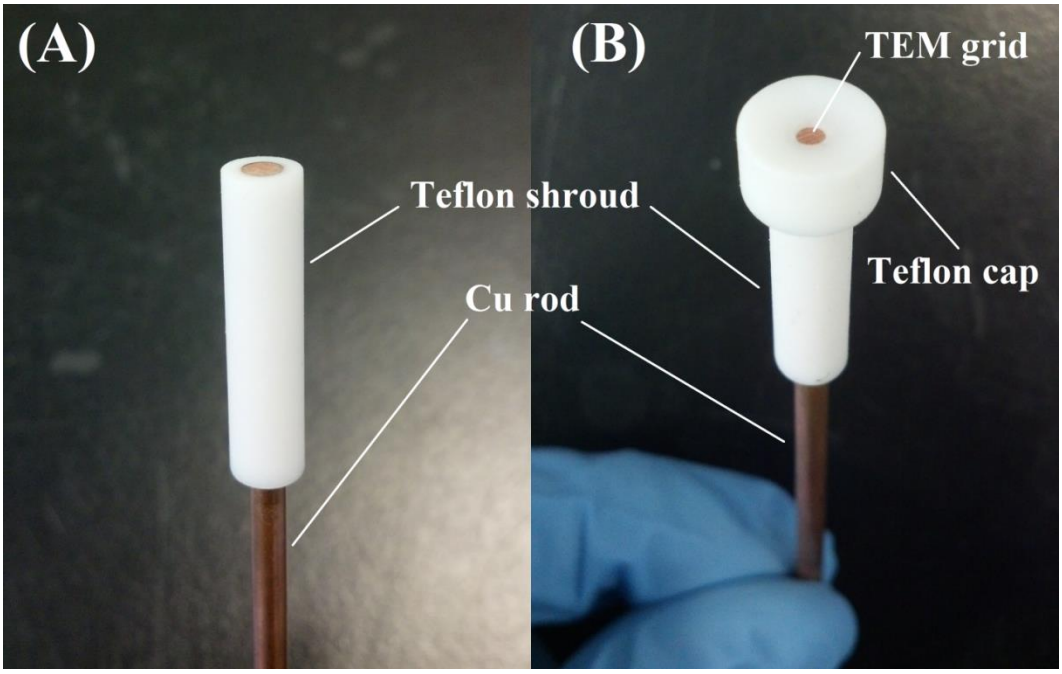

Figure 7.2. Pictures of (A) Teflon-shrouded copper rod electrode alone and (B) electrode with Teflon cap holding Cu TEM grid in place.

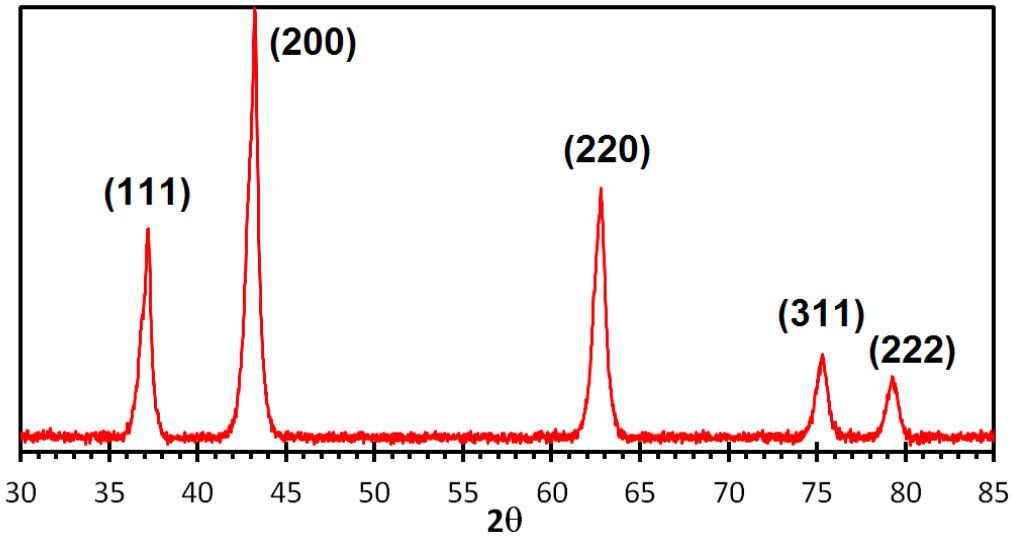

Figure 7.3. XRD spectrum for OMNiO. Acquisition rate was 1.3°/min.

along with corresponding crystal faces, were identified at 37.2° (111), 43.2° (200), 62.8° (220), 75.3° (311), and 79.3° (222) [107,128]. The Scherrer Equation was used to estimate the OMNiO average grain boundary size, Equation 7.1:

$$D = \frac{k\lambda}{\beta \cos\theta} \tag{7.1}$$

where D is the grain boundary size, k is the shape factor (taken as 0.89), λ is the X-ray wavelength, β is the peak width at half the maximum, and θ is the Bragg angle. Applying Eq. 7.1 to the first three peaks, the average grain boundary size was 18.5nm.

N_2 adsorption isotherm and pore size distribution data for OMNiO are shown in Figure 7.4. The BET specific surface area (obtained from the monolayer adsorption region between values of P/P_o of 0.05 to 0.2) was 80.4 m^2/g, and along with the Scherrer Equation average grain boundary size, these values were comparable to those found in the literature for similar template-based NiO nanoparticles [57,177,178]. The isotherm seen in Fig. 7.4A exhibited type IV behavior with a hysteresis loop at higher relative pressures, which resulted from capillary condensation in mesopores [156,175]. The extension of the hysteresis loop to relative pressures of around 0.7 – 0.75 indicated a varying range of mesopore sizes, which was also confirmed by the pore size distribution seen in

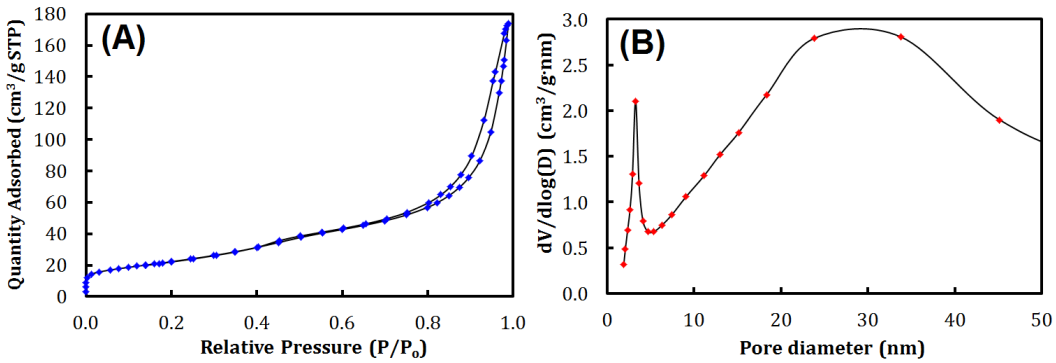

Figure 7.4. (A) N_2 adsorption isotherm and (B) pore size distribution for OMNiO.

Fig. 7.4B [156,175]. A bimodal distribution was observed with a sharp peak around 3.3nm and a broad peak around 25-35nm. This likely occurred due to partial expulsion of $Ni(NO_3)_2$ from the SBA-15 template via melting/redistribution during calcination, resulting in larger, agglomerated NiO particles that crystallized outside the template walls [179]. This may also explain the small discrepancy between apparent nanoparticle sizes observed in TEM images (ca. 8-10nm) and the larger average grain boundary size calculated from the Scherrer Equation (18.5nm).

7.2.2 Charge/Discharge Coin Cell Analysis

OMNiO anode coin cell lithium-ion batteries (LIBs) were fabricated and exposed to charge/discharge cycles at a C/5 rate. As shown in Figure 7.5A, the capacity retention for these cells was very poor; the capacity faded rapidly to under 50 mAh/g after just 20 cycles, and even faded below the theoretical capacity for graphite (372 mAh/g) after only 8 cycles. To test the influence of the conductivity on the capacity retention of MO anodes, additional coin cells were made with 10% and 40% carbon black added to the OMNiO, and charge/discharge cycles at a C/5 rate are shown in Fig. 7.5B and C, respectively, along with capacities listed as a function of cycle number for all three anodes shown in Fig. 7.5D. Over 70 cycles, the addition of 10% carbon improved

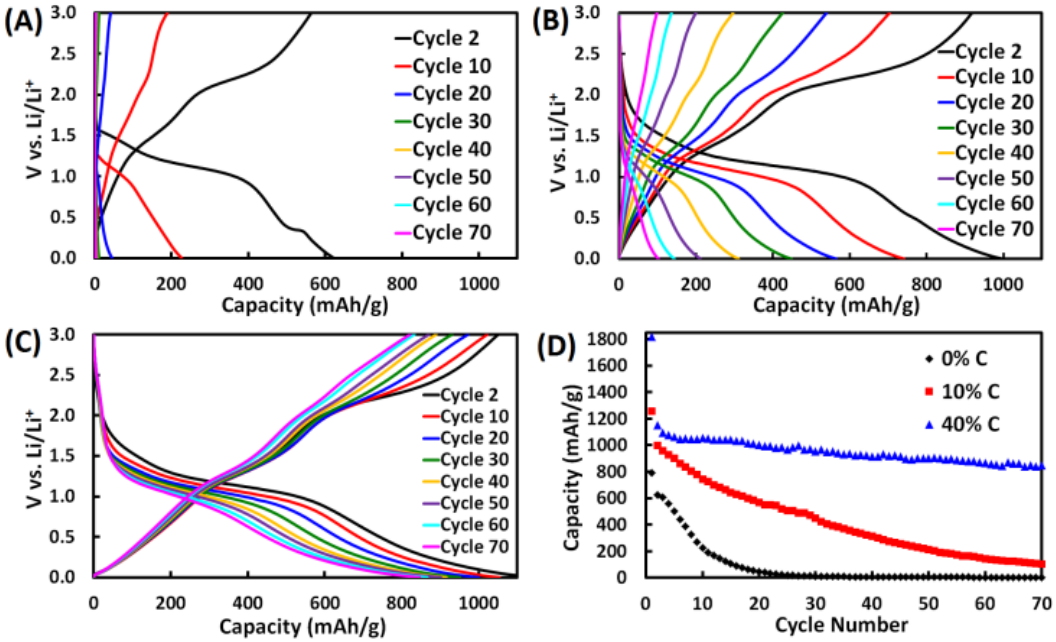

Figure 7.5. Charge/discharge curves for OMNiO anodes with (A) 0%, (B) 10%, and (C) 40% carbon black added. (D) shows C/5 capacity retention vs. cycle number.

capacity retention, and with 40% carbon the capacity fade drastically reduced, maintaining a reversible capacity of 847 mAh/g.

The inflated capacity compared to the theoretical value for NiO, 718 mAh/g, was caused by secondary Li storage in the SEI and the high surface area carbon. Figure 7.6 shows charge/discharge curves for the carbon black conductive additive as an anode by itself (with 10% PVDF binder). No voltage plateau was observed, which was expected, and this suggested a lack of Li^+ intercalation into the carbon structure. However, sloping curves repeatedly reaching about 200 mAh/g likely resulted from electrolyte decomposition and SEI formation over the high surface area carbon, creating secondary Li^+ storage sites and accounting for the boost in OMNiO capacity above the theoretical value observed in anodes containing 40% carbon (Fig. 7.5C-D) [180,181]. Therefore, it was likely the lack of electronic conductivity in the anode that led to the capacity fade. Additionally, these results may explain the high capacity and good retention reported for some other NiO electrodes where the electrodes either contained a large percentage of carbon or else had a low loading such that the current collector carried the majority of the charge, rather than the active material, artificially maintaining the electronic conductivity even after phase segregation [46,57].

With increasing cycle number, the change in the initial NiO nanostructure

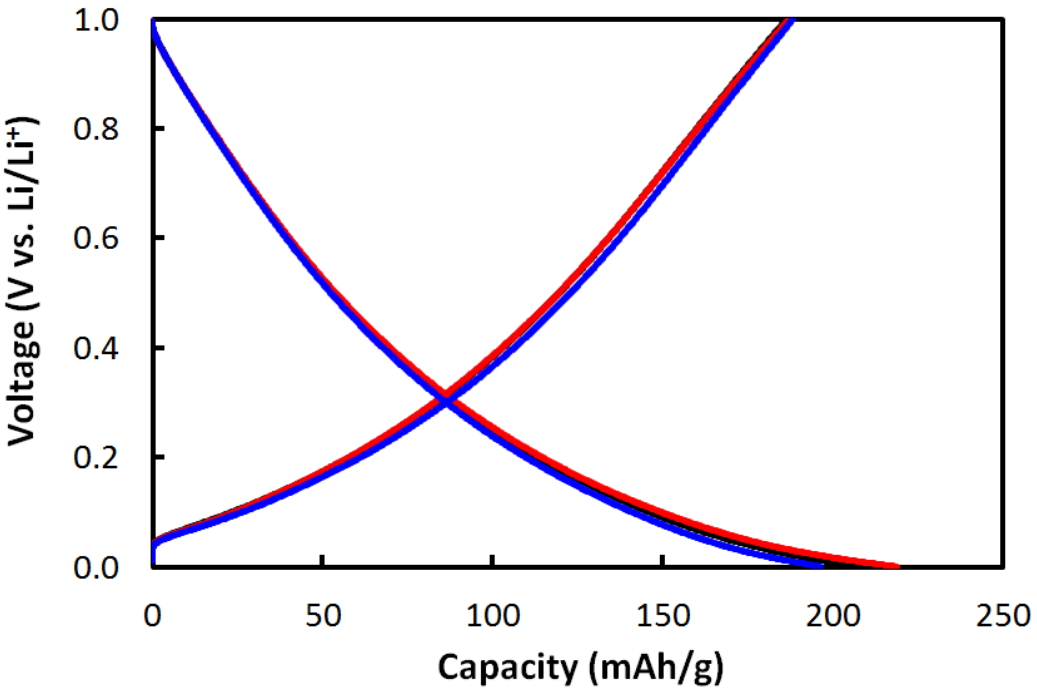

Figure 7.6. Charge/discharge curves for plain carbon black anode with 10% binder at C/5 rate.

is met with an increase in the length of the Ni and non-conducting Li_2O phases, so much so that after prolonged cycling, the Ni phase can be detected by bulk techniques like X-ray Diffraction [155]. The formation of the Ni and Li_2O phases occurred via the decomposition charge/discharge reaction for NiO, Equation 7.2 [45,46,49,53-55,155]:

$$NiO + 2Li^+ + 2e^- \leftrightarrow Ni + Li_2O \quad (7.2)$$

Figure 7.7 shows XRD spectra for NiO electrodes before and after 100 charge/discharge cycles [107,155]. Before cycling, clear peaks for NiO were identified at 37.2° (111), 42.9° (200), and 62.9° (220) [107], and for the Cu current collector at 42.9° (111), 50.4° (200) and 74.1° (220) [161]. However, after cycling, the peaks for NiO were absent, and instead a low, broad peak around 44.5° was visible and corresponded to the (111) crystal face for metallic Ni [162]. This showed that the NiO became essentially "stuck" in the charged state, likely resulting from large, inactive Li_2O growth from NiO decomposition [38]. Electronically-inactive Li_2O formed from NiO decomposition, thus connecting structural degradation to capacity loss; however, the root cause can be tied to the lack of conductivity of Li_2O, which was corroborated by the retention in capacity shown in Fig. 7.5 for anodes with increased carbon black.

The importance of conductivity can be examined in light of the individual electronic conductivities of each species as well. NiO as a bulk-phase crystal has

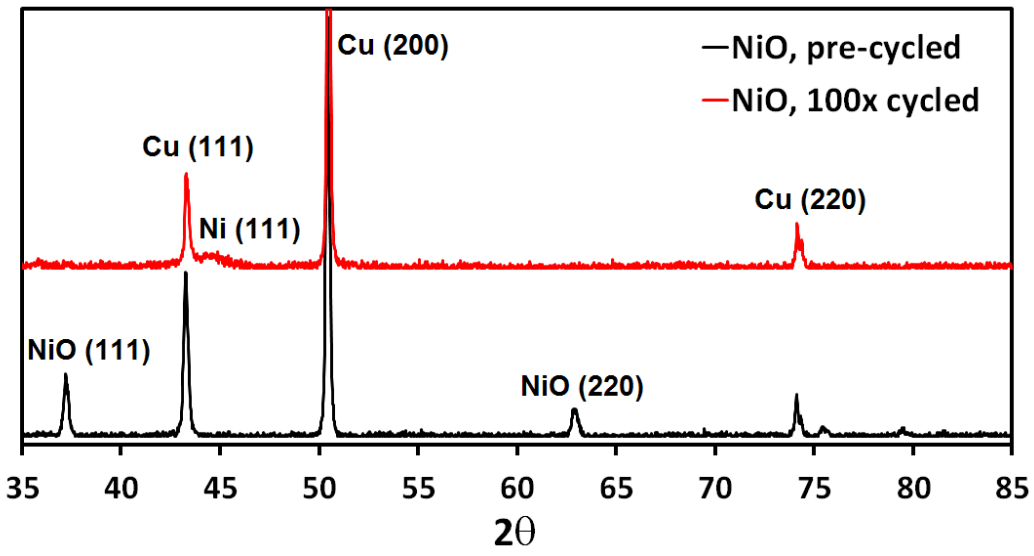

Figure 7.7. XRD spectra for NiO on Cu foil anode before and after 100 charge/discharge tests at C/5 rate. Acquisition rate was 1.3°/min.

been reported to possess an electronic conductivity as low as 0.01 mS/cm, however as a nanostructured powder or thin-film its conductivity can be as high as about 200 mS/cm [182,183]. Therefore, for the NiO fabricated in this study, it is likely that the conductivity was closer to the upper limit rather than the value for bulk-phase crystals. While the conductivity of pure Ni metal is very high, around 1 x 10^5 S/cm [184], Li_2O is an electronic insulator [32] and is likely responsible for the majority of the conductivity loss. Therefore, during repeated charge-discharge cycling, as the Li_2O domain size grows too large, phase separation occurs and limits the interfacial area between Li_2O and Ni which prevents further discharge, decreases overall conductivity, and causes the anode to become "stuck" in the charged state. The addition of carbon black (Vulcan XC-72R), which has a conductivity of 4 S/cm [185] (at least one order of magnitude greater conductivity than NiO), improved the OMNiO capacity retention dramatically by imparting electronic conductivity to insulating Li_2O particles and also acting as a buffer for volume expansion during charge-discharge [55].

Another aspect of increased conductivity that improved the capacity retention was the enhancement of the electron mobility. Equation 7.3 shows the fundamental relationship between conductivity and electron mobility [186]:

$$\sigma = pe\mu \tag{7.3}$$

where σ is the conductivity, p is the density of holes for a p-type semiconductor, e

is the elementary charge, and μ is the electron mobility. Therefore, since the electron mobility is directly proportional to the electronic conductivity, by enhancing electrode conductivity through the addition of carbon black, the electron mobility also increased, further enabling better electron transport to active sites during charge-discharge and resulting in better cyclability.

7.2.3 Identical-Location TEM

OMNiO was an ideal material for this study since it functioned as a suitable LIB anode while possessing a well-defined mesoporous structure that could be conveniently imaged using TEM. Using IL-TEM [187-189], the root cause for capacity loss was linked directly to structural changes during cycling before and after two separate stages of charge/discharge. OMNiO was deposited onto a Cu TEM grid, and Figure 7.8A-B shows a schematic of the experimental setup for cycling the OMNiO-coated TEM grid electrode. Fig. 7.8C-F and Figure 7.9 show the progression of TEM images for identical-location spots. After taking initial TEM images, the OMNiO-coated electrode was cycled twice, imaged, and then cycled five more times and imaged again. Figure 7.10A-B and Figure 7.11A-B show the structural time progression for the spots indicated in Fig. 7.8E-F and Fig. 7.9A-B, respectively. Before cycling, the ordered mesoporous structure was clearly visible with 8-10nm diameter nanorods. After

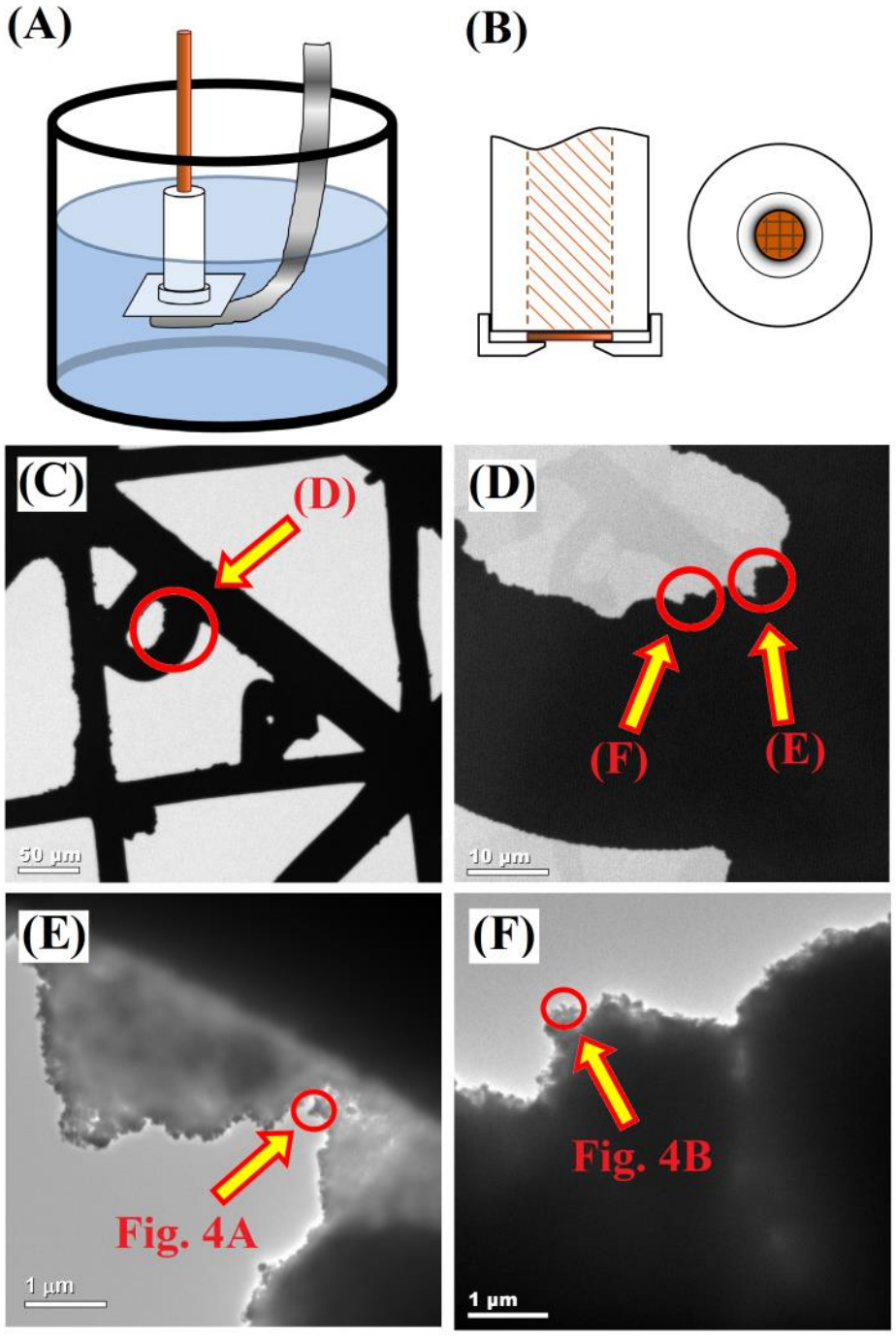

Figure 7.8. Experimental setup for IL-TEM grid cycling is illustrated in (A) and (B). (C) through (F) show progression of TEM grid spots for identical-location images.

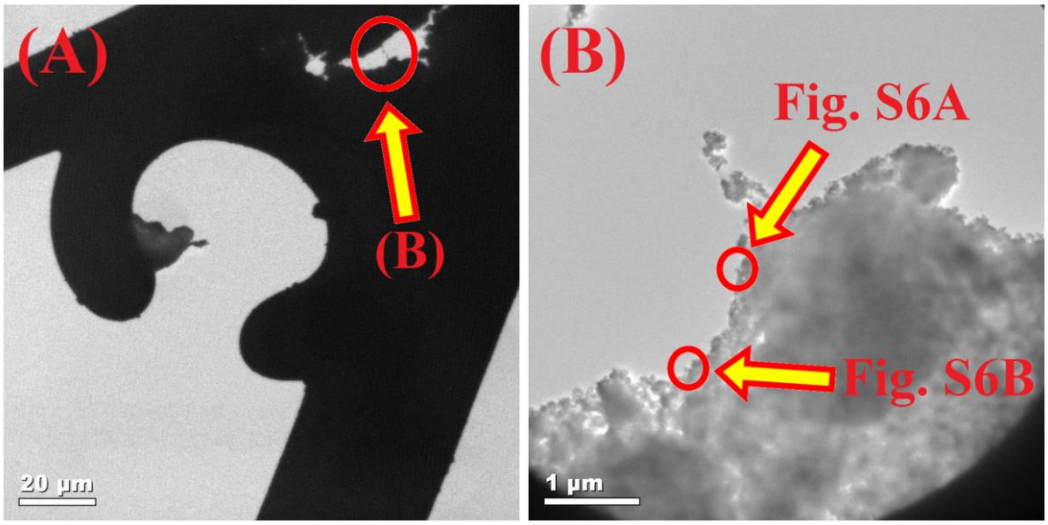

Figure 7.9. Progression of spots for IL-TEM images for OMNiO.

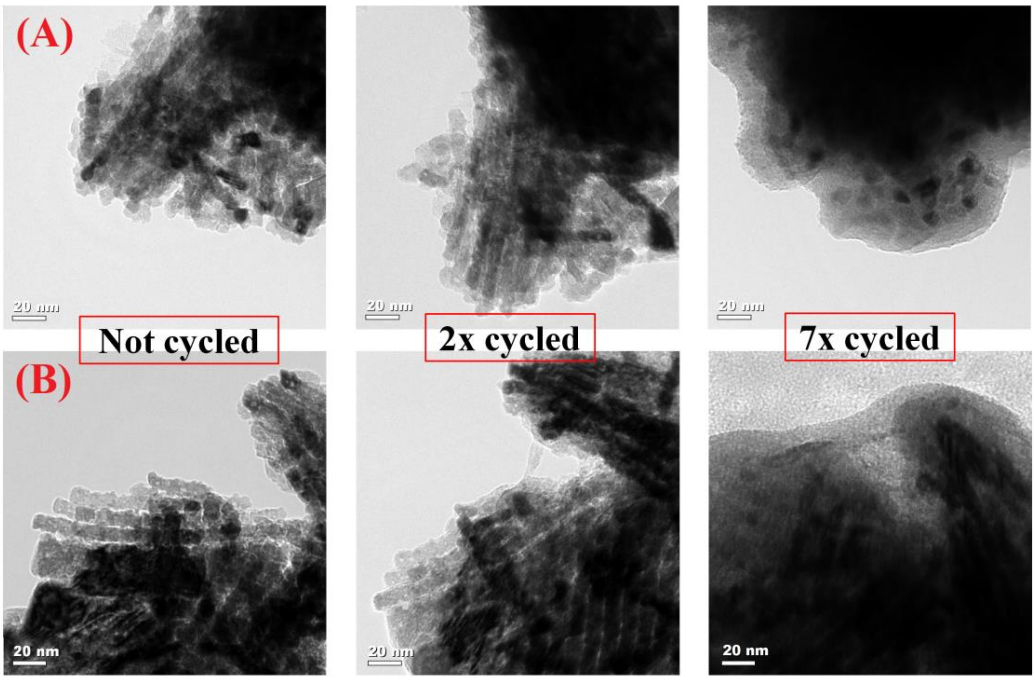

Figure 7.10. IL-TEM images for OMNiO on a Cu TEM grid before cycling, after two cycles, and after seven total cycles. Cyclic Voltammetry was performed at 0.1mV/s between 0.001-3V vs. Li/Li^+, in a 1M $LiPF_6$ in (1:1:1) EC:DMC:DEC electrolyte.

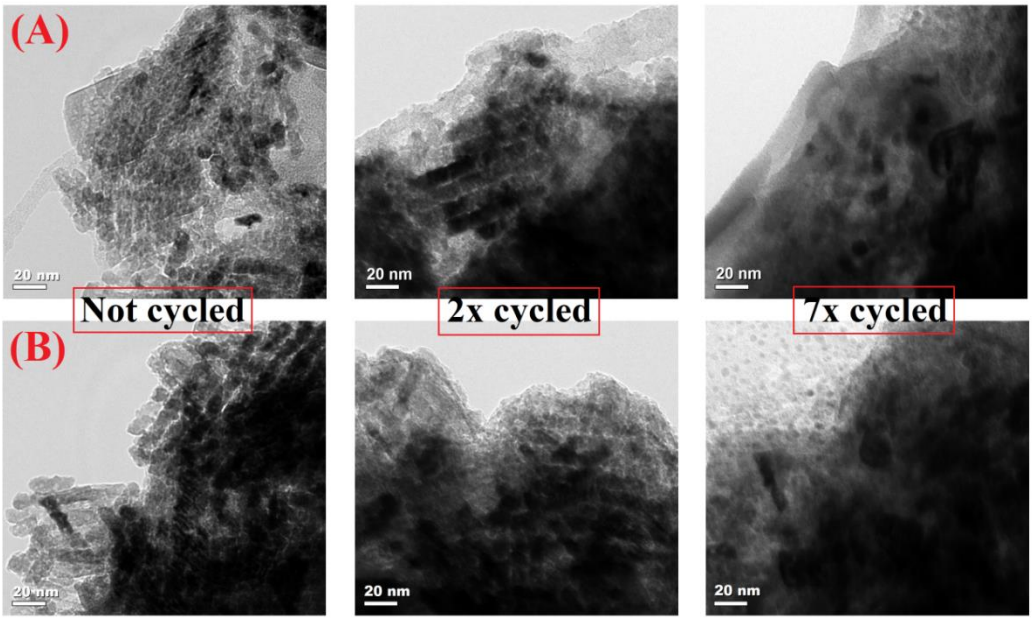

Figure 7.11. IL-TEM images for OMNiO on a Cu TEM grid. Images obtained before cycling, after two cycles, and after seven total cycles at 0.1mV/s between 0.001-3.0V.

two cycles the OMNiO structure was still visible, though a thin overlayer was also apparent, which was likely the solid-electrolyte interphase (SEI). The retention in the OMNiO structure after two cycles matches well with the cycling data in Fig. 7.5A, where the capacity of OMNiO was still close to its theoretical value. However, after five more cycles (seven total) the ordered mesoporous structure was either barely visible or altogether absent, which was mirrored in the coin cell tests with a catastrophic loss in the capacity.

IL-TEM images were also taken for OMNiO with 40% carbon black and Figure 7.12 shows the progression of spots used for identical-location TEM images for OMNiO with 40% carbon black. The corresponding TEM images before and after two cycles are shown in Figure 7.13. Surprisingly, after only two cycles the ordered mesoporous structure was completely absent, compared to the plain OMNiO which largely retained its structure through two cycles, only showing dramatic structural degradation after seven cycles. This result was in stark contrast to the superior capacity retention observed in Fig. 7.5C-D, and suggests that structure alone may not be the only contributor to performance losses. The presence of 40% carbon black likely improved overall conductivity enough to ensure cyclability even after almost complete degradation of the original OMNiO mesoporous structure. This provides further evidence for the importance of electronic conductivity in the performance of MO anodes in LIBs.

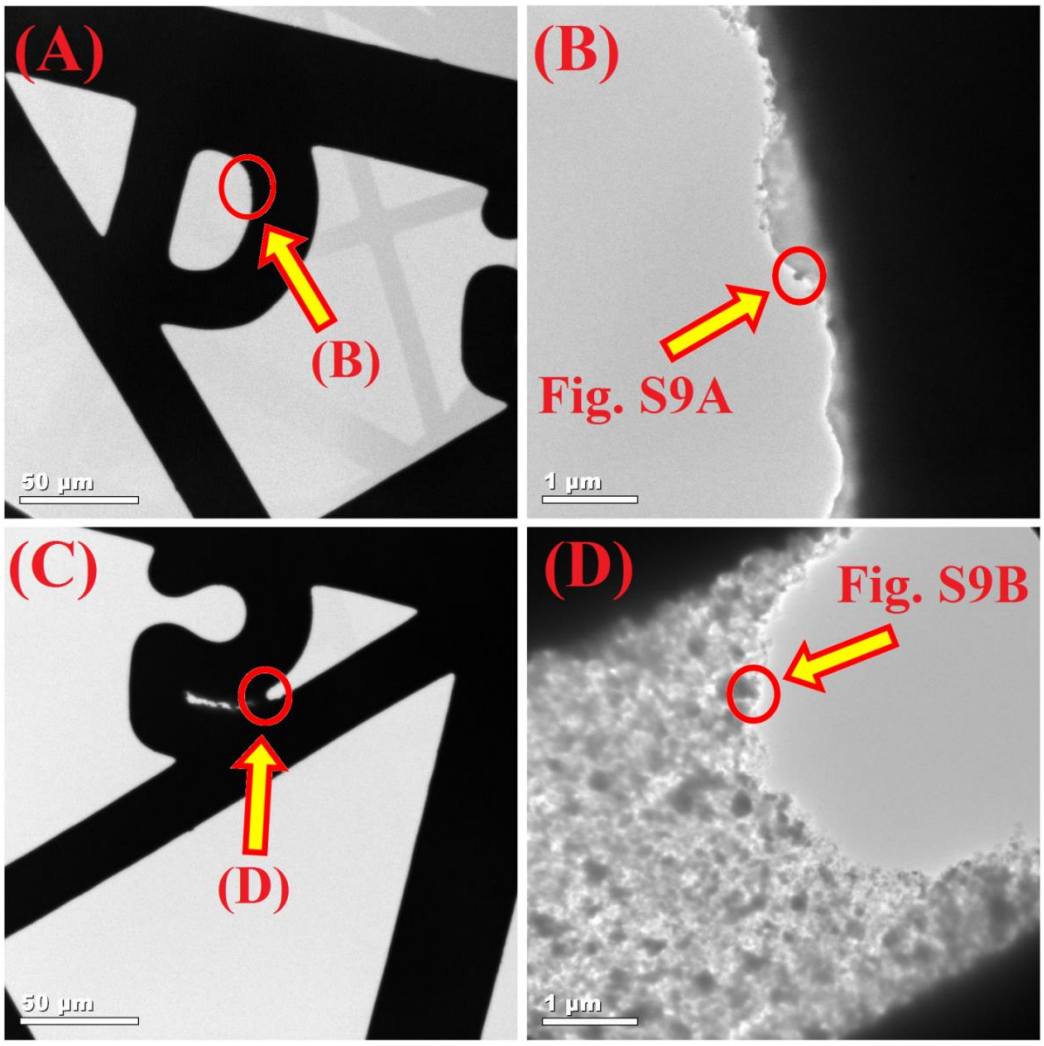

Figure 7.12. Progression of spots for IL-TEM images for OMNiO with 40% carbon black.

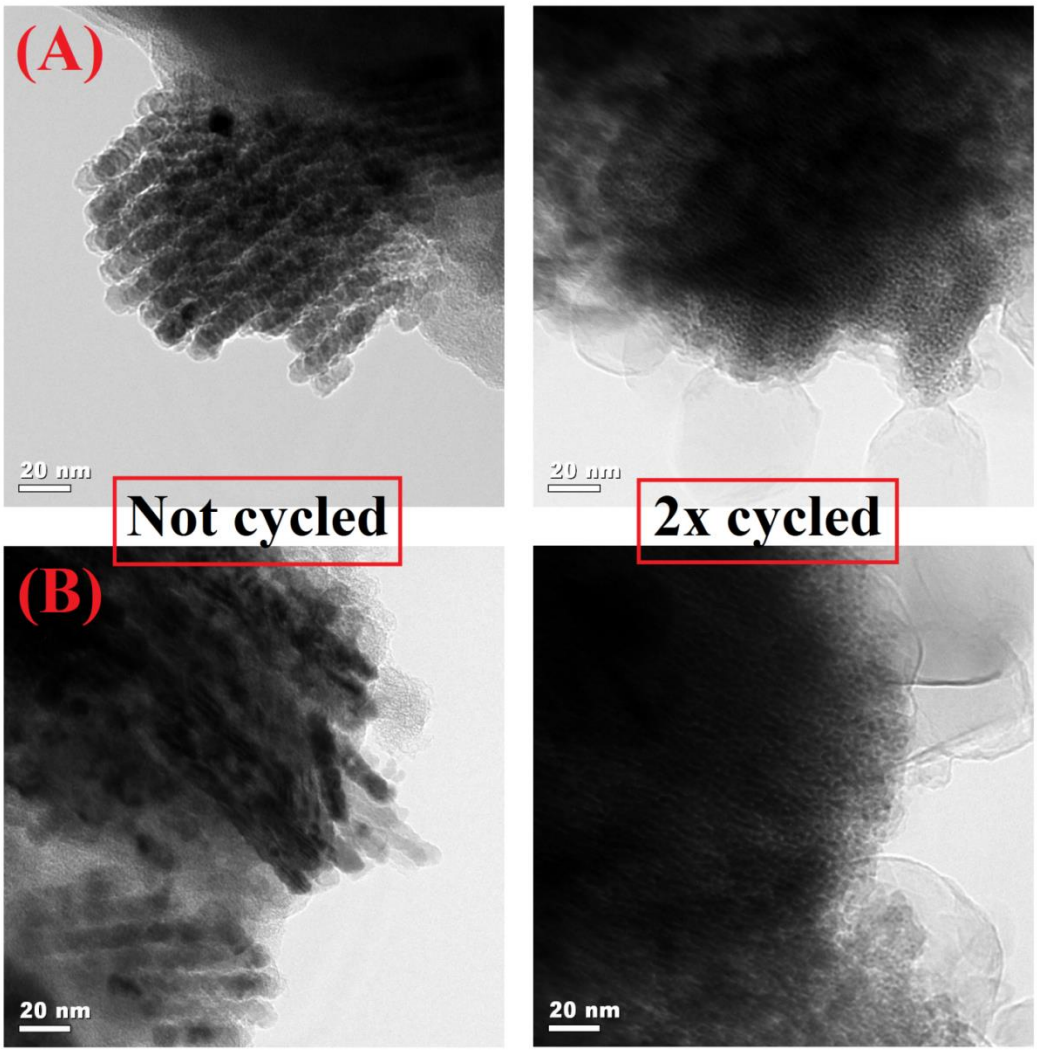

Figure 7.13. IL-TEM images for OMNiO with 40% carbon black on a Cu TEM grid. Images obtained before cycling and after two cycles at 0.1mV/s between 0.001-3.0V.

7.2.4 Electrochemical Impedance Spectroscopy

EIS was performed on OMNiO coin cells with varying amounts of carbon black added, and the corresponding Nyquist plots are shown in Figure 7.14. Several conclusions can be drawn from the data shown in Fig. 7.14: the leftmost, high frequency Zr (x-axis) intercept corresponded to the Ohmic resistance of the electrolyte; the semicircle(s) at medium frequencies corresponded to the charge transfer resistances of the SEI film and/or Li^+ transport at the electrode/electrolyte interface; and the inclined line at low frequency corresponded to the Warburg impedance of Li^+ ion diffusion in the electrode [190,191]. For all anodes, the electrolyte resistance observed was virtually negligible. Two distinct semicircles could be fitted to all anodes, and the widths of these can be attributed to the SEI and Li^+ charge-transfer resistances, respectively [190,191]. The widths of the first semicircle for 0%, 10% and 40% were found to be 188Ω, 52Ω and 21Ω, respectively, and the widths of the second semicircle for 0%, 10% and 40% were found to be 293Ω, 72Ω and 41Ω, respectively. This clear trend of decreasing charge transfer resistances for both the SEI and Li^+ transport as the carbon black percentage increased corresponded to the increase in overall conductivity in the anode.

The second distinct trend observed in Fig. 7.14 was in the low frequency Warburg impedance region. The angle of the inclined line was approximately 45°

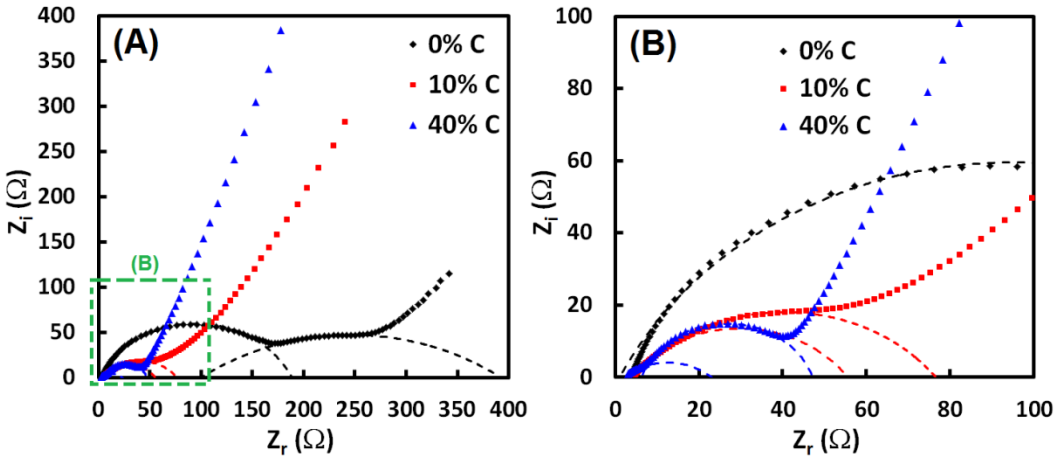

Figure 7.14. EIS Nyquist plots for OMNiO anode coin cells with 0%, 10% and 40% carbon black. (B) shows green boxed section zoomed in. Batteries were cycled three times each at a 1C charge/discharge rate, and then allowed to rest several hours until a stable voltage was reached before conducting impedance tests. EIS was taken at the battery's open circuit voltage between frequencies of 100kHz – 50mHz with a 5mV voltage amplitude.

for the 0% carbon anode; however, the slope increased to around 61° for the 10% carbon anode and to 71° for the 40% carbon anode. The increase in angle of the Warburg impedance region can be attributed to a diffusion process in a porous layer that is approaching pure capacitive behavior (which is represented by a vertical line) [192,193]. This may suggest that in addition to better conductivity and reduced charge transfer resistance, increasing the carbon percentage in the anode also improved the Li^+ diffusion via the pore structure of the carbon black additive [194].

7.3 Summary

Metal oxides are a promising category of materials which could potentially replace graphite as the anode in lithium-ion batteries. They offer high capacity, are inexpensive, and easily-synthesized. However, they suffer from capacity fade during repeated charge/discharge tests that could hinder their commercialization. In this work, we show that structural degradation, observed through IL-TEM and XRD results, along with a loss of electronic conductivity, are responsible for capacity fading, with the conductivity playing the pivotal role. This was evidenced by greater capacity retention, higher overall capacities, decreased charge transfer resistances, and improved porous layer Li^+ diffusion observed with an increased carbon black percentage, despite the accelerated

structural degradation seen with 40% carbon black. The remaining challenge is to engineer new battery architectures that decouple these two effects to yield high capacity, high rate, high stability LIBs for emerging technologies like (hybrid) electric vehicles and grid-scale energy storage. Additionally, the usefulness of IL-TEM in being able to view structural degradation on the nanoscale may lead to greater developments in LIB anode technology for future applications.

SECTION IV:

OUTREACH ACTIVITIES

CHAPTER 8: UCONN NSF GK-12 PROGRAM

For two years, I was privileged to be a recipient of the National Science Foundation's Graduate STEM (Science, Technology, Engineering and Mathematics) Fellows in K-12 Education (GK-12) Fellowship (See Figure 8.1 for photograph of GK-12 Fellows and Teachers). As a GK-12 Fellow, I partnered with Mr. John Hoyle and Mr. Fred Huhn at Howell Cheney Technical High School in Manchester, CT and mentored to students in grades 9-12 on topics relating to STEM. Working primarily in the Computer-Aided Drafting and Design (CADD) shop, I engaged students with fun and exciting projects and demonstrations, including speaking on the importance of higher education and encouraging college applications for juniors and seniors.

One of the first projects I initiated at Cheney Tech. was an egg drop survival competition for new freshmen in their exploratory phase, which is a period of time where freshmen have the opportunity to visit several technology shops (such as CADD, Automotive, Manufacturing, Culinary, and Carpentry) to "try them out" and discover which one they would like to pursue permanently during their high school career. To entice students into the CADD shop, they were tasked with designing and building devices that would prevent an uncooked egg from breaking after being dropped from increasing heights. The students

Figure 8.1. Photograph of UConn NSF GK-12 Fellows and Teachers. Notable people: 1st row, first person on the left – Aida Ghiaei, GK-12 Program Manager; 2nd row, first person on the left – Doug Cooper, GK-12 PI; 1st row, second person from the right – myself; 2nd row, fifth person from the right – Mr. John Hoyle, CADD Teacher at Howell Cheney Technical High School in Manchester, CT.

were given limited resources and time, and the teams with the eggs that survived the longest were awarded a small prize (see Figure 8.2 for photograph of students building their egg drop device).

For the second phase of the freshman exploratory period, I created a bottle rocket activity where students were again given limited resources and time, and were told to transform a 2L soda bottle into an aerodynamic bottle rocket. Students then designed and fabricated (with help from the Manufacturing Shop) a platform and mechanism for pressurizing the bottles with compressed air using an in-house compressor, followed by the subsequent release and launch (see Figure 8.3 for photo and diagram of the custom-built and designed platform). Creativity was on display as many different fins, wings, and even parachutes were constructed and fitted to the bottle rockets, and using the athletic field behind the school students were able to watch their rockets soar high into the air.

Seniors in the CADD shop participated in a zipline bomber competition, and took a field trip to Lake Compounce Amusement Park in Bristol, CT to test their devices against students from around the state (see Figure 8.4). They designed contraptions that would slide along a zipline and release a small weight after a certain distance traveled along the zipline. The parameters for the mass of the weight and distance traveled before dropping were specified on the day of the competition. I aided the students with designing of their devices and

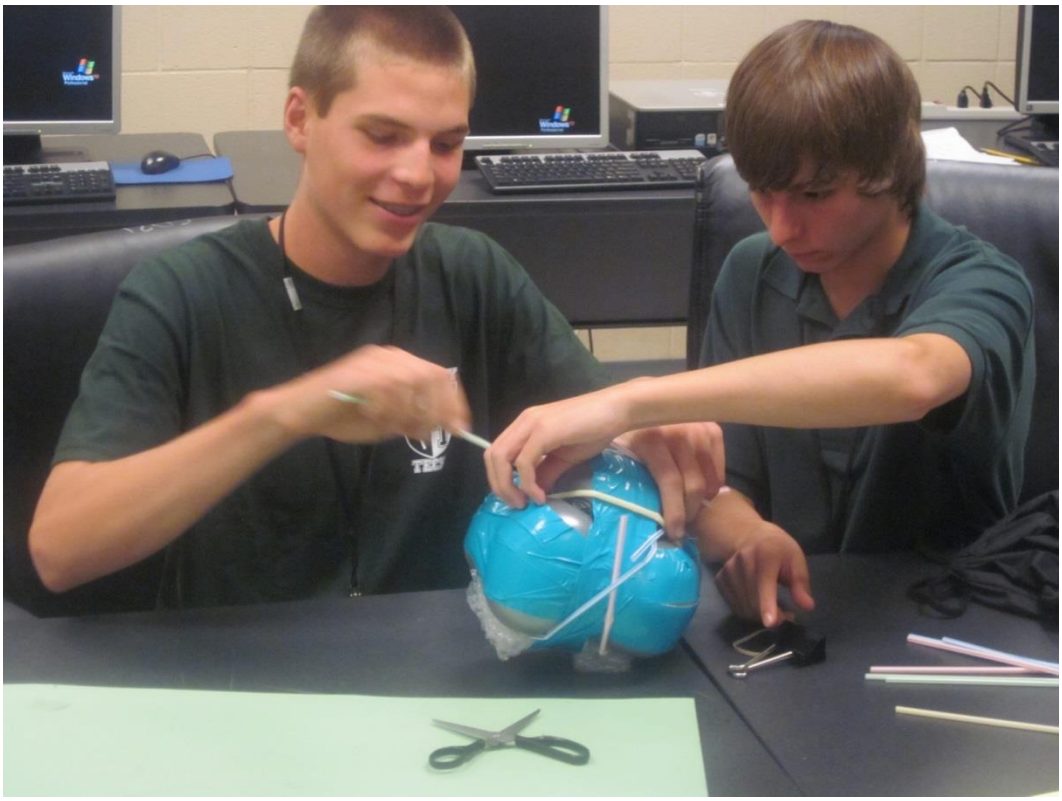

Figure 8.2. Photograph of freshmen in the CADD shop building an egg drop survival device.

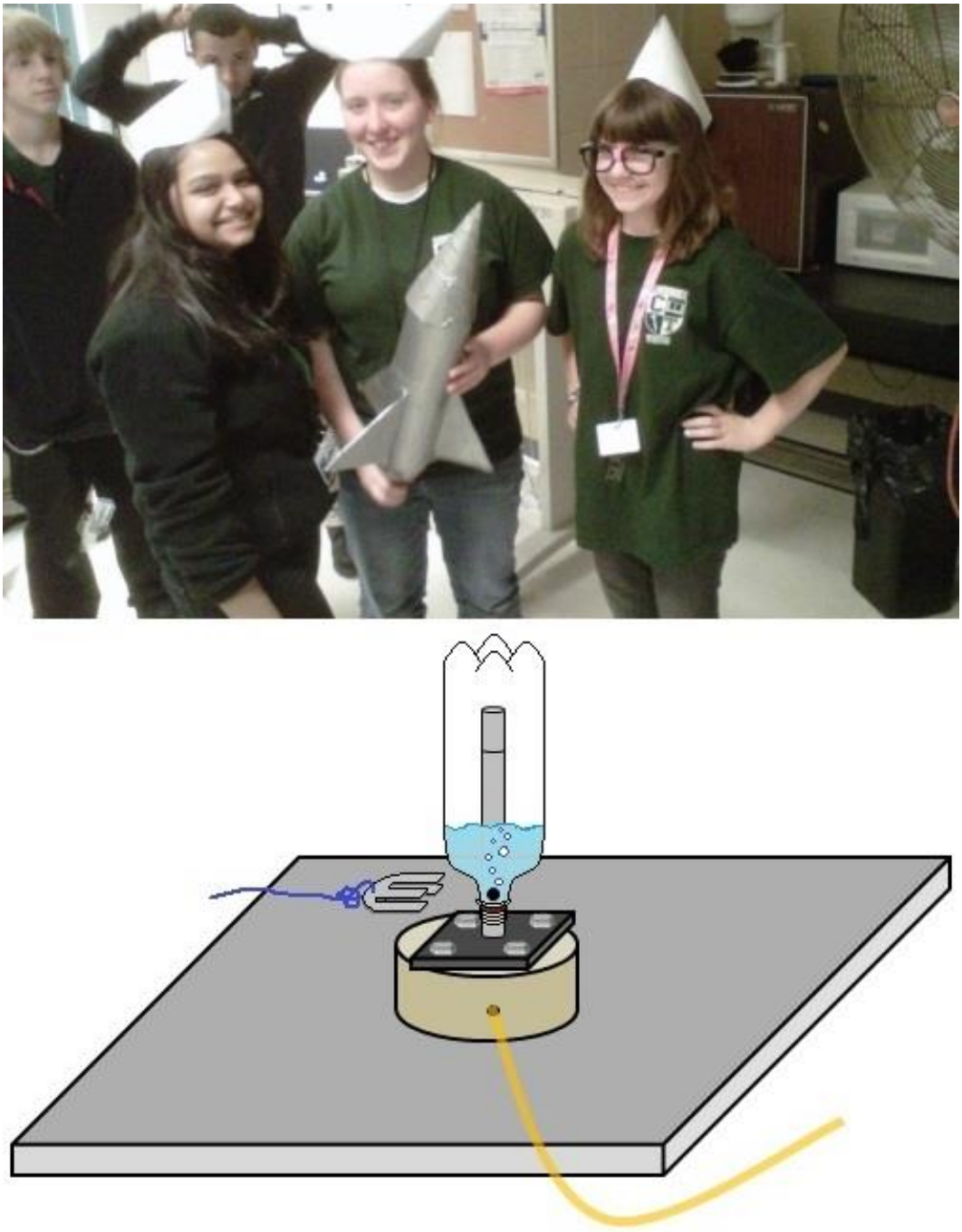

Figure 8.3. Photograph of students with their bottle rocket modified from a 2L soda bottle and diagram of custom-designed and built platform for launching the bottle rockets with compressed air.

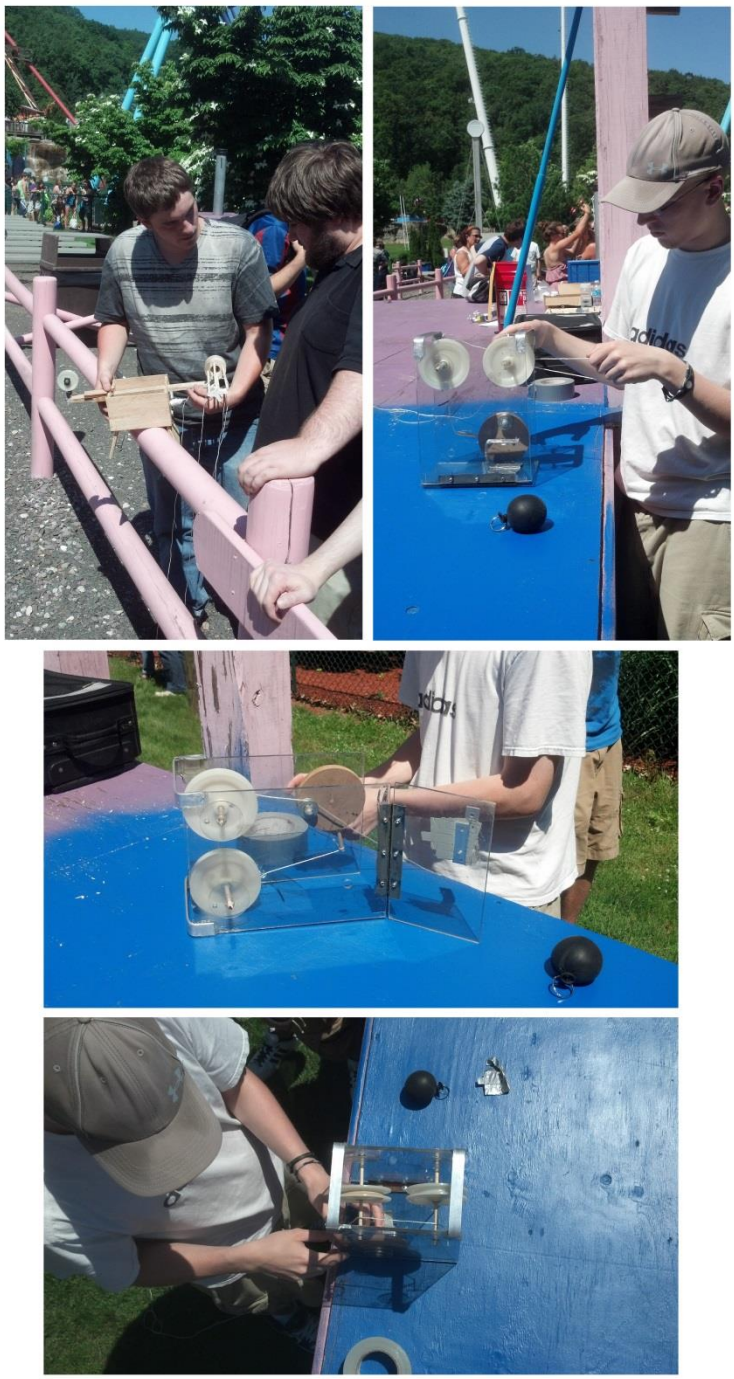

Figure 8.4. Photographs of senior CADD students working on their zipline bombers at a statewide competition held at Lake Compounce Amusement Park in Bristol, CT.

mathematical calculations to determine numerous parameters, including velocity and distance. The complexity of the zipline bombers showcased the seniors' ingenuity and engineering skills.

Another exciting event that students from all four grades participated in was a mousetrap car competition (see Figure 8.5). The students were tasked with creating small cars that were powered only by a single mousetrap, and they were scored based on three categories: total distance traveled, speed, and "closest to the pin"-type accuracy. The winning team at Cheney was then invited to UConn for an inter-school mousetrap car design competition that was held on May 17th, 2012. As a coordinator of this event, I helped by organizing the day's events and gathering and preparing the supplies used by the students for fabricating their mousetrap cars. Participating technical high schools with the GK-12 Program from around the state attended this inaugural event, and students' engineering skills and creativity were put to the test as both UConn faculty members and GK-12 Fellows judged their mousetrap car performances.

The largest project I initiated with the CADD shop was the complete design and fabrication of a vertical-axis wind turbine (VAWT) (see Figure 8.6 for photos of the completed VAWT and images of the alternator). This project took two full years to complete, and with the help of several other shops it was finally constructed and tested for power output. The VAWT was as much a learning

Figure 8.5. Photographs of students at Cheney Tech with their mousetrap cars.

Figure 8.6. Photographs of the VAWT, including alternator and various parts.

experience for me as it was for the CADD students who designed it. Together, we learned about wind turbines and power generation using an alternator. Fabrication of the alternator was especially interesting since it involved the use of exciting materials like powerful magnets and copper magnet wire. The VAWT gave the students experience working on a multifaceted project and they learned how to collaborate with other shops as they would in a real company setting.

I can say without a doubt that the GK-12 Program was one of the highlights of my time at UConn. I will always be grateful to NSF and UConn for awarding me this fellowship, and my visits to Cheney to work with the students and teachers provided lasting memories. In addition to my time at Cheney, working with the other GK-12 Fellows, and Program Director Aida Ghiaei and PIs Kazem Kazerounian and Doug Cooper, was an absolute joy and I am confident I've created friendships that will last beyond the GK-12 Program and my time at UConn.

YouTube links for UConn GK-12 videos:

- http://www.youtube.com/watch?v=-LEL1QyS2nA
- http://www.youtube.com/watch?v=z4hyKvGtl2g
- http://www.youtube.com/watch?v=UyHnJad31cQ
- http://www.youtube.com/watch?v=zsjT2o6zI1U
- http://www.youtube.com/watch?v=Gu8feshrVwY

SECTION V:

CONCLUSIONS

In this work, the morphology of NiO was controlled through the use of numerous synthesis procedures, and the resulting effects on its electrochemical reactivity were investigated. Multiple environment changes were studied, including an electrocatalyst additive and different media, both aqueous and non-aqueous. The reactivity of NiO was found to be strongly dependent on its morphology for both aqueous applications, such as the electrocatalytic oxidation of methanol, and non-aqueous applications, i.e. lithium-ion battery anodes. Environment changes such as varying the electrolyte or using a catalyst additive also revealed a distinct connection to the NiO reactivity, either through improved activity or the enabling of novel chemistry in the case of room temperature methane activation.

Electrocatalytic oxidation of methanol was studied using NiO synthesized using three different synthesis methods. Electrochemical tests were performed in both hydroxide and carbonate alkaline aqueous media, and carbonate electrolytes demonstrated average current ranges 3-4 times greater than hydroxide electrolytes of comparable alkalinity. Room temperature NaOH-precipitated NiO showed the highest activity and stability for methanol oxidation compared to reflux-precipitated NiO. Rapid degradation of electrocatalysts was attributed to microcracking and disintegration of the overcharged γ-NiOOH/α-$Ni(OH)_2$ redox couple, in addition to repeated scans in the oxygen evolution region.

Tetragonal-phase zirconia was used as a non-conducting electrocatalyst additive to facilitate the room temperature partial oxidation of methane to oxygenates. A $NiO\text{-}ZrO_2$ composite was synthesized using a co-precipitation technique and tested for electrocatalytic activity in both hydroxide and carbonate media. No activity was observed in hydroxide media; however, in carbonate media a new electrochemical reaction was observed in the presence of methane. Non-conducting ZrO_2 enabled adsorption of CO_3^{2-} anions and subsequent abstraction and donation of oxygen to active sites on NiO, which provided electronic conductivity and facilitated activation of adsorbed methane molecules. This discovery potentially opens the door for new avenues of research for alternative low temperature alkaline electrochemical devices operating on CO_3^{2-} as opposed to conventional OH^-.

Room temperature methane activation over the $NiO\text{-}ZrO_2$ composite electrocatalyst was further analyzed, and products were identified using ^1H-Nuclear Magnetic Resonance Spectroscopy and Mass Spectrometry. Oxygenates formed included CH_3OH, HCHO, CO, and $HCOO^-$, and O_2 and CO_2 were also observed likely as a result of carbonate electrolysis and/or the oxygen evolution reaction. The likely first step for CH_4 activation was the addition of oxygen to form methoxy (or methanol), followed by further reaction to HCHO and then CO. Theoretical pathways were proposed for the formation of all species observed,

and mechanisms for the creation of new C-O and C-C bonds were suggested.

For a non-aqueous application, NiO was studied as a high-capacity anode material for lithium-ion batteries. Two different synthesis methods were used to produce different NiO morphologies, and their performance was investigated in coin cells using Cyclic Voltammetry and charge/discharge tests. Degradation observed over repeated cycles was attributed to phase separation of the Li_2O+Ni and NiO phases and formation of large, inactive Li_2O particles. Li^+ diffusion coefficients were calculated using the current pulse relaxation technique, and a multiphase parallel resistance model was derived and applied to deconvolute the Li^+ diffusivity through the NiO and Li_2O+Ni phases during charge/discharge. These results suggest that controlled, nanosized crystallites of NiO should be preferred over bulk, macrosized particles to provide optimum cyclability and rate capacity.

Ordered mesoporous NiO was fabricated using a template-based synthesis procedure, and it was investigated as an anode for lithium-ion batteries. Identical-location TEM experiments were conducted to observe the progression of structural changes on individual OMNiO particles. Through identical-location TEM experiments, structural degradation was linked directly to capacity fade before and after multiple charge/discharge cycles. Conductive carbon black was also added in varying percentages to OMNiO anodes, and the results showed that

conductivity also plays a key role in the rate of capacity loss. Despite accelerated structural degradation observed through identical-location TEM images of OMNiO with 40% carbon black, the charge/discharge tests showed markedly improved cyclability and rate capability. This suggests that electronic conductivity, not structure, may be the most important characteristic to the performance of metal oxide anodes in next generation lithium-ion batteries.

SECTION VI:

RECOMMENDATIONS FOR

FUTURE WORK

For recommendations of future work, I can identify three main areas where more research would be greatly beneficial. The first area is in the membrane-electrode assembly procedure and materials used therein. Secondly, more in-depth analysis and quantification is needed for the room temperature activation of methane experiments. Finally, a more thorough investigation of the roles of conductivity and structure of metal oxide anodes for lithium-ion batteries would be important for determining the relative importance of both factors on rate capability and cyclability.

The current procedure for fabricating MEAs has a few limitations that could potentially inhibit future results. First, the maximum possible operating temperature allowed by the Ralex AM-PAD membranes is around 50°C, which prevents both operation at higher temperatures and the ability to hot press MEAs for better electrode contact. Second, the ionomer is only compatible with polar aprotic solvents, which eliminates the chance to use a more common and facile solvent like water or isopropanol for catalyst inks. Third, the ionomer has a narrow window of 30 minutes with which to work before it is fully polymerized, creating a major time constraint during fabrication. For future experiments, it would be useful to find new and better membrane and ionomer materials to improve MEA performance.

For the room temperature activation of methane, a more sophisticated

product analysis is needed to confirm and quantify product identities. In addition to ^{1}H-NMR and MS, techniques like Gas Chromatography and in-situ Attenuated Total Reflectance Fourier Transform Infrared Spectroscopy would provide detailed information on the oxygenates formed during reaction. Additionally, product selectivity can be examined by adjusting device parameters, such as cell voltage, flow rates, temperature, and cell construction.

To test whether conductivity or structure is the determining factor for NiO anodes in lithium-ion batteries, a series of tests is necessary which will vary both the NiO morphology and percentage of carbon black added. Different synthesis procedures for NiO can be used to produce numerous NiO structures, and increasing the carbon black present will improve conductivity. Charge/discharge, IL-TEM, and current pulse relaxation experiments should be carried out to investigate the effects of both factors on lithium-ion battery performance.

REFERENCES

[1] A. Atkinson, S. Barnett, R. Gorte, J. Irvine, A. McEvoy, M. Mogensen, S. Singhal, and J. Vohs, *Nat. Mater.*, **3**, 17 (2004).

[2] R. Beck, P. Maroni, D. Papageorgopoulos, T. Dang, M. Schmid, and T. Rizzo, *Science*, **302**, 98 (2003).

[3] G. Olah, B. Gupta, M. Farina, J. Felberg, W. Ip, A. Husain, R. Karpeles, K. Lammertsma, A. Melhotra, and N. Trivedi, *J. Am. Chem. Soc.*, **107**, 7097 (1985).

[4] B. Steele, *Nature*, **400**, 619 (1999).

[5] A. El-Shafei, *J. Electroanal. Chem.*, **471**, 89 (1999).

[6] M. Rahim, R. Hameed, and M. Khalil, *J. Power Sources*, **134**, 160 (2004).

[7] K. Nagashree and M. Ahmed, *J. Solid State Electrochem.*, **14**, 2307 (2010).

[8] J. Kubisztal and A. Budniok, *Int. J. Hydrogen Energy*, **33**, 4488 (2008).

[9] I. Danaee, M. Jafarian, F. Forouzandeh, F. Gobal, and M. Mahjani, *Int. J. Hydrogen Energy*, **33**, 4367 (2008).

[10] M. Wu, C. Yang, and M. Wang, *Electrochim. Acta*, **54**, 155 (2008).

[11] A. Golikand, S. Shahrokhian, M. Asgari, M. Maragheh, L. Irannejad, and A. Khanchi, *J. Power Sources*, **144**, 21 (2005).

[12] I. Casella and M. Gatta, *J. Electrochem. Soc.*, **149**, B465 (2002).

[13] J. Estellé, P. Salagre, Y. Cesteros, M. Serra, F. Medina, and J. Sueiras, *Solid State Ionics*, **156**, 233 (2000).

[14] C. Yu, L. Zhang, J. Shi, J. Zhao, J. Gao, and D. Yan, *Adv. Funct. Mater.*, **18**, 1544 (2008).

[15] M. Marciuš, M. Ristić, M. Ivanda, and S. Musić, *J. Mol. Struct.*, **1044**, 231 (2013).

[16] J. Azurdia, A. McCrum, and R. Laine, *J. Mater. Chem.*, **18**, 3249 (2008).

[17] I. Garduño-Wilches and J. Alonso, *Int. J. Hydrogen Energy*, **38**, 4213 (2013).

[18] J. Yu and D. Kim, *Powder Technol.*, **235**, 1030 (2013).

[19] H. Kim, C. Kim, and S. Kim, *J. Non-Cryst. Solids*, **352**, 2204 (2006).

[20] L. Kadam and P. Patil, *Sol. Energy Mater. Sol. Cells*, **69**, 361 (2001).

[21] U. Muecke, N. Luechinger, L. Schlagenhauf, and L. Gauckler, *Thin Solid Films*, **517**, 1522 (2009).

[22] W. Xing, F. Li, Z. Yan, and G. Lu, *J. Power Sources*, **134**, 324 (2004).

[23] C. Liu and Y. Li, *J. Alloys Compd*, **478**, 415 (2009).

[24] Y. Hattori, T. Konishi, and K. Kaneko, *Chem. Phys. Lett.*, **355**, 37 (2002).

[25] C. Wang, G. Gau, S. Gau, C. Tang, and J. Bi, *Catal. Lett.*, **101**, 241 (2005).

[26] Q. Song, Y. Li, and S. Chan, *J. Appl. Electrochem.*, **35**, 157 (2005).

[27] T. Ramesh and P. Kamath, *J. Power Sources*, **156**, 655 (2006).

[28] M. Fleischmann, K. Korinek, and D. Pletcher, *J. Electroanal. Chem.*, **31**, 39 (1971).

[29] A. Golikand, J. Raoof, M. Baghayeri, M. Asgari, and L. Irranejad, *Russ. J. Electrochem.*, **45**, 192 (2009).

[30] R. Singh, A. Singh, D. Mishra, Anindita, and P. Chartier, *J. Power Sources*, **185**, 776 (2008).

[31] J. Tarascon and M. Armand, *Nature*, **414**, 359 (2001).

[32] N. Choi, Z. Chen, S. Freunberger, X. Ji, Y. Sun, K. Amine, G. Yushin, L. Nazar, J. Cho, and P. Bruce, *Angew. Chem. Int. Ed.*, **51**, 9994 (2012).

[33] K. Mizushima, P. Jones, P. Wiseman, and J. Goodenough, *Mat. Res. Bull.*, **15**, 783 (1980).

[34] A. Padhi, K. Nanjundaswamy, and J. Goodenough, *J. Electrochem. Soc.*, **144**, 1188 (1997).

[35] R. Yazami and P. Touzain, *J. Power Sources*, **9**, 365 (1983).

[36] M. Reddy, G. Subba Rao, and B. Chowdari, *Chem. Rev.*, **113**, 5364 (2013).

[37] B. Dunn, H. Kamath, and J. Tarascon, *Science*, **334**, 928 (2011).

[38] P. Poizot, S. Laruelle, S. Grugeon, L. Dupont, and J. Tarascon, *Nature*, **407**, 496 (2000).

[39] Y. Oumellal, A. Rougier, G. Nazri, J. Tarascon, and L. Aymard, *Nat. Mater.*, **7**, 916 (2008).

[40] J. Feng, M. Lai, and L. Lu, *Mat. Res. Bull.*, **47**, 1693 (2012).

[41] W. Wei, Z. Wang, Z. Liu, Y. Liu, L. He, D. Chen, A. Umar, L. Guo, and J. Li, *J. Power Sources*, **238**, 376 (2013).

[42] C. Liang, M. Gao, H. Pan, Y. Liu, and M. Yan, *J. Alloys Compd.*, **575**, 246 (2013).

[43] Z. Chen, A. Xiao, Y. Chen, C. Zuo, S. Zhou, and L. Li, *Mater. Res. Bull.*, **47**, 1987 (2012).

[44] X. Huang, J. Tu, X. Xia, X. Wang, and J. Xiang, *Electrochem. Commun.*, **10**, 1288 (2008).

[45] S. Needham, G. Wang, and H. Liu, *J. Power Sources*, **159**, 245 (2006).

[46] M. Wu and Y. Lin, *Electrochim. Acta*, **56**, 2068 (2011).

[47] S. Sloop, J. Kerr, and K. Kinoshita, *J. Power Sources*, **119-121**, 330 (2003).

[48] X. Huang, J. Tu, Z. Zeng, J. Xiang, and X. Zhao, *J. Electrochem. Soc.*, **155**, A438 (2008).

[49] Y. Yuan, X. Xia, J. Wu, J. Yang, Y. Chen, and S. Guo, *Electrochem. Commun.*, **12**, 890 (2010).

[50] B. Varghese, M. Reddy, Z. Yanwu, C. Lit, T. Hoong, G. Rao, B. Chowdari, A. Wee, C. Lim, and C. Sow, *Chem. Mater.*, **20**, 3360 (2008).

[51] X. Yan, X. Tong, J. Wang, C. Gong, M. Zhang, and L. Liang, *J. Alloys Compd.*, **556**, 56 (2013).

[52] Y. NuLi, P. Zhang, Z. Guo, H. Liu, J. Yang, and J. Wang, *Mater. Res. Bull.*, **44**, 140 (2009).

[53] Y. Mai, J. Tu, X. Xia, C. Gu, and X. Wang, *J. Power Sources*, **196**, 6388 (2011).

[54] I. Kottegoda, N. Idris, L. Lu, J. Wang, and H. Liu, *Electrochim. Acta*, **56**, 5815 (2011).

[55] Y. Zhu, G. Cao, J. Xie, T. Zhu, and X. Zhao, *Nanosci. Nanotechnol. Lett*., **4**, 35 (2012).

[56] X. Huang, J. Tu, B. Zhang, C. Zhang, Y. Li, Y. Yuan, and H. Wu, *J. Power Sources*, **161**, 541 (2006).

[57] H. Liu, G. Wang, J. Liu, S. Qiao, and H. Ahn, *J. Mater. Chem*., **21**, 3046 (2011).

[58] M. Etheridge, L. Steele, R. Langenfelds, R. Francey, J. Barnola, and V. Morgan, "Historical CO_2 record from the Law Dome DE08, DE08-2, and DSS ice cores (atmospheric CO_2 concentrations, Antarctic ice cores)", in: *Trends: A Compendium of Data on Global Change*, online at the Carbon Dioxide Information Analysis Center, <http://cdiac.esd.ornl.gov/>, June 1998.

[59] C. Keeling and T. Whorf. "Atmospheric CO_2 records from sites in the SiO air sampling network", in: *Trends: A Compendium of Data on Global Change*. Carbon Dioxide Information Analysis Center, Oak Ridge National Laboratory, U. S. Department of Energy, Oak Ridge, TN, USA, 2005.

[60] S. Levin, *Ecology*, **73**, 1943 (1992).

[61] J. Melillo, A. Mcguire, D. Kicklighter, B. Moore, C. Vorosmarty, and A. Schloss, *Nature*, **363**, 234 (1993).

[62] D. Schimel, *Glob. Change Biol.*, **1**, 77 (1995).

[63] N. Spinner, J. Vega, and W. Mustain, *Catal. Sci. Technol.*, **2**, 19, (2012). Reproduced by permission of The Royal Society of Chemistry. <http://pubs.rsc.org/en/content/articlelanding/2012/cy/c1cy00314c#!divAbstract>

[64] V. Belyaev, V. Galvita, and V. Sobyanin, *React. Kinet. Catal. Lett.*, **63**, 341 (1998).

[65] T. Huang and C. Chou, *Electrochem. Comm.*, **11**, 1464 (2009).

[66] T. Kim, S. Moon, and S. Hong, *Appl. Catal. A-Gen.*, **224**, 111 (2002).

[67] V. Choudhary, A. Rajput, and B. Prabhakar, *Catal. Lett.*, **32**, 391 (1995).

[68] F. Bidrawn, G. Kim, G. Corre, J. Irvine, J. Vohs, and R. Gorte, *Electrochem. Solid St.*, **11**, B167 (2008).

[69] S. Furukawa, M. Okada, and Y. Suzuki, *Energy Fuel*, **13**, 1074 (1999).

[70] H. Yano, F. Shirai, M. Nakayama, and K. Ogura, *J. Electroanal. Chem.*, **533**, 113 (2002).

[71] C. Delacourt, P. Ridgway, J. Kerr, and J. Newman, *J. Electrochem. Soc.*, **155**, B42 (2008).

[72] M. Shibata and N. Furuya, *Electrochim. Acta*, **48**, 3953 (2003).

[73] M. Gattrell, N. Gupta, and A. Co, *J. Electroanal. Chem.*, **594**, 1 (2006).

[74] M. Gattrell, N. Gupta, and A. Co, *Energy Convers. Manage.*, **48**, 1255 (2007).

[75] M. Gonçalves, A. Gomes, J. Condeço, R. Fernandes, T. Pardal, C. Sequeira, and J. Branco, *Energy Convers. Manage.*, **51**, 30 (2010).

[76] K. Ogura, R. Oohara, and Y. Kudo, *J. Electrochem. Soc.*, **152**, D213 (2005).

[77] H. Yano, T. Tanaka, M. Nakayama, and K. Ogura, *J. Electroanal. Chem.*, **565**, 278 (2004).

[78] J. Yano, T. Morita, K. Shimano, Y. Nagami, and S. Yamasaki, *J. Solid State Electrochem.*, **11**, 554 (2007).

[79] S. Ikeda, T. Takagi, and K. Ito, *B. Chem. Soc. Jpn.*, **60**, 2517 (1987).

[80] H. Yano, F. Shirai, M. Nakayama, and K. Ogura, *J. Electroanal. Chem.*, **519**, 93 (2002).

[81] A. Bard and L. Faulkner, *Electrochemical Methods, Fundamentals and Applications, Second Edition*. John Wiley & Sons, New Jersey, 2001.

[82] B. Smith, D. Irish, P. Kedzierzawski, and J. Augustynski, *J. Electrochem. Soc.*, **144**, 4288 (1997).

[83] M. Shibata and N. Furuya, *J. Electroanal. Chem.*, **507**, 177 (2001).

[84] S. Narayanan, B. Haines, J. Soler, and T. Valdez, *J. Electrochem. Soc.*, **158**, A167 (2011).

[85] M. Saha, T. Furuta, and Y. Nishiki, *Electrochem. Comm.*, **6**, 201 (2004).

[86] N. Sonoyama and T. Sakata, *Chem. Lett.*, **31**, 444 (2002).

[87] C. Sanchez-Sanchez, V. Montiel, D. Tryk, A. Aldaz, and A. Fujishima, *Pure Appl. Chem.*, **73**, 1917 (2001).

[88] Z. Yoshida, H. Yosue, and G. Nogami, *J. Electrochem. Soc.*, **148**, D55 (2001).

[89] S. Kaneco, K. Iiba, M. Yabuuchi, N. Nishio, H. Ohnishi, H. Katsumata, T. Suzuki, and K. Ohta, *Ind. Eng. Chem. Res.*, **41**, 5165 (2002).

[90] S. Kaneco, H. Katsumata, T. Suzuki, and K. Ohta, *Energy Fuel*, **20**, 409 (2006).

[91] S. Kaneco, Y. Ueno, H. Katsumata, T. Suzuki, and K. Ohta, *Chem. Eng. J.*, **119**, 107 (2006).

[92] S. Kaneco, R. Iwao, K. Iiba, S. Itoh, K. Ohta, and T. Mizuno, *Environ. Eng. Sci.*, **16**, 131 (1999).

[93] R. Aydin and F. Köleli, *Synthetic Met.*, **144**, 75 (2004).

[94] R. Aydin and F. Köleli, *J. Electroanal. Chem.*, **535**, 107 (2002).

[95] E. Gülzow, *J. Power Sources*, **61**, 99 (1996).

[96] A. Tewari, V. Sambhy, M. Macdonald, and A. Sen, *J. Power Sources*, **153**, 1, (2006).

[97] S. Suzuki, H. Muroyama, T. Matsui, and K.Eguchi, *Electrochim. Acta*, **88**, 552 (2013).

[98] E. Gülzow and M. Schulze, *J. Power Sources*, **127**, 243 (2004).

[99] M. Unlu, J. Zhou, and P. Kohl, *Electrochem. Solid State Lett.*, **12**, B27 (2009).

[100] C. Lang, K. Kim, and P. Kohl, *Electrochem. Solid State Lett.*, **9**, A545 (2006).

[101] J. Zhou, M. Unlu, J. Vega, and P. Kohl, *J. Power Sources*, **190**, 285 (2009).

[102] J. Vega, C. Chartier, and W. Mustain, *J. Power Sources*, **195**, 7176 (2010).

[103] J. Varcoe and R. Slade, *Fuel Cells*, **5**, 187 (2005).

[104] J. Vega, S. Smith, and W. Mustain, *J. Electrochem. Soc.*, **158**, B349 (2011).

[105] J. Vega, S. Shrestha, M. Ignatowich, and W. Mustain, *J. Electrochem. Soc.*, **159**, B12 (2011).

[106] J. Vega, N. Spinner, M. Catanese, and W. Mustain, *J. Electrochem. Soc.*, **159**, B18 (2011).

[107] N. Spinner and W. Mustain, *Electrochim. Acta*, **56**, 5656 (2011).

[108] N. Spinner and W. Mustain, *ECS Trans.*, **35**, 43 (2011).

[109] J. Zhu et al, *Mater. Lett.*, **58**, 3324 (2004).

[110] Q. Song, C. Chiu, and S. Chan, *J. Appl. Electrochem.*, **36**, 97 (2006).

[111] T. Ramesh and P. Kamath, *Mater. Res. Bull.*, **43**, 2827 (2008).

[112] M. Morishita et al, *J. Electrochem. Soc.*, **155**, A936 (2008).

[113] Y. Dwivedi and S. Rai, *J. Am. Ceram. Soc.*, **93**, 727 (2010).

[114] B. Mani and J. de Neufville, *Mat. Res. Bull.*, **19**, 377 (1984).

[115] M. Lenglet, F. Hochu, J. Dürr, and M. Tuilier, *Solid State Commun.*, **104**, 793 (1997).

[116] C. Li, A. Proctor, and D. Hercules, *Appl. Spectrosc.*, **38**, 880 (1984).

[117] P. Selvam, B. Viswanathan, and V. Srinivasan, *J. Electron Spectrosc. Relat. Phenom.*, **49**, 203 (1989).

[118] B. Löchel and H. Strehblow, *J. Electrochem. Soc.*, **131**, 713 (1984).

[119] N. McIntyre and M. Cook, *Anal. Chem.*, **47**, 2208 (1975).

[120] K. Nagashree and M. Ahmed, *Synth. Met.*, **158**, 610 (2008).

[121] J. Vega and W. Mustain, *Electrochim. Acta*, **55**, 1638 (2010).

[122] M. Sattar and B. Conway, *Electrochim. Acta*, **14**, 695 (1969).

[123] G. Snook, N. Duffy, and A. Pandolfo, *J. Electrochem. Soc.*, **155**, A262 (2008).

[124] H. Bode, K. Dehmelt, and J. Witte, *Electrochim. Acta*, **11**, 1079 (1966).

[125] J. Luo et al, *Catal. Today*, **99**, 291 (2005).

[126] T. Page, R. Johnson, J. Hormes, S. Noding, and B. Rambabu, *J. Electroanal. Chem.*, **485**, 34 (2000).

[127] N. Priyantha, P. Jayaweera, D. Macdonald, and A. Sun, *J. Electroanal. Chem.*, **572**, 409 (2004).

[128] N. Spinner and W. Mustain, *J. Electrochem. Soc.*, **159**, E187 (2012). Reproduced by permission of The Electrochemical Society. <http://jes.ecsdl.org/content/159/12/E187.full.pdf+html?sid=e6e37861-8ab1-4bce-abeb-7b6f5794203a>

[129] T. Ramesh and P. Kamath, *Electrochim. Acta*, **53**, 8324 (2008).

[130] Z. Xu and H. Zeng, *Chem. Mater.*, **11**, 67 (1999).

[131] T. Dickinson, A. Povey, and P. Sherwood, *J. Chem. Soc. Farad. Trans. I,* **73**, 327 (1977).

[132] C. Wagner, D. Zatko, and R. Raymond, *Anal. Chem.*, **52**, 1445 (1980).

[133] S. Sinha, S. Badrinarayanan, and A. Sinha, *J. Less-Common Met.*, **125**, 85 (1986).

[134] S. Guerrero, P. Araya, and E. Wolf, *Appl. Catal. A: Gen.*, **298**, 243 (2006).

[135] A. Bhagwat, A. Ramaswamy, A. Tyagi, and V. Ramaswamy, *Mater. Res. Bull.*, **38**, 1713 (2003).

[136] Z. Zhang, J. Liu, F. Wang, J. Kong, and X. Wang, *Ceram. Int.*, **37**, 2549 (2011).

[137] J. Makinson, J. Lee, S. Magner, R. De Angelis, W. Weins, and A. Hieronymus, *JCPDS-Int. Ctr. Diffr. Data, Adv. X-ray Anal.*, **42**, 407 (2000).

[138] M. Wu and H. Hsieh, *Electrochim. Acta*, **53**, 3427 (2008).

[139] H. Zhu et al., *Mater. Lett.*, **58**, 3107 (2004).

[140] S. Liu, L. Liao, Q. Tao, Y. Chen, and S. Ye, *Phys. Chem. Chem. Phys.*, **13**, 9725 (2008).

[141] Y. Amenomiya, V. Birss, M. Goledzinowski, J. Galuszka, and A. Sanger, *Catal. Rev. Sci. Technol.*, **32**, 163 (1990).

[142] N. Spinner and W. Mustain, *J. Electrochem. Soc.*, **160**, F1275 (2013). Reproduced by permission of The Electrochemical Society.

<http://jes.ecsdl.org/content/160/11/F1275.full.pdf+html?sid=e6e37861-8ab1-4bce-abeb-7b6f5794203a>

[143] N. Spinner and W. Mustain, *ECS Trans.*, **53**, 1 (2013).

[144] A. Couper, D. Pletcher, and F. Walsh, *Chem. Rev.*, **90**, 837 (1990).

[145] Z. Ma, C. Yang, W. Wei, W. Li, and Y. Sun, *J. Mol. Catal. A: Chem.*, **227**, 119 (2005).

[146] H. Ahn and T. Marks, *J. Am. Chem. Soc.*, **120**, 13533 (1998).

[147] B. Samaranch, P. Piscina, G. Clet, M. Houalla, P. Gélin, and N. Homs, *Chem. Mater.*, **19**, 1445 (2007).

[148] J. Schattka, D. Shchukin, J. Jia, M. Antonietti, and R. Caruso, *Chem. Mater.*, **14**, 5103 (2002).

[149] K. Kuhl, E. Cave, D. Abram, and T. Jaramillo, *Energy Environ. Sci.*, **5**, 7050 (2012).

[150] S. Bradley, A. Ouyang, J. Purdie, T. Smitka, T. Wang, and A. Kaemer, *J. Am. Chem. Soc.*, **132**, 9531 (2010).

[151] H. Gottlieb, V. Kotlyar, and A. Nudelman, *J. Org. Chem.*, **62**, 7512 (1997).

[152] A. Peterson, F. Abild-Pedersen, F. Studt, J. Rossmeisl, and J. Nørskov, *Energy Environ. Sci.*, **3**, 1311 (2010).

[153] Y. Kwon, S. Lai, P. Rodriguez, and M. Koper, *J. Am. Chem. Soc.*, **133**, 6914 (2011).

[154] National Institute of Standards and Technology (NIST) Webbook, <http://webbook.nist.gov/cgi/cbook.cgi?ID=C50000&Units=SI&Mask=200#Mass-Spec>.

[155] N. Spinner and W. Mustain, *J. Electroanal. Chem.*, **711**, 8 (2013).

[156] K. Sing, *Pure & Appl. Chem.*, **54**, 2201 (1982).

[157] G. Girishkumar, B. McCloskey, A. Luntz, S. Swanson, and W. Wilcke, *J. Phys. Chem. Lett*., **1**, 2193 (2010).

[158] C. Wang, X. Zhang, A. Appleby, X. Chen, and F. Little, *J. Power Sources*, **112**, 98 (2002).

[159] K. Sawai and T. Ohzuku, *J. Electrochem. Soc.*, **150**, A674 (2003).

[160] T. Uchida, Y. Morikawa, H. Ikuta, M. Wakihara, and K. Suzuki, *J. Electrochem. Soc.*, **143**, 2606 (1996).

[161] J. Zhong, W. Xiang, H. Zhao, W. Zhao, G. Chen, and X. Liang, *J. Alloys Compd*., **537**, 269 (2012).

[162] N. Mahata, A. Cunha, J. Órfão, and J. Figueiredo, *Chem. Eng. J*., **188**, 155 (2012).

[163] S. Basu and W. Worrell, "Chemical diffusivity of lithium in Li_xTaS_2 and Li_xTiS_2 at 30°C", in: P. Vashishta, J. Mundy, G. Shenoy (Eds.), *Fast Ion Transport in Solids*, Elsevier, North Holland, 1979, pp. 149-152.

[164] J. Crank, *The Mathematics of Diffusion*, Clarendon Press, Oxford, 1956, pp. 9-12.

[165] B. Ratnakumar, G. Nagasubramanian, S. Di Stefano, and C. Bankston, *J. Electrochem. Soc*., **139**, 1513 (1992).

[166] J. Lee, K. An, J. Ju, B. Cho, W. Cho, D. Park, and K. Yun, *Carbon*, **39**, 1299 (2001).

[167] N. Kumagai, T. Fujiwara, K. Tanno, and T. Horiba, *J. Electrochem. Soc*., **140**, 3194 (1993).

[168] P. Fensham, *J. Am. Chem. Soc*., **76**, 969 (1953).

[169] Z. Wei, T. Xia, J. Ma, W. Feng, J. Dai, Q. Wang, and P. Yan, *Mater. Char*., **58**, 1019 (2007).

[170] Y. Zhuravlev, D. Korabel'nikov, and M. Aleinikova, *Phys. Solid State*, **54**, 1518 (2012).

[171] B. Taylor, C. Kuyatt, NIST Technical Note 1297, "Guidelines for Evaluating and Expresing the Uncertainty of NIST Measurement Results", U.S. Dept. of Commerce Technology Administration (1994) 7-8. <http://physics.nist.gov/Pubs/guidelines/TN1297/tn1297s.pdf> Accessed February 25th 2013.

[172] W. Preis, E. Bucher, and W. Sitte, *Fuel Cells*, **12**, 543 (2012).

[173] R. Montalvo-Lozano, S. Montemayor, K. Padmasree, and A. Fuentes, *J. Alloys Compd*., **525**, 184 (2012).

[174] N. Spinner, L. Zhang, and W. Mustain, *J. Mater. Chem. A*, **Accepted**. Reproduced by permission of The Royal Society of Chemistry.

[175] S. Shrestha and W. Mustain, *J. Electrochem. Soc.*, **157**, B1665 (2010).

[176] S. Shrestha, S. Asheghi, J. Timbro, and W. Mustain, *Carbon*, **60**, 28 (2013).

[177] F. Jiao, A. Hill, A. Harrison, A. Berko, A. Chadwick, and P. Bruce, *J. Am. Chem. Soc.*, **130**, 5262 (2008).

[178] H. Lu, L. Shi, W. Weng, C. Huang, and H. Wan, *Acta Phys. –Chim. Sin.*, **28**, 2697 (2012).

[179] E. Marceau, M. Che, J. Čejka, and A. Zukal, *ChemCatChem*, **2**, 413 (2010).

[180] M. Pinson and M. Bazant, *J. Electrochem. Soc.*, **160**, A243 (2013).

[181] J. Pan, Q. Huang, Z. Koh, D. Neo, X. Wang, and Q. Wang, *ACS Appl. Mater. Interfaces*, **5**, 6292 (2013).

[182] G. Aydogdu, D. Ruzmetov, and S. Ramanathan, *J. Appl. Phys.*, **108**, 113702 (2010).

[183] J. Keem and J. Honig, "Selected Electrical and Thermal Properties of Undoped Nickel Oxide", Cindas Report 52, West Lafayette, Indiana, August 1978.

[184] R. Sayer, J. Zeng, H. Hsu, D. Peroulis, and T. Fisher, *J. Microelectromech. Syst.*, **21**, 850 (2012).

[185] L. Dong, *Nanotechnology*, **20**, 465602 (2009).

[186] <http://ece-www.colorado.edu/~bart/book/>.

[187] K. Mayrhofer, J. Meier, S. Ashton, G. Wiberg, F. Kraus, M. Hanzlik, and M. Arenz, *Electrochem. Commun.*, **10**, 1144 (2008).

[188] K. Mayrhofer, S. Ashton, J. Meier, G. Wiberg, M. Hanzlik, and M. Arenz, *J. Power Sources*, **185**, 734 (2008).

[189] K. Schlögl, K. Mayrhofer, M. Hanzlik, and M. Arenz, *J. Electroanal. Chem.*, **662**, 355 (2011).

[190] A. Rai, L. Ahn, C. Park, and J. Kim, *Ceram. Int.*, **39**, 6611 (2013).

[191] S. Yang, H. Song, and X. Chen, *Electrochem. Commun.*, **8**, 137 (2006).

[192] O. Devos, C. Gabrielli, and B. Tribollet, *Electrochim. Acta*, **51**, 1413 (2006).

[193] Y. Yamada, T. Sasaki, N. Tatsuda, D. Weingarth, K. Yano, and R. Kötz, *Electrochim. Acta*, **81**, 138 (2012).

[194] B. Liu and S. Creager, *J. Power Sources*, **195**, 1812 (2010).